# ELASTIC STRESS WAVE PROPAGATION IN CELLULAR SYSTEMS

**LAN RAN**

**A THESIS SUBMITTED**

**FOR THE DEGREE OF MASTER OF ENGINEERING**

**DEPARTMENT OF MECHANICAL ENGINEERING**

**NATIONAL UNIVERSITY OF SINGAPORE**

**2004**

# ACKNOWLEDGEMENTS

I would like to express my sincere gratitude to my supervisor, Professor Victor P.W. Shim, for his dedicated supervision, guidance and constant encouragement throughout the project. I am also thankful to Dr. Yang Liming, as his enlightening suggestions have played a significant role towards the successful completion of the project.

I also wish to express my appreciation to Mr. Alvin Goh Tiong Lai, Mr. Joe Low Chee Wah, Mr. Chiam Tow Jong and Mr. Abdul Malik, technical staff from the Impact Mechanics and Strength of Materials Laboratories, for their assistance in the experimental phase of this study.

My appreciation also extends to all colleagues and friends in the Impact Mechanics Laboratory during the course of the project, for building a friendly environment for research.

# TABLE OF CONTENTS

# SUMMARY

In this study, elastic wave propagation through cellular systems (ring arrays) is investigated experimentally and analytically. Five types of metal rings, which differ in material, wall thickness and diameter, are packed in three different arrangements: square packed, transverse close packed and vertical close packed. The effects of these factors on elastic wave propagation are found through undertaking quasi-static and dynamic experiments on selected ring materials, single rings and ring arrays. A characteristic equation governing in-plane movements in a single ring is derived from first principles and solved for approximate solutions and numerical results; this yields theoretical velocity distributions for three modes of wave propagation ─ extensional, flexural and shear waves. A comparison between theoretical and experimental results shows that the group velocities detected from experiments exhibit good general correlation with the theoretical velocities of flexural waves. The effects of material property, ring wall thickness and wave frequency on wave propagation speed follow theoretical predictions. Application of the proposed theoretical model is limited to the long wavelength/low frequency spectrum and thin wall rings. However, as actual cellular materials and structures generally possess a low relative density (thin cell walls) and exhibit low-pass filter characteristics, the theoretical model presented has the potential to be utilized in analysing them.

# LIST OF SYMBOLS

| | |
|---|---|
| $\rho_s$ | Density of solid component of cellular material |
| $\rho^*$ | Overall density of cellular material |
| $\phi$ | Relative density of cellular material |
| $E$ | Young's modulus |
| $E^*$ | Apparent Young's modulus of cellular material |
| $E_S$ | Elastic modulus of ring material |
| $C_s$ | One-dimensional extensional wave speed ( $=\sqrt{\frac{E}{\rho}}$ ) |
| $C^*$ | Apparent wave speed through cellular system |
| $C_E^*$ | Apparent wave speed through ring diameter, obtained from impact test |
| $C_E$ | Propagation speed of stress wave along solid walls in cellular systems |
| $C_T^*$ | Apparent wave speed through ring diameter, defined by $\sqrt{\frac{E^*}{\rho^*}}$ , where $E^*$ and $\rho^*$ are determined experimentally. |
| $D$ | Outer diameter of ring |
| $R$ | Radius of ring |
| $h$ | Wall thickness of ring |
| $R_c$ | Radius to the centroid of the ring cross section, (= *R-h/2*) |
| $b$ | Width of ring |
| $\varepsilon$ | Strain |
| $\sigma$ | Stress |
| $\upsilon$ | Poisson's ratio |
| $G$ | Shear Modulus |
| $C_0$ | Velocity of elastic extensional waves in thin rods |
| $f$ | Frequency |

| | |
|---|---|
| $\lambda$ | Wavelength |
| $P, Q, M$ | Respective axial tension, shear and bending moment applied to a cross section |
| $\beta$ | Flexural rigidity of ring |
| $\sigma_p$ | Extensional rigidity |
| $\sigma_q$ | Shear rigidity |
| $k$ | Radius of gyration of cross section |
| $u, v$ | Displacements of centroid of ring cross section |
| $\omega$ | Circular wave frequency |
| $\eta$ | Wave number |
| $V$ | Phase velocity |
| $V_g$ | Group velocity |
| $T$ | Period of cycle |

# LIST OF FIGURES

# LIST OF TABLES

# CHAPTER ONE
# INTRODUCTION

Natural cellular materials are very common — wood, cork, sponge and coral are typical examples. People have used these materials for centuries and in modern times, have made synthetic cellular solids. Everyday examples include honeycomb arrangements used in structural components, polymeric foams and more recently, even foamed metals, ceramics and glasses. One common feature of these materials is that their volume comprises both solid and gas, the solid component generally constituting an interconnected network of struts or plates. Many of these newer foams are increasingly used for insulation, as cushioning, and in systems for absorbing kinetic energy in impacts.

Cellular structures are important for several reasons, both technical and commercial. Hilyard and Cunningham [1] have highlighted several advantages of cellular materials from a technical viewpoint:

1. high specific stiffness and strength
2. almost ideal energy absorption characteristics
3. facilitates ergonomic comfort .

These favourable characteristics make cellular materials suitable for structural applications, thermal and acoustic insulation, vibration damping, acoustic absorption, shock mitigation and other domestic applications.

In contrast with the large deformation response of cellular materials, the elastic behaviour of cellular materials, particularly in terms of dynamic responses, has been relatively less studied. With respect to stress wave propagation in cellular materials, researchers have generally adopted analyses applicable to homogeneous solids. A recent study has shown that this approach may not be valid [2]. The present investigation focuses on the dynamic analysis of an idealized representation of cellular materials to study and simulate stress wave transmission through actual materials. This will establish whether or not traditional continuum analysis applied to homogeneous materials without voids can be expanded to cellular structures, or whether an alternative approach must be adopted.

# CHAPTER TWO
# LITERATURE REVIEW

## 2.1 Structures of Cellular Solids

Gibson and Ashby have given a definition of a cellular solid as, *"A cellular solid is one made up of an interconnected network of solid struts or plates which form the edges and faces of cells."* [3]. They showed graphically three typical examples of cellular solids, as depicted in Figure 2-1 [3]. With regard to the three types of cellular solids, Fig. 2-1(a) shows a honeycomb which can be regarded as being primarily two-dimensional; the other two are three-dimensional and are foams. Open-celled foams contain only cell edges, while a closed-celled foam comprises cells sealed by solid faces. Apart from the material properties of the solid phase, the way the solid is distributed in the cell edges and faces critically determine the

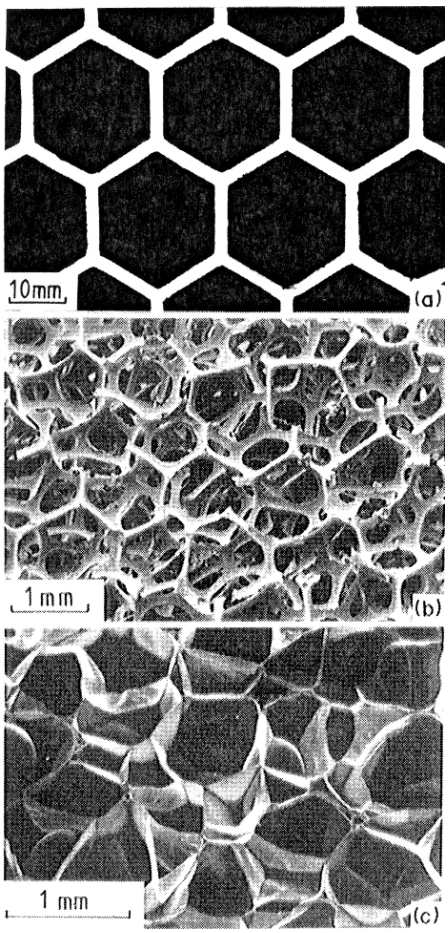


**Fig. 2-1** Examples of cellular solids: (a) a two-dimensional honeycomb; (b) a three-dimensional foam with open cells; (c) a three- dimensional foam with closed cells. [3]

properties of cellular materials. Gibson and Ashby have tried to quantify their structures by applying topological laws. They presented several shapes for a unit cell that can be packed together to fill a plane in two dimensions, as shown in Figure 2-2 [3]. With different packing arrangements, a single cell shape can yield structures with differing edge connectivities and properties (Figure 2-3) [3]. Many cell geometries that can be packed together to fill a three dimensional space have also been presented by Gibson and Ashby, as shown in Figure 2-4 [3].

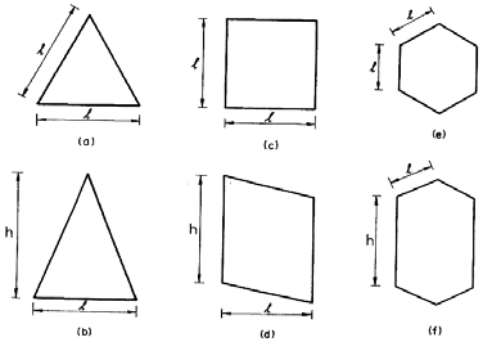

**Fig. 2-2** Polygons found in two-dimensional cellular materials: (a) equilateral triangle, (b) isosceles triangle, (c) square, (d) parallelogram, (e) regular hexagon, (f) irregular hexagon. [3]

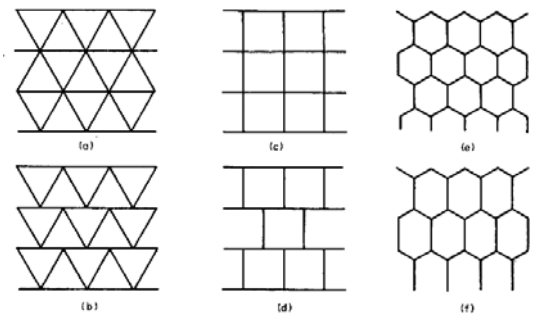

**Fig. 2-3** Packing of two-dimensional cells to fill a plane [3]

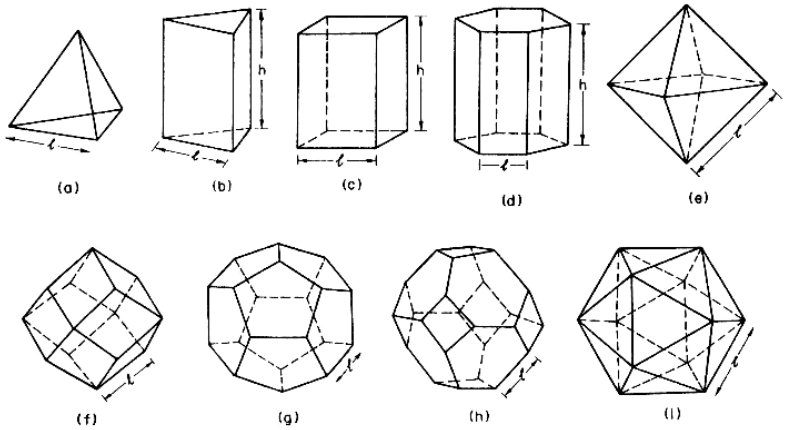

**Fig. 2-4** Three-dimensional polyhedral cells: (a) tetrahedron, (b) triangular prism, (c) rectangular prism, (d) hexagonal prism, (e) octahedron, (f) rhombic dodecahedron, (g) pentagonal dodecahedron, (h) tetrakaidecahedron, (i) icosahedron. [3]

## 2.2 Physical Behaviour of Cellular Materials – An Overview

Foaming dramatically expands the range of material properties of a homogeneous solid, such as the resultant physical, mechanical and thermal properties. By employing measurement methods similar to those used for homogeneous solids, four of these properties are shown in Fig 2-5 by Gibson and Ashby [3]; i.e. density, thermal conductivity, Young's modulus and compressive strength. The solid bars, representing foam properties, always cover a wider range than that of conventional solids (shaded bars). Compared with fully dense solids, cellular materials generally possess specific properties such as a low density, low thermal conductivity, low stiffness, low strength, high compressibility, etc. These properties bring foams into applications that cannot be fulfilled by homogeneous solids, e.g. thermal insulation, packaging, structural usage and buoyancy. Most of the foams produced today are used in these four areas. These various applications motivate research related to cellular materials; i.e. study of their thermal and heat transfer characteristics [4], impact response [5], energy absorption, acoustic properties [6], etc.

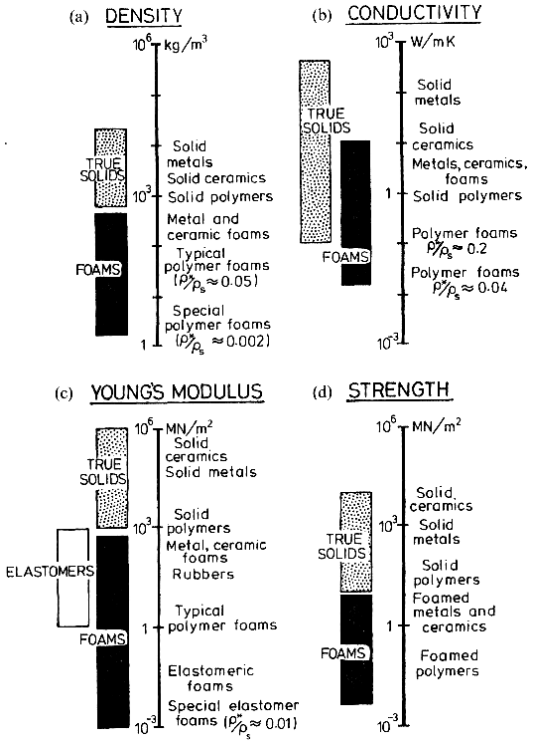


**Fig. 2-5** Range of properties available to the engineer through foaming: (a) density; (b) thermal conductivity; (c) Young's modulus; (d) compressive strength [3]

## 2.3 Relative Density－ A Unique Feature of Cellular Materials

A unique feature and arguably the most important one for cellular solids, is their relative density, $\rho^*/\rho_s$ — the ratio of the overall density of the cellular material $\rho^*$, to that of the solid from which the cell walls are made, $\rho_s$ [3]. Foams can be made with a relative density as low as 0.001. Cushioning and packaging foams generally possess relative densities ranging from 0.05 to 0.20. Natural porous materials such as soft woods and cork have values between 0.15 and 0.40. Materials with a relative density below 0.3 are termed cellular solids; those with values higher than this are better thought of as solids containing isolated pores. Gibson and Ashby provided two diagrams to demonstrate this difference, as shown in Figure 2-6. In this study, the focus is on cellular solids with relative densities of less than 0.3.

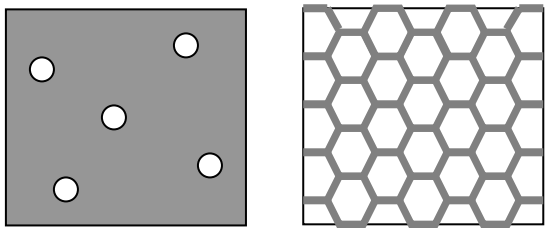

**Fig. 2-6** Comparison between a cellular solid and a solid with isolated pores [3].

The properties of a honeycomb or a foam depend primarily on its relative density. Although this definition is in terms of density, relative density is actually a dimensionless structural parameter, which represents the solid fraction contained in the total apparent volume of a cellular material. Therefore, relative density can be related to $t/l$, where $t$ is the cell wall thickness and $l$ is the cell edge length. Gibson and Ashby [3] concluded that "*the relative density of a honeycomb and of a closed-cell foam always scales as* $t/l$*; that of an open-celled foam as* $(t/l)^2$*, with a constant of proportionality near unity*". They have provided some expressions for relative density in terms of $t/l$; these are listed in Appendix I.

## 2.4 Investigation of the Elastic Moduli of Cellular Materials

The mechanical behaviour of cellular solids is determined by their structure and the mechanical behaviour of their components. Cellular plastics in particular, which are also referred to as foams, are available with a wide range of mechanical responses because they can be produced with very different cell structures and from various kinds of polymers. Practical engineering applications of these cellular plastics motivate investigation into their structure-property relationships.

In general, polymeric foams possess highly irregular three-dimensional cell structures, and their cell wall material exhibits nonlinear viscoelasticity. Polymeric foams are often expected to function under conditions involving large, complex deformations. Previous experimental and theoretical studies involving the mechanical properties of foams have mostly been concerned with static elastic behaviour.

The first theory to relate the apparent Young's modulus $E^*$ of an open-cell foam to the volume fraction of solid material $\phi$, was proposed by Gent and Thomas [7]. They modelled the foam structure as a collection of thin elastic threads of material that are connected by spherical joints which do not deform. They also assumed that when the foam is deformed, the displacement of the joints is affine; therefore, the motion of the thread ends is determined entirely by macroscopic deformation. The total strain energy of the foam is obtained by summing the contributions from individual, randomly oriented threads, which only deform by stretching. For low-density foams where $\phi$ is small, following result was obtained

$$\frac{E^*}{E} = \frac{\phi}{6} \qquad (2\text{-}1)$$

where $E$ is the Young's modulus of the solid material.

Gibson and Ashby [3] also tried to relate the ratio of these two moduli, $\frac{E^*}{E}$, to the relative density of cellular materials $\frac{\rho^*}{\rho_S}$. By representing an open-cell foam via a three-dimensional cubic model (Figure 2-7), they established a relationship between the ratio of the elastic moduli and the density ratio:

$$\frac{E^*}{E_S} = C\left(\frac{\rho^*}{\rho_S}\right)^n \qquad (2\text{-}2)$$

where $C$ is a constant involving all geometric constants of proportionality and $n$ is determined by the assumed deformation mode of the struts. In the case of $C$ = 1 and $n$ = 2, the proposed relationship predicted values that were close to experimental data.

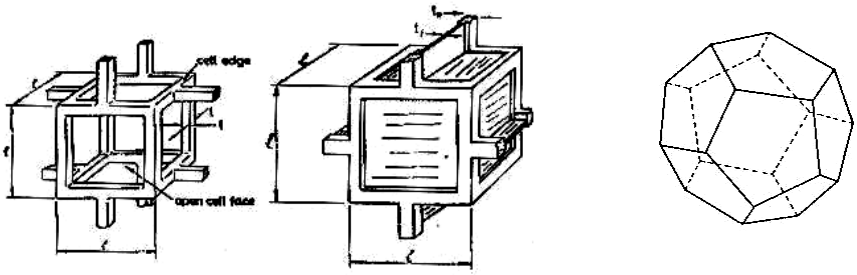


Open cell Closed cell (a) (b)

**Fig. 2-7** Modelling of a cell in cellular materials

(a) Three-dimensional Cube (Gibson & Ashby [3])
(b) Pentagonal Dodecahedron (Patel & Finnie [8])

To obtain more accurate relationships between the constants *C*, *n* and the cell-wall material properties, Patel and Finnie [8] studied more complex cell shapes such as the pentagonal dodecahedron. They found that such a geometry better approximates the physics of the foaming process in the formation of cellular materials.

## 2.5 Deformation Behaviour of Foams

Gibson and Ashby [3] classified the response of foams under compression into three types: elastomeric, elasto-plastic and elastic-brittle. Schematic stress-stain curves for these three types of responses are shown in Fig.2-8. Generally, three phases are found in each of these stress-stain curves: a linear elastic response at small strains, followed by an extended plateau and finally a steep rise in stress at large strains. Different deformation mechanisms are involved in each phase.

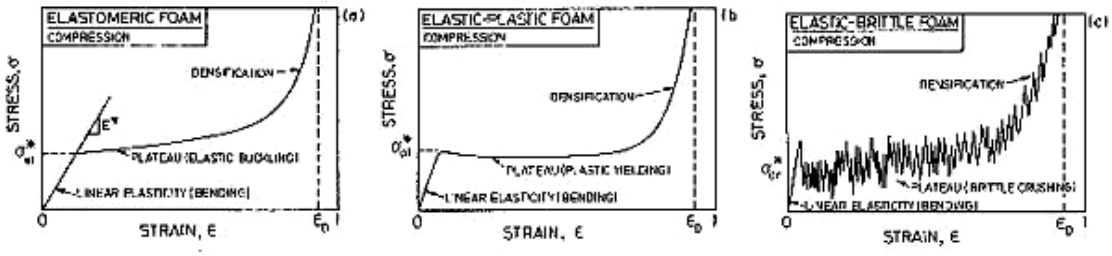


**Fig.2-8** Typical compressive stress-stain curves for foams (Gibson & Ashby [3]): (a) elastomeric foam, (b) elastic-plastic foam and (c) elastic-brittle foam.

For cellular materials, the initial elastic response corresponds to uniform deformation of cells, resulting from bending of cells walls and/or stretching of cell faces. In this phase, only a small fraction of the total strain occurs, and the apparent elastic modulus of the cellular material $E^*$ is defined by the initial slope of the stress-strain curve. Following the elastic response phase is a long collapse plateau. Here, the principal mode of deformation is the elastic buckling of cells in elastomeric foams, plastic yielding in elasto-plastic foams and brittle-crushing in elastic-brittle foams. The major portion of the total strain occurs in this phase and the crushing force does not change much, as shown in Figure 2-8. In the final phase, known as the densification region, the cell walls and/or faces have almost completely collapsed and cell material is compacted together as the strain further increases, resulting in the rapidly increasing stress.

The relative density of foam is a primary factor that affects the values of stress and strain demarcating each phase, but the general trend remains. For example, increasing the foam density will increase the apparent elastic modulus, raise the plateau stress and reduce the strain at which densification begins.

## 2.6 Elastic Wave Speed Through Cellular Solids

There is now interest in the dynamic response of cellular solids. The properties mentioned earlier — i.e. impact response and energy absorption, are some of the dynamic characteristic of a cellular material. Under dynamic loading, the response of a structure becomes time dependent. In many branches of engineering mechanics such as *statics, kinematics, solid-body dynamics, basic strength of materials* and *classical elasticity* theory, the entire body of interest is considered to be in equilibrium with the applied forces. However, when forces are applied over a short time duration and measurements or observations are made during these very small intervals of time, stress wave effects must be considered [9].

The theory of elastic stress wave propagation through homogeneous continua is well-established. From fundamental equations of motion for an element of material, the speed at which a one-dimensional extensional wave propagates can be shown to be defined by the elastic modulus and the material density.

$$C_s = \sqrt{\frac{E}{\rho}} \qquad (2\text{-}3)$$

With respect to a cellular solid, it is expected that this expression can be used to determine the elastic extensional wave speed through the cell wall material. However, from a macro or structural perspective, the stress in a cellular structure involves not only extensional stresses, but also flexure, shear, torsion, etc, on the solid microstructure. Furthermore, the paths along which the stresses travel in the solid phase of the cells are not straight, as voids or gas pockets exist within the material.

Prediction of the apparent wave speed at which stress travels through a block of cellular material, is therefore not a straightforward process. It requires information on the microstructure of the cells, such as cell size, shape and the way cells are packed. To avoid having to deal with complex microscopic details, some researchers have attempted to employ the apparent elastic modulus, $E^*$ and apparent density, $\rho^*$ in Eqn. (2-3). In their investigation on the response of one-dimensional metal ring systems to end impact [10, 11, 12], S. R. Reid *et al.* have used this approach to calculate the elastic wave speed through a single column of metal rings with and without plates separating adjacent rings. Figure 2-9 shows the plated and unplated rings chains used in their experiments. Table 2-1 shows the elastic wave speeds they measured along with the values calculated using Eqn. (2-3).

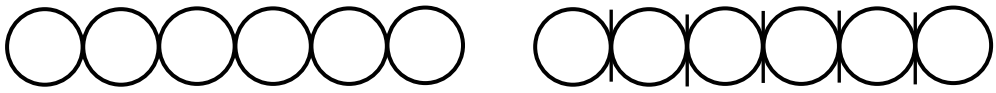

(a) Unplated ring chain (b) Plated ring chain

**Fig. 2-9** Ring chains used in the experiments conducted by S. R. Reid *et al.* [12]

**Table 2-1** Elastic wave speeds in mild steel ring chains ($D$ =50.8 mm, $h$ = 1.6 mm) [12]

| Type of Chain | $C_e$ (*m/s*) | |
|---|---|---|
| | Theory | Experiment |
| Unplated | 189.2 | 170.9 |
| Plated | 133.8 | 120.7 |

From the results shown in Table 2-1, Reid *et al.* thought that the observed elastic wave speeds appears to agree reasonably well with theoretical results based on equation (2-3). However, it should be noted that this was based on a very limited number of experiments. They considered only one size of mild steel rings with a 50.8 mm diameter and 1.6 mm wall thickness, in one packing arrangement of a single column. Tests on a single configuration may not be conclusive with regard to the elastic wave speed being governed by the apparent elastic modulus and apparent density. Furthermore, the fact that the elastic waves transmitting in the plated ring chain are slower that that in the unplated ring chain is most probably because they were delayed by the plates placed between adjacent rings. Therefore, further investigation needs to be undertaken to examine whether or not traditional continuum analysis applied to homogeneous materials without voids can be expanded to accommodate cellular structures, or whether an alternative approach must be adopted.

In general, the propagation of elastic waves is dispersive. Characteristic equations of wave motion show the relationship between the phase velocity of the wave, the wavelength, the lateral dimensions and material properties. Starting with the general theory of elasticity and applying the boundary conditions, the exact theory is so complex that only a few simple cases have exact characteristic equations. A number of approximate theories have thus been developed. There are three levels of approximation in the analysis of flexural waves in a straight rod. In elementary theory, also called the Bernoulli-Euler theory, it is assumed that plane sections originally normal to the centroidal axis of the beam remain plane and normal to the deformed axis after bending. The next level of approximation assumes that elements undergo rigid body rotation in addition to transverse motion; this corresponds to the

Rayleigh theory [13]. As a further refinement, the analysis by Timoshenko [14, 15], assumed that elements are subjected to shear stresses in addition to transverse motion and rigid body rotation. Figure 2-10 [16] shows a comparison between results for flexural waves based on these three theories and exact theory. It is seen that the Timoshenko theory agrees best with exact theory.

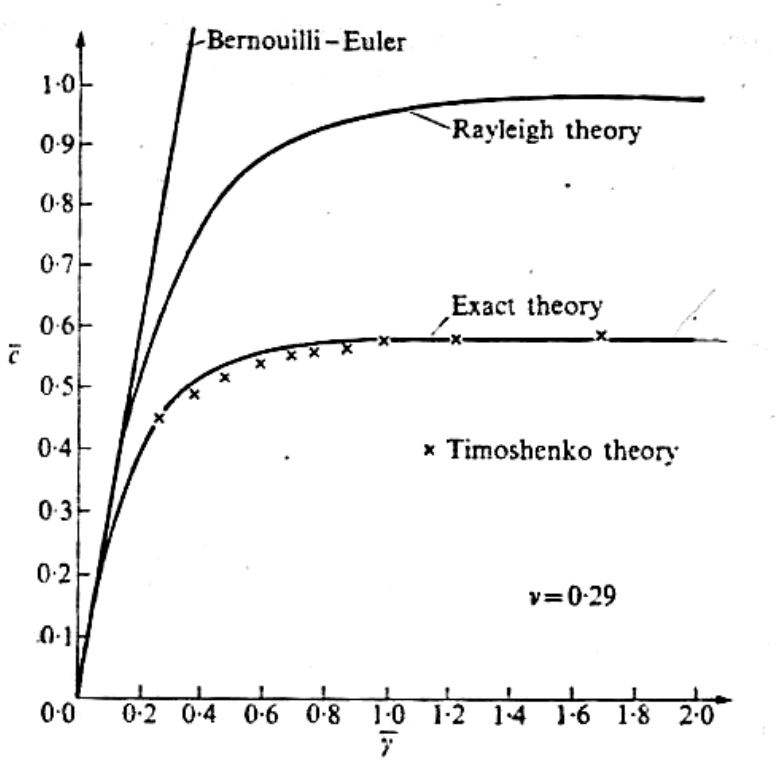


**Fig. 2-10** Dispersion relations from Timoshenko, exact, Rayleigh and Bernoulli-Euler beam theories [16, 20]

In Morley's theoretical approach [17] to wave motion in a circular ring, correction for radial shear was incorporated, as was done by the Timoshenko theory. The non-dimensional phase velocity distribution according to Morley's theory is shown graphically in Figure 2-11. The three branches of the dispersion curves shown in the figure are associated with flexural, longitudinal and radial shear modes.

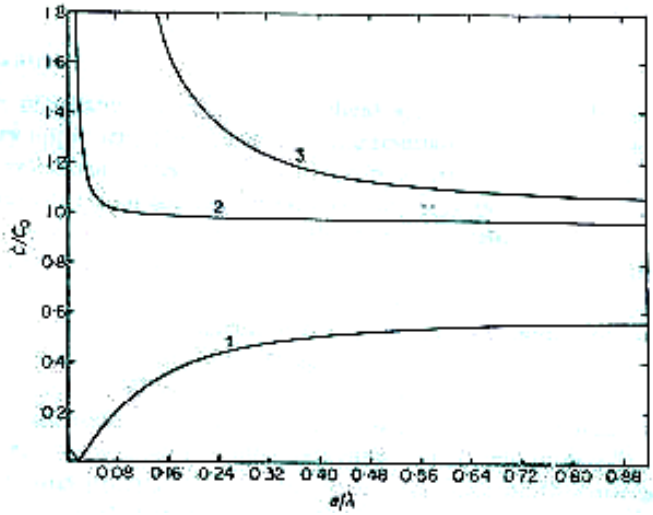


**Fig. 2-11** Phase velocity distributions based on the Morley theory for a ring with *a/R*=0.106 [18]
$C_0$ is the phase velocity of extensional waves in a straight thin bar, given by $\sqrt{E/\rho}$
*a* is the radius of the circular cross section of the ring
Curves 1, 2 and 3 are respectively associated with flexural, longitudinal and radial shear modes.

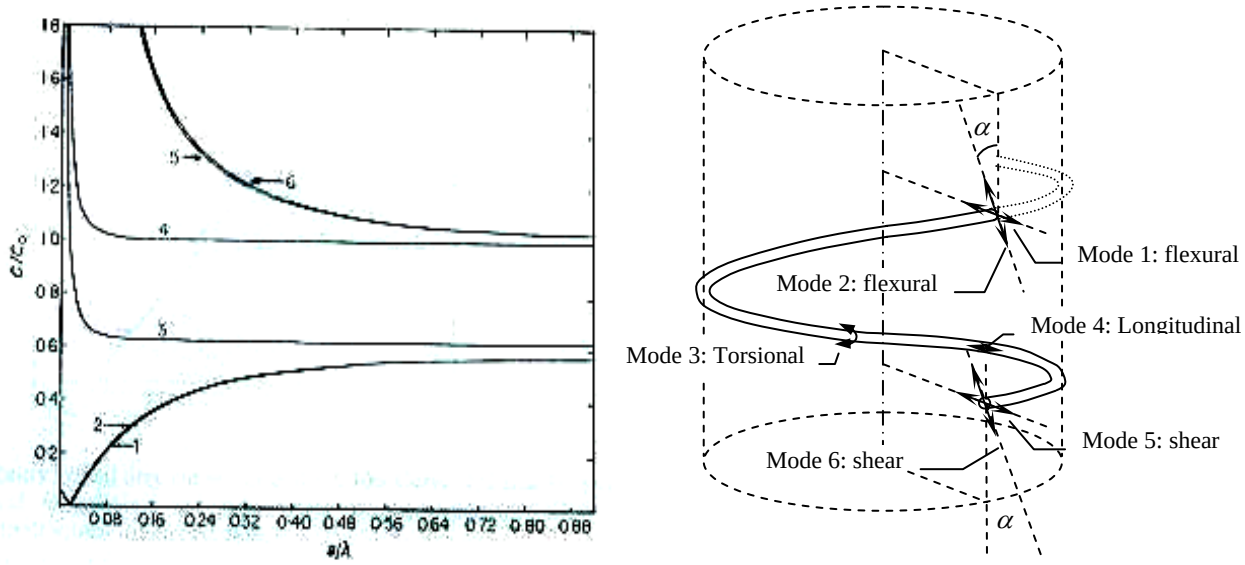


**(a)** **(b)**

**Fig. 2-12** (a) Phase velocity distributions based on the Wittrick theory for a helical spring with *a/R*=0.106 and $\alpha$ =3.9° [18]
(b) Motion directions of solid element for the six wave modes
$C_0$ is the phase velocity of extensional waves in a straight thin bar, given by $\sqrt{E/\rho}$
*a* is the radius of the circular cross section of the spring

With respect to elastic wave propagation along a helical spring, Wittrick [19] presented a Timoshenko-type theory, in which the curvature is assumed to be slight. Six distinct roots can be obtained from his resultant characteristic equation, which includes both in-plane and out-of-plane motions. Figure 2-12 shows graphically the non-dimensional phase velocity results from Wittrick's theory.

Britten and Langley [18] conducted some experimental studies on wave propagation in helical springs to compare experimental results with those predicted by the Morley and Wittrick theories. Figure 2-13(a) shows the test specimen and (b) the diagrammatic experimental set up. A stress pulse is induced by utilizing the magnetostrictive properties of nickel. The results are shown as distributions of arrival-time in non-dimensional form in Figure 2-14. The solid lines are theoretical predictions of wave arrival-time for a value of $a/R$ = 0.106. The parameters $t$ and $T_P$ are respectively time and the predominant period of the stress wave. $T_a$ (=$a/C_0$) and $T_0$ (=$x/C_0$) represent respectively the time taken by stress wave to travel the radius $a$ and the distance $x$ in terms of the bar velocity $C_0$. Curves 1 and 2 are associated with flexural and longitudinal modes of propagation in a circular ring, while curve 3 is for flexural waves in a Timoshenko straight rod. The arrival time together with the predominant period was measured in their experiments, and plotted as points in Figure 2-14. It can be seen that the experimental results agree well with the theoretical predictions.

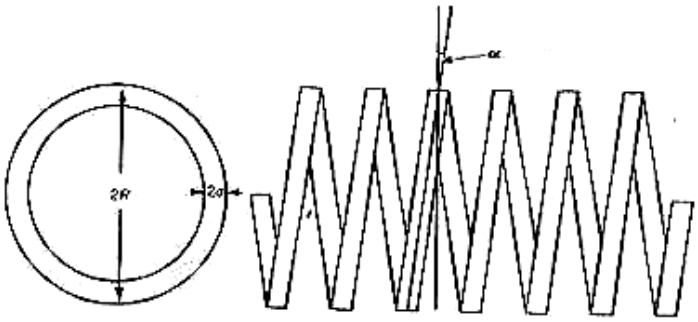


(a)

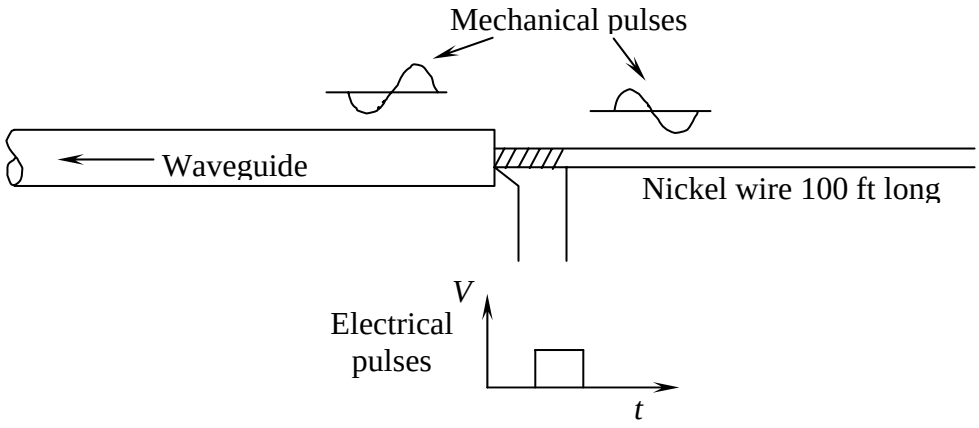


(b)

**Fig. 2-13** (a) Helical spring specimen
(b) Devices for initiating stress pulses into the helix
(after Britton and Langley [18])

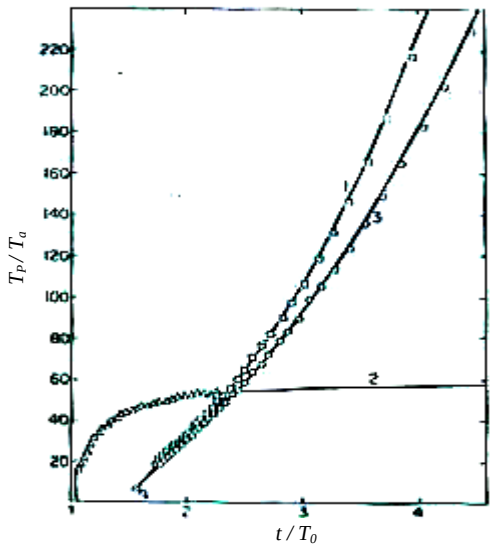


(a) the Morley theory

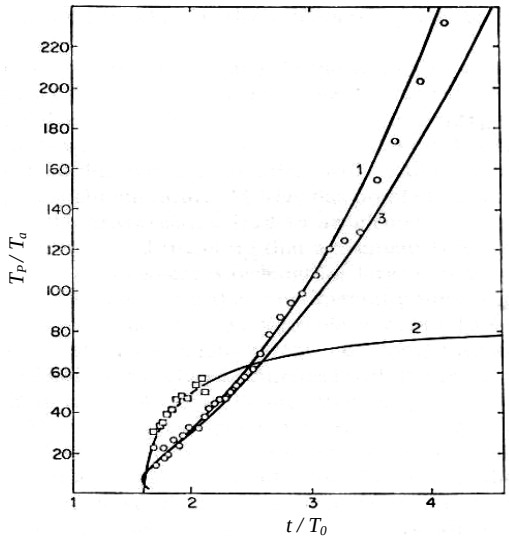


(b) the Wittrick Theory

**Fig. 2-14** Comparison of experimental data on wave propagation in rings with predictions by the (a) Morley and (b) Witrrick theories. [18]
$a/R$ = 0.106 (curves 1 and 2); curve 3 is for a straight-rod

From the theoretical and experimental efforts described, it is found that elastic waves propagate through a circular ring via several modes; motion in the plane of curvature corresponds to flexural, extensional and shear waves. One fundamental result from these studies is that the propagation of elastic waves, regardless of mode, is wavelength (or frequency) dependent; i.e. elastic wave with different wavelengths or frequencies travel through a curved rod at different velocities. Obviously, the wave velocity determined from the expression of $\sqrt{E/\rho}$ is unable to capture this feature of wavelength/frequency dependence. Therefore, present study is directed at the dynamic response of a cellular system (made of rings) subjected to planar impact at one end, to investigate the effects of structural factors such as ring size and packing arrangement, as well as wave characteristics (wavelength/frequency) on the propagation of elastic waves through the system.

## 2.7 Objective and Scope of Present Work

The objective of this investigation is to undertake an analysis of an idealized representation of a cellular structure to simulate stress wave transmission through actual cellular materials. The establishment of an idealized representation of a cellular material is effected by employing a metal ring array; various experiments are then conducted to determine the static and dynamic responses of such systems. Subsequently, wave propagation through a ring system is analysed theoretically from first principles, and experimental results are compared with theoretical predictions. In simulating actual cellular materials by ring systems, various parameters such as apparent density and modulus, relative density, cell shape/size, packing arrangement, and cell wall material properties are studied. It is envisaged that this will help establish a more global model that describes elastic stress wave propagation in cellular structures. The rest of this chapter discusses briefly the framework of the study.

As highlighted in the literature review, actual cellular materials such as polyurethane (PU) foam usually possess complicated three-dimensional structures, making direct analysis of stress propagation through them very difficult. Because a two-dimensional situation is easier to visualize, formulate, and solve, it is an attractive starting point for the development of micro-mechanical models for cellular solids. As an initial simplification, identical thin-walled rings, packed in different ways, are examined. This results in the three ring array arrangements shown in Figure 2-15. These relatively simple structures are then studied in terms of how they can simulate the structure of actual cellular materials.

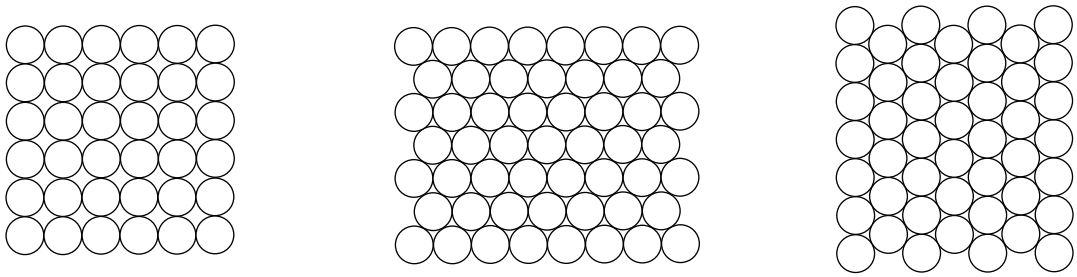

(a) (b) (C)

**Fig. 2-15** Three arrangements of ring systems;
(a) square-packed (b) transverse close-packed (c) vertical close-packed

Metal ring systems were assembled from five types of rings of different material, cell wall thickness and diameter. The shape of a ring is shown in Figure 2-16 and details of these rings are listed in Table 2-2. Actual photographic images are shown in Figure AF-1.

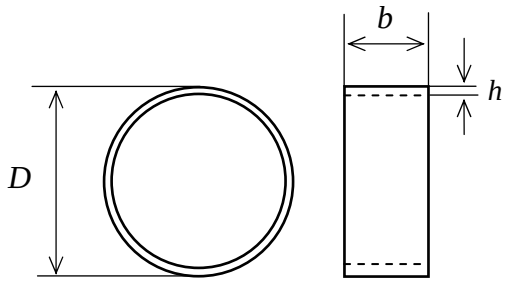


**Fig. 2-16** Ring geometry

**Table 2-2** Dimensions of rings

| Serial | Material | Size (mm) | |
|---|---|---|---|
| | | $D \times h$ | $b$ |
| 1 | Brass | 25.4×1 | 10 |
| 2 | Brass | 38.1×1 | |
| 3 | Brass | 38.1×3 | |
| 4 | Aluminum | 38.1×1 | |
| 5 | Aluminum | 38.1×3 | |

Such representations possess many features that can be utilized to model actual cellular materials. Rings of different diameters can be used to simulate foams with larger or smaller cells. This can also be correlated with the relative density of the ring array, if the wall thickness remains unchanged. The three packing arrangements shown in Figure 2-15 might also represent variations of anisotropy in foams.

To investigate stress wave propagation in the three ring arrays shown in Fig. 2-15, some of their properties must be determined through calculations or experiments. Their relative densities can be computed based on the dimensions of the rings. The apparent global elastic modulus can be determined from load-deflection tests and the apparent stress wave speed through them from impact experiments.

The simple structure of these idealized representations makes it possible to apply theoretical analysis to stress wave propagation through ring arrays. As a circular ring is the basic element in these systems, propagation of stress through the ring systems can be studied by analyzing stress wave transmission through a single ring. The results of the theoretical analysis can then be compared with experimental data and the degree of correlation will provide information on the dynamic response of actual cellular materials.

# CHAPTER THREE
# EXPERIMENTAL TESTS AND ANALYSIS

The preceding chapter introduced the concept of an idealized representation of cellular material via a tight packing of identical circular metal rings in three arrangements. Such ring arrays are employed in this study to investigate elastic wave propagation in cellular structures. Experimental tests are undertaken to determine their static mechanical properties (e.g. apparent Young's modulus) and dynamic response (e.g. apparent stress wave speed).

With respect to these ring arrays that constitute an idealized representation of cellular structures, the properties of primary interest are the overall density ($\rho^*$), density of the ring material ($\rho_S$), apparent elastic modulus of the ring array ($E^*$), elastic modulus of the ring material ($E_S$) and the apparent wave speed through the ring array ($C^*$). These parameters can be related to corresponding properties of actual cellular materials. Determination of the values of $\rho^*$ and $\rho_S$ is straightforward; the volume occupied by a ring array and the mass of all rings in the array are measured, and the volume of the solid fraction of the ring array is calculated from the ring dimensions, e.g. outer diameter, width and wall thickness. The value of $\rho^*$ is defined by the ratio of the mass to the apparent volume, and $\rho_S$ can be calculated from the ratio of the mass to the volume of the solid fraction of the ring array.

The value of $E_S$ can be determined through tensile tests on the ring material. Material property reference books also present values that can be compared with those obtained from experimental tests, to check the acceptability of experimental values. With regard to the apparent elastic modulus $E^*$ and the apparent wave speed $C^*$, these are determined by employing specially designed experimental arrangements. The value of the elastic modulus is determined from quasi-static compression tests, while the speed of elastic wave propagation is measured through impact tests.

## 3.1 Determination of Density and Young's Modulus of Ring Material

Density $\rho$ and Young's modulus $E$ are two fundamental mechanical properties of a material. These values are used to calculate the bar velocity $C$ of extensional waves in a given material through the expression $C = \sqrt{E/\rho}$. This velocity is generally taken as a reference for comparison with other wave velocities determined theoretically and experimentally. Therefore, a primary requirement is to determine these two properties for the materials in this study.

### 3.1.1 Material Density Measurement

The density of the rings is obtained from their weight, volume and dimensions. Table 4-1 presents the quantities measured and the density values obtained.

**Table 3-1** Measurement of material density

| Sample | Dimension ($m$) | | | Solid Volume ($m^3$) | Mass ($Kg$) | Density ($Kg/m^3$) |
|---|---|---|---|---|---|---|
| | Outer diameter $D$ | Wall thickness $h$ | Ring width $b$ | | | |
| Al alloy tube | 0.038 | 0.003 | 0.483 | $1.593\times10^{-4}$ | 0.429 | 2,693 |
| Brass tube | 0.038 | 0.003 | 0.512 | $1.689\times10^{-4}$ | 1.385 | 8,199 |

Compared with the values of similar materials listed in a material property reference [21], as shown in Table 3-2, the values obtained correlate closely and are used in subsequent analyses.

$$\rho_{Al} = 2{,}693 \quad Kg/m^3$$
$$\rho_{Br} = 8{,}199 \quad Kg/m^3 \qquad (3\text{-}1)$$

**Table 3-2** Density of Aluminum Alloy and Brass [21]

| Aluminum Alloy | Density ($Kg/m^3$) | Brass Alloy | Density ($Kg/m^3$) |
|---|---|---|---|
| EC, 1060 | 2,700 | Red bass, 85% | 8,750 |
| EC, 2011 | 2,710 | Yellow brass | 8,470 |
| EC, 3003 | 2,730 | Forging brass | 8,440 |
| EC, 5056 | 2,640 | Naval brass | 8,410 |

Data from *ASM Metals Reference Book, Third Edition, Michael Bauccio, Ed.*, ASM International, Materials Park, Ohio, P152 (1993)

### 3.1.2 Determination of Modulus of Elasticity

The modulus of elasticity is the slope of the elastic portion of the stress–strain curve, as shown in Figure 3-1. To obtain the stress–strain response of the ring material, metal tubes were cut into longitudinal strips, as shown in

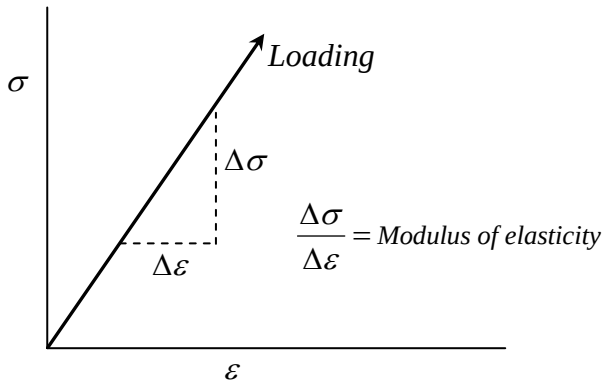


**Fig. 3-1** Elastic stress-strain relationship showing how the modulus of elasticity is determined

Figure 3-2, and subjected to quasi-static tension at a rate of 2 mm/min using an Instron universal testing machine (Model 8510). Figure AF-2 shows a picture of this test device.

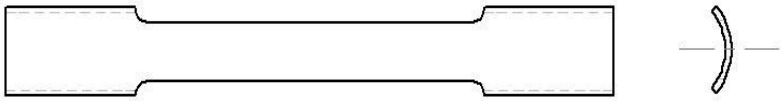

**Fig. 3-2** Shape of tensile test specimen

Strain gauges were glued onto the centre of each specimen to record the change in strain during tensile loading. The corresponding stress applied was calculated from the force reading of the Instron Machine and the cross-sectional area of the specimen. The resulting stress-strain curves were then plotted; an example is shown in Figure 3-3. The elastic modulus $E$ is determined from the slope of the straight line that fits the elastic portion of the stress-strain curve.

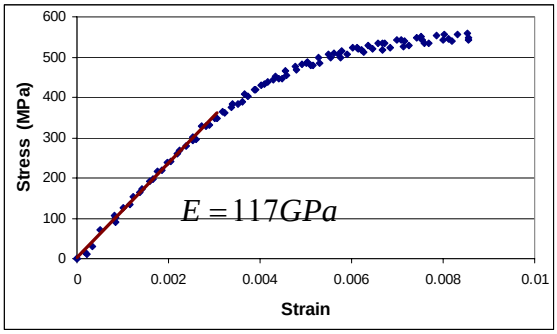


**Fig. 3-3** Stress-strain curve for a brass sample

Six samples, comprising three made of aluminum alloy and three made of brass, were subjected to tensile tests. The samples tested were photographed and are shown in Figure AF-3. All the six stress-strain curves obtained are presented in Appendix B and Table 3-3 summarizes the results obtained.

**Table 3-3** Elastic moduli determined from tensile tests

| Material | Young's Modulus $E$ (GPa) | | | Average $E$ (GPa) |
|---|---|---|---|---|
| | Sample 1 | Sample 2 | Sample 3 | |
| Al alloy | 66.3 | 64.2 | 67.1 | 65.9 |
| Brass | 117.0 | 116.6 | 127.5 | 120.4 |

The average values of $E$ listed in Table 3-3 were then taken to be the Young's moduli of the ring materials, i.e.

$$\begin{aligned} E_{Al} &= 65.9 \quad \text{GPa} \\ E_{Br} &= 120.4 \quad \text{GPa} \end{aligned} \tag{3-2}$$

## 3.2 Determination of Extensional Wave Velocity

$C_0$ denotes the velocity of elastic extensional waves that propagate in thin rods; its value is given by [22]

$$C_0 = \sqrt{\frac{E}{\rho}} \tag{3-3}$$

Substituting the values of $E$ and $\rho$ determined for aluminium alloy and brass, equation (3-3) gives the speed of extensional waves transmitting in thin rods made of those materials.

$$\begin{cases} C_0\big|_{Al} = \sqrt{\dfrac{E_{Al}}{\rho_{Al}}} = \sqrt{\dfrac{65.9\times10^9}{2693}} = 4947 \quad m/s \\ C_0\big|_{Br} = \sqrt{\dfrac{E_{Br}}{\rho_{Br}}} = \sqrt{\dfrac{120.4\times10^9}{8199}} = 3832 \quad m/s \end{cases} \tag{3-3}$$

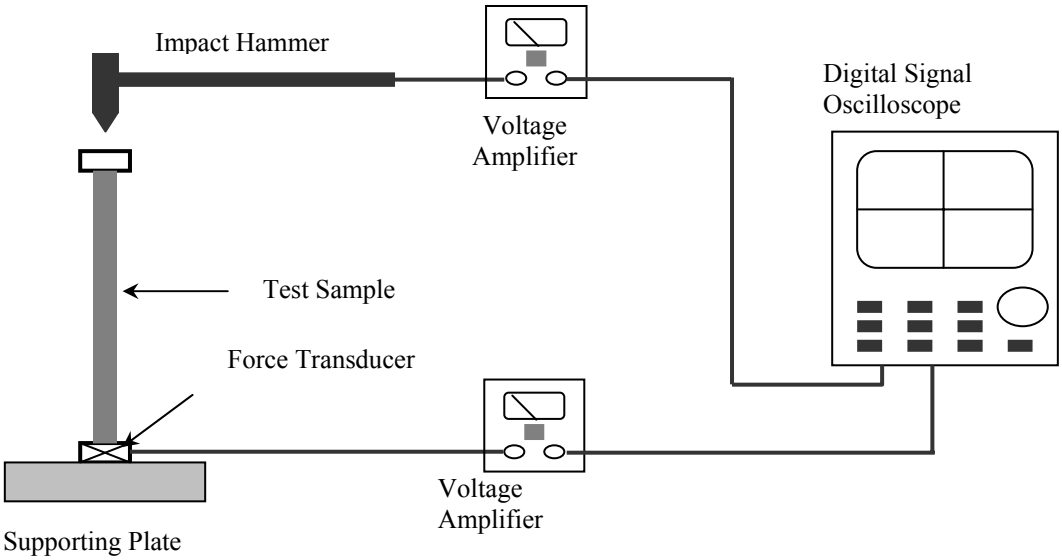


**Fig. 3-4** Experimental setup to determine the velocity of extensional waves

To verify if these calculated speeds compare well with actual values, the velocities of extensional waves are also obtained experimentally. Therefore, aluminium alloy and brass tubes were subjected to axial impact tests to determine the elastic wave propagation speeds in the direction of the tube axis. The experimental setup is shown in Figure 3-4. An impact hammer was used to strike the top of the metal tube to generate stress waves that travel down the tube. The force transducer built into the hammer was triggered and the force converted into a voltage signal recorded by a Digital Signal Oscilloscope (DSO). When the stress wave reached the bottom of the tube, it triggered another force transducer placed there and the resulting voltage signal was also recorded simultaneously by the same

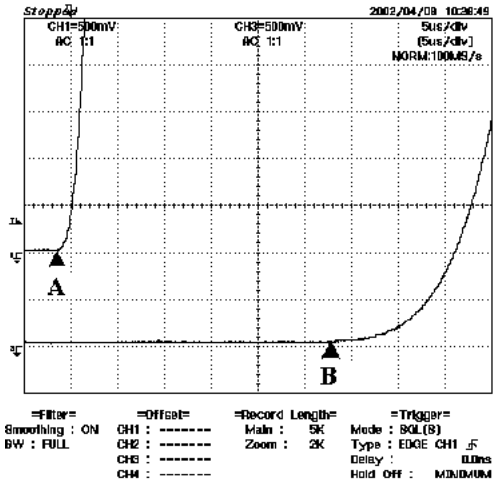


**Fig. 3-5** Typical force-time signals recorded on a DSO showing commencement of stress waves

DSO. Figure 3-5 shows a typical signal recorded on a DSO, where the commencements of the force signals are marked by A and B. The time interval between points A and B gives the time taken by the stress wave to transmit through the tube. A FORTRAN program was written to ascertain objectively the point of commencement of the signals; Appendix C describes the algorithm used and the program.

For each material ─ aluminium alloy and brass ─ six tubes of different lengths (as shown in Figure AF-4) were subjected to impact tests to determine the travel times for the stress waves generated. All DSO signals obtained in these tensile tests are presented in Appendix J. Graphs were then plotted with travel time as the abscissa and tube length as the ordinate, as shown in Figure 3-6, for aluminium alloy and brass tubes.

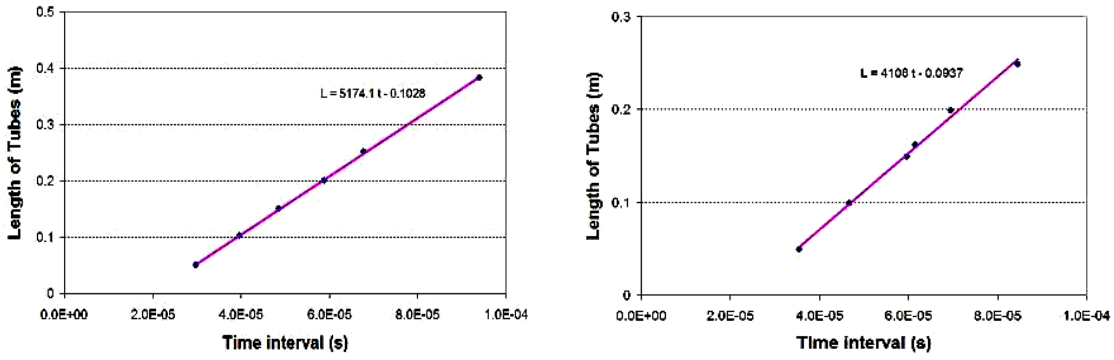


(a) Aluminum alloy tube (b) Brass tube

**Fig. 3-6** Linear fit for time taken for stress to travel through a tube

When a trend line is fitted to the points in each diagram in Figure 3-6, the velocity of the extensional wave can be determined from the slope of the line,

$$\begin{cases} C_{Al} = 5174 \\ C_{Br} = 4108 \end{cases} \quad (m/s) \qquad (3\text{-}4)$$

Comparing the values in Equations (3-3) and (3-4), the wave speeds determined from impact tests are comparable with those calculated from the expression $\sqrt{\frac{E}{\rho}}$. This shows that the densities, elastic moduli and wave velocities determined from the experiments are consistent with elastic wave propagation characteristics.

## 3.3 Response of a Single Metal Ring to Quasi-static and Dynamic Loading

A single metal ring is the basic unit of a ring array, which are considered idealized representations of cellular structures. Therefore, it is necessary to investigate the response of a single ring under quasi-static and dynamic loading. Through various tests, the apparent elastic moduli of different rings under lateral loading, the response of a ring under impact loading and the stress wave velocities through single rings are determined.

### 3.3.1 Compression Tests on a Single Ring

To determine the equivalent elastic modulus of a ring loaded laterally across its diameter, ring samples were subjected to quasi-static compression at a rate of 2 cm/min using an Instron universal testing machine (Model 8510). As with determination of the elastic modulus of a material described earlier, the load-

deflection response for ring compression is plotted and the equivalent modulus $E^*$ is given by the slope of the line that fits the linear portion of the curve. Five different rings were subjected to compression tests and their load-deflection responses, converted into stress-strain curves, are listed in Appendix H. The average value is taken as the equivalent elastic modulus for each type of ring (see Table 3-4).

In addition to experimental determination of the equivalent elastic modulus of a circular ring, this can also be calculated based on its material properties and dimensions. As shown in Figure 3-7, the change in diameter of a ring subjected to an opposing pair of forces P, is [23]

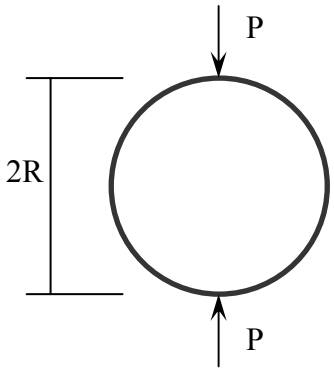


**Fig. 3-7** A ring subject to diametrically opposed forces

$$\begin{cases} D_H = \dfrac{PR_c^3}{EI}\left(\dfrac{2}{\pi}-\dfrac{1}{2}\right) \\ D_V = -\dfrac{PR_c^3}{EI}\left(\dfrac{\pi}{4}-\dfrac{2}{\pi}\right) \end{cases} \qquad (3\text{-}5)$$

where $D_H$ and $D_V$ are the changes in the horizontal and vertical diameters respectively, (an increase is positive), and $R_c$ is the radius of the centroid of the ring cross section, given by $\dfrac{D-h}{2}$.

Based on Hooke's law, the equivalent elastic modulus of the ring is then given by

$$\overline{E}^* = \frac{\sigma}{\varepsilon}$$

and $$\sigma = \frac{P}{2R_c b} \quad , \quad \varepsilon = \frac{|D_V|}{2R_c}$$

where $b$ is the axial thickness of the ring.

Substituting $D_V$ into equation (3-5), the equivalent elastic modulus $\overline{E}*$ is

$$\overline{E}* = \frac{EI}{0.149bR_c^3} \qquad (3\text{-}6)$$

The equivalent elastic moduli of the five different rings subjected to compression tests were calculated using Equation (3-6) and compared with values determined experimentally. Table 3-4 summarizes the results from compression tests and from calculations. Comparing each $E^*$ with its corresponding $\overline{E}^*$, there is only a small difference. This indicates that the experimental results for $E^*$ are acceptable.

**Table 3-4** Results from compression tests and calculation of related parameters

| Serial | Material | $E$ (GPa) | Size (mm) | | $\rho*$ (kg/m$^3$) | $E^*$ (MPa) | $\overline{E}^*$ (MPa) | $C_T^* = \sqrt{\frac{E^*}{\rho*}}$ (m/s) |
|---|---|---|---|---|---|---|---|---|
| | | | $D \times h$ | $b$ | | | | |
| 1 | Brass | 120.4 | $25.4 \times 1$ | 10 | 974 | 34.2 | 37.1 | 187.4 |
| 2 | Brass | | $38.1 \times 1$ | | 658 | 8.53 | 10.55 | 113.8 |
| 3 | Brass | | $38.1 \times 3$ | | 1868 | 303.2 | 336.3 | 402.8 |
| 4 | Al alloy | 65.9 | $38.1 \times 1$ | | 216 | 6.89 | 5.77 | 178.5 |
| 5 | Al alloy | | $38.1 \times 3$ | | 614 | 187.3 | 184.0 | 552.4 |

1. *D, h* and *b* are outer diameter, wall thickness and width of ring, respectively
2. Material moduli *E* were determined in previous section, as given in Eqn (4-2)
3. Equivalent density $\rho*$ is given by *(mass of a ring)/(bD$^2$)*

From the equivalent elastic moduli and densities determined, elastic wave speeds can be calculated using the expression $\sqrt{\frac{E}{\rho}}$; these theoretical velocities are also listed in Table 3-4. Their values will be compared with those determined experimentally to ascertain whether or not the expression $\sqrt{\frac{E}{\rho}}$ appropriately describes the propagation of elastic waves through circular rings.

### 3.3.2 Determination of Elastic Wave Speed in a Single Ring by Impact Testing

To determine experimentally the speed that an elastic wave takes to travel through a ring, single rings were subjected to lateral impact, as shown in Figure 3-8. An accelerometer was attached to an impinging mass, which can slide smoothly along guide rods. When the impacting mass is dropped to achieve free fall impact against a ring sample, the accelerometer output describes the change in acceleration of the mass. From the mass of the body, the impact force can be calculated using Newton's Second Law. A force transducer is placed underneath the ring sample to record the impact force that is transmitted through the sample.

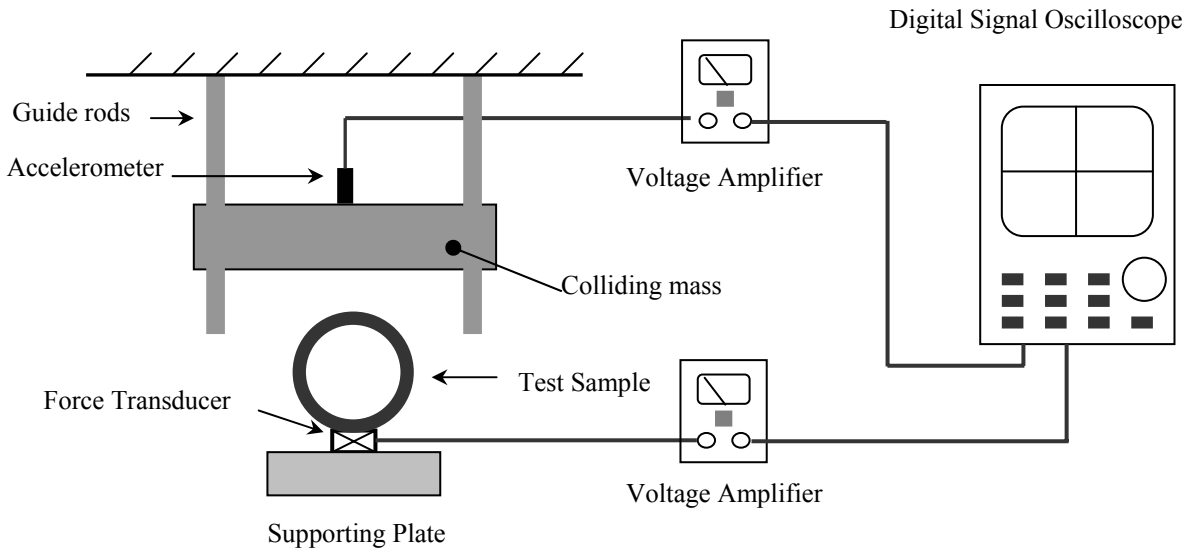


**Fig. 3-8** Experimental setup to investigate wave transmission through a single ring

All the five types of rings listed in Table 3-4 were subjected to such impact tests. Figure 3-9 shows two typical diagrams obtained. In both diagrams, the blue signal is from the accelerometer and the pink one from the force transducer. Figure 3-9(a) provides a complete view of the entire impact duration and (b) shows a magnification

of the wave front. Note that a second ordinate is used in (b) to describe the amplitude of the force transducer response, which is actually much smaller than that of the accelerometer. (All signals recorded by the DSO are presented in Appendix K.)

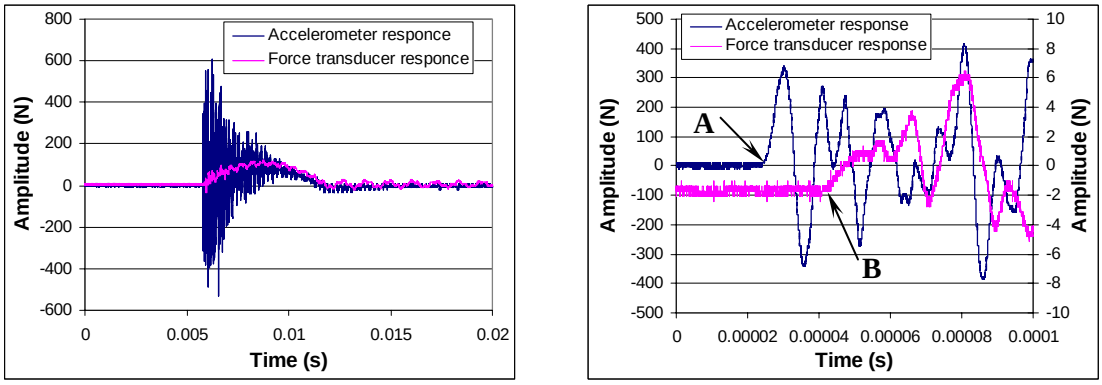


**(a)** complete wave form **(b)** wave front of impact signal

**Fig. 3-9** Impact signals for a single metal ring

From Figure 3-9(a), it can be seen that the signal produced by the accelerometer contains many high frequency components, while most of them are filtered out after transmission through the ring, as shown by the force transducer signal. To further illustrate this, Discrete Fourier Transformation (DFT) is applied to the two signals to convert them from the time domain to the frequency domain. The result is shown in Figure 3-10. It is evident that high frequency components around 100,000 Hz were filtered and absent in the output signal. Another feature evident in Figure 3-10 is that some

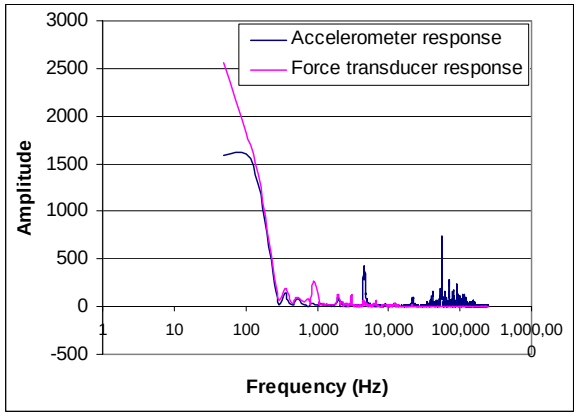


**Fig. 3-10** Discrete Fourier Transform of signals

frequency components in the output signal possess much higher amplitudes than in the input signal. To identify the cause of this unexpected phenomenon, the DFT signal is filtered and an inverse Fourier transform applied to show the stress wave for specified frequencies.

Through filtering unwanted frequency components in the DFT spectrum of the signals and then applying the inverse Fourier transform, stress waves corresponding to specified frequencies can be isolated in the time domain. Figure 3-11 shows one signal recorded by the force transducer and four of its filtered components corresponding to specified frequencies. The low frequency signal ( $f < 500Hz$ ) contains most of the impact energy. It also indicates that the colliding mass contacted the ring at about 0.005s, and lost contact at 0.012s. The 2,050 Hz Signal is also within the impact contact duration, while the 950 Hz and 3100 Hz signals appear only after loss of contact. This indicates that these two frequency components were the result of free vibration of the ring after impact. These vibrations result in some of the

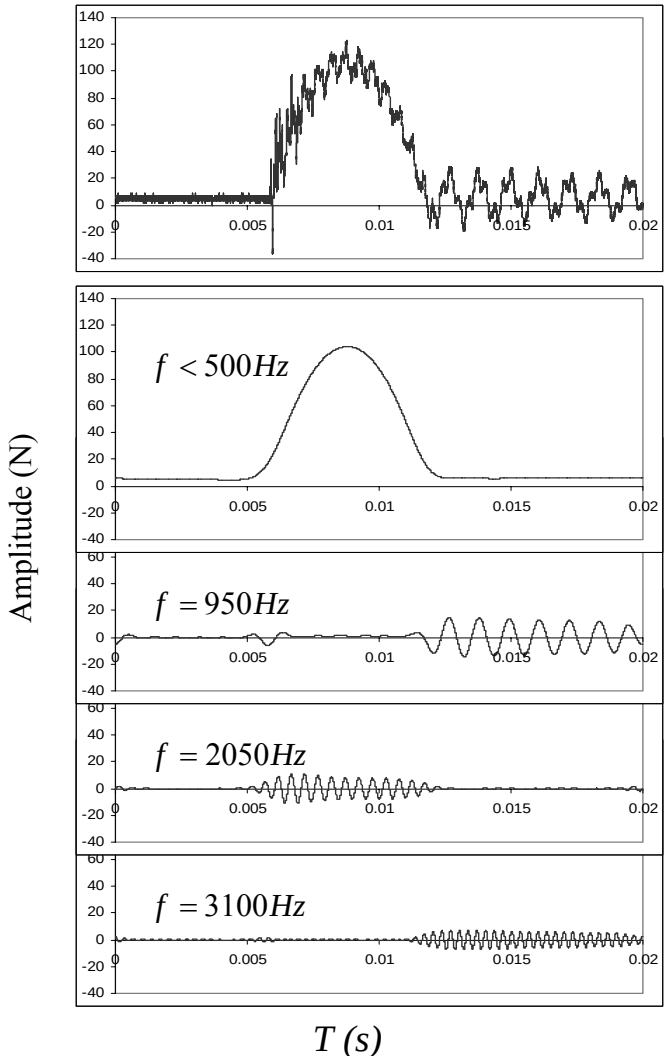


**Fig. 3-11** DSO signal and its filtered components

components of the output signal having higher amplitudes than the input force, as illustrated in the DFT spectrum in Figure 3-10.

To determine the wave propagation speed through a single ring, one has to measure the time interval between the commencements of the input and output signals. The FORTRAN program list in Appendix C is again used to locate the starting points of these signals, from which the time interval can be determined. Table 3-5 presents the wave travel times for all five types of rings. From the diameters of these rings, the apparent wave speeds $C_E^*$ can be calculated by dividing the respective ring diameters by the travel times. As stress waves can only travel along the solid wall of a ring, the actual wave speed $C_E$ along the ring wall is also calculated by dividing the semi-circumference of a ring by the travel time. The values of $C_T^*$, determined from $\sqrt{\frac{E^*}{\rho^*}}$ in Table 3-4, are also listed in Table 4-5 for comparison.

**Table 3-5** Wave speeds determined from impact tests on single rings

| Serial | Material | Size (mm) | | Time interval $T$ ($\mu s$) | Apparent wave speed through ring diameter $C_E^*$ (m/s) | Wave speed through ring wall $C_E$ (m/s) | $C_T^* = \sqrt{\frac{E^*}{\rho *}}$ (m/s) |
|---|---|---|---|---|---|---|---|
| | | $D \times h$ | $b$ | | | | |
| 1 | Brass | 25.4×1 | 10 | 10.84 | 2344 | 3682 | 187.4 |
| 2 | Brass | 38.1×1 | 10 | 16.98 | 2244 | 3525 | 113.8 |
| 3 | Brass | 38.1×3 | 10 | 15.83 | 2407 | 3781 | 402.8 |
| 4 | Al alloy | 38.1×1 | 10 | 11.41 | 3341 | 5247 | 178.5 |
| 5 | Alalloy | 38.1×3 | 10 | 11.69 | 3259 | 5120 | 552.4 |

1. *D, h* and *b* are respectively the outer diameter, wall thickness and width of ring;
2. $C_E^* = D/T$ , apparent wave speed through the ring diameter;
3. $C_E = (\pi D)/(2T)$, actual wave speed through the ring solid wall.

Based on the data listed in Table 3-5, it is evident that the values of the measured apparent wave speeds through ring diameter $C_E^*$ are much larger than $C_T^*$ determined using $\sqrt{\frac{E^*}{\rho^*}}$ . Furthermore, $C_T^*$ is affected by ring dimensions, such as the diameter and wall thickness, while $C_E^*$ remains roughly constant if the ring material is unchanged. Obviously, the speed $C_T^*$ calculated from $\sqrt{\frac{E^*}{\rho^*}}$ is not suitable for describing propagation of the fastest stress wave in circular rings.

The question to address is the type of stress wave that travels fastest in a circular ring. It is noted that the values of $C_E$ listed in Table 3-5 are the actual velocities at which stress propagates through the solid wall of a ring. They are much closer to the respective extensional wave velocities given in equation (3-4), i.e.

$$\begin{cases} C_{Al} = 5174 \\ C_{Br} = 4108 \end{cases} \quad (m/s)$$

Moreover, $C_E$ remains constant even though the ring diameter and wall thickness vary, as long as the ring material is the same. This is also the case for extensional wave propagation in a thin rod, as long as the lateral dimensions of the rod are sufficiently smaller than the wave length. Therefore, it appears that the fastest wave detected in experiments corresponds to extensional stress waves, which travel through the solid wall of the ring at the bar velocity.

Nevertheless, extensional waves may not be the prevalent stress wave propagating through a circular ring, although they are the fastest. Figure 3-9(b) shows that the amplitude of the extensional wave reduces to a very small magnitude after it propagates through a circular ring. It is reasonable to expect that extensional waves

will vanish after travelling through a few rings in an array. This raises the issue of the type of stress wave that carries the most energy and how it travels through a cellular system. The experiments described in the following section constitute a primary investigation into identifying these aspects.

## 3.4 Determination of Wave Velocity in Ring Arrays

### 3.4.1 Experimental Procedure

To investigate the propagation of elastic wave propagation in cellular systems, tightly packed arrays of identical circular metal rings are subjected to impact loading at one end to determine the propagation velocities of the impact-generated stress waves. As shown in Figure 3-12, the five types of rings were packed in three arrangements. The apparent elastic wave velocities through them were measured.

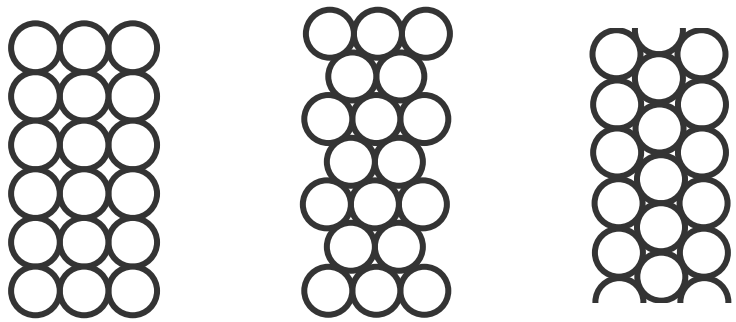


**Fig. 3-12** Three arrangements of ring arrays for determination of stress wave speeds
(a) Square packed; (b) Transverse close-packed; (c) Vertical close-packed

Figure 3-13 shows the experimental arrangement for impact tests. An accelerometer was attached to a colliding mass, which is dropped onto a ring array. The falling mass was guided by vertical rods and generated stress waves upon impact. The accelerometer recorded the deceleration of the colliding mass. As the impact-generated stress wave transmitted down through the ring array, the force transducer placed at the bottom of the array recorded the stress that passed through the array. Two voltage signals were then generated respectively by the accelerometer and the force transducer. After magnification by voltage amplifiers, these signals were recorded on a Digital Signal Oscilloscope (DSO). Figure 3-14 shows typical signals obtained. In both diagrams, the blue signal is from the accelerometer and the pink one from the force transducer. Fig 3-14(a) shows the complete impact duration, and Fig 3-14(b) is a magnification of the stress wave front. For every ring arrangement, the impact mass was released from three different heights — 20mm, 40mm and 60mm — with respect to the top of the array, to investigate the effect of the impact force amplitude on stress wave propagation.

Data recorded in the DSO was processed to determine the time required for the elastic wave to travel through the ring array. The travel time is defined by the duration between the commencements of the two signals, identified from plots like those in Figure 3-14 (b). From the heights of the arrays and the length of the shortest routes travelled by the stress waves, the apparent velocity and actual wave velocity (through the solid wall of the ring array) were calculated. Discrete Fourier Transformation was applied to the signals to analyze the frequency components and their effects on stress wave propagation.

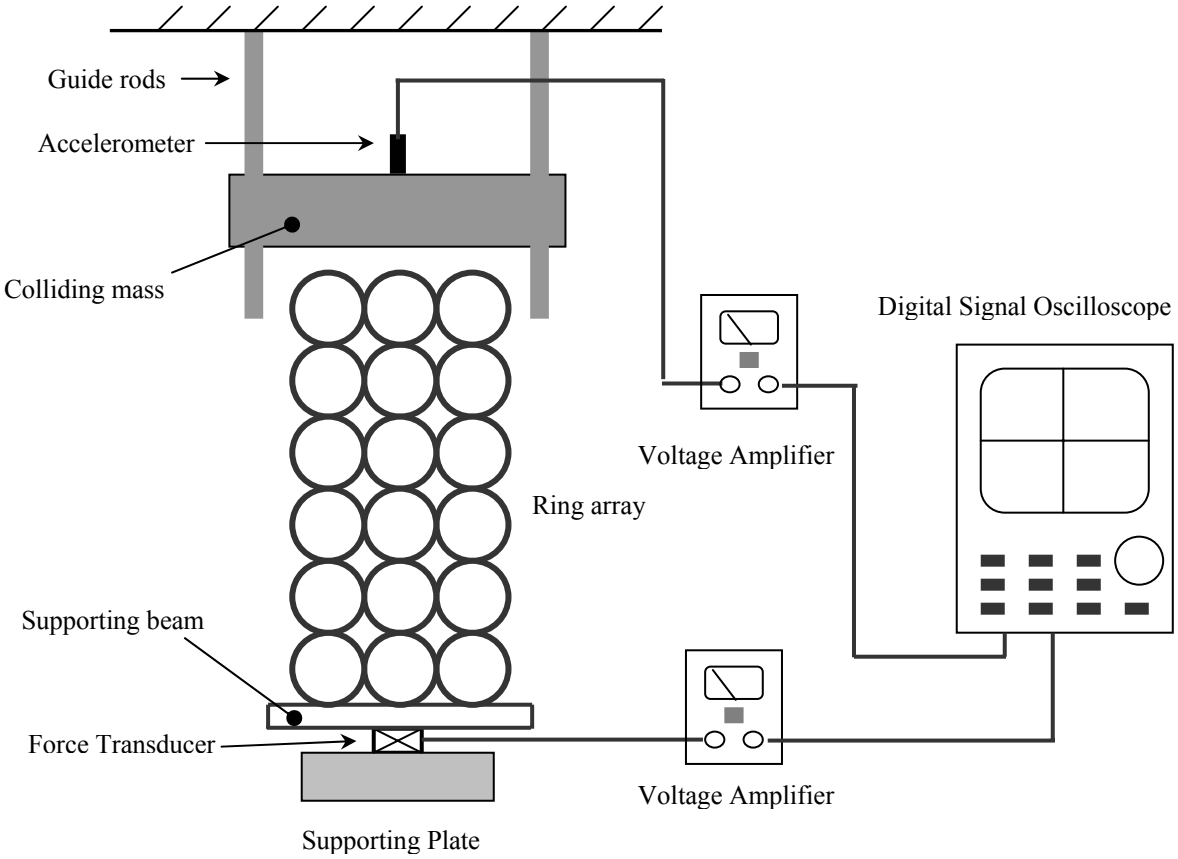


**Fig. 3-13** Experimental setup for determination of stress wave velocities in ring arrays

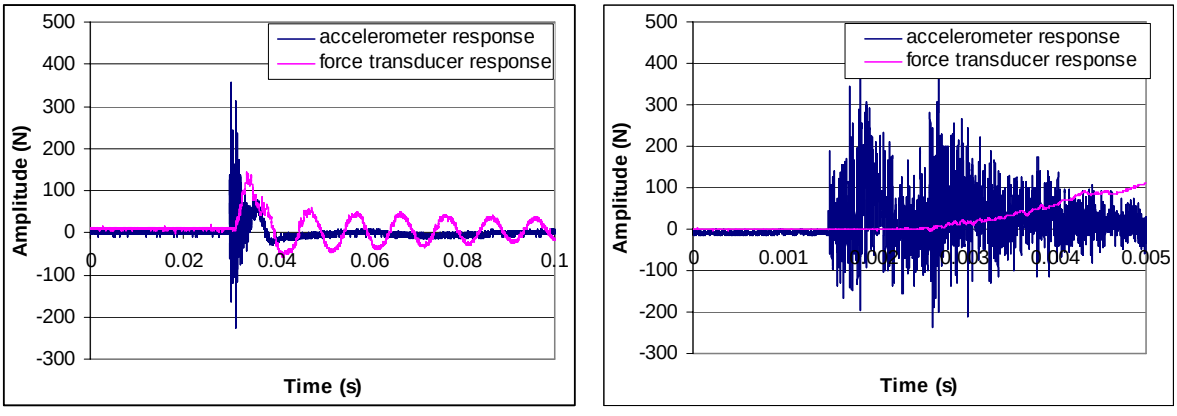


**(a)** Total duration of signals **(b)** Close-up of wavefronts

**Fig. 3-14** Impact signals for ring array

### 3.4.2 Results of Impact Tests on Ring Arrays

Two types of metal rings ─ aluminium alloy and brass ─ were tightly packed in different arrangements and subjected to impact by a falling mass to determine the velocities at which stresses transmit through them. To identify factors that might affect the propagation of stress waves, a variety of ring arrays were tested. For example, rings with different wall thicknesses and outer diameters were used; they were packed in three arrangements, namely square packed, transverse closed packed and vertical closed packed; the array were packed with and without constraints at their sides to respectively prevent and allow lateral expansion; the drop height was also varied. All DSO signals obtained are consolidated in Appendix L. Table 3-6 presents the overall wave velocities determined from these impact tests. Analyses with respect to various factors are presented in the following sections.

### 3.4.3 Data Analysis

Although the overall data on wave velocities for the various ring arrays are presented in Table 3-6, it is necessary to analyze the test results with reference to specified parameters, such as ring wall thickness, presence of side constraints, packing arrangements and drop height. Identification of the effects of each parameter on stress wave propagation provides an understanding of elastic stress wave transmission through cellular systems.

**Table 3-6** Apparent wave speeds determined from impact tests on ring arrays

| Ring Material | Diameter (mm) | Wall Thickness (mm) | Constraint at sides of the array (Y/N) | Packing Arrangement | Drop Height (mm) | Apparent Velocity (m/s) |
|---|---|---|---|---|---|---|
| Aluminium Alloy | 38.1 | 1 | N | Square | 20 | 326 |
| | | | | | 40 | 372 |
| | | | | | 60 | 335 |
| | | | | Transverse | 20 | 554 |
| | | | | | 40 | 617 |
| | | | | | 60 | 596 |
| | | | | Vertical | 20 | 575 |
| | | | | | 40 | 859 |
| | | | | | 60 | 830 |
| | | | Y | Square | 60 | 584 |
| | | | | Transverse | 60 | 1241 |
| | | | | Vertical | 60 | 669 |
| | | 3 | N | Square | 20 | 959 |
| | | | | | 40 | 1077 |
| | | | | | 60 | 1144 |
| | | | | Transverse | 20 | 1543 |
| | | | | | 40 | 1714 |
| | | | | | 60 | 1793 |
| | | | | Vertical | 20 | 1938 |
| | | | | | 40 | 1856 |
| | | | | | 60 | 1946 |
| Brass | 38.1 | 1 | N | Square | 20 | 234 |
| | | | | | 40 | 344 |
| | | | | | 60 | 382 |
| | | | | Transverse | 20 | 457 |
| | | | | | 40 | 487 |
| | | | | | 60 | 611 |
| | | | | Vertical | 20 | 703 |
| | | | | | 40 | 710 |
| | | | | | 60 | 617 |
| | | | Y | Square | 60 | 487 |
| | | | | Transverse | 60 | 946 |
| | | | | Vertical | 60 | 535 |
| | | 3 | N | Square | 20 | 913 |
| | | | | | 40 | 894 |
| | | | | | 60 | 911 |
| | | | | Transverse | 20 | 1110 |
| | | | | | 40 | 1113 |
| | | | | | 60 | 1156 |
| | | | | Vertical | 20 | 1042 |
| | | | | | 40 | 1139 |
| | | | | | 60 | 1116 |
| | 25.4 | 1 | N | Square | 20 | 413 |
| | | | | | 40 | 399 |
| | | | | | 60 | 371 |
| | | | | Transverse | 20 | 414 |
| | | | | | 40 | 395 |
| | | | | | 60 | 392 |
| | | | | Vertical | 20 | 617 |
| | | | | | 40 | 672 |
| | | | | | 60 | 691 |

1. Effect of impact force intensity on wave propagation

As mentioned previously, the impacting mass was released from three different heights, 20mm, 40mm and 60mm, to strike a ring array. This would result in different impact energies. Figure 3-15 shows three sets of results for an array subjected to impacts from different heights. It is evident that the amplitudes of the stress signals vary with the drop height.

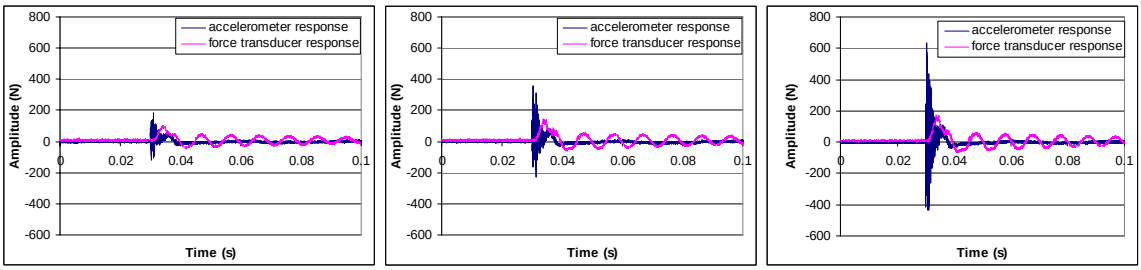


(a) 20mm (b) 40mm (c) 60mm

**Fig. 3-15** Acceleration and force signals obtained by impacting the same sample from three different heights

It is intuitive that different drop heights would generate impact forces of different amplitudes. The issue is whether or not this results in different frequency components in the signals. To examine this, Discrete Fourier Transformation is applied to the signals and their resulting frequency distributions compared. From the DFT plots in Figure 3-16, it is found that the frequency spectra of both the accelerometer and force transducer responses are similar for the three signals corresponding to different drop heights. The obvious difference is found in their amplitudes, which seem to be

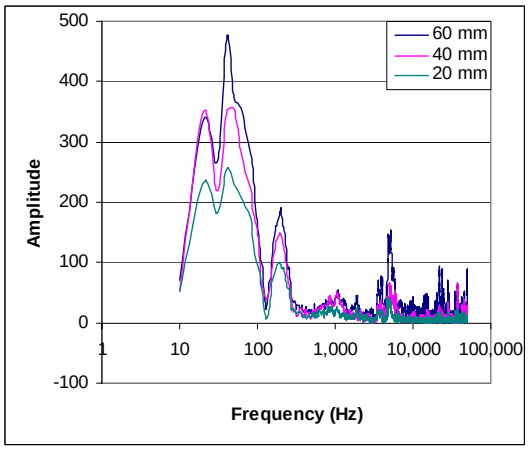


(a) DFT of Accelerometer Responses

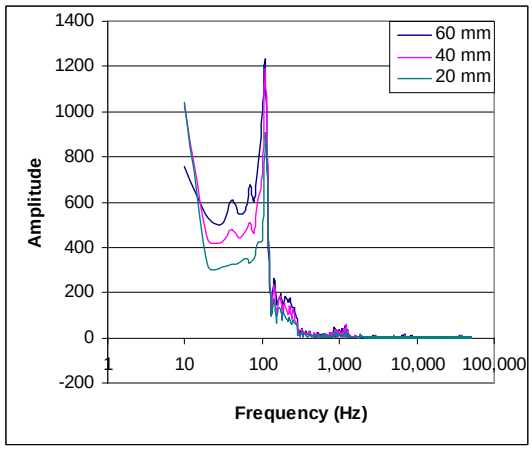


(b) DFT of Force Transducer Responses

proportional to the drop height. Therefore, the drop height only alters the amplitude of the stress induced, but does not affect the frequency spectrum.

Figure 3-17 presents data to illustrate whether there are differences in wave velocity caused by different drop heights. Each diagram represents a particular ring arrangement. The three columns in each diagram represent the velocities corresponding to three drop heights. There does not seem to be a consistent trend, indicating that there is probably no relationship between wave velocity and drop height. It should also be noted that the difference among the three velocities in each diagram is small and are probably caused by experimental scatter.

The conclusion is that the impact force amplitude does not affect wave propagation velocity. Therefore, for convenience in assessing the other parameters investigated, average values are calculated from the wave velocities corresponding to the three drop height. Consequently, the apparent velocities in Table 3-6 are revised, as shown in Table 3-7.

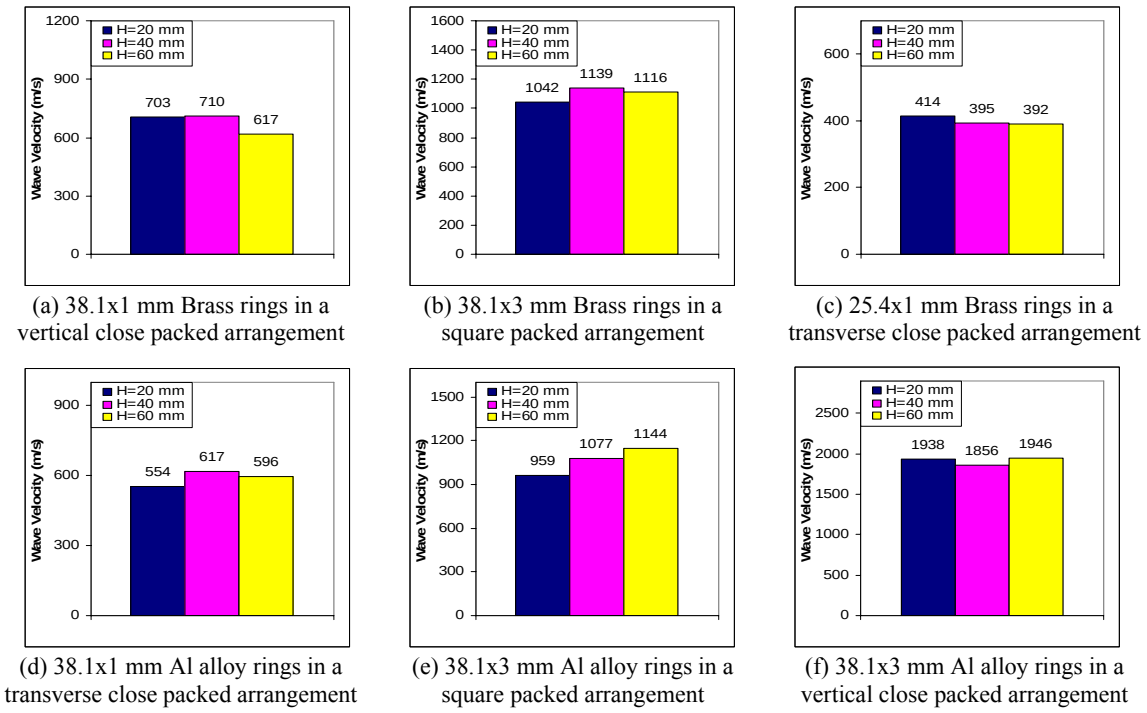


(a) 38.1x1 mm Brass rings in a vertical close packed arrangement

(b) 38.1x3 mm Brass rings in a square packed arrangement

(c) 25.4x1 mm Brass rings in a transverse close packed arrangement

(d) 38.1x1 mm Al alloy rings in a transverse close packed arrangement

(e) 38.1x3 mm Al alloy rings in a square packed arrangement

(f) 38.1x3 mm Al alloy rings in a vertical close packed arrangement

**Fig. 3-17** Examples for comparison of wave velocities corresponding to different drop heights of 20, 40 and 60 mm

**Table 3-7** Average apparent wave speeds determined from impact tests on ring arrays

| Ring Material | *D* *mm* | *h* *mm* | Constraint at sides (Y/N) | Packing Arrangement | Apparent Velocity (*m/s*) |
|---|---|---|---|---|---|
| Aluminum | 38.1 | 1 | N | Square | 344 |
| | | | | Transverse | 589 |
| | | | | Vertical | 844 |
| | | | Y | Square | 584 |
| | | | | Transverse | 1241 |
| | | | | Vertical | 669 |
| | | 3 | N | Square | 1060 |
| | | | | Transverse | 1683 |
| | | | | Vertical | 1913 |
| Brass | 38.1 | 1 | N | Square | 320 |
| | | | | Transverse | 518 |
| | | | | Vertical | 677 |
| | | | Y | Square | 487 |
| | | | | Transverse | 946 |
| | | | | Vertical | 535 |
| | | 3 | N | Square | 906 |
| | | | | Transverse | 1126 |
| | | | | Vertical | 1099 |
| | 25.4 | 1 | N | Square | 394 |
| | | | | Transverse | 400 |
| | | | | Vertical | 660 |

2. Effect of ring material properties on wave propagation

Aluminium alloy and brass rings were tested. To determine the effect of material properties on stress wave propagation in rings system, wave velocities through ring arrays with rings of the same size but different materials are compared.

In Figure 3-18, each pair of columns shows a comparison of the wave velocities in aluminium alloy and brass ring arrays. For a pair of columns, the packing arrangement and ring size are identical; only the ring material is different. From the relative heights of the columns in each pair, it is evident that stress transmission in aluminium alloy ring arrays is always faster than in brass ring arrays. This is expected because it has been established that $C_0|_{Al} > C_0|_{Br}$, where $C_0 = \sqrt{\frac{E}{\rho}}$ is the extensional wave velocity in thin bars. The values of $C_0$ for the two materials have been determined experimentally, as shown in Eqn (3-4). Figure 3-18 also gives the ratio of

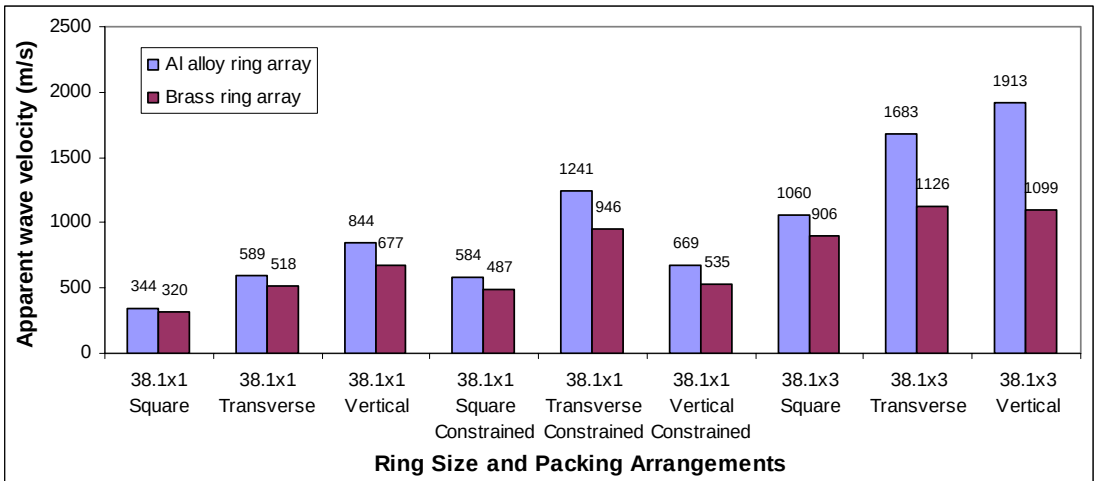


| $\frac{C_{Al}}{C_{Br}}$ | 1.08 | 1.14 | 1.25 | 1.20 | 1.31 | 1.25 | 1.17 | 1.49 | 1.74 |
|---|---|---|---|---|---|---|---|---|---|

**Fig. 3-18** Comparison of stress wave velocities
for similar packing arrangements but different materials

the wave velocities for the two materials, i.e. $\frac{C_{Al}}{C_{Br}}$. Since $\frac{C_0|_{Al}}{C_0|_{Br}} = \frac{5174}{4108} = 1.26$, it is found that most of the $\frac{C_{Al}}{C_{Br}}$ values shown in Figure 3-18 are close to this number, except those for thicker wall ring arrays. It appears that the effect of material property on wave propagation in thin bars is similar to that on ring arrays, particularly for thin wall ring systems. By converting the apparent wave velocities in Figure 3-18 into non-dimensional values by dividing them by $C_0$, one can evaluate the effect of material difference on stress wave propagation in ring arrays. Figure 3-19 presents a comparison in the form of non-dimensionalised wave velocities. Obviously, for thin-wall ($t$=1mm) ring arrays, the non-dimensional velocities for different ring materials are almost identical, regardless of whether the ring arrays are constrained at their sides or not. Nevertheless, for thick-walled ($t$=3mm) ring arrangements, the non-dimensional velocities are not similar, especially for transverse and vertical closed packed arrangements. Therefore, it appears that the material properties of the ring affect wave propagation in arrays with thicker-walled rings. Further investigation into this, combined with a theoretical analysis, is presented in the next chapter.

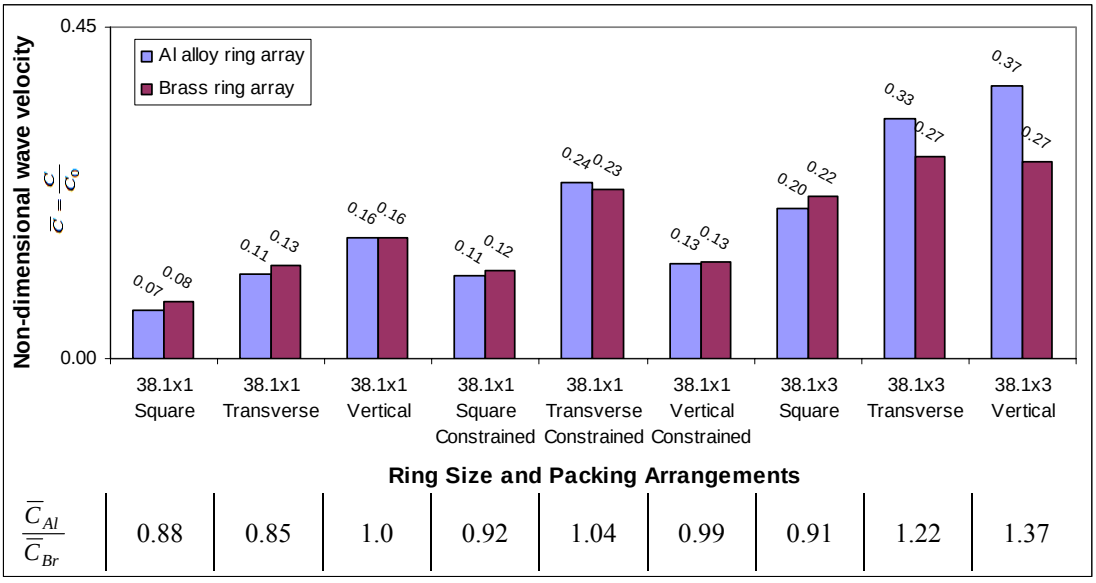


| $\frac{\overline{C}_{Al}}{\overline{C}_{Br}}$ | 0.88 | 0.85 | 1.0 | 0.92 | 1.04 | 0.99 | 0.91 | 1.22 | 1.37 |
|---|---|---|---|---|---|---|---|---|---|

**Figure 3-19** Comparison of non-dimensional stress wave velocities for similar packing arrangements but different ring materials

3. Effect of ring wall thickness on wave propagation

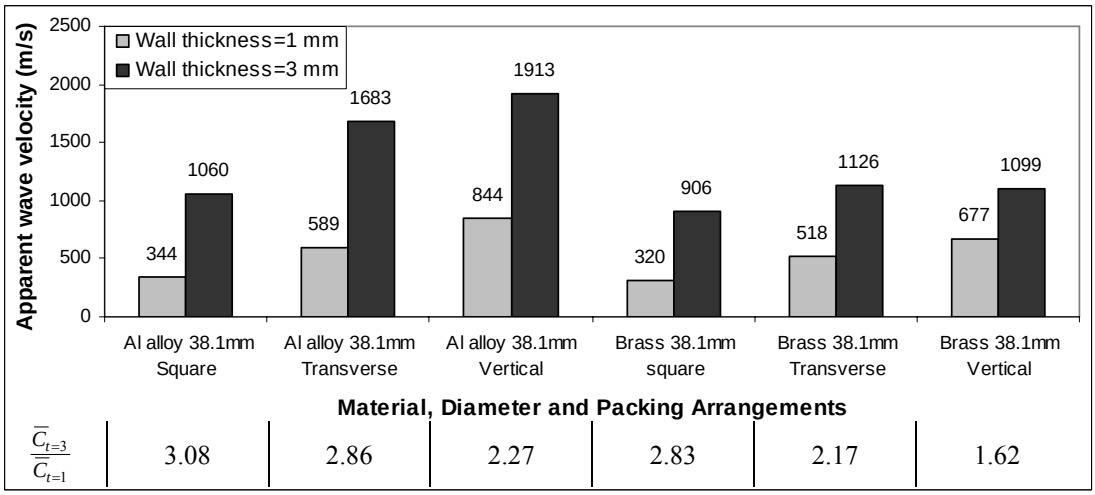


**Figure 3-20** Comparison of wave velocities for different ring wall thicknesses

From the results of impact tests on ring arrays, it is found that the stress wave velocities are affected by the ring wall thickness. Figure 3-20 shows a comparison of stress wave velocities in arrays with rings of different thicknesses. Each pair of columns in the diagram shows two wave velocities, one for thin-walled (1mm) ring arrays and the other for thicker-walled (3mm) ring arrays. It is evident that stress waves transmit much faster in thicker-walled ring arrays. When the ring wall thickness is changed from 1 mm to 3mm, the stress wave velocity speeds up by at least two times, except for the brass ring array with a vertical close packing.

This characteristic differs from that found in tests on single rings, where the extensional waves travel at constant speed even though the ring wall thickness varies. This indicates that the velocities associated with stress transmission in ring arrays may not be extensional waves, which might have diminished after travelling a short distance.

4. Effect of packing arrangements on wave propagation

In the tests, there are three ways to pack rings in an array ─ square packing, transverse close packing and vertical close packing. The effect of packing arrangements on stress wave propagations is examined.

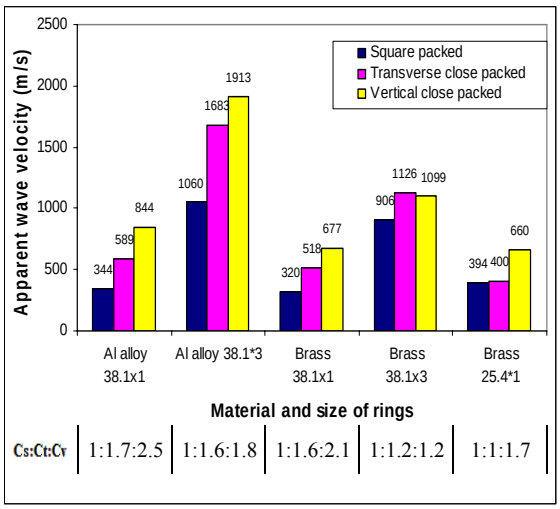


**Figure 3-21** Comparison of wave velocities for different packing arrangements

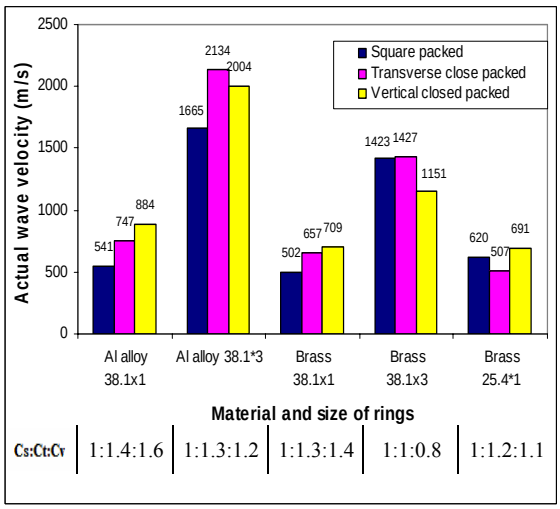


**Figure 3-22** Comparison of actual wave velocities along ring walls for different packing arrangements

Figure 3-21 compares the wave velocities corresponding to the three packing arrangements. Each of the five groups of columns depicts the velocities for the three packing arrangements. A comparison of the heights of the columns in each group shows that stress waves travel slowest in a square packed arrangement. A vertical closed packed arrangement allows the stresses to transmit fastest, except for the case of 38.1x3 brass.

Note that the shortest route for stress wave transmission through a ring array differs for the three packing arrangements. The issue to address is whether stress waves travel along the shortest route via the solid ring walls at a constant speed, and

whether the resultant apparent velocities through the ring arrays are different only because of the difference in distance travelled. Figure 3-22 shows the values of wave velocities based on distance travelled along the ring walls. A comparison of the three values in each group shows that a difference in velocity for the three arrangements still exists, although the three values are now closer to one another than those for apparent velocities shown in Figure 3-21. This indicates that the wave speed might be affected by factors that are dependent on packing arrangement. Further analysis on this will be presented after a theoretical model is established in the next chapter.

5. Effect of boundary conditions on wave propagation

As shown in Figure 3-23, two types of boundary conditions were imposed on ring arrays in impact tests ─ i.e. free and constrained sides. The wave velocities for these two conditions are compared to identify how different boundary conditions affect wave propagation.

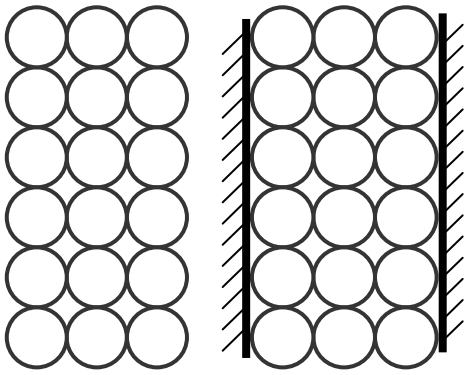


**Fig. 3-23** Ring arrays in (a)side free and (b)side-constrained boundary conditions

Figure 3-24 shows a comparison of the stress wave velocities in ring arrays with different boundary conditions. Each pair of columns in the diagram depicts the velocities corresponding to the two boundary conditions. The effect of boundary conditions on wave speeds depends on the packing arrangements. In a square packed arrangement, stress waves transmit a little faster in side-constrained arrays than in unconstrained ones. For a transverse close packed arrangement, the wave velocity for side-constrained arrays is double that of unconstrained ones. However, for a vertical

close packed arrangement, it appears that stress waves travelled slightly slower in constrained ring arrays than in unconstrained ones. From the results obtained, it is difficult to draw a conclusion for the effects of boundary conditions on stress wave propagation. Friction between the frames and the ring array might have affected the data recorded from impact tests.

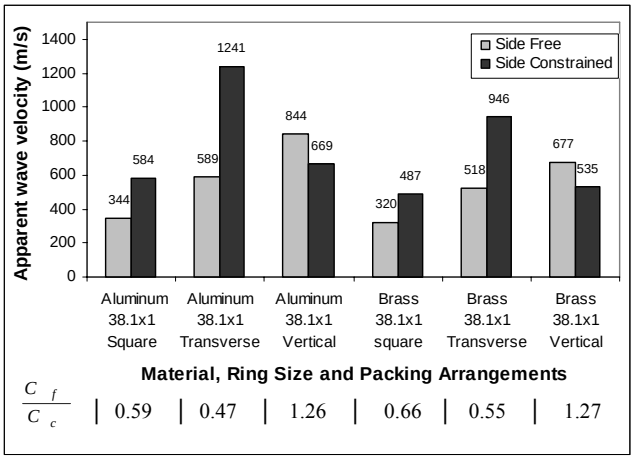


**Figure 3-24** Comparison of wave velocities for different boundary conditions

6. Summary of experimental observations for impact tests on ring arrays

From the wave speeds determined in impact tests on various ring arrays, it is found that stress wave propagation in a ring system is affected by several factors, such as the material properties of the ring, the ring wall thickness, the ring packing arrangement and boundary conditions.

In general, the impact force intensity does not affect the wave speed and only contributes to the energy carried by the waves. Material properties have a greater effect on wave velocity and stress wave transmission is much faster in an array comprising thicker walled rings than thin walled ones. A difference in packing arrangement result in different wave propagation speeds and the shortest route of travel may not be the only factor. The influence of boundary conditions on wave propagation varies with packing arrangement.

Further examination of these phenomena will be presented when a theoretical model is established in the next chapter.

## 3.5 Determination and Analysis of Apparent Young's Modulus

In order to apply the well-known expression $\sqrt{\frac{E}{\rho}}$ to ascertain if it is suitable for predicting the stress wave velocity in a ring array, the equivalent Young's modulus $E^*$ and apparent density $\rho^*$ of a ring array must be determined. $\rho^*$ can be calculated easily by weighing a ring array and measuring the space it occupies. $E^*$ of a ring array needs to be determined experimentally. To do this, all the ring arrays subjected to impact tests were also subjected to quasi-static compression using an Instron Universal Testing Machine. The detailed procedure, test results and a brief analysis are presented in the following sections.

### 3.5.1 Test Procedure

As shown in Figure 3-25, ring arrays were tightly clipped together and subjected to quasi-static compression at a rate of 2 mm/min. All clamps were examined carefully during compression to guarantee none of them open up. Before the onset of plastic deformation, the compression

**Fig. 3-25** Ring Array in Compression Test

process is stopped and the ring array unloaded. The data recorded, in terms of force and displacement values, were processed to determine the apparent overall elastic modulus. This test was repeated three times to obtain an average value of the properties.

### 3.5.2 Results of Compression Tests

Stress-strain curves resulting from the compression of different ring array arrangements were plotted. Figure 3-26 shows a typical curve; assuming Hooke's law for the overall structural response, the slope of the initial linear phase defines the apparent elastic modulus of the ring array. All stress-strain curves obtained from compression tests on ring arrays and resulting apparent moduli are presented in Appendix M.

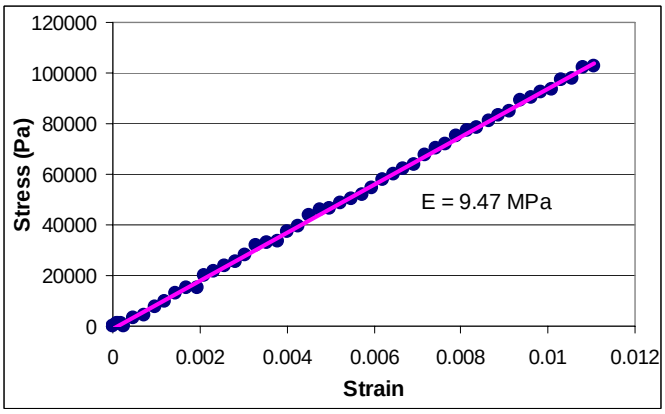


**Fig. 3-26** A stress-strain curve obtained from a compression test on a ring array

Table 4-8 lists the apparent moduli $E^*$ determined from compression tests on different ring array arrangements, together with the equivalent densities $\rho^*$ of the arrays and wave velocities $C^*$ computed from $\sqrt{\frac{E^*}{\rho^*}}$. The experimental wave velocities $C_E^*$ are also shown for comparison.

**Table 3-8** Apparent Compressive Elastic Moduli from Tests:

| Ring Material | $D$ mm | $h$ mm | Constraint at sides (Y/N) | Packing Arrangement | $E^*$ (MPa) | $\rho^*$ (kg/m$^3$) | $C^*$ (m/s) ($\sqrt{E^*/\rho^*}$) | $C_E^*$ (m/s) | $C_E^*/C^*$ |
|---|---|---|---|---|---|---|---|---|---|
| Al Alloy | 38.1 | 1 | N | Square | 7.38 | 194.8 | 194.6 | 344 | 1.768 |
| | | | | Transverse | 8.46 | 224.9 | 193.8 | 589 | 3.039 |
| | | | | Vertical | 7.48 | 224.9 | 182.4 | 844 | 4.627 |
| | | | Y | Square | 47.93 | 194.8 | 496 | 584 | 1.177 |
| | | | | Transverse | 126.50 | 224.9 | 749.9 | 1241 | 1.655 |
| | | | | Vertical | 101.80 | 224.9 | 672.7 | 669 | 0.994 |
| Brass | 38.1 | 1 | N | Square | 9.45 | 658.3 | 119.8 | 320 | 2.671 |
| | | | | Transverse | 10.95 | 760.1 | 120 | 518 | 4.317 |
| | | | | Vertical | 10.04 | 760.1 | 114.9 | 677 | 5.892 |
| | | | Y | Square | 55.27 | 658.3 | 289.8 | 487 | 1.680 |
| | | | | Transverse | 137.75 | 760.1 | 425.7 | 946 | 2.222 |
| | | | | Vertical | 97.03 | 760.1 | 357.3 | 535 | 1.497 |

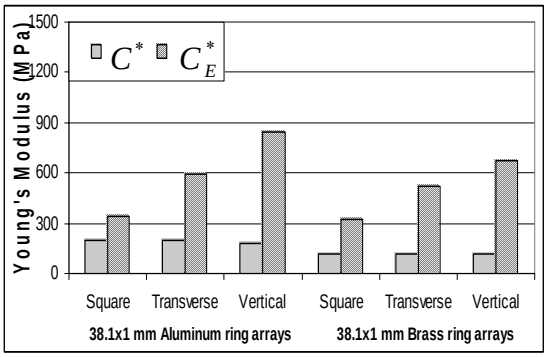


| $\frac{C_E^*}{C^*}$ | 1.768 | 3.039 | 4.627 | 2.671 | 4.317 | 5.892 |
|---|---|---|---|---|---|---|

(a) Unconstrained sides

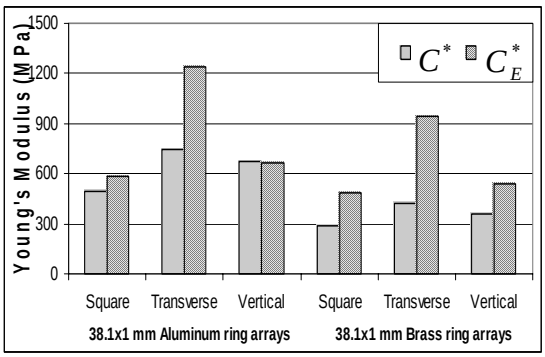


| $\frac{C_E^*}{C^*}$ | 1.177 | 1.655 | 0.994 | 1.680 | 2.222 | 1.497 |
|---|---|---|---|---|---|---|

(b) Constrained sides

**Fig. 3-27** Comparison of theoretical ($C^*$) and experimental ($C_E^*$) apparent wave speeds

Figure 3-27 provides a visual comparison of $C^*$ and $C_E^*$, whereby the wave speeds are represented by the column heights. Figure 3-27(a) and (b) show the wave speeds for ring arrays with different boundary conditions ─ unconstrained and constrained sides. For the case of a free boundary condition, it is evident that $C_E^*$ is much larger than $C^*$. Furthermore, $C_E^*$ for the three packing arrangements with both aluminium

alloy and brass rings exhibit the same trends ─ slowest for a square packed array, faster for a transverse close packed array and fastest in a vertical close packed system. Such a trend does not apply to $C^*$ which is based on $\sqrt{\frac{E^*}{\rho^*}}$. For the case of constrained sides shown in Figure 3-27(b), the velocity pattern differs from that for free sides. Firstly, almost all the values of $C^*$ and $C_E^*$ increase when the arrays are side-constrained, except for $C_E^*$ for a vertical close packed arrangement. Secondly, the differences between $C_E^*$ and $C^*$ are relatively smaller. Thirdly, $C_E^*$ and $C^*$ for the three packing arrangements possess the same characteristics that differ from the case of unconstrained sides ─ slowest in square packed arrays, faster in vertical close packed arrays and fastest in transverse close packed arrays.

Based on the visual comparison illustrated in Figure 3-27 and the above analysis, little correlation exists between the actual stress wave velocity $C^*$ determined from impact tests and that predicted theoretically based on $C_E^* = \sqrt{\frac{E^*}{\rho^*}}$. This indicates that the expression $\sqrt{\frac{E^*}{\rho^*}}$ is not valid for estimating the velocity of stress waves in a cellular system.

## 3.6 Summary

In this chapter, various experiments on single rings and ring arrays are described and the test data analyzed. Some features of stress wave propagation in ring systems are identified.

Basic properties of each ring material, such as the density $\rho$ of the ring wall and its elastic modulus $E$ were determined experimentally and compared with corresponding values from material property references to verify their acceptability. Extensional wave velocities ( $C_0$ ) along the axial direction of tubes were also measured through impact tests and compared with values given by $\sqrt{\frac{E}{\rho}}$. Results show that the values of $\rho$, $E$ and $C_0$ determined from experiments are acceptable. These values of the fundamental properties provide a reliable basis for other experiments and analyses.

As the basic component of a ring array, single rings were subjected to compression and impact tests to determine the apparent elastic moduli and stress wave velocities in the transverse direction. It was found that the fastest waves detected correspond to extensional waves which travel at the speed $C_0$ along the solid wall of the rings. Experimental results shows that stress propagation in a single ring cannot be described by the expression $\sqrt{\frac{E^*}{\rho^*}}$, where $E^*$ and $\rho^*$ are respectively the equivalent elastic modulus and density of a ring.

Stress wave velocities through various ring arrays were determined from impact tests. It was found that several factors affect stress wave propagation through the ring systems, these being the ring material properties, ring wall thickness, packing arrangement and boundary conditions. Although these factor also affect the values of the equivalent elastic modulus $E^*$ , apparent density $\rho^*$ and resulting theoretical wave velocity $C^*$, test results shows little correlation when $C^*$ is compared with the actual wave velocity $C_E^*$ determined from impact tests.

These experiments provide an insight into elastic stress wave propagation in ring systems. In the next chapter, a theoretical model is formulated and its predictions are compared with experimental data.

# CHAPTER FOUR
# THEORETICAL ANALYSIS FOR STRESS WAVE PROPAGATION IN A CIRCULAR RING

As an idealization of an actual cellular material, ring arrays in three packing arrangements are used to study stress wave propagation in cellular structures. Appropriate experiments were conducted and have been described in the preceding chapter. In these idealized systems, a circular ring is taken to represent a unit cell in a cellular material. Propagation of stress through the system can be studied by analyzing stress wave transmission in a single ring. A theoretical analysis of elastic stress propagation in a single ring is now presented; this provides a foundation for subsequent studies on stress wave propagation in cellular structures.

## 4.1 Theoretical Analysis of Wave Propagation in a Circular Ring

To investigate the propagation of elastic waves in a circular ring with a rectangular cross-section, a theoretical analysis is formulated via an extension of the well-known Timoshenko approximation for extensional, shear and flexural motion in a straight beam. The basic assumption is that plane cross-sections remain plane after deformation. The total transverse displacement of the beam axis is obtained by superposing the displacements due to bending and shear.

From first principles, it can be shown that the forces and moments acting on a cross-section are related to the displacements and rotations by the following set of six equations. Appendix D shows their derivation.

$$\begin{cases} \dfrac{\partial \Theta}{\partial s} = \dfrac{M}{\beta} & (4.1) \\ \dfrac{P}{\sigma_p} = \dfrac{\partial u}{\partial s} - \dfrac{v}{R} & (4.2) \\ \dfrac{Q}{\sigma_q} + \Theta = \dfrac{\partial v}{\partial s} + \dfrac{u}{R} & (4.3) \\ \dfrac{\partial P}{\partial s} - \dfrac{Q}{R} = m\dfrac{\partial^2 u}{\partial t^2} & (4.4) \\ \dfrac{\partial Q}{\partial s} + \dfrac{P}{R} = m\dfrac{\partial^2 v}{\partial t^2} & (4.5) \\ \dfrac{\partial M}{\partial s} + Q = mk^2\dfrac{\partial^2 \Theta}{\partial t^2} & (4.6) \end{cases}$$

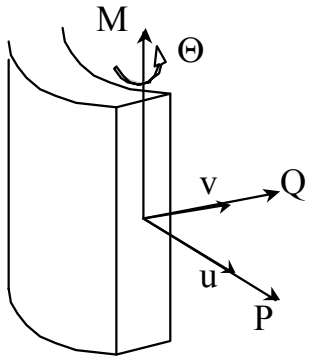


**Fig. 4-1** Definition of cross-sectional displacements, rotations and stress resultants

where

| | |
|---|---|
| *P, Q, M* | Axial tension, shear and bending moment, respectively |
| $\beta$ | Flexural rigidity of the ring $\{EI\}$ * |
| $\sigma_p$ | Extensional rigidity $\{EA\}$ * |
| $\sigma_q$ | Shear rigidity ** |
| *k* | Radius of gyration of the cross section |
| *R* | Radius of the ring |
| *m* | Mass per unit length |
| *t* | Time |
| *s* | Co-ordinate measured along the circumferential axis |
| *u v* | Displacements of the centroid of a ring cross section |

* $E$ is the Young's modulus of the ring material; $I$ is the second moment of area of the cross-section about the axis of bending; $A$ is the cross-sectional area

** shear rigidity $\sigma_q$ is derived by integrating the shear strain energy, due to the parabolic shear stress distribution generated by a shear force, over the cross-section. Appendix E shows the derivation of $\sigma_q$ for a beam with a rectangular cross-section, resulting in $\sigma_q = \frac{5}{6}Gbh$, where $G$ is the shear modulus, *b* and *h* are the width and height of the cross-section, respectively.

Let the circumferential and radial displacements, and the rotation of the cross-section be

$$u = Ae^{i(\eta s-\omega t)} \qquad v = Be^{i(\eta s-\omega t)} \qquad \Theta = Ce^{i(\eta s-\omega t)}$$

where

| | |
|---|---|
| A, B, C | Amplitudes |
| $\omega$ | Circular frequency of wave |
| $\eta$ | Wave number |

The following relationships are inherently assumed:

$$\omega = \eta V \qquad \omega = 2\pi f \qquad T = \frac{1}{f} \qquad \lambda = \frac{2\pi}{\eta}$$

where

| | |
|---|---|
| $f$ | Frequency |
| $\lambda$ | Wavelength |
| $V$ | Phase velocity |
| $T$ | Period of cycle |

Elimination of M, P and Q by substitution of equations (4.1), (4.2) and (4.3) into the left-hand sides of equations (4.4), (4.5) and (4.6), yields the following set of three homogeneous linear simultaneous equations, which can be written in matrix form:

$$\begin{bmatrix} \frac{\omega^2\sigma_p}{V^2}+\frac{\sigma_q}{R^2}-m\omega^2 & \frac{(\sigma_p+\sigma_q)\omega}{RV} & -\frac{\sigma_q}{Rk} \\ \frac{(\sigma_p+\sigma_q)\omega}{RV} & \frac{\omega^2\sigma_q}{V^2}+\frac{\sigma_p}{R^2}-m\omega^2 & -\frac{\omega\sigma_q}{Vk} \\ -\frac{\sigma_q}{Rk} & -\frac{\omega\sigma_q}{Vk} & \frac{\omega^2\beta}{k^2V^2}+\frac{\sigma_q}{k^2}-m\omega^2 \end{bmatrix} \begin{bmatrix} A \\ Bi \\ kC \end{bmatrix} = 0 \qquad (4.7)$$

Note that the coefficient matrix in equation (4.7) is symmetrical.

In order that equation (4.7) should have non-zero solutions, it is necessary for the determinant of the coefficient matrix to vanish; thus

$$Det\begin{bmatrix} \frac{\omega^2\sigma_p}{V^2}+\frac{\sigma_q}{R^2}-m\omega^2 & \frac{(\sigma_p+\sigma_q)\omega}{RV} & -\frac{\sigma_q}{Rk} \\ \frac{(\sigma_p+\sigma_q)\omega}{RV} & \frac{\omega^2\sigma_q}{V^2}+\frac{\sigma_p}{R^2}-m\omega^2 & -\frac{\omega\sigma_q}{Vk} \\ -\frac{\sigma_q}{Rk} & -\frac{\omega\sigma_q}{Vk} & \frac{\omega^2\beta}{k^2V^2}+\frac{\sigma_q}{k^2}-m\omega^2 \end{bmatrix}=0$$

This results in the following characteristic equation:

$$\frac{\beta}{k^2}\sigma_p\sigma_q\delta^2\left(\delta^2-1\right)^2-\left\{\frac{\beta}{k^2}\sigma_q\delta^2\left(\delta^2+1\right)+\frac{\beta}{k^2}\sigma_p\delta^2\left(\delta^2+1\right)+\sigma_p\sigma_q\left[\left(\delta^2-1\right)^2+\gamma^2\left(\delta^2+1\right)\right]\right\}\Omega$$
$$+\left[\frac{\beta}{k^2}\delta^2+\sigma_p\left(1+\delta^2\right)+\sigma_q\left(1+\delta^2+\gamma^2\right)\right]\Omega^2-\Omega^3=0 \qquad (4.9)$$

where $\gamma=\frac{R}{k}$ $\delta=\frac{2\pi R}{\lambda}$ $\Omega=m\delta^2V^2$

Equation (4.9) is a cubic equation in terms of $\Omega$, which contains the wave velocity variable. Extraction of explicit expressions for the roots is not practical. Two approaches are undertaken to solve this equation and analyze the relationships between wave velocity and other parameters in the equation. One is to obtain approximate solutions by adopting certain assumptions to simplify Eqn (4.9); the other is to employ numerical methods.

## 4.2 Approximate Solutions for Phase Velocity

Note that the derivation of the characteristic equation (4.9) is based on the assumption that plane cross-sections of the circular ring remain plane after deformation. In addition, lateral expansions and contractions caused by the Poisson's ratio effect for a propagating longitudinal wave are also ignored in this theoretical analysis. When the lateral dimensions of the circular ring are much smaller than the

wavelength, the kinetic energy of lateral expansion and contraction is small compared with that associated with longitudinal motion. This means that the solution of equation (4.9) is sufficiently accurate if $\lambda >> h$, where $h$ is the wall-thickness of the circular ring. For thin walled rings in this study, $R >> h$, resulting in $\gamma >> 1$. This is generally true for low-density cellular structures, whereby the cell size is much larger than the wall thickness.

Actual cellular materials generally possess a relatively small cell size, usually of the order of a millimeter or a centimeter at most. It is more practical to analyze the stress wave characteristics when the wavelength is greater than the cell size. Consider the situation whereby the wavelength $\lambda$ is larger than the ring circumference ($\lambda > 2\pi R$); consequently, $\delta = \frac{2\pi R}{\lambda} < 1$ and $\gamma >> \delta$ because $\gamma >> 1$. Therefore, equation (4.9) can be simplified to yield the following set of expressions for the stress wave velocities:

$$\Rightarrow \begin{cases} V_1 = \pm\left(\dfrac{\lambda}{2\pi k}\right)\sqrt{\dfrac{\sigma_q}{m}} \\ V_2 = \pm\dfrac{1-\left(\dfrac{2\pi R}{\lambda}\right)^2}{R\sqrt{1+\left(\dfrac{2\pi R}{\lambda}\right)^2}}\sqrt{\dfrac{\beta}{m}} \\ V_3 = \pm\sqrt{1+\left(\dfrac{\lambda}{2\pi R}\right)^2}\sqrt{\dfrac{\sigma_p}{m}} \end{cases} \qquad (4.10)$$

Appendix F shows the detailed derivation of this approximate solution

Apart from the parameters related to material properties, such as $\beta$, $\sigma_p$, $\sigma_q$ and $m$, each equation in (4.10) is also a function of wavelength, illustrating that stress wave velocities in a circular ring are wavelength dependent.

With regard to shear wave propagation, the expression for $V_1$ shows that its velocity is proportional to wavelength. Moreover, the radius of gyration of the cross section, $k$, is another factor that influences the shear wave velocity; $k$ is inversely proportional to the shear wave velocity. This means that the thicker the ring cross section, the slower the shear wave. Figure 4-2 illustrates schematically the relationship between shear wave velocity and wavelength.

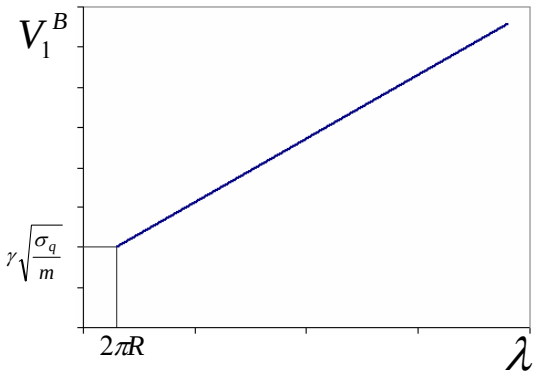


**Fig. 4-2** Relationship between the phase velocity of a shear wave and wavelength

Figure 4-3 shows the relationship between flexural wave velocity and wavelength. Notice that the velocity vanishes when the wavelength approaches the ring circumference of $2\pi R$, while it tends to $\frac{1}{R}\sqrt{\frac{\beta}{m}}$ as the wavelength approaches infinity.

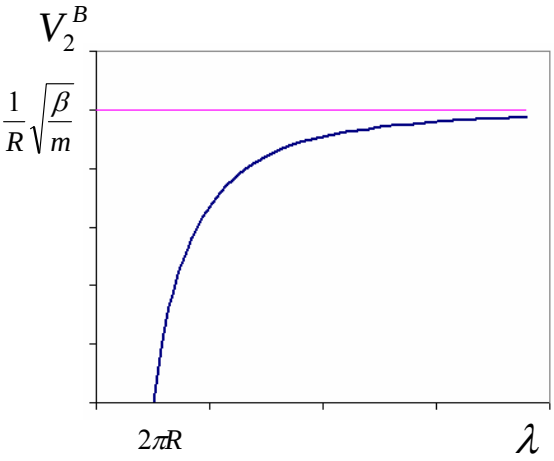


**Fig. 4-3** Relationship between the phase velocity of a flexural wave and wavelength

Figure 4-4 shows the relationship between extensional wave velocity and wavelength. The wave velocity

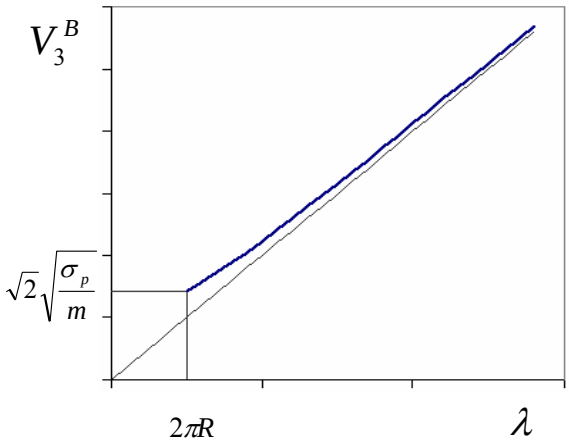


**Fig. 4-4** Relationship between the phase velocity of an extensional wave and wavelength

becomes almost directly proportional to wavelength as the wavelength increases. The expression for extensional wave velocity in Eqn (4.10) also indicates that a larger ring radius decreases the speed at which extensional waves transmit through it.

## 4.3 Group Velocity

### 4.3.1 Definition of Group Velocity

In the impact tests described in the preceding chapter, the profile of a stress wave changes considerably when it passes through a ring column. This difference is obvious from Figure 3-14(b), when the wave fronts of the signals from the accelerometer attached to colliding mass and the force transducer at the bottom of ring array are compared. This indicates that stress wave propagation in a ring system is dispersive. Therefore, what was determined from impact tests is actually the group velocity at which energy is transported by the waves [24]. The expression for the group is [22],

$$V_g = \frac{d\omega}{d\eta} \tag{4.11}$$

where $\omega$ is the circular frequency and $\eta = 2\pi/\lambda$ is the wave number.

From the fundamental relationship $\omega = \eta V$, equation (4.11) can be re-written as

$$V_g = \frac{d(\eta V)}{d\eta} = V + \eta \frac{dV}{d\eta} \tag{4.12}$$

This can also be expressed in terms of wavelength, resulting in

$$V_g = V - \lambda \frac{dV}{d\lambda} \tag{4.13}$$

### 4.3.2 Deriving Group Velocities of Stress Waves

When the wavelength is larger than the circumference of a ring, the wave velocities are wavelength dependant, as shown by equations (4.10). Substitution of the three individual equations in (4.10) into (4.13) yields the corresponding group velocities:

$$\begin{cases} V_{g1} = 0 \\ V_{g2} = \pm\dfrac{1}{R}\sqrt{\dfrac{\beta}{m}}\left\{\dfrac{\left[\lambda^4 - 3(2\pi R)^2\lambda^2 - 2(2\pi R)^4\right]\sqrt{1+\left(\dfrac{2\pi R}{\lambda}\right)^2}}{\left[(2\pi R)^2 + \lambda^2\right]^2}\right\} \\ V_{g3} = \pm\sqrt{\dfrac{\sigma_p}{m}}\dfrac{1}{\sqrt{1+\left(\dfrac{\lambda}{2\pi R}\right)^2}} \end{cases} \tag{4.14}$$

What is notable from equations (4.14) is that the group velocity of shear waves is zero when $\lambda > 2\pi R$. Although a simplification has been assumed in the derivation of this velocity expression, it still shows that cellular structures are likely to significantly block the propagation of shear stresses with large wavelengths.

Figure 4-5 shows a schematic diagram of the relationship between the group velocity $V_{g2}$ of flexural waves and wavelength $\lambda$. When $\lambda \to \infty$, the group velocity tends to

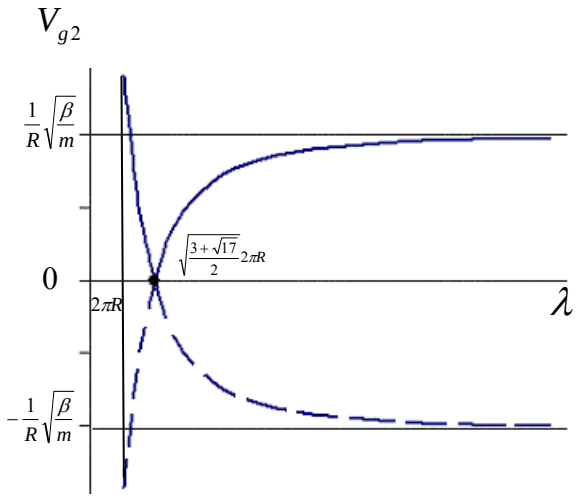


**Fig 4-5**. Relationship between the group velocity of a flexural wave and wavelength

$\frac{1}{R}\sqrt{\frac{\beta}{m}}$, which is also the limiting phase velocity, as shown in Figure 4-3. Moreover, the group velocity seems to vanish when the wavelength decreases to $\sqrt{\frac{3+\sqrt{17}}{2}}(2\pi R)$. Negative values of $V_{g2}$ shown as dashed line in Figure 4-3 correspond to flexural waves traveling in the negative or opposite direction.

Figure 4-6 shows the relationship between the group velocity of extensional waves $V_{g3}$ and wavelength $\lambda$. When the wavelength assumes the value of $2\pi R$, the group velocity equals $\pm\frac{1}{\sqrt{2}}\sqrt{\sigma_p/m}$, i.e. $\frac{1}{\sqrt{2}}$ times the speed of an extensional wave transmitting in a thin circular bar. The negative sign of the velocity denotes stress waves propagating along the ring in the opposite direction. As $\lambda$ increases, the group velocity tends to zero.

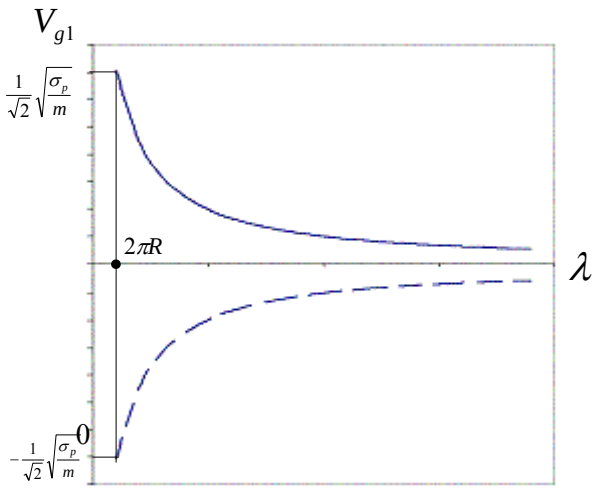


**Fig. 4-6** Relationship between the group velocity of an extensional wave and wavelength

The approximate solutions presented above are limited by several assumptions and yield an incomplete spectrum for the relationships between wave velocity and wavelength; i.e. $\lambda > 2\pi R$. The following numerical solutions of the governing equations supplement the preceding analysis.

## 4.4 Numerical Solutions for Wave Velocities

Bearing in mind that the quantities measured in experiments are frequency and group velocity, it is more meaningful to show the relationship between these two parameters, rather than to focus on phase velocity and wavelength in equations (4.10) and (4.14). These relationships are not amenable to explicit solutions and results must be obtained numerically (using Newton's Method) and displayed graphically (Appendix G describes briefly Newton's Method).

To compute the numerical solutions, values of all the parameters in the governing equations must be defined. Consequently, actual quantitative data is required. Five types of metal rings were used in the experiments and Table 4-1 shows their physical properties, while the ring geometry is depicted in Fig 4-7.

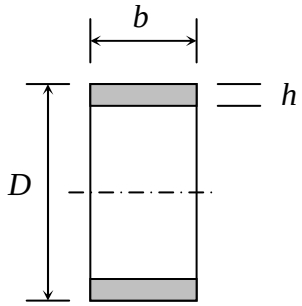


**Fig 4-7**. Geometry of a ring

**Table 4-1** Physical properties and dimensions of rings

| Symbol | Parameter | Unit | Al alloy rings | | Brass rings | | | Expresion |
|---|---|---|---|---|---|---|---|---|
| | | | 38.1x1 | 38.1x3 | 38.1x1 | 38.1x3 | 25.4x1 | |
| $\rho$ | Density | $Kg/m^3$ | 2693 | | 8199 | | | |
| $E$ | Young's Modulus | $GPa$ | 65.9 | | 120.4 | | | |
| $\upsilon$ | Poisson's Ratio | | 0.34 | | 0.34 | | | |
| $G$ | Shear Modulus | $GPa$ | 24.6 | | 44.9 | | | $=E/[2(1+\upsilon)]$ |
| $D$ | Outer diameter | $mm$ | 38.1 | | 38.1 | | 25.4 | |
| $h$ | Wall thickness | $mm$ | 1 | 3 | 1 | 3 | 1 | |
| $b$ | Ring width | $mm$ | 10 | | | | | |
| $I$ | Second moment of gyration | $m^4$ | $8.33\text{x}10^{-13}$ | $2.25\text{x}10^{-11}$ | $8.33\text{x}10^{-13}$ | $2.25\text{x}10^{-11}$ | $8.33\text{x}10^{-13}$ | $=\frac{1}{12}bh^3$ |
| $\beta$ | Flexural Rigidity | $N$ | 0.0549 | 1.48 | 0.10 | 2.71 | 0.10 | $=E\cdot I$ |
| $\sigma_p$ | Extensional Rigidity | $N$ | $6.59\text{x}10^{5}$ | $1.98\text{x}10^{6}$ | $1.20\text{x}10^{6}$ | $3.61\text{x}10^{6}$ | $1.20\text{x}10^{6}$ | $=E\cdot A$ |
| $\sigma_q$ | Shear Rigidity | $N$ | $2.05\text{x}10^{5}$ | $6.14\text{x}10^{5}$ | $3.74\text{x}10^{5}$ | $1.12\text{ x}10^{6}$ | $3.74\text{x}10^{5}$ | $=\frac{5}{6}Gbh$ |
| k | Radius of gyration | $m$ | $2.89\text{x}10^{-4}$ | $8.66\text{x}10^{-4}$ | $2.89\text{x}10^{-4}$ | $8.66\text{x}10^{-4}$ | $2.89\text{x}10^{-4}$ | $=\sqrt{I/(bt)}$ |
| m | Mass per unit length | $Kg/m$ | 0.027 | 0.081 | 0.082 | 0.246 | 0.082 | $=\rho(bt)$ |

By substituting the parameter values for each type of ring into the characteristic equation ─ Eqn (4.9) ─ and solving for phase velocities using Newton's method, the velocities can be obtained as functions of wavelength. The corresponding group velocities are derived using equation (4-13). Figures 4-8 to 4-10 show how the group velocity varies with wavelength for shear, flexural and extensional waves. Both dimensional and non-dimensionalized plots are shown. The non-dimensional wavelength $\bar{\lambda}$ is defined by $\lambda/2\pi R$, where $\lambda$ and $R$ are respectively the wavelength and outer radius of a ring. $\bar{C}$, the non-dimensionalized velocity, is defined by $C/C_0$, where $C_0 = \sqrt{E/\rho}$ is the extensional wave velocity in a thin straight rod. From the fundamental relationship $f = V/\lambda$, the group velocity plots can be transformed into the frequency domain, as shown in Figures 4-11 to 4-13. Non-dimensional frequency $\bar{f}$ is defined by $\frac{f}{f_0}$, where $f_0 = \frac{C_0}{2\pi R}$.

Limitations in the current theory adopted come from the assumptions that plane cross-sections in the rings remain plane after deformation. In addition, as the wavelength becomes comparable or shorter than the thickness of the cross-section, lateral inertia due to Poisson's effect becomes significant and affects stress wave propagation. Therefore, the current theory does not apply to short wavelengths. (In Figs 4-8 to 4-13, the portions of the curves shown in thin lines are beyond the scope of current theory.)

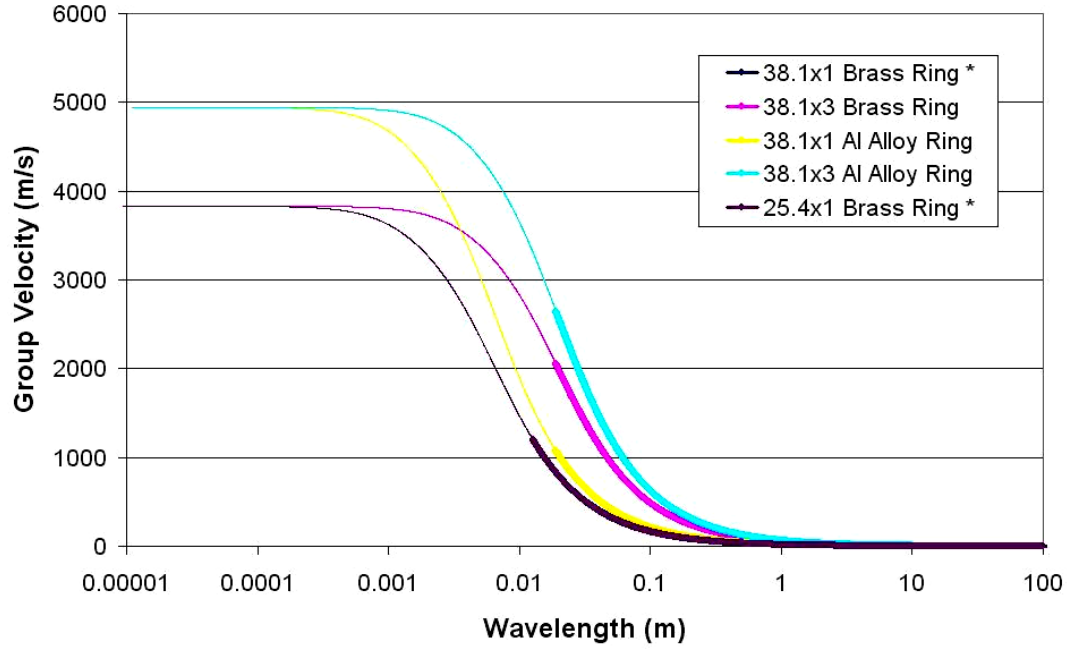


**(a)** Dimensionalized quantities

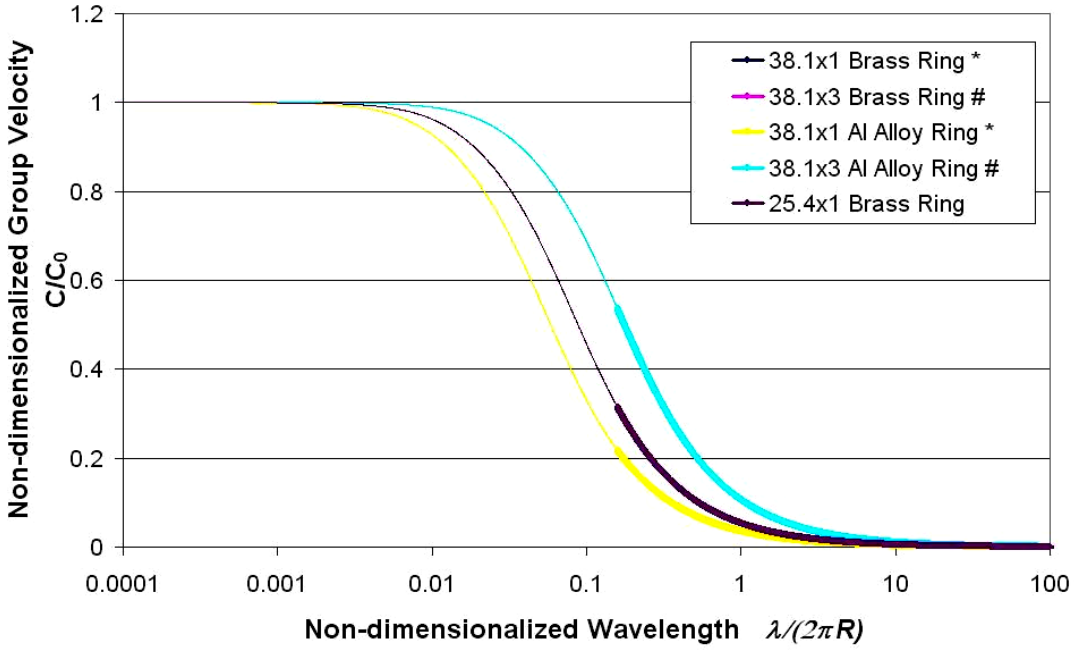


**(b)** Non-Dimensionalized quantities

**Fig 4-8**. Variation of shear wave group velocity with wavelength for transmission in a single ring

[The thin lines define regions beyond the limits of current theory]

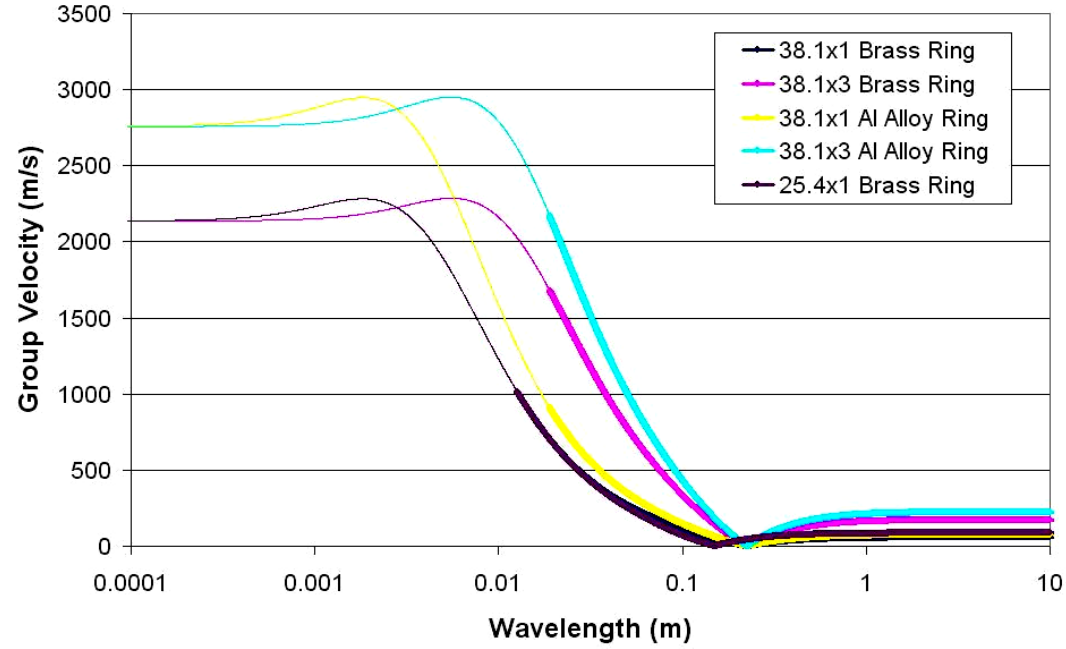


**(a)** Dimensionalized quantities

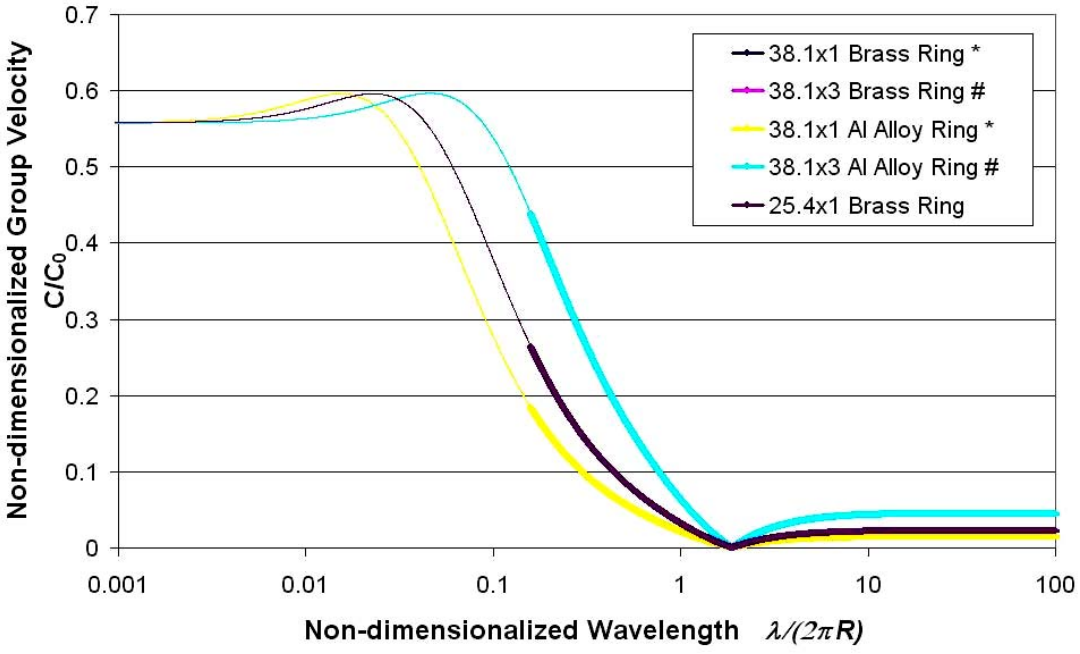


**(b)** Non-Dimensionalized quantities

**Fig 4-9**. Variation of flexural wave group velocity with wavelength for transmission in a single ring

[The thin lines define regions beyond the limits of current theory]

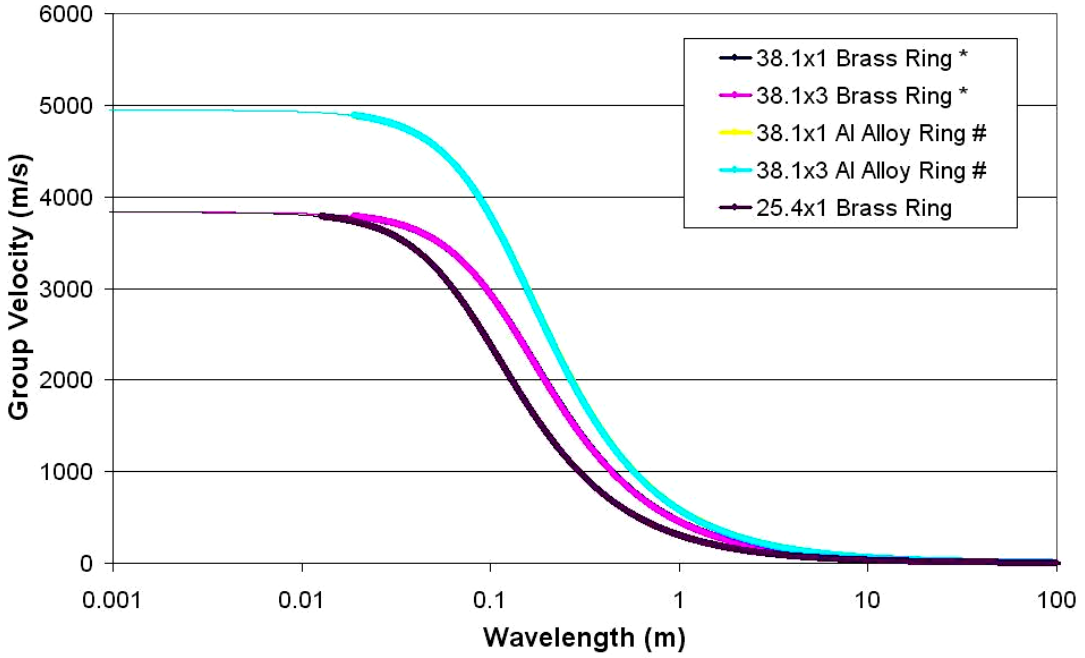


**(a)** Dimensionalized quantities

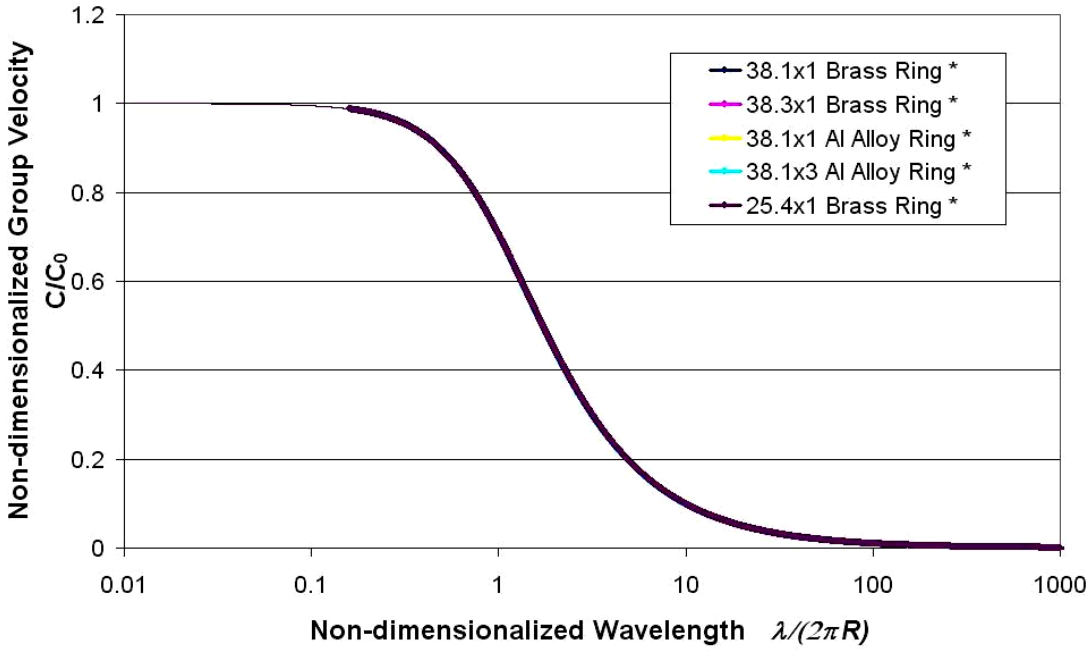


**(b)** Non-Dimensionalized quantities

**Fig 4-10**. Variation of extensional wave group velocity with wavelength for transmission in a single ring

[The thin lines define regions beyond the limits of current theory]

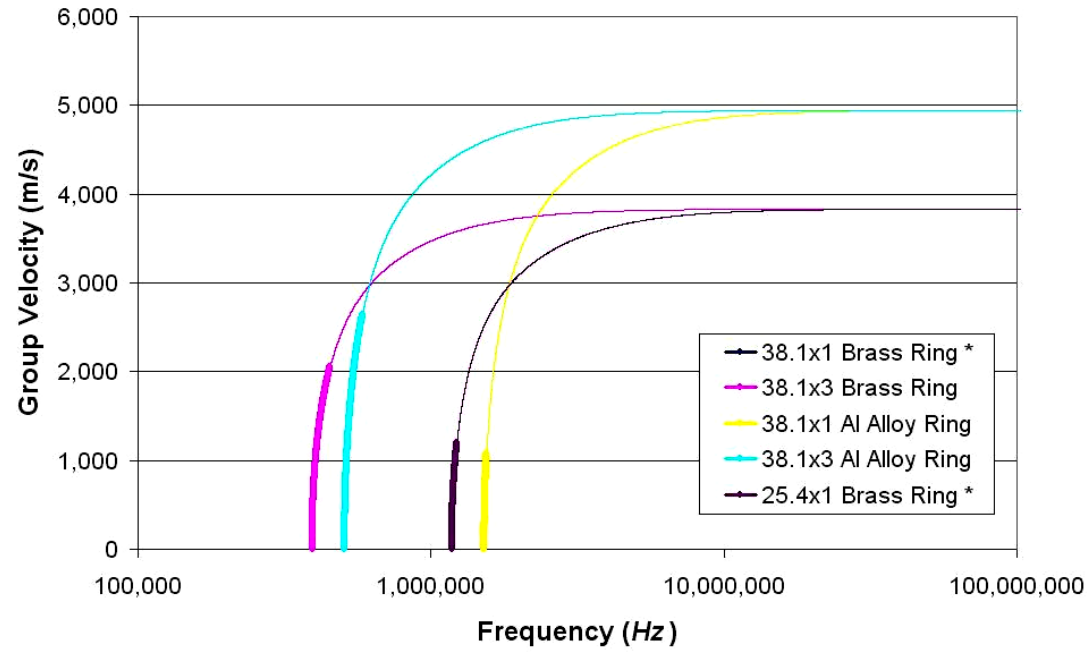


**(a)** Dimensionalized quantities

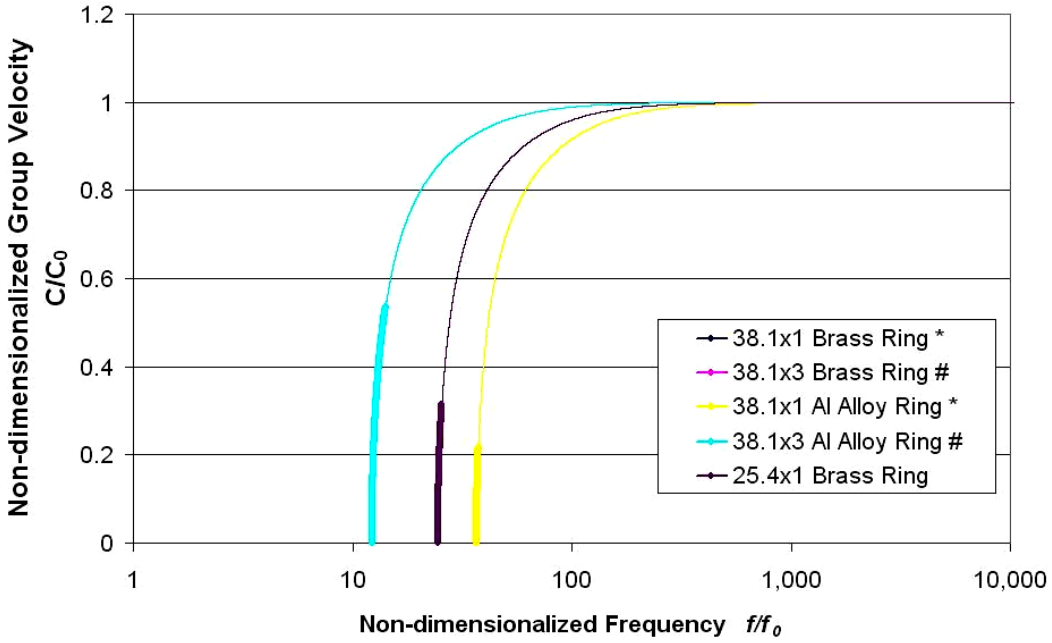


**(b)** Non-Dimensionalized quantities

**Fig 4-11**. Variation of shear wave group velocity with frequency for transmission in a single ring

[The thin lines define regions beyond the limits of current theory]

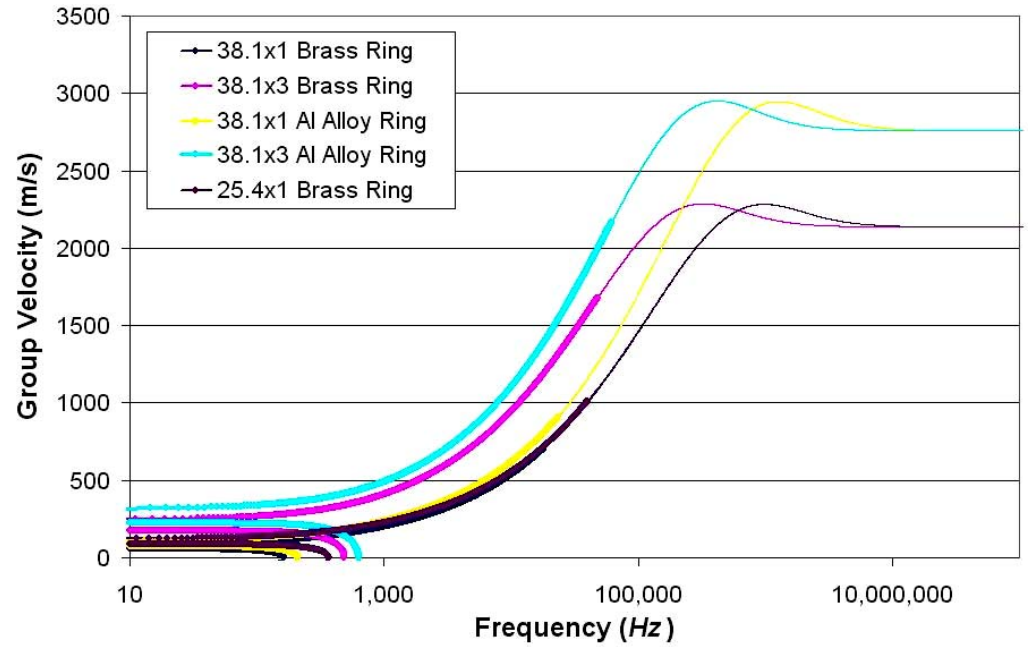


**(a)** Dimensionalized quantities

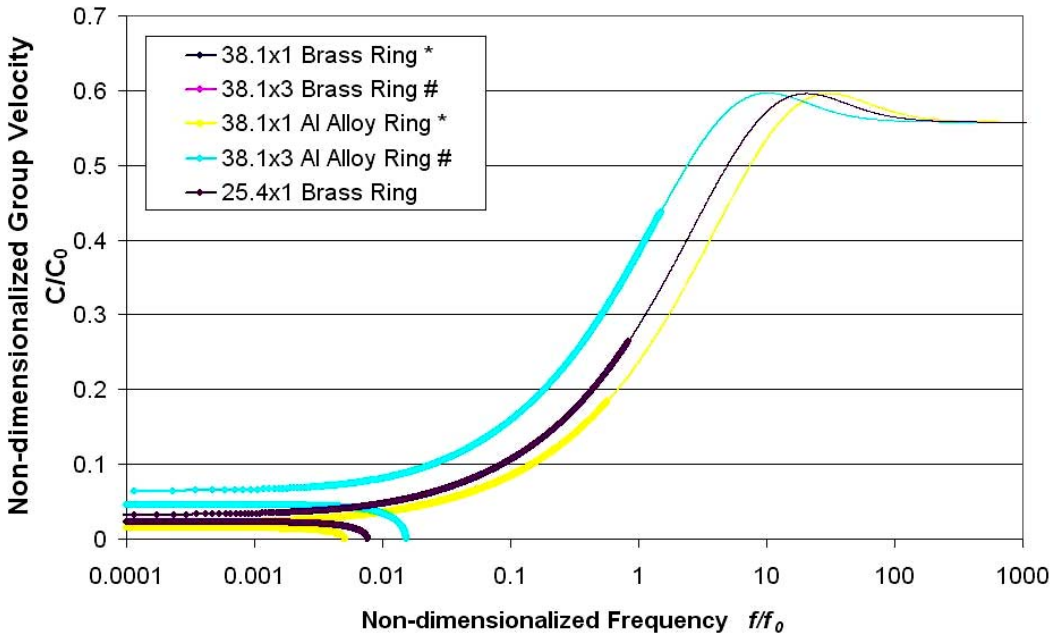


**(b)** Non-Dimensionalized quantities

**Fig 4-12**. Variation of flexural wave group velocity with frequency for transmission in a single ring

[The thin lines define regions beyond the limits of current theory]

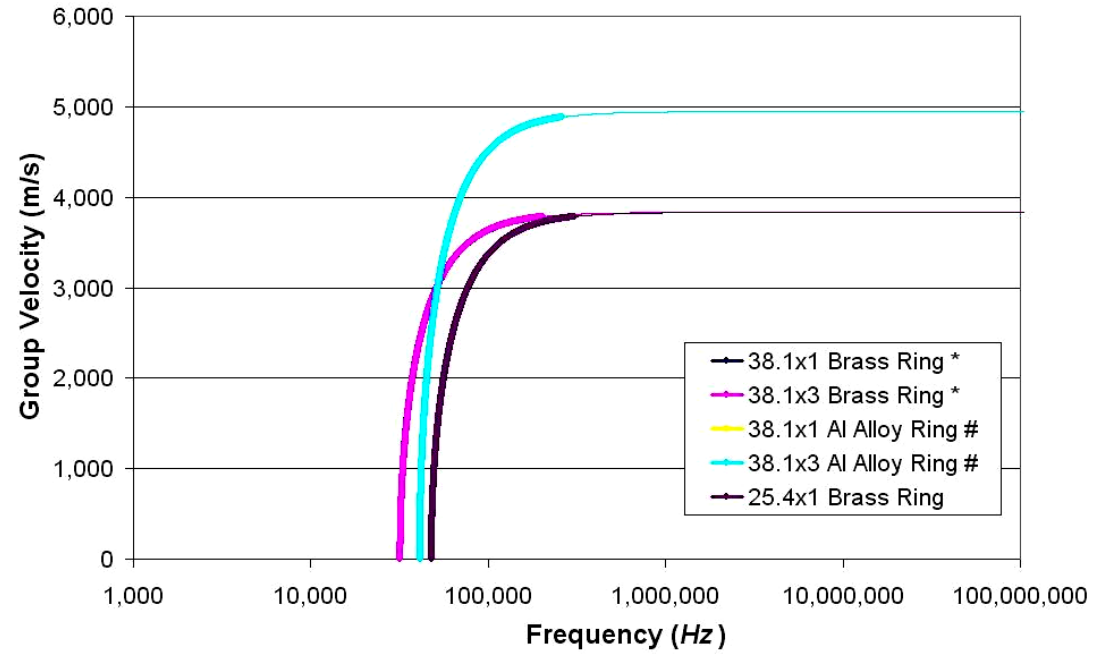


**(a)** Dimensionalized quantities

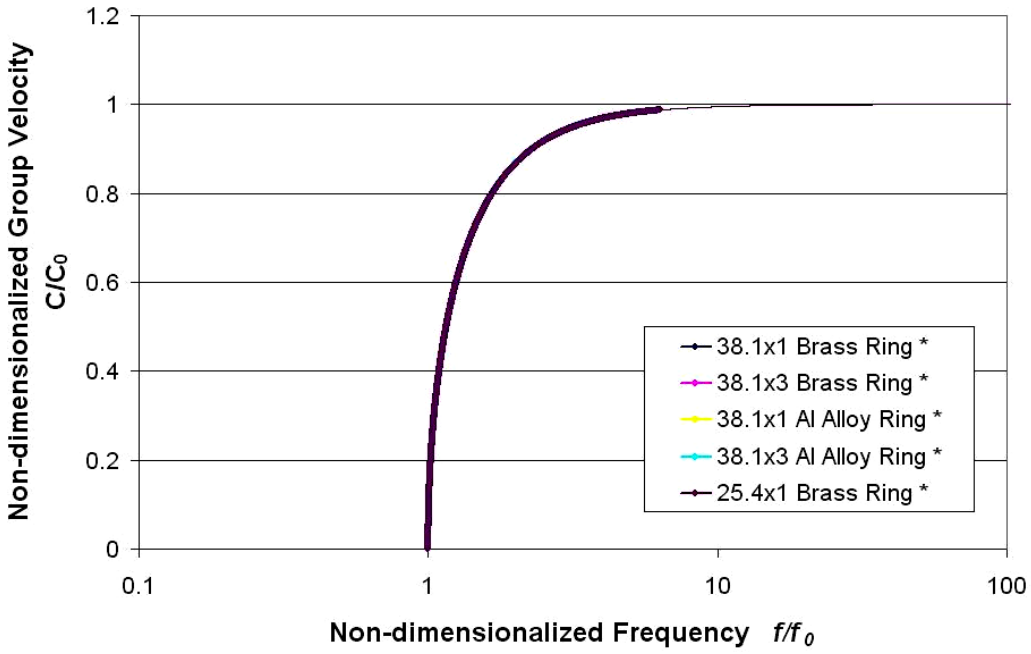


**(b)** Non-Dimensionalized quantities

**Fig 4-13**. Variation of extensional wave group velocity with frequency for transmission in a single ring

[The thin lines define regions beyond the limits of current theory]

With reference to the stress wave velocities for various types of rings, as shown in Figure 4-10 to 4-13, some features of wave propagation for extensional, shear and flexural waves can be identified.

With respect to non-dimensionalized quantities, the group velocity relationships for extensional waves for the five types of rings lie on top of one another, as shown in Figures 4-10(b) and 4-13(b). Because $C_0$ (which represents material properties) and $2\pi R$ are the reference parameters with regard to non-dimensionalization, this indicates that material properties and the ring circumference (or radius) are the only parameters that affect the propagation of extensional waves, while the wall thickness does not. This is also observed in the corresponding diagrams for dimensional quantities (Figures 4-10(a) and 4-13(a)), where the curves for 38.1x1 and 38.1x3 Al alloy rings lie on top of one another; this is also the case for brass rings. This is similar to longitudinal wave propagation in a thin circular bar, whereby propagation speed is independent of the lateral dimensions of a bar. The group velocities for Al alloy rings are always larger than those for brass ones; this is a result of the difference in material properties (the bar velocity in Al alloy is higher than that in brass). Furthermore, a comparison of the curves for 38.1x1 and 25.4x1 brass rings shows that extensional waves travel faster in a larger ring. This indicates that curvature in a structure slows the propagation of extensional wave. If the curvature of a ring tends to zero (the case of a straight beam), the group velocity of extensional waves in the ring tends to the bar velocity $C_0$.

For shear waves, the wall thickness affects its propagation; this differs from extensional waves, as discussed earlier. As shown in the plots for group velocity in Figures 4-8 and 4-11, shear waves travel faster in rings with thicker walls. However, the ring radius does not affect the shear wave velocity, as shown in Figures 4-8(a) and 4-11(a), where the velocity distributions for 38.1mm-diameter and 25.4mm-diameter rings lie on top of one another. With respect to the difference in material properties, shear waves travel faster in Al alloy rings than in brass ones, which is similar to the behaviour of extensional waves.

Figures 4-9 and 4-12 show that flexural wave propagation is affected by several factors ─ material properties, ring size (radius/diameter) and wall thickness. Flexural wave group velocities are proportional to $C_0$ (i.e. dependent on material properties), which is what has been found for shear and extensional waves. As shown in Figure 4-12(a) and (b), a comparison of the velocity relationships for 38.1x1 and 25.4x1 brass rings reveals that they are close to each other, but rings with a smaller diameter transmit flexural waves more quickly. The effect of wall thickness on flexural wave propagation is evident in the diagrams showing non-dimensionalized quantities, i.e. Figures 4-9(b) and 4-12(b). Flexural waves generally travel faster in rings with a thicker wall, which correspond to a higher flexural rigidity $\beta$.

## 4.5 Summary

In this chapter, a characteristic equation (Eqn 4.9) for phase velocities was derived from first principles to describe wave propagation in a circular ring with a rectangular cross section. A basic assumption is that plane cross-sections in the ring remain plane after deformation. This assumption requires a large radius to wall thickness ratio for it to be valid.

There are three modes of wave propagation captured by the characteristic equation ─ extensional, flexural and shear waves. To identity the relationship between wave velocity and wavelength, approximate explicit solutions and numerically evaluated results were derived. Although the approximate solutions can be expressed in closed form (Eqns 4.10 and 4.14), these relationships are based on additional assumptions which limit their range of validity, making comparison with experimental results difficult. Newton's Method was subsequently also applied to solve the characteristic equation (Eqn 4.9) numerically and the results are presented graphically. As wavelength components in signals obtained from experiments are difficult to determine, the wave velocity distributions were computed as functions of frequency. Discrete Fourier Transformation was applied to the acceleration and force signals captured in experiments to determine the frequency spectrum. Consequently, group velocities corresponding to several frequency components were determined and compared with theoretical results.

The theoretical model adopted captures the features corresponding to stress wave propagation in a ring. A comparison with experimental results will now be undertaken, from which the applicability of the model described will be examined.

# CHAPTER FIVE
# COMPARISON BETWEEN THEORETICAL AND EXPERIMENTAL RESULTS

The theoretical results in Figures 4-8 to 4-13 in the preceding chapter show how the three wave velocities vary with wavelength/frequency. For comparison with experimental results, the wave velocities corresponding to different frequency components in actual signals are determined. This requires specific filtering of experimental data and determination of the propagation speed of selected frequency components.

## 5.1 Isolation of Frequency Components

Transmitted signals obtained from impact tests are processed using Discrete Fourier Transformation (DFT) to determine dominant frequency components. Figure 5-1(a) shows a typical result of DFT and (b) is an enlarged view of the range from 1,000 to 100,000 Hz. Several frequency peaks can be identified from the two plots, i.e. 500, 4,000, 8,500 and 15,500 Hz. By filtering out unwanted frequency components and then applying inverse Fourier transformation, signals of specified frequencies can be isolated in the time domain. Appendix I describes the process for determining the starting points of waves corresponding to different frequency components and how to ascertain the propagation time.

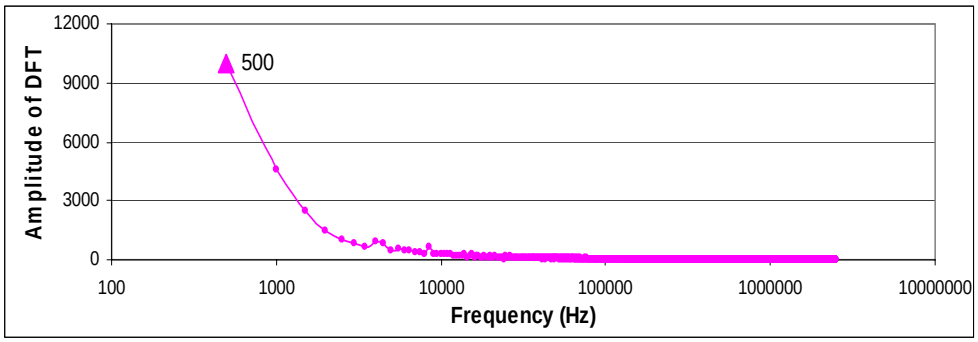


(a)

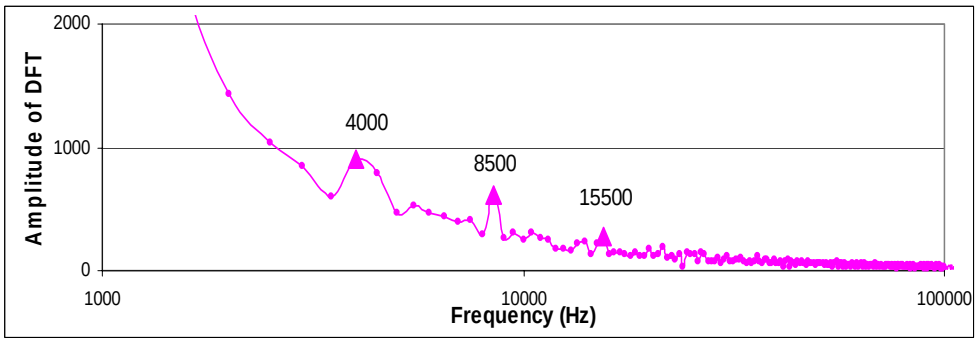


(b)

**Fig. 5-1** DFT result for a typical output signal

(a) Complete DFT (b) DFT from 1,000 to 100,000 *Hz*

The theoretical results define the velocities at which stress waves travel along the solid wall of a ring; hence, the length of the shortest route along solid ring walls in a ring array is then taken as the distance travelled by the stress wave. By considering the time taken by a selected frequency component to travel from the top to the bottom of a ring array, the velocity for that frequency component can be computed. Table 5-1 lists actual wave velocities of selected frequency components in the ring arrays.

**Table 5-1** Experimental flexural wave speeds for identified frequency components

| Ring Material & Size($D \times h$) | Arrangement | Frequency (*Hz*) | Actual velocity along transmit path (*m/s*) |
|---|---|---|---|
| Brass (38.1x1) | Square | 200 | 230.7 |
| | | 12600 | 544.7 |
| | Transverse | 200 | 214.3 |
| | Vertical | 200 | 146.9 |
| | | 4600 | 569.6 |
| Brass (38.1x3) | Square | 500 | 630.2 |
| | | 8500 | 1190.2 |
| | | 15500 | 1356.6 |
| | Transverse | 500 | 503.4 |
| | Vertical | 500 | 395.7 |
| | | 5000 | 974.0 |
| Brass (25.4x1) | Square | 200 | 240.4 |
| | | 4200 | 485.6 |
| | Transverse | 200 | 213.7 |
| | | 5200 | 472.7 |
| | Vertical | 200 | 200.5 |
| | | 3800 | 544.2 |
| Al alloy (38.1x1) | Square | 200 | 228.4 |
| | | 7000 | 513.2 |
| | Transverse | 200 | 223.8 |
| | Vertical | 200 | 162.9 |
| | | 4400 | 563.4 |
| Al alloy (38.1x3) | Square | 500 | 808.6 |
| | | 6500 | 1410.9 |
| | | 9500 | 1757.6 |
| | Transverse | 500 | 618.1 |
| | Vertical | 500 | 518.2 |
| | | 7500 | 1473.7 |

As shown previously in Figures 4-11 to 4-13, the theoretical results for shear and extensional wave velocities are restricted to the upper portion of the frequency spectrum. Only the results for flexural wave propagation cover the entire frequency domain. All the frequency components that can be identified after filtering the transmitted signals are lower than the cut-off frequencies below which shear and extensional waves theoretically do not propagate. As a result, only the theoretical results for flexural wave velocities can be compared with experimental results.

## 5.2 Comparison between Theoretical and Experimental Results

The five plots in Figure 5-2 show graphically the results listed in Table 5-1 and each of them corresponds to one of the five types of rings tested. The experimental wave velocities for selected frequency components are shown as points and the theoretical group velocity distributions for flexural waves are plotted as curves for comparison.

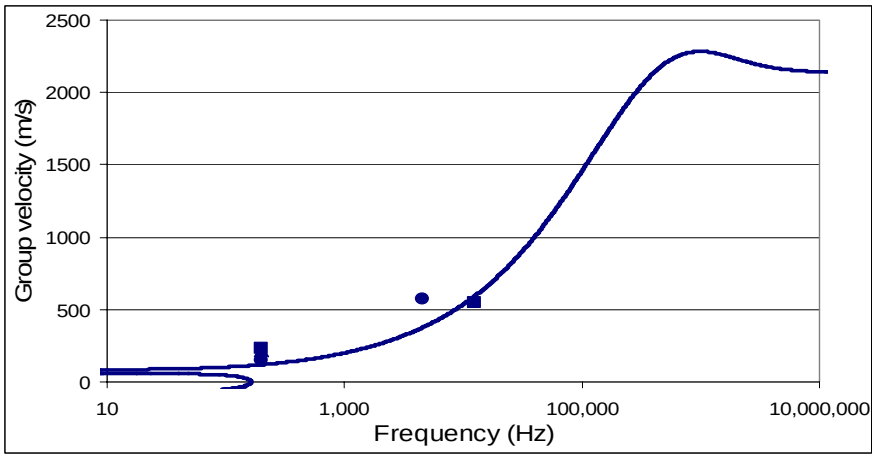


(a) 38.1x1 Brass rings

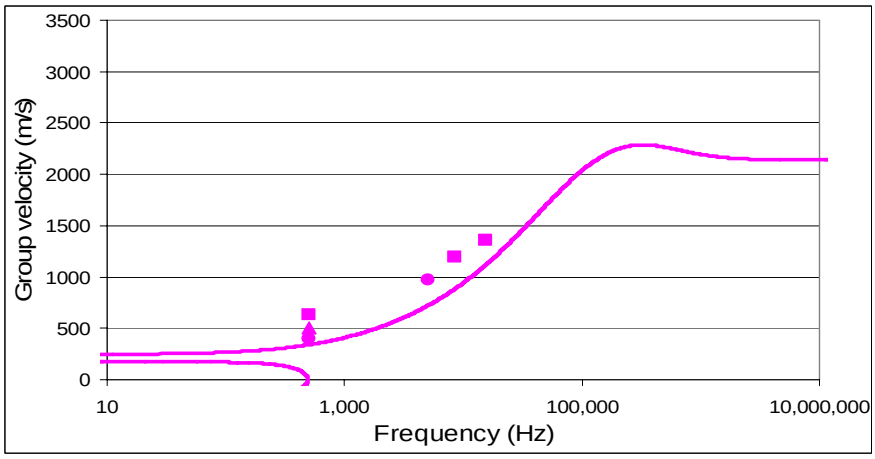


(b) 38.1x3 Brass rings

**Fig. 5-2** Comparison between theoretical velocity distribution and experimental results

∗ Square ■, triangular ▲ and circular ● points denote respectively experimental data for square-packed, transverse close-packed and vertical close-packed ring arrays.

**Fig. 5-2** (continued)

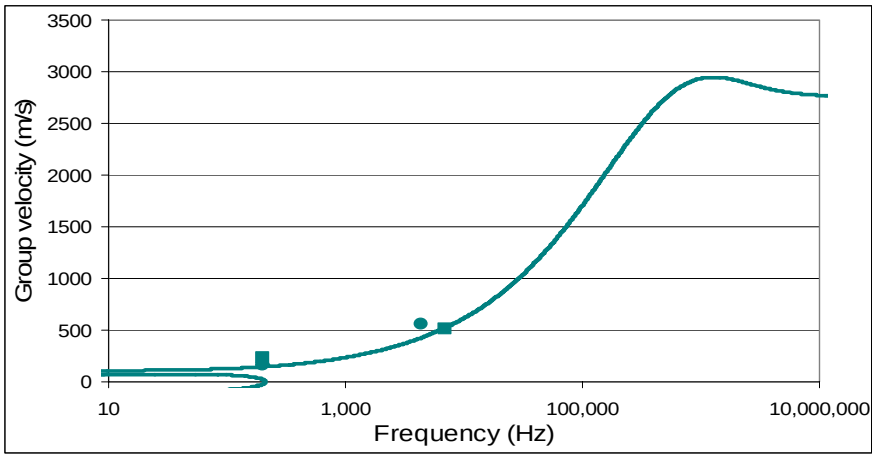


(c) 38.1x1 Al alloy rings

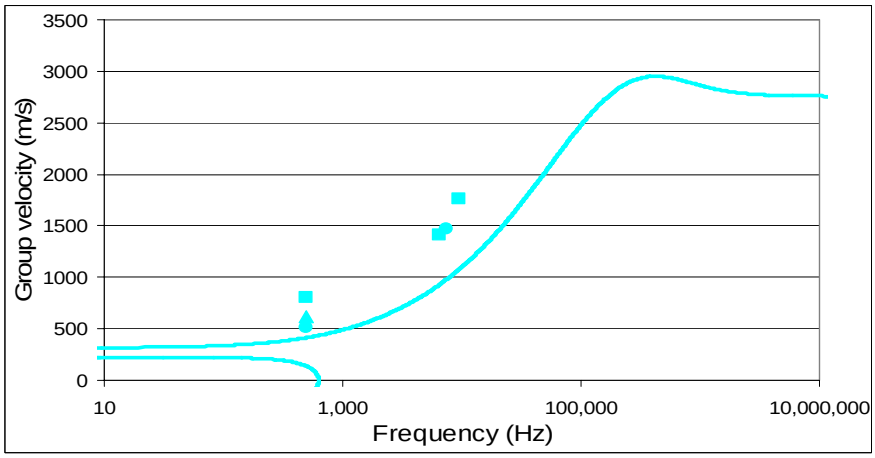


(d) 38.1x3 Al alloy rings

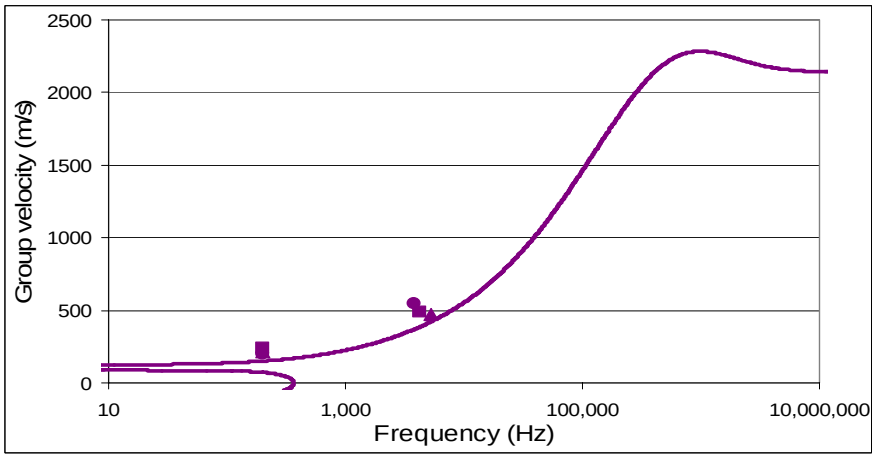


(e) 25.4x1 Brass rings

The graphs in Figure 5-2 show that the experimental flexural wave velocity data generally follow the theoretical curves. For all five types of rings, higher frequency components travel faster, confirming that the theoretical model adopted is acceptable.

However, with regard to thicker rings (3*mm*), as shown in Figs 5-2(b) and (d), the correlation is not as good as that for thin rings (1*mm*). It appears that stress waves travel faster in thicker rings than what is theoretically predicted, especially for low frequency components. It is suspected that the wave transmission mode changes for arrays of thicker rings; i.e. the theoretical model is not sufficiently adequate for 38.1x3 rings because of the noticeable error caused by the assumption that cross sections of thicker wall rings remain plane after deformation. This reveals another limitation with regard to applicability of the theoretical model; i.e. predictions are better for thin-walled ring arrays. For thicker-walled ring arrays, the theory underestimates the velocities.

The theoretical model presented in the current study is based on a single ring and independent of ring array arrangement, i.e. square, transverse close packed or vertical close packed ─ the theoretical wave speeds through the solid wall are the same.

An analysis of the experimental results presented earlier shows that the fastest apparent wave speed detected differs with ring packing arrangement. There are two factors that might cause this difference. One is the length of the shortest route along the ring walls from the top to the bottom of the array. For a common ring array height but different ring packing arrangement, the shortest path travelled by a stress wave along ring walls is longest for square packing; a transverse close-packed arrangement has a shorter path length and a vertical close-packed arrangement has the shortest path

length. Therefore, the apparent wave speed will appear different, since the actual distances travelled are not identical for the three packing arrangements. The other factor that results in differences in the apparent wave speed is that the detectable frequency components of the stress waves transmitting through the three arrangements are not the same. As shown in Table 5-1, a transverse close-packed array can only transmit low frequency components (<200 Hz for thin wall rings, <500 Hz for thick wall rings), while higher frequency components can be detected with the other two packing arrangements. Theoretical analysis has shown that stress waves with higher frequencies generally travel faster. Therefore, the identifiable apparent wave speeds are determined by the frequency components that pass through the ring arrays. Furthermore, these two factors of path length and frequency might not be independent of each other. Even if a specific type of ring is used, different packing arrangements allow different frequency components to pass through. For example, three major frequency components can be detected for square packed arrays of 38.1x3 aluminium alloy rings, while only two for a vertical close-packed array and only low frequency components pass through transverse close-packed arrays.

Nevertheless, although some high frequency components are detected in the transmitted signals, only a small fraction of energy is carried by them. This shows that ring arrays exhibit low-pass filter characteristics.

The five graphs in Figure 5-2 can be combined in to a single diagram, as shown in Figure 5-3, from which the group velocity relationships for different ring systems can be compared. This shows that the theoretical group velocities follow a general descending sequence in the order of 38.1x3 aluminium, 38.1x3 brass, 38.1x1 aluminium, 38.1x1 brass and 25.4x1 brass. The experimental data exhibit the same

trend. This shows that stress waves travel faster in aluminium ring arrays than in brass ones, because of differences in material properties. In addition, the ring wall thickness in an array affects the wave velocity. Stress wave transmission via thick walled rings is much faster than in thin walled rings. This is because wall thickness is an important parameter governing flexural rigidity of a ring, and in turn determines flexural wave speed.

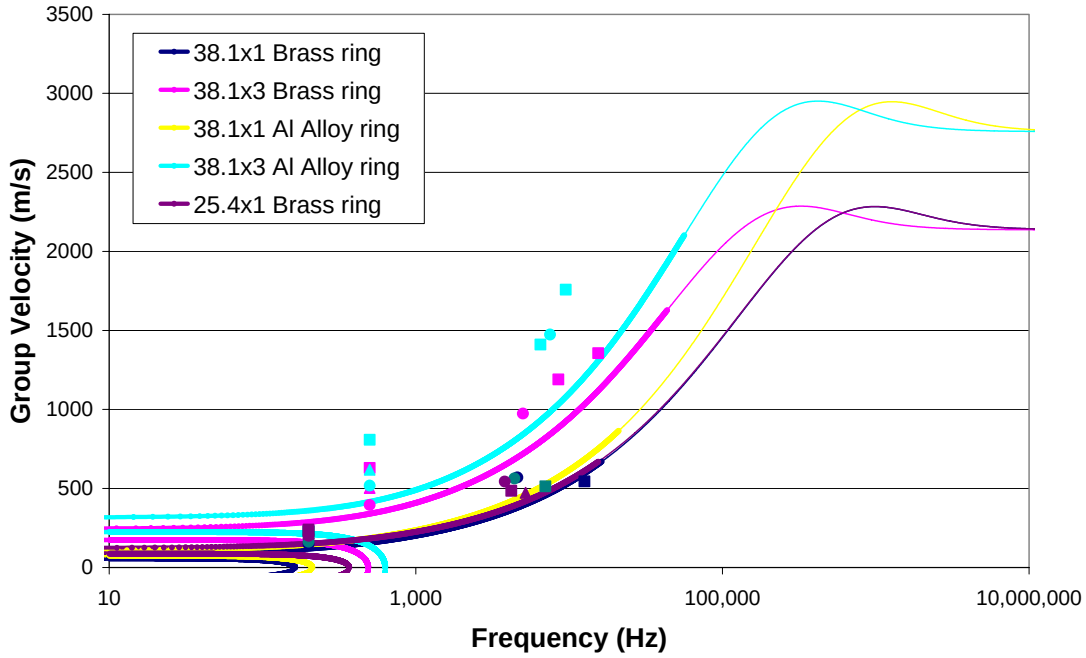


**Figure 5-3** Comparison between theoretical velocity distributions and experimental data for different ring systems

## 5.3 Summary

This chapter described the isolation of detectable frequency components in transmitted signals from experiments and determination of their corresponding velocities, enabling a comparison between experimental and theoretical results.

Comparisons between theoretical group velocities and experimental results in Figures 5-2 and 5-3 show that the group velocities detected in experiments exhibit good general correlation with theoretical predictions for flexural waves. There is correlation with the effects of material property, ring wall thickness and wave frequency on wave propagation speed. Two limitations of the current theoretical model were identified. Firstly, lateral inertia caused by Poisson's effect limits application of the proposed theoretical model to the long wavelength/low frequency spectrum. Secondly, the theory underestimates group velocities in thicker wall rings. The present study has focused on cellular systems with a low relative density (thin cell walls) and identified their low pass filter characteristics. Consequently, the theoretical model presented may be applicable to actual cellular materials and structures.

# CHAPTER SIX
# CONCLUSIONS AND RECOMMENDATIONS

## 6.1 Conclusions

In this study, various experiments and a theoretical analysis were undertaken to ascertain the basic features of elastic wave propagation in cellular systems, i.e. metal ring arrays in the present context.

Quasi-static tensile tests and impact tests were conducted on the ring materials – Brass and Al alloy – to determine their Young's modulus and corresponding bar velocities. Experimental results support the well-accepted expression $C_0 = \sqrt{E/\rho}$ , and this provided reliable fundamental material property data for the associated experiments and analysis.

The ring arrays constituted idealized representation of cellular material and their basic units – single rings – were subjected to transverse impact tests to determine the apparent stress wave velocities in the lateral direction. The fastest waves detected in the various single rings were found to be extensional waves travelling at the bar velocity $C_0$ along the solid wall of a ring. As with extensional wave propagation in straight thin bars, experimental observations indicate that material properties affect extensional wave propagation in single rings, while lateral dimensions such as ring

wall thickness and ring diameter have little effect. However, the amplitudes of extensional waves reduce rapidly as they propagate through a ring array, indicating that the packing together of rings (cells) can efficiently block their transmission. The dominant forms of stress transmission in such ring systems therefore correspond to other deformation modes – e.g. flexure.

Stress wave propagation velocities through various ring arrays were determined from impact tests. The results show that the factors affecting stress wave propagation include ring material properties, ring wall thickness, packing arrangement and boundary conditions. Material properties affect stress wave propagation in rings, especially thin walled rings, in a way similar to that for longitudinal waves travelling in a thin bar, i.e. a material with a lower density and higher Young's modulus transmits elastic stress waves more quickly. Ring wall thickness has a significant influence on wave propagation speed because thicker walled rings possess a larger flexural rigidity and this increases the speed of flexural wave propagation. Different packing arrangements affect the path length travelled by a wave, resulting in different apparent velocities. Rings of different diameters were also examined to verify the effect of size on wave speed; results showed little dependence on this. In addition, it was established that the impact force intensity does not affect the frequency components of the stress waves transmitted and their corresponding velocities; only the energy carried by the waves are altered.

The apparent Young's moduli $E^*$ and overall densities $\rho^*$ of the ring arrays were determined experimentally to facilitate evaluation of the expression $C^* = \sqrt{E^*/\rho^*}$, which is traditionally used to determine longitudinal wave propagation in non-porous elastic continua. Some researchers have also attempted to apply this to estimate wave propagation velocity in cellular systems. However, a comparison between $C^*$ and the

wave velocities detected in experiments shows no correspondence, indicating that traditional elastic continuum analysis for homogeneous materials cannot be expanded to encompass cellular structures. The propagation of elastic stress waves in cellular systems involves a structural response, which is not captured by the elementary theory for homogenous solids.

A theoretical model developed for wave propagation in a circular ring highlights an important factor governing wave speed, namely frequency. The variation of group velocity of the three wave propagation modes – shear, flexure and extension – with frequency or wavelength, point to flexural waves as the dominant mode in transmitting elastic energy along solid paths in ring arrays. Good general correlation between experimental results and theoretical predictions for flexural waves confirms this. The proposed theoretical model is able to predict the dependence of wave velocity on frequency and the relationships with ring material, wall thickness and diameter. The predicted flexural group velocity distributions with respect to frequency, for two rings of different diameters are very similar; this correlated with experimental findings. Theoretically, the packing arrangement and boundary conditions of a ring array would not affect the flexural wave velocity distribution with respect to frequency. However, these factors might give rise to different frequency components in the flexural waves transmitted, resulting in differences in the apparent velocities detected.

As a consequence of the basic assumptions adopted – i.e. plane cross-sections remaining plane after deformation and neglect of lateral inertia associated with Poisson's effect – the current theoretical model for elastic wave transmission in cellular systems is not suitable for wavelengths comparable with or shorter than the ring wall thickness and for rings with walls that are thick relative to the ring diameter.

Nevertheless, the theory provides useful insights into elastic wave propagation in cellular systems and has the potential to provide good estimates of elastic wave propagation velocities in cellular systems with a low relative density.

## 6.2 Recommendations

The present study shows that the packing arrangement of a ring array is a factor that changes the frequency components contained in the waves transmitted. Further investigation into the propagation of various frequency components may reveal how packing arrangement affect the frequency components of elastic waves transmitting in ring arrays.

To ascertain whether the proposed model provides a good description of elastic wave propagation in actual cellular materials with complex cell structures, similar experiments and analysis should be conducted on typical cellular materials such as polyurethane foams.

# REFERENCES


1. N. C. Hilyard and A. Conningham, *Low density cellular plastics : physical basis of behaviour;* London : Chapman & Hall, 1994.
2. Goh Hock Chye**,** *Transmission of Transient Elastic Stress Through Cellular Structure*, National University of Singapore, 1995
3. Lorna J. Gibson and Michael F. Ashby, *Cellular solids : structure and properties*, 2nd Edition; Cambridge ; New York : Cambridge University Press, 1997.
4. Leon R. Glicksman, Heat Transfer in foams, in *Low density cellular plastics : physical basis of behaviour,* eds. N. C. Hilyard and A. Conningham*;* London : Chapman & Hall, 1994.
5. Tu Zhi Hua, *A Study of the Two-dimensional Impact Response of Crushable Foam*, National University of Singapore, 1999
6. Walter Lauriks, Acoustic characteristics of low density foams, in *Low density cellular plastics : physical basis of behaviour,* eds. N. C. Hilyard and A. Conningham*;* London : Chapman & Hall, 1994.
7. Gent, A. N. and Thomas, A. G. *Mechanics of Foamed elastic Materials,* Ruber Chem. Tech., 36, 597-610.
8. Patel, M. R. and I. Finnie, *Structural Features and Mechanical Properties of Rigid Cellular Plastics. J. Materials,* JMLSA, 5(4), Dec 909-932 (1970)
9. Joseph W. Tedesco, William G. McDougal, C. Allen Ross. *Structural dynami;* Menlo Park, Calif. : Addison Wesley Longman, c1999.
10. Reid, S.R and W. W. Bell, *Structural Response of One-dimensional Metal Ring Systems to End Impact.* Int. Phys Confs. Ser. No. 70, 471-478 (1984)

11. S. R. Reid, T. Y. Reddy. Experimental Investigation of Inertia Effects in One-dimensional Metal Ring Systems Subjected to End Impact — I. Fixed-ended Systems, *Int. J. Impact Engng.* Vol.1, No.1, pp.85-106, Great Britain, 1983
12. T. Y. Reddy, S. R. Reid, R. Barr. Experimental Investigation of Inertia Effects in One-dimensional Metal Ring Systems Subjected to End Impact — II. Free-ended Systems, *Int. J. Impact Engng.* Vol.11, No.4, pp.463-480, Great Britain, 1991
13. Rayleigh, J. W. S. *The theory of sound,* Vols. I and II. Dover Publications, New York 1945
14. S.P. Timoshenko 1921 *Phil. Mag.* 41, 744. On the correction for shear of the differential equation for transverse vibrations of prismatic bars.
15. S.P. Timoshenko 1922 *Phil. Mag.* 43, 125. On the transverse vibrations of bars of uniform cross-section.
16. Kolsky, H. *Stress Waves in Solids*. Dover Publications, New York (1963)
17. L. S. D. Morley, Elastic waves in a Naturally Curved Rod, Quart. *J. Mech. And Applied Math.*, Vol. XIV, Pt. 2, 1961
18. W. G. B. Britton, G. O. Langley, Stress pulse dispersion in curved Mechanical waveguides, *J. Sound Vib.*, 7(3), 417-430, 1968
19. W.H. Wittrick , On Elastic Wave Propagation in Helical Springs, *International Journal of Mechanical Science*, Vol. 8, pp. 25-47, 1966
20. Marc Andre Meyers, *Dynamic Behavior of Materials*. New York: Wiley, 1994
21. Michael Bauccio. *ASM Metals Reference Book, Third Edition,* ASM International, Materials Park, Ohio, 1993.
22. Karl F. Graff. *Wave motion in elastic solids.* Oxford : Clarendon Press , 1975.
23. Raymond J. Roark, Warren C. Young. *Formulas for stress and strain , 5th ed.* New York : McGraw-Hill , c1975.

24. J. Billingham, A.C. King. *Wave motion.* Cambridge; New York: Cambridge University Press, 2000.

25. Jeanne C. Adams, *Fortran 90 handbook : complete ANSI/ISO reference,* New York : Intertext Publications : McGraw-Hill Book Co. , 1992.

26. Meinecke, E. A. and Clark, R. C. *Mechanical Properties of Polymeric Foams***,** Technomic, Westport, CT. 1973.

27. Hilyard, N. C. (ed.)**,** *Mechanics of Cellular Plastics,* Macmillan, New York. 1982.

28. Hilyard, N. C. and Cunningham A (ed.)**,**. *Low density cellular plastics: physical basis of behaviour* London: Chapman & Hall, 1994.

29. Ko, W. L. *Deformations of foamed elastomers. J. Cellular plastics* , 1, 45-50

30. Murray, G. T. *Introduction to Engineering Materials : Behavior, Properties, and Selection,* New York Marcel Dekker, Inc., 1993.

31. K. H. Huebner, E. A. Thornton, T. G. Byrom, *The finite element method for engineers*, 3rd ed. New York : Wiley , 1995

# List of Additional Figures

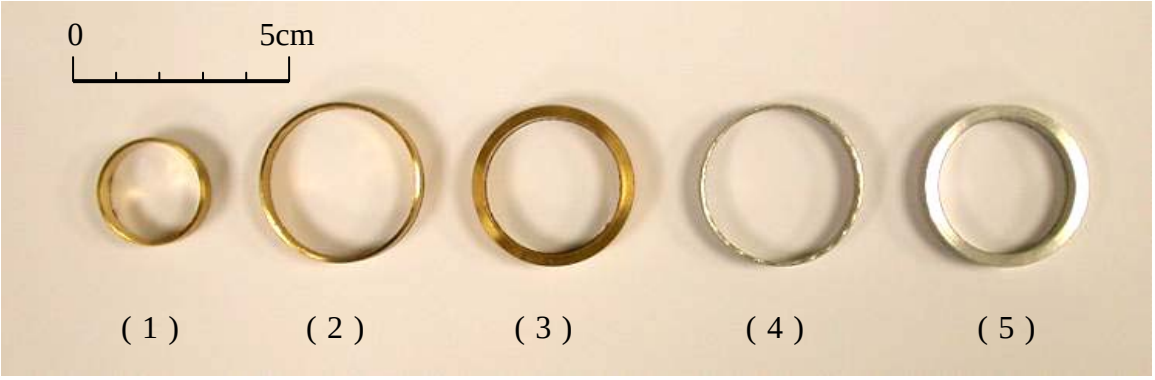


**Fig. AF-1** Five types of metal rings used in experiments
(1) Brass 25.4x1mm (2) Brass 38.1x1mm (3) Brass 38.1x3mm
(4) Al alloy 38.1x1mm (5) Al alloy 38.1x3mm


**Fig. AF-2** Instron machine (Dynamic Testing Machine 8501)

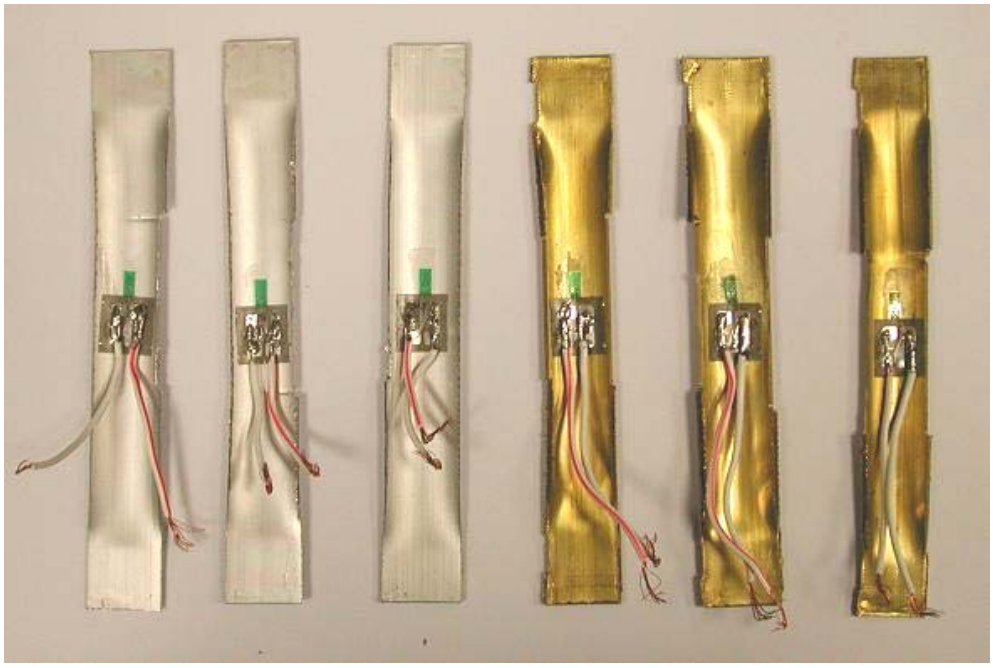

**Fig. AF-3** Samples after testing for determination of Young's modulus
(Strain Gauges were attached for measuring tensile strains)

**Fig. AF-4** Metal tubes of different lengths
for determination of extensional wave speed in axial direction

**Fig. AF-5** Test procedure for quasi-static compression of a single ring

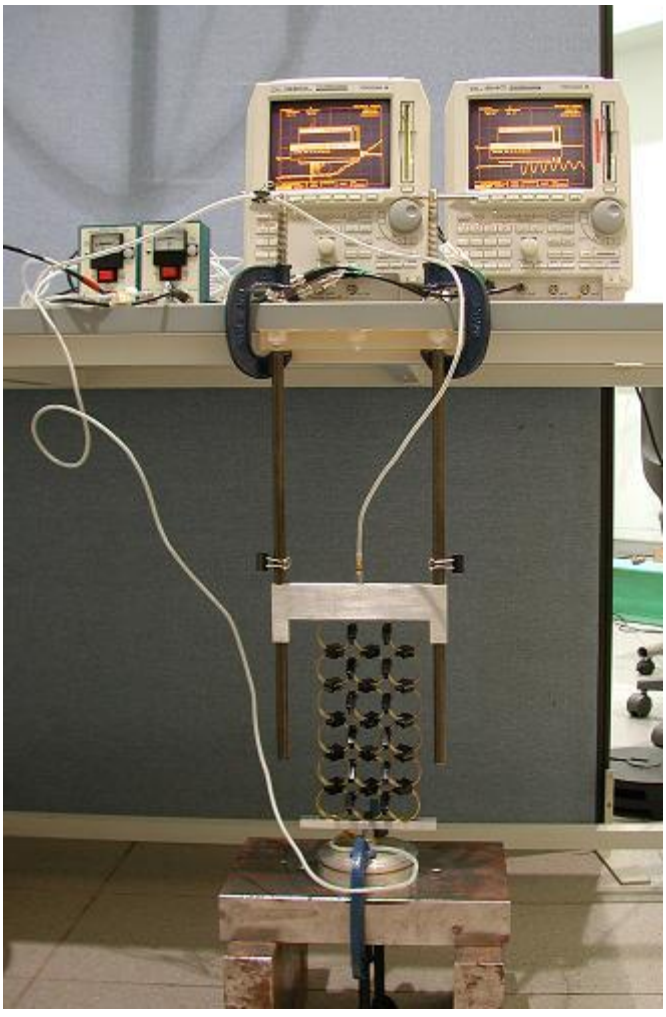

**Fig. AF-6** Experimental setup for impact tests

**Appendix A** Relative Densities of Cell Assemblies (Gibson and Ashby [3])

| | |
|---|---|
| ***Honeycombs*** | |
| Equilateral trangles<br>($Z_e = 6, n = 3$ or $Z_e = 4$, or $n = 4$) | $\frac{\rho^*}{\rho_S} = 2\sqrt{3}\frac{t}{l}\left(1 - \frac{\sqrt{3}}{2}\frac{t}{l}\right)$ |
| Squares<br>($Z_e = 4, n = 4$ or $Z_e = 3$, or $n = 6$) | $\frac{\rho^*}{\rho_S} = 2\frac{t}{l}\left(1 - \frac{1}{2}\frac{t}{l}\right)$ |
| Regular hexagons<br>($Z_e = 3, n = 6$) | $\frac{\rho^*}{\rho_S} = \frac{2}{\sqrt{3}}\frac{t}{l}\left(1 - \frac{1}{2\sqrt{3}}\frac{t}{l}\right)$ |
| ***Three dimensions: open cells (aspect ratio $A_r = h/l$)*** | |
| Triangular prisms<br>($Z_e = 8, Z_f = 4.5\ \bar{n} = 3.6\ \bar{f} = 5$) | $\frac{\rho^*}{\rho_S} = \frac{2}{\sqrt{3}}\frac{t^2}{l^2}\left\{1 + \frac{3}{A_r}\right\}$ |
| Square prisms<br>($Z_e = 6, Z_f = 4\ \bar{n} = 4\ \bar{f} = 6$) | $\frac{\rho^*}{\rho_S} = \frac{t^2}{l^2}\left\{1 + \frac{2}{A_r}\right\}$ |
| Hexagonal prisms<br>($Z_e = 5, Z_f = 3.6\ \bar{n} = 4.5\ \bar{f} = 8$) | $\frac{\rho^*}{\rho_S} = \frac{4}{3\sqrt{3}}\frac{t^2}{l^2}\left\{1 + \frac{3}{2A_r}\right\}$ |
| Rhombic dodecahefra<br>($Z_e = 5.33, Z_f = 3\ \bar{n} = 4\ \bar{f} = 12$) | $\frac{\rho^*}{\rho_S} = 2.87\frac{t^2}{l^2}$ |
| Tetrakaidecahedra<br>($Z_e = 4,\ Z_f = 3,\ \bar{n} = 5.41\ \ \bar{f} = 14$) | $\frac{\rho^*}{\rho_S} = 1.06\frac{t^2}{l^2}$ |
| ***Three dimensions: closed cells (aspect ratio $A_r = h/l$)*** | |
| Triangular prisms<br>($Z_e = 8, Z_f = 4.5\ \bar{n} = 3.6\ \bar{f} = 5$) | $\frac{\rho^*}{\rho_S} = 2\sqrt{3}\frac{t}{l}\left\{1 + \frac{1}{2\sqrt{3}A_r}\right\}$ |
| Square prisms<br>($Z_e = 6, Z_f = 4\ \bar{n} = 4\ \bar{f} = 6$) | $\frac{\rho^*}{\rho_S} = 2\frac{t}{l}\left\{1 + \frac{1}{2A_r}\right\}$ |
| Hexagonal prisms<br>($Z_e = 5, Z_f = 3.6\ \bar{n} = 4.5\ \bar{f} = 8$) | $\frac{\rho^*}{\rho_S} = \frac{2}{\sqrt{3}}\frac{t}{l}\left\{1 + \frac{\sqrt{3}}{2A_r}\right\}$ |
| Rhombic dodecahefra<br>($Z_e = 5.33, Z_f = 3\ \bar{n} = 4\ \bar{f} = 12$) | $\frac{\rho^*}{\rho_S} = 1.90\frac{t}{l}$ |
| Tetrakaidecahedra<br>($Z_e = 4,\ Z_f = 3,\ \bar{n} = 5.41\ \ \bar{f} = 14$) | $\frac{\rho^*}{\rho_S} = 1.18\frac{t}{l}$ |

**Appendix B** List of Stress-strain Curves from Tensile Tests

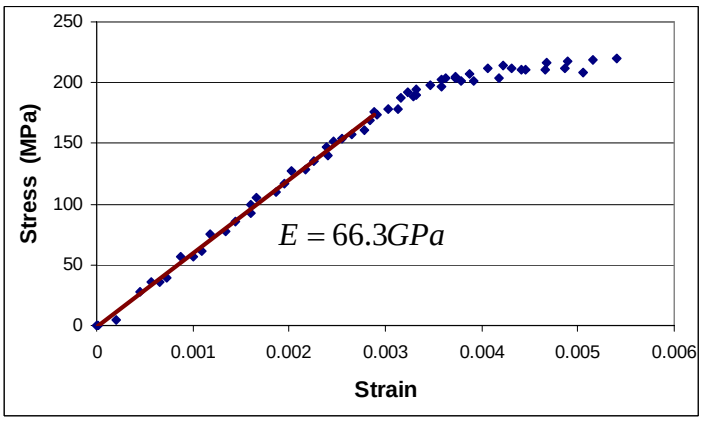


Al alloy Sample 1

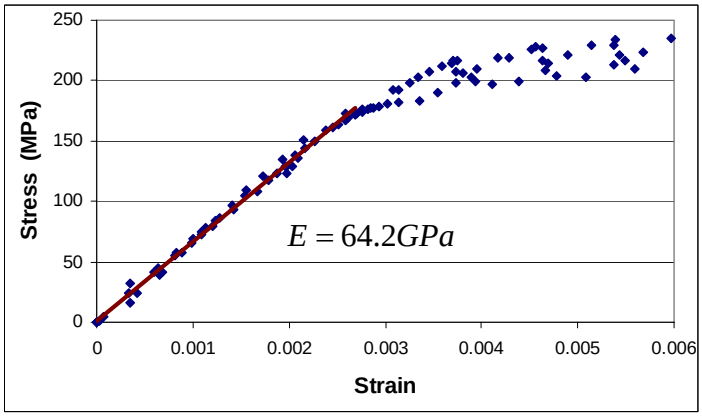


Al alloy Sample 2

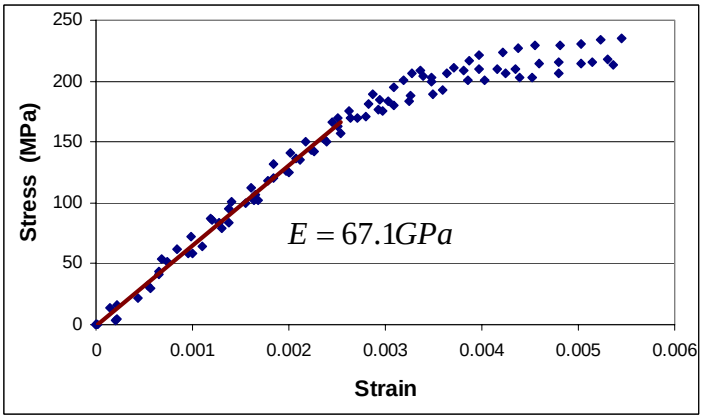


Al alloy Sample 3

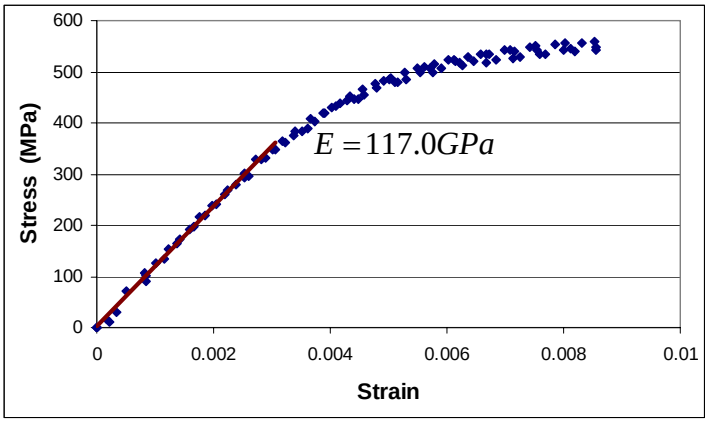


Brass Sample 1

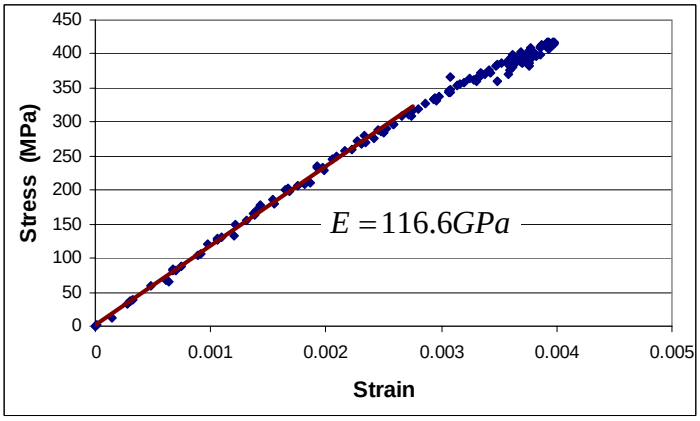


Brass Sample 2

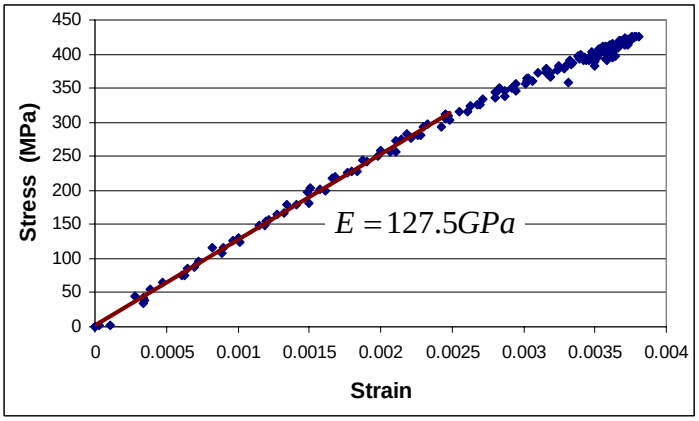


Brass Sample 3

**Appendix C** FORTRAN Program for Determination of Wave Commencement Point

In impact tests for determining stress wave speeds, a digital signal oscilloscope (DSO) recorded a series of discrete values that represent the variation in wave amplitude with time. Figure C-1 shows an example, where the dark blue curve is the input (acceleration) signal and the pink curve is the output force at the bottom of the test ring or array. To calculate the stress wave speed, it is necessary to determine the time of travel, which is the time interval between the commencements of the two signals. To minimize subjectivity in the determination of these points, identification of wave commencement was done using a FORTRAN program [25]. The flow chart of the program is shown in Fig C-2, followed by a listing of the source program.

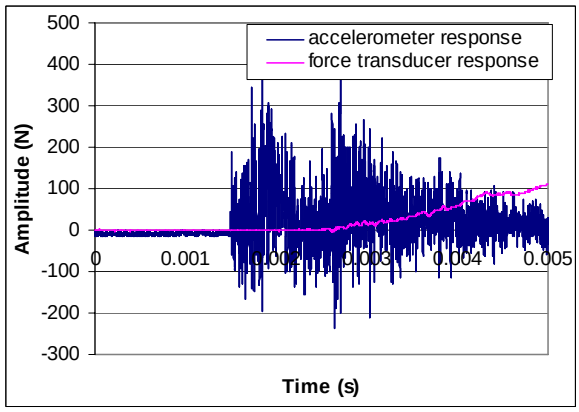


**Fig. C-1** A typical signal recorded by a DSO

The amplitude of a signal before commencement of a wave is essentially constant. The variance in a small segment of data is defined as a parameter; this value is monitored for any change as the data segment advances along the signal trace. When the magnitude of the segment variance increases beyond a threshold (e.g. by 2.5 times), commencement of the wave is deemed to be included in the data segment. By subsequently reducing the size of the data segment, the commencement of the stress wave can be identified.

**Fig. C-2** Flow chart of FORTRAN program for determination of wave commencement

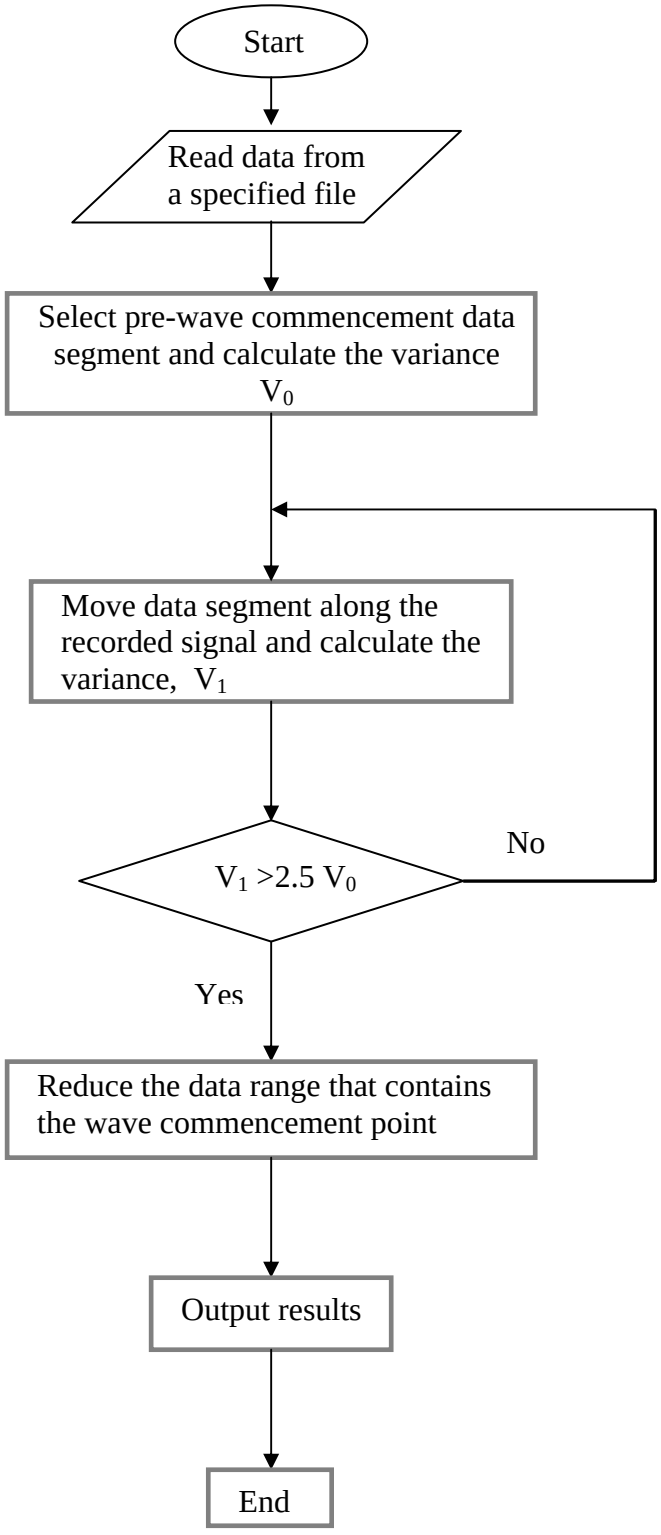

```
**********************************************************************

module global_variables
        implicit none

        ! In this module block, all variables that will be used in program are declared.

        !declare global variables
        real, dimension(10000,2) :: s          !array s will store the data output from oscilloscope
        integer :: n                           !a changeable number, which will control
                                               !the number of data analyzed at one time.
        character(len=15) :: filename                  !the name of the source data file
        integer :: open_status                         !to determine if the file is opened properly
        integer :: read_stat                           !to determine data reading status
        integer :: write_stat                          !to determine data writing status
        integer :: i ,j                                !integers for do loop
        integer, parameter :: base_number=1000         !number of data for calculation of variance
        real, dimension(2) :: var                      !basic variances
        integer, dimension(2) :: tpp                   !to store the trigger point position

end module global_variables


real function variance(a,b,c)
        use global_variables
        implicit none

        !declare dummy arguments
        integer, intent(in) :: a, b, c         !integers a, b and c will select which elements in array
                                               !that will involve in the calculation of Variance. 'a' and
                                               !'b' is the lower and upper bound; 'c'  is dimension, and in
                                               !this program, it has only two possible values: 1 or 2.

        !local variable declaration
        real :: sum2,mean2                     !sum2 is mean value of squire
                                               !mean2 is squire of mean value

        !calculate the variance of elements specified

        sum2=0
        mean2=0
        do i=a,b
                sum2=sum2+s(i,c)**2            !calculate the sum of squire
                mean2=mean2+s(i,c)             !calculate the sum
        end do
        mean2=mean2/(b-a+1)                    !average
        variance=sum2/(b-a+1)-mean2**2         !variance

end function variance


subroutine data_transfer

        !this subroutine will try to open a raw data file specified by user,
        !then transfer the data in to array s

        use global_variables
        implicit none
```

```
        do
                print *,"Please give the name of raw data file:"
                read '(a)', filename
                !open data file on unit number "3"
                open (unit=3,file=filename,iostat=open_status,status="old",action="read")

                !repeat request if file are not opened successfully
                if (open_status==0) exit
                print *, "Unable to open file - please try again"
        end do


        !pass all data in file to the array s

        do i=1,10000
                read (unit=3,iostat=read_stat,fmt='(2f12.8)') s(i,1),s(i,2)
                !exit when reach file end
                if (read_stat==-1) exit

        end do

 end subroutine data_transfer



program commencement

!The purpose  of this program is to analysis the data output from oscilloscope,
!and determine the time taken that for wave traveling from one sensor to another

        use global_variables
        implicit none

        !declare external function
        real , external :: variance

        !call a subroutine to open the raw data file and transfer the data into array s

        call data_transfer

        !DSO signals always contain a constant/neutral  part at the front.
        !calculate the variance of the first 1000 values as basic value and compare it with others
        !supposed that in the first 1000 points the signals did not triggered.

        var(1)=2.5*variance(1,base_number,1)
        var(2)=2.5*variance(1,base_number,2)
        print *,"variance of noice in 1st signal is:",var(1)
        print *,"variance of noice in 2nd signal is:",var(2)

        !take 200 as a step, move calculation range forward through array s

        !the signals in first dimension: input signal
        do j=200,10000,200

                !when reaching trigger point, call subroutine mean to narrow the range

                if (variance(j+1,base_number+j,1)>var(1)) then
                        print *, j
                        call mean(base_number+j,tpp(1),1)
```

```
                exit
            end if

        end do


        !the signals in second dimension: output signal
        do j=200,10000,200

            !when reaching trigger point, call subroutine mean to narrow the range

            if (variance(j+1,base_number+j,2)>var(2)) then
                print *, j
                call mean(base_number+j,tpp(2),2)
                exit
            end if

        end do

        print *, " Wave commencement of input signal is point No " ,  tpp(1)
        print *, " Wave commencement of output signal is point No" ,  tpp(2)

        pause


end program commencement



subroutine mean(end_point,trigger_point,c)

        !this subroutine will reduce the range which contains the trigger point
        !then return the position of trigger point.

        use global_variables
        implicit none

        !declare external function
        real , external :: variance

        !declare dummy arguments, which define which part of elements will be
        !involved in calculation.
        integer, intent(in) :: end_point        ! trigger point is within the 1000 points before end_point
        integer, intent(in) :: c                !which set of signal will be determined, input or output
        integer, intent(out) :: trigger_point   !it will save the final point detected by the program

        !local variable declaration
        integer :: lower_bound, upper_bound          !variables that will use to narrow the range.

        !calculate the initial range for calculation of variance
        lower_bound=end_point-base_number+1
        upper_bound=end_point

        !narrow the range that contains trigger point
        do i=1,upper_bound-lower_bound-30          !final range will be narrowed to 30  points.

            if (variance(lower_bound,upper_bound,c)<var(c)) then
                lower_bound=lower_bound+1
            else
                upper_bound=upper_bound-1
```

```
            end if

        end do

        !the trigger point is taken as the middle point of reduced range
        trigger_point=(lower_bound+upper_bound)/2

end subroutine mean
```

Figure C-3 shows two examples of determination of wave commencement, whereby the red and black triangular points defining the start points are identified by the program described. This demonstrates that the wave commencement identification algorithm is effective.

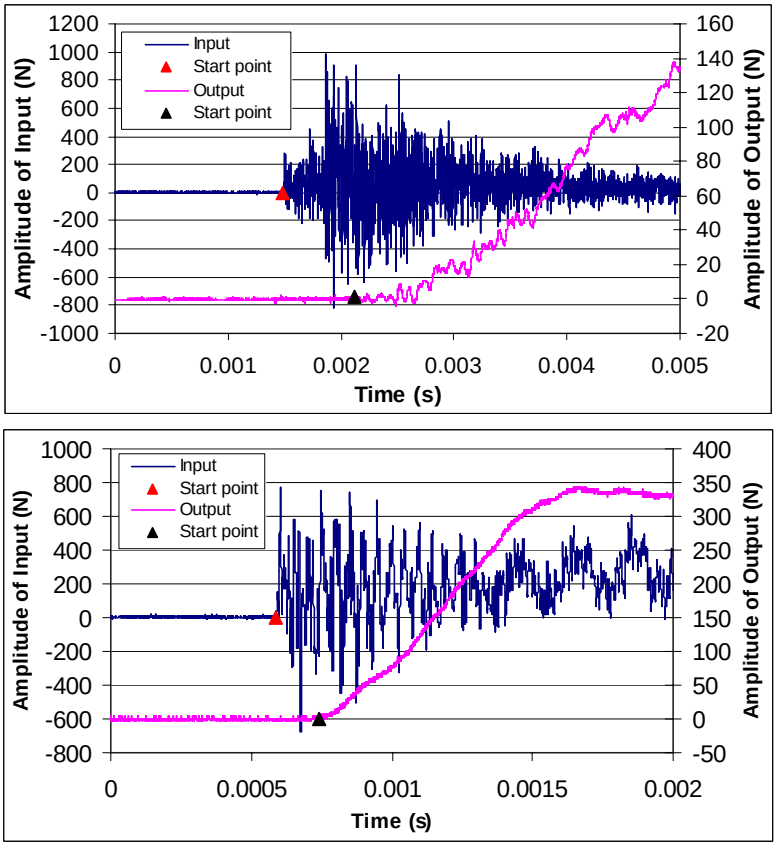


**Fig. C-3** Two examples of wave commencement determination
(red and black triangular points mark the commencements of input and output waves, respectively)

**Appendix D** Theoretical Analysis for Stress Wave Propagation in a Flat Ring

For a circular ring with a rectangular cross-section as shown in Figure D-1, $\vec{e}_1$, $\vec{e}_2$ , $\vec{e}_3$ define unit vectors in the circumferential, radial and axial directions. At an incremental distance *ds* farther along the ring curvature, the frame of reference will undergo a rotation $d\psi$ , resulting in new unit vectors $\vec{e}_1'$ and $\vec{e}_2'$. As shown in Figure D-2 these transformed unit vectors can be expressed as

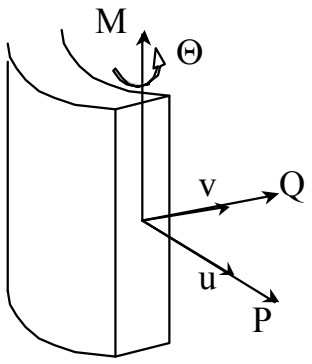


**Fig. D-1** Definitions of displacements, rotation and stress resultants on cross-section

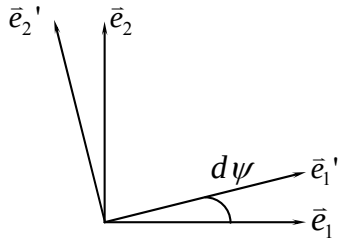


**Fig. D-2** Transformation of unit vectors

$$\vec{e}_1' = \vec{e}_1 \cos d\psi + \vec{e}_2 \sin d\psi$$
$$\vec{e}_2' = \vec{e}_2 \cos d\psi - \vec{e}_1 \sin d\psi$$

In the limit $d\psi \to 0$ , $\sin d\psi \to d\psi$ and $\cos d\psi \to 1$ ,

$$\frac{d\vec{e}_1}{ds} = \frac{\vec{e}_1' - \vec{e}_1}{ds} = \frac{\vec{e}_1 \cos d\psi + \vec{e}_2 \sin d\psi - \vec{e}_1}{ds} = \vec{e}_2 \frac{d\psi}{ds} = \frac{\vec{e}_2}{R} \qquad \text{(D-1)}$$

$$\frac{d\vec{e}_2}{ds} = \frac{\vec{e}_2' - \vec{e}_2}{ds} = \frac{\vec{e}_2 \cos d\psi - \vec{e}_1 \sin d\psi - \vec{e}_2}{ds} = -\vec{e}_1 \frac{d\psi}{ds} = -\frac{\vec{e}_1}{R} \qquad \text{(D-2)}$$

Let $\vec{U}$ , $\vec{N}$ , $\vec{M}$ and $\vec{\Theta}$ be vectors representing respectively the displacement, force, bending moment, and resultant rotation at a cross-section, so that

$$\vec{U} = u\vec{e}_1 + v\vec{e}_2; \quad \vec{N} = P\vec{e}_1 + Q\vec{e}_2; \quad \vec{M} = M\vec{e}_3; \quad \vec{\Theta} = \Theta\vec{e}_3 \qquad \text{(D-3)}$$

| | | |
|---|---|---|
| where | u v | Circumferential and axial displacements of the centroid |
| | P, Q, M | Axial tension, shear and bending moment |
| | Θ | Rotation of the cross section |

Let $\beta$ denote the flexural rigidity of the ring, $\sigma_p$ the extensional rigidity and $\sigma_q$ the shear rigidity. If denote

$$\begin{aligned} \frac{\partial \vec{\Theta}}{\partial s} &= \left(\frac{\partial \vec{\Theta}}{\partial s}\right)_d \vec{e}_3 \\ \frac{\partial \vec{U}}{\partial s} &= \left(\frac{\partial u}{\partial s}\right)_d \vec{e}_1 + \left(\frac{\partial v}{\partial s}\right)_d \vec{e}_2 \end{aligned} \tag{D-4}$$

Then,

$$\begin{cases} \left(\dfrac{\partial \Theta}{\partial s}\right)_d = \dfrac{M}{\beta} \\ \left(\dfrac{\partial u}{\partial s}\right)_d = \dfrac{P}{\sigma_p} \\ \left(\dfrac{\partial v}{\partial s}\right)_d = \dfrac{Q}{\sigma_q} + \Theta \end{cases} \tag{D-5}$$

Note that the radial displacement *v* is generated by contributions from both the shear force $Q$ and the bending moment $M$, resulting the expression of $\partial v/\partial s$ given in (D-5).

The first and the fourth equations in (D-3) by differentiation with respect to *s* yield:

$$\begin{aligned} \frac{\partial \vec{U}}{\partial s} &= \frac{\partial \vec{e}_1}{\partial s} u + \vec{e}_1 \frac{\partial u}{\partial s} + \frac{\partial \vec{e}_2}{\partial s} v + \vec{e}_2 \frac{\partial v}{\partial s} \\ &= \vec{e}_2 \frac{u}{R} + \vec{e}_1 \frac{\partial u}{\partial s} - \vec{e}_1 \frac{v}{R} + \vec{e}_2 \frac{\partial v}{\partial s} \\ &= \vec{e}_1 \left(\frac{\partial u}{\partial s} - \frac{v}{R}\right) + \vec{e}_2 \left(\frac{\partial v}{\partial s} + \frac{u}{R}\right) \end{aligned}$$

$$\frac{\partial \vec{\Theta}}{\partial s} = \frac{\partial \Theta}{\partial s} \vec{e}_3 \qquad \left(\frac{\partial \vec{e}_3}{\partial s} = 0\right)$$

Where equations (D-1) and (D-2) are used.

A comparison of the above expression with equation (D-4) and considering equation (D-5) shows that

$$\begin{cases} \dfrac{M}{\beta} = \dfrac{\partial \Theta}{\partial s} \\ \dfrac{P}{\sigma_p} = \dfrac{\partial u}{\partial s} - \dfrac{v}{R} \\ \dfrac{Q}{\sigma_q} + \Theta = \dfrac{\partial v}{\partial s} + \dfrac{u}{R} \end{cases} \tag{D-6}$$

The equations of motion for both circumferential and radial directions can be expressed in vector form as

$$\frac{\partial \vec{N}}{\partial s} = m\frac{\partial^2 \vec{U}}{\partial t^2} = m\frac{\partial^2 u}{\partial t^2}\vec{e}_1 + m\frac{\partial^2 v}{\partial t^2}\vec{e}_2 \tag{D-7}$$

where $m$ is the mass per unit length and $t$ is time.

while $\dfrac{\partial \vec{N}}{\partial s}$ can be also derived from

$$\begin{aligned} \frac{\partial \vec{N}}{\partial s} &= \frac{\partial P}{\partial s}\vec{e}_1 + \frac{\partial \vec{e}_1}{\partial s}P + \frac{\partial Q}{\partial s}\vec{e}_2 + \frac{\partial \vec{e}_2}{\partial s}Q \\ &= \frac{\partial P}{\partial s}\vec{e}_1 + \frac{\vec{e}_2}{R}P + \frac{\partial Q}{\partial s}\vec{e}_2 - \frac{\vec{e}_1}{R}Q \\ &= \left(\frac{\partial P}{\partial s} - \frac{Q}{R}\right)\vec{e}_1 + \left(\frac{\partial Q}{\partial s} + \frac{P}{R}\right)\vec{e}_2 \end{aligned}$$

A comparison of the above with equation (D-7) results in

$$\begin{cases} \dfrac{\partial P}{\partial s} - \dfrac{Q}{R} = m\dfrac{\partial^2 u}{\partial t^2} \\ \dfrac{\partial Q}{\partial s} + \dfrac{P}{R} = m\dfrac{\partial^2 v}{\partial t^2} \end{cases} \tag{D-8}$$

The equation for rotational motion resulting from bending and shear can be expressed as

$$\frac{\partial M}{\partial s} + Q = mk^2 \frac{\partial^2 \Theta}{\partial t^2} \tag{D-9}$$

where k is the radius of gyration of the cross-section

Combining the results of the proceeding analysis results in the following six equations relating the forces and moment to displacements and rotations of a circular ring with a rectangular cross-section:

$$\begin{cases} \dfrac{\partial \Theta}{\partial s} = \dfrac{M}{\beta} \\ \dfrac{P}{\sigma_p} = \dfrac{\partial u}{\partial s} - \dfrac{v}{R} \\ \dfrac{Q}{\sigma_q} + \Theta = \dfrac{\partial v}{\partial s} + \dfrac{u}{R} \\ \dfrac{\partial P}{\partial s} - \dfrac{Q}{R} = m\dfrac{\partial^2 u}{\partial t^2} \\ \dfrac{\partial Q}{\partial s} + \dfrac{P}{R} = m\dfrac{\partial^2 v}{\partial t^2} \\ \dfrac{\partial M}{\partial s} + Q = mk^2 \dfrac{\partial^2 \Theta}{\partial t^2} \end{cases} \tag{D-10}$$

**Appendix E** Shear Rigidity of a Beam with a Rectangular Cross-section

Shear rigidity is a measure of material resistance against distortion by shear. This is defined as the shear force that causes a unit displacement in the direction of its action and has units of force. It can be determined by integrating over the cross-section, the shear strain energy associated with the parabolic shear stress distribution corresponding to the shear force at that location.

Let $\sigma_q$ denote the shear rigidity.

As shown in Figure E-1, the shear stress distribution in a rectangular cross section ($b \times h$) associated with the existing shear force is given by

$$\tau_{xy} = \frac{F_{xy} A' \cdot \bar{y}'}{I_z \cdot b} \qquad \text{(E.1)}$$

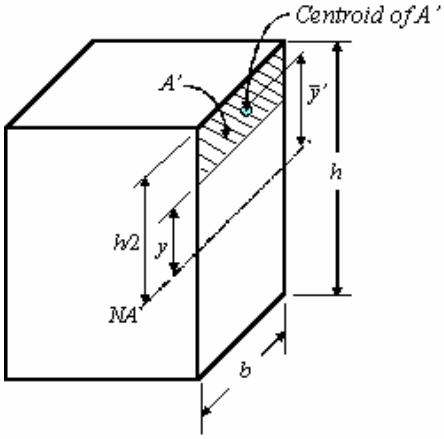


**Fig. E-1** Computation of shear stress in a rectangular cross section

where:

$F_{xy}$ shear force carried by the cross-section

$I$ second moment of area of cross-section

$b$ width of cross section

$A'$ area of cross-sectional portion beyond a distance $y$ to the neutral axis (NA)

$\bar{y}'$ distance from the NA to the centroid of $A'$

Equation E.1 can be expand and simplified:

$$\tau_{xy} = \frac{F_{xy} b\left(\frac{h}{2} - y\right) \cdot \frac{1}{2}\left(\frac{h}{2} + y\right)}{\frac{1}{12} b h^3 \cdot b} = \frac{6F_{xy}\left(\frac{h^2}{4} - y^2\right)}{bh^3} = \frac{h^2}{4} \frac{6F_{xy}\left[1 - 4\left(\frac{y}{h}\right)^2\right]}{bh^3}$$

Let $\zeta = \frac{y}{h}$, then

$$\tau_{xy} = \frac{3F_{xy}\left(1-4\zeta^2\right)}{2bh} \qquad \text{(E.2)}$$

The shear strain energy associated with a rectangular element $b \times dx \times dy$, at a distance y to the neutral axis (NA) as shown in Figure E-2, is given by

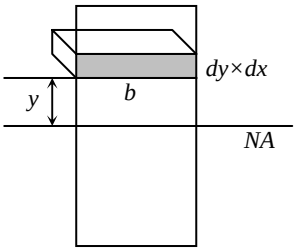


**Fig. E-2** Calculation of shear strain energy in an element $b \times dx \times dy$

$$du = \left(\frac{1}{2}\tau_{xy}\gamma_{xy}\right)\cdot b \cdot dx \cdot dy \qquad \text{(E.3)}$$

where $\gamma_{xy} = \frac{\tau_{xy}}{G}$ is the shear strain (G is shear modulus of material). Equation E.3 can then be expressed by

$$du = \frac{b}{2G}\tau_{xy}^2 dxdy \qquad \text{(E.4)}$$

Consequently, the total shear strain energy contained in the beam cross-section with an elemental depth *dx* is given by

$$\frac{U}{dx} = \frac{b}{2G}\int \tau_{xy}^2 dy$$

where *dy* can be expressed by $dy = h\frac{dy}{h} = hd\zeta$ ; then

$$\begin{aligned}\frac{U}{dx} &= \frac{b}{2G}\int \tau_{xy}^2 hd\zeta \\ &= \frac{bh}{2G}\int \frac{9F_{xy}^2\left(1-4\zeta^2\right)^2}{4b^2h^2}d\zeta \\ &= \frac{9F_{xy}^2}{8bhG}\int_{-\frac{1}{2}}^{\frac{1}{2}}\left(1-8\zeta^2+16\zeta^4\right)d\zeta \\ &= \frac{9F_{xy}^2}{8bhG}\left[1-\frac{2}{3}+\frac{1}{5}\right] \\ &= \frac{3F_{xy}^2}{5bhG} \qquad \text{(E.5)}\end{aligned}$$

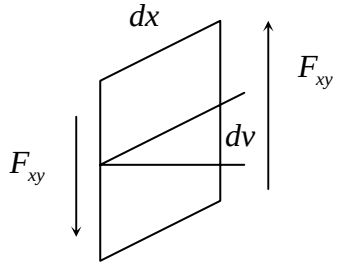


**Fig. E-3** Shear force acting on cross section and resulting displacement

If *dv* is the resulting displacement of the beam element *dx* arising from the shear force $F_{xy}$, as shown in figure E.3, the definition of shear rigidity is

$$\sigma_q = \frac{F_{xy}}{dv}$$

So $$\frac{U}{dx} = \frac{1}{2} F_{xy} \cdot dv = \frac{1}{2} \frac{F_{xy}^2}{\sigma_q} \qquad \text{(E.6)}$$

Combining equations (E.5) and (E.6) yields

$$\frac{1}{2} \frac{F_{xy}^2}{\sigma_q} = \frac{3F_{xy}^2}{5bhG}$$

Consequently, the shear rigidity of a beam with a rectangular cross-section is given by

$$\sigma_q = \frac{5}{6} Gbh$$

**Appendix F** Simplified Expressions for Phase Velocities of Elastic Stress Waves

Derived from fist principles, equation (4.9) contains the velocities of three waves – flexural, shear and extensional – that transmit along a circular ring. A solution of this equation facilitates analysis of the relationships between wave velocity and other parameter such as material rigidity, ring radius, cross sectional geometry, etc. However, it is not practical to extract explicit expressions for the roots of this complicated equation. Therefore, certain assumptions are made with respect to different situations, enabling the equation to be simplified to permit approximate solutions. To achieve this, equation (4.9) is manipulated as follows.

$$\frac{\beta}{k^2}\sigma_p\sigma_q\delta^2\left(\delta^2-1\right)^2-\left\{\frac{\beta}{k^2}\sigma_q\delta^2\left(\delta^2+1\right)+\frac{\beta}{k^2}\sigma_p\delta^2\left(\delta^2+1\right)+\sigma_p\sigma_q\left[\left(\delta^2-1\right)^2+\gamma^2\left(\delta^2+1\right)\right]\right\}\Omega$$
$$+\left[\frac{\beta}{k^2}\delta^2+\sigma_p\left(1+\delta^2\right)+\sigma_q\left(1+\delta^2+\gamma^2\right)\right]\Omega^2-\Omega^3=0 \qquad (4.9)$$

where $\gamma=\frac{R}{k}$ $\delta=\frac{2\pi R}{\lambda}$ $\Omega=m\delta^2V^2$

| | |
|---|---|
| P, Q, M | Axial tension, shear and bending moment |
| $\beta$ | Flexural rigidity of the ring |
| $\sigma_p$ | Extensional rigidity |
| $\sigma_q$ | Shear rigidity |
| k | Radius of gyration of the cross section |
| R | Radius of the ring |
| m | Mass per unit length |
| $\lambda$ | Wavelength |

Consider the situation whereby the wavelength $\lambda$ is greater than the ring circumference ($\lambda > 2\pi R$); therefore, $\delta = \frac{2\pi R}{\lambda} < 1$. For the thin wall rings in this study, $R >> k$, resulting in $\gamma = \frac{R}{k} >> 1$; consequently, $\gamma >> \delta$. In addition, $\frac{\beta}{k^2}$, $\sigma_p$ and $\sigma_q$ are generally of the same order of magnitude.

Consider the coefficient of the second term in Eqn (4.9):

$$\frac{\beta}{k^2}\sigma_q\delta^2\left(\delta^2+1\right)+\frac{\beta}{k^2}\sigma_p\delta^2\left(\delta^2+1\right)+\sigma_p\sigma_q\left[\left(\delta^2-1\right)^2+\gamma^2\left(\delta^2+1\right)\right] \qquad \text{(F.1)}$$

$\frac{\beta}{k^2}\sigma_q$, $\frac{\beta}{k^2}\sigma_p$ and $\sigma_p\sigma_q$ are of the same order. $\delta^2\left(\delta^2+1\right)$, $\delta^2\left(\delta^2+1\right)$ and $\left(\delta^2-1\right)^2$ are at most of unit order; they are very small values compared to $\gamma^2\left(\delta^2+1\right)$ because $\gamma >> 1$. Therefore, the expression (F.1) can be simplified to $\sigma_p\sigma_q\gamma^2\left(1+\delta^2\right)$.

Consider the coefficient of the third term in Eqn (4.9):

$$\frac{\beta}{k^2}\delta^2+\sigma_p\left(1+\delta^2\right)+\sigma_q\left(1+\delta^2+\gamma^2\right) \qquad \text{(F.2)}$$

$\frac{\beta}{k^2}$, $\sigma_p$ and $\sigma_q$ are of the same order. $\delta^2$ and $\left(1+\delta^2\right)$ are at most of unit order; they are very small values compared with $\gamma^2$ because $\gamma >> 1$. Therefore, the expression (F.2) can be simplified to $\sigma_q\gamma^2$.

As a result, Equation (4.9) can be simplified to

$$\frac{\beta}{k^2}\delta^2\sigma_p\sigma_q\left(\delta^2-1\right)^2-\sigma_p\sigma_q\gamma^2\left(1+\delta^2\right)\Omega+\sigma_q\gamma^2\Omega^2-\Omega^3=0 \qquad \text{(F.3)}$$

Explicit expressions for the roots of equation (F.3) in terms of $\Omega$ are also very complicated; however, an approximate solution can be obtained conveniently. The

order of magnitude of $\Omega$ are governed by the magnitude of the parameter $\gamma$; the three roots $\Omega$ of the cubic equation (F.3) are respectively of the order of $1/\gamma^2$, $\gamma^2$ and unity. Since $\gamma >> 1$, then $1/\gamma^2 << 1$ and $\gamma^2 >> 1$.

When $\Omega$ is of the order of $1/\gamma^2$, the two high order terms, i.e. $\sigma_q \gamma^2 \Omega^2$ and $\Omega^3$, can be eliminated because they are much smaller compared with the other two terms. Eqn (F.3) then reduces to

$$\frac{\beta}{k^2}\delta^2\sigma_p\sigma_q\left(\delta^2-1\right)^2-\sigma_p\sigma_q\gamma^2\left(1+\delta^2\right)\Omega=0$$

and $$\Omega_1=\frac{\beta\delta^2\left(\delta^2-1\right)^2}{k^2\gamma^2\left(1+\delta^2\right)}$$

Similarly, the other two roots of $\Omega$ can be extracted and are shown below, together with $\Omega_1$:

$$\begin{cases}\Omega_1=\sigma_q\gamma^2\\ \Omega_2=\dfrac{\beta\delta^2\left(\delta^2-1\right)^2}{k^2\gamma^2\left(1+\delta^2\right)}\\ \Omega_3=\sigma_p\left(1+\delta^2\right)\end{cases} \tag{F.4}$$

In the solutions corresponding to (F.4), the relative error involved in each root is of the order of $1/\gamma^2$.

Substituting $\Omega = m\delta^2 V^2$ into equations (F.4), three expressions for *V* can be extracted

$$\Rightarrow \begin{cases} V_1 = \pm\left(\dfrac{\lambda}{2\pi k}\right)\sqrt{\dfrac{\sigma_q}{m}} \\ V_2 = \pm\dfrac{1-\left(\dfrac{2\pi R}{\lambda}\right)^2}{R\sqrt{1+\left(\dfrac{2\pi R}{\lambda}\right)^2}}\sqrt{\dfrac{\beta}{m}} \\ V_3 = \pm\sqrt{1+\left(\dfrac{2\pi R}{\lambda}\right)^2}\sqrt{\dfrac{\sigma_p}{m}} \end{cases} \qquad \text{where } \lambda > 2\pi R$$

It can be also shown that $V_1$, $V_2$ and $V_3$ are respectively the phase velocities for shear, flexural and extensional waves. The positive and negative signs in each expression represent the two opposite directions of transmission along the curvature of the ring.

**Appendix G** Newton's Method for Finding the Roots of an Equation

If $f(x)$ is a differentiable function and $x_0$ is some point which is suspected to be in the vicinity of a solution to the equation $f(x)=0$, a linear approximation of $f(x)$ at $x_0$ can be made and solved.

Denote $x_1$ as the solution to $l(x)=f(x_0)+f'(x_0)(x-x_0)=0$. In other words,

$$f(x_0)+f'(x_0)(x_1-x_0)=0$$

then $$x_1-x_0=-\frac{f(x_0)}{f'(x_0)}$$

so $$x_1=x_0-\frac{f(x_0)}{f'(x_0)}$$

If the initial estimate of $x_0$ is good, the approximate solution $x_1$ yields an even closer approximation to the solution of $f(x)=0$. With $x_1$, the process can be repeated to obtain $x_2$, $x_3$ and so on. If, after *n* iterations, the approximate solution is $x_n$, then the next step is

$$x_{n+1}=x_n-\frac{f(x_n)}{f'(x_n)}$$

Figure G-1 shows the progression of this iteration process. Provided that the initial value of $x_0$ is properly selected and makes the iteration process convergent, this method will

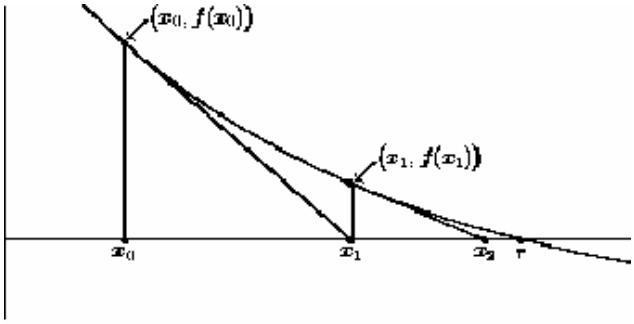


**Fig. G-1** Iteration process to obtain an approximate solution for $f(x)=0$

produce approximate solutions to any degree of accuracy.

In the case that $f(x)=0$ is a cubic equation, one of the three roots, $x^1$, can be calculated using the method just described. Following that, the other two roots can be obtained by solving a quadratic equation, which is obtained by dividing $f(x)=0$ by $(x-x^1)$.

**Appendix H** Stress-strain Curves from Compression Tests on Single Rings

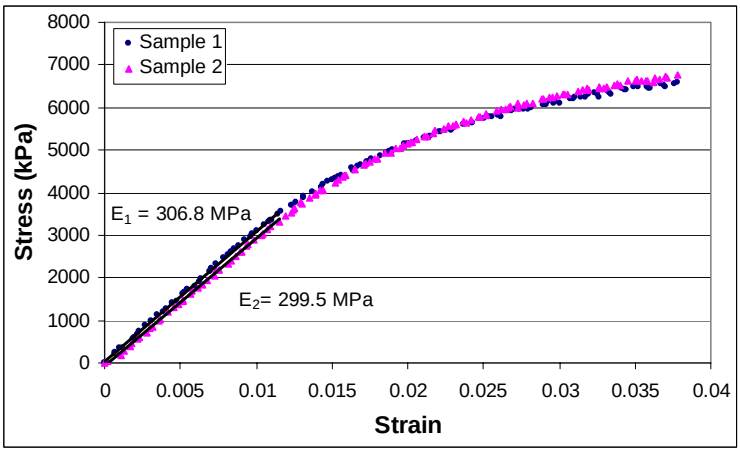


(a) 38.1x3 Brass rings
Average apparent elastic modulus = 303.2 MPa

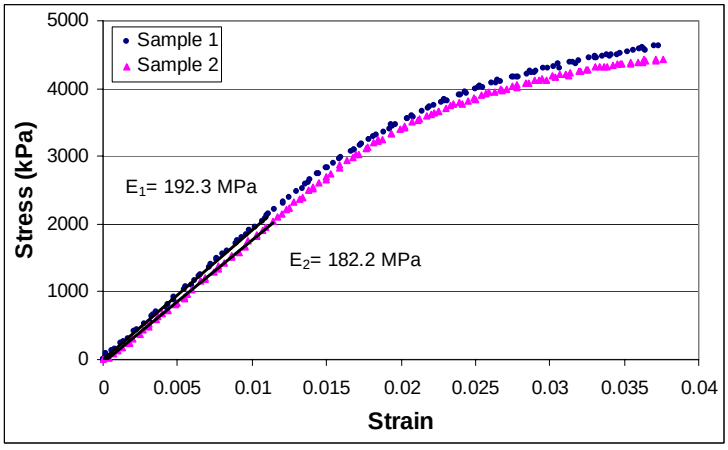


(b) 38.1x3 Al alloy rings
Average apparent elastic modulus = 187.3 MPa

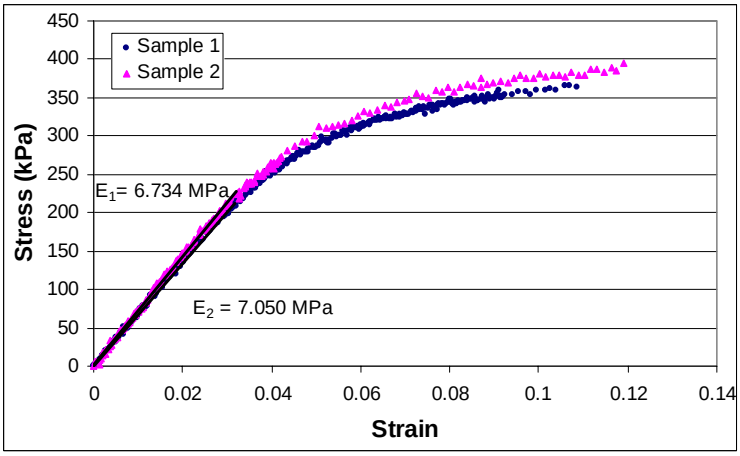


(c) 38.1x1 Al alloy rings
Average apparent elastic modulus = 6.89 MPa

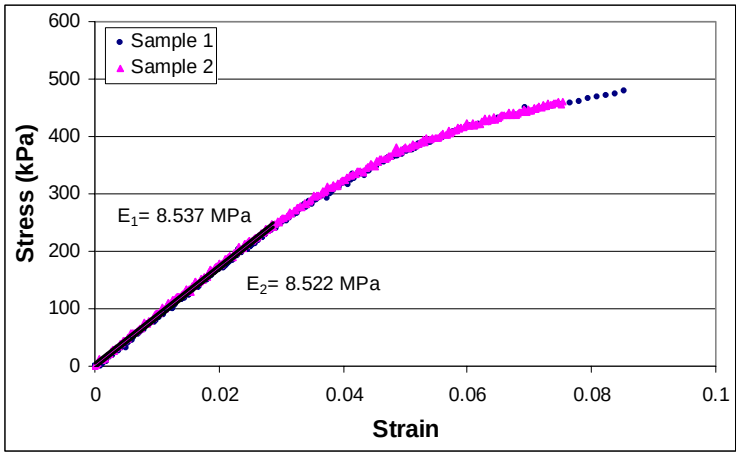


(d) 38.1x1 Brass rings
Average apparent elastic modulus = 8.53 MPa

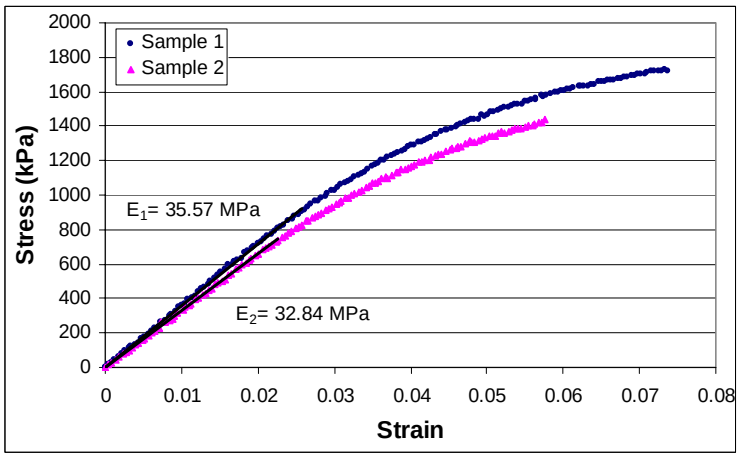


(e) 25.4x1 Brass rings
Average apparent elastic modulus = 34.2 MPa

# **Appendix I** Determination of Wave Commencement of Selected Frequency Component

Discrete Fourier Transformation (DFT) decomposes a signal into a series of discrete frequency components. To determine the wave speeds associated with dominant components, it is necessary to locate the commencements of these waves. For the convenience in analyzing the effect of signal processing on changes to the wave commencement point, a synthesized signal assembled from several sinusoidal waves is established and analyzed.

Consider a synthesized signal comprising four simple waves, where three of them are sinusoids and the $4^{th}$ is a constant. Each of these four components possesses a commencement point whose position is differs from the others, as shown in Figure I-1. The frequencies of the three sinusoidal components are also different from each other.

By applying a DFT to the synthesized signal, its frequency components can be identified by the positions of three peaks along the abscissa of the DFT, as shown in Figure I-2. It is noted that results of DFT are actually a series of complex numbers, while the Figure I-2 only shows their modulus.

To effect filtering of the DFT spectrum to extract a single frequency, all data in the DFT spectrum are set as zero, except one of the three dominant frequency components. Then, inverse DFT is applied to obtain the filtered signal in the time domain, as shown in Figure I-3(a).

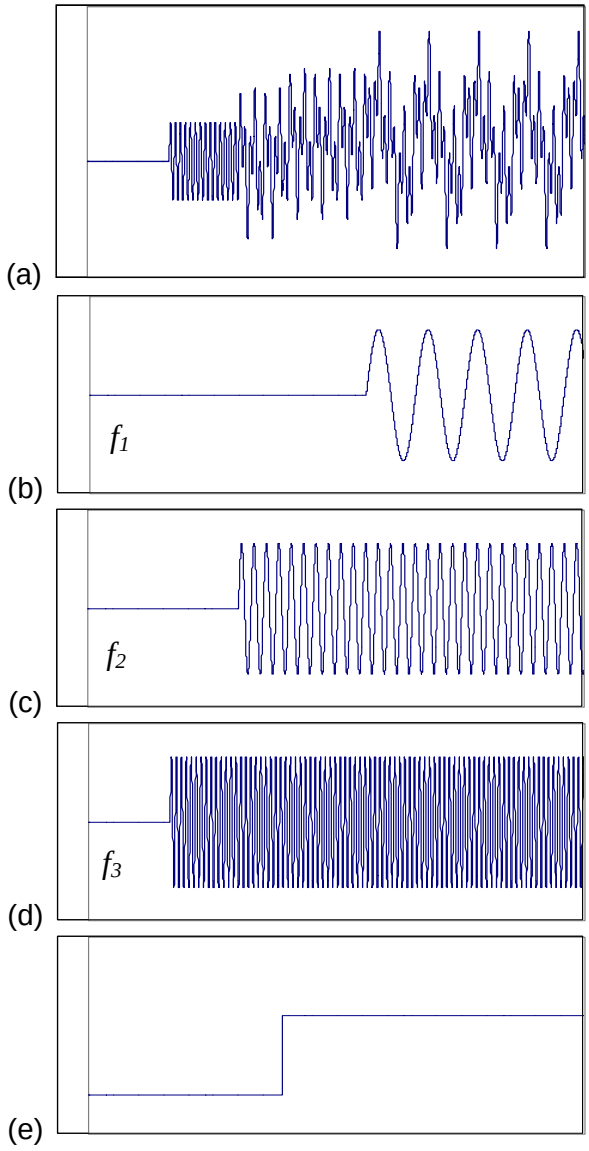


**Fig. I-1** A synthesized signal and its components
(a) Synthesized signal
(b), (c) and (d): component sinusoids with frequencies $f_1$, $f_2$ and $f_3$, respectively.
(e) Constant signal

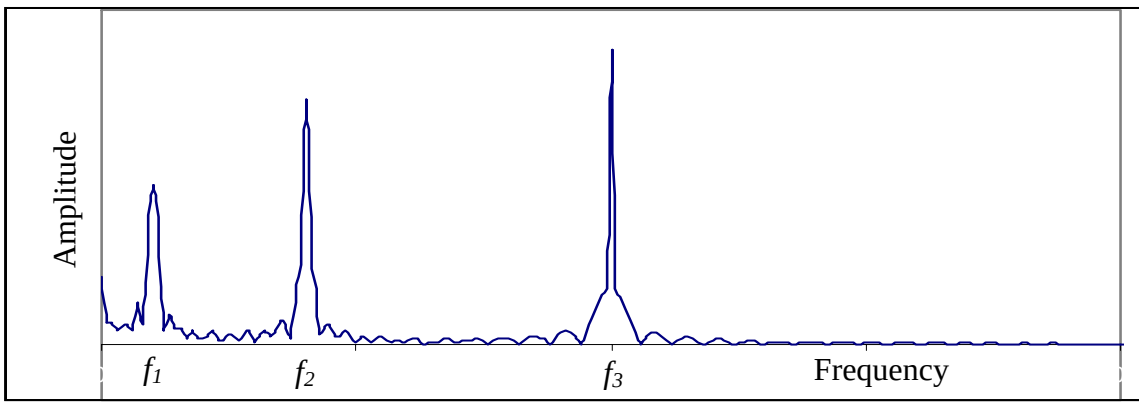


**Fig. I-2** DFT of the synthesized signal

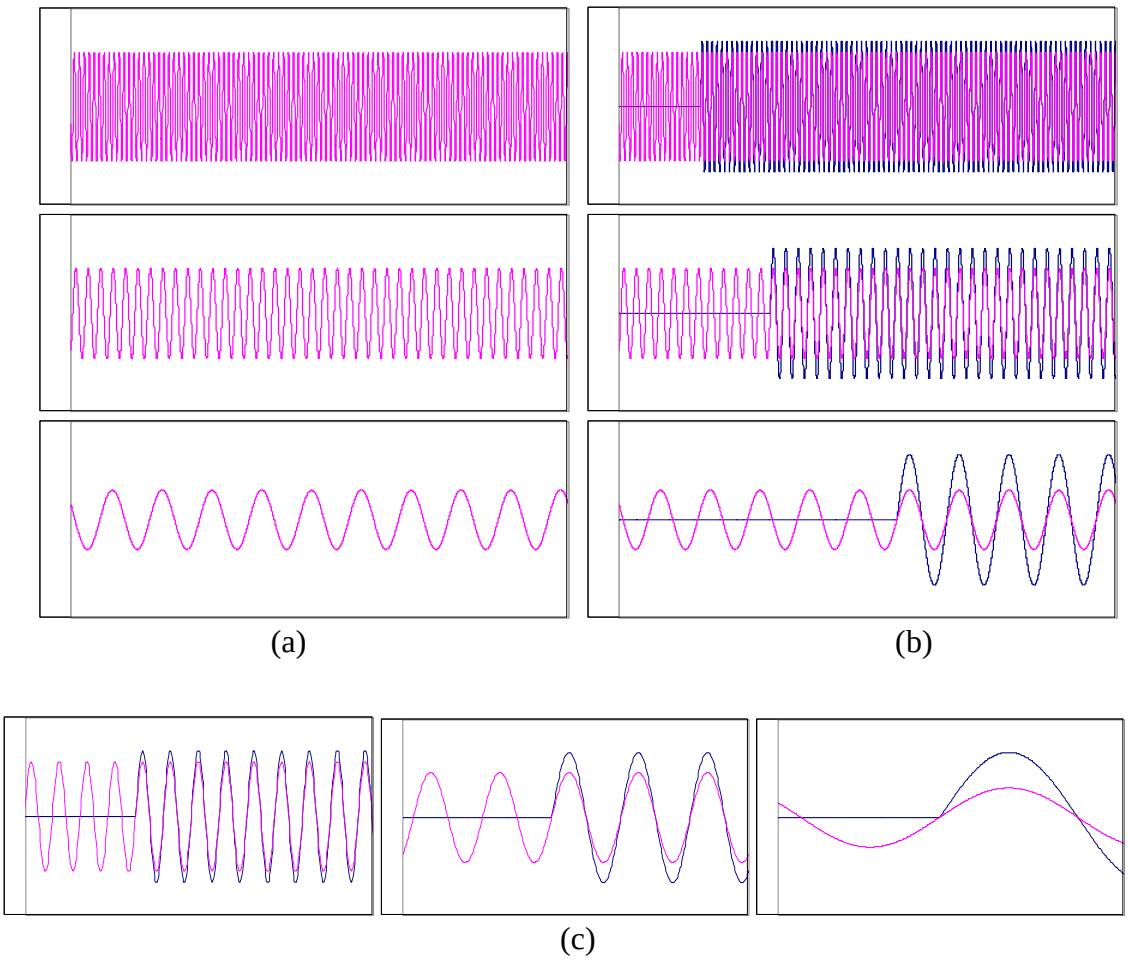


**Fig. I- 3** Filtered signals and comparison with original components
(a) Three filtered signals with different frequency components
(b) Comparison of filtered signals with corresponding components
(c) Close-up views of wave commencement

Obviously, the filtered signals are simple sinusoidal waves that cover the whole window. Comparing the filtered signals with corresponding components in the original signal, as shown in Figure I-3 (b) and (c), the starting point of the original signal is exactly the point where the filtered signal crosses the zero level. This indicates that the filtering and inverse DFT processes do not change the position of wave commencement.

Take an example of actual signals obtained from an impact test on a ring array; determination of the commencement of different frequency components is illustrated as follows.

Figure I-4 shows an example of an input and output signal. For the input signal, its commencement is easy to locate because there is a sharp rise defining the front of the wave, and all frequency components start at that point in time. Although the exact commencement of the output signal can be located, the algorithm presented earlier to determine the commencements of different frequency components must be used. The DFT of the output signal in Figure I-5 shows that low frequency components (<500Hz) have the largest amplitudes and carry most of the energy. There are two small peaks corresponding to 6500 *Hz* and 9500 *Hz* and these components, together with the 500 Hz component are selected to study how frequency affects the speed of flexural wave propagation.

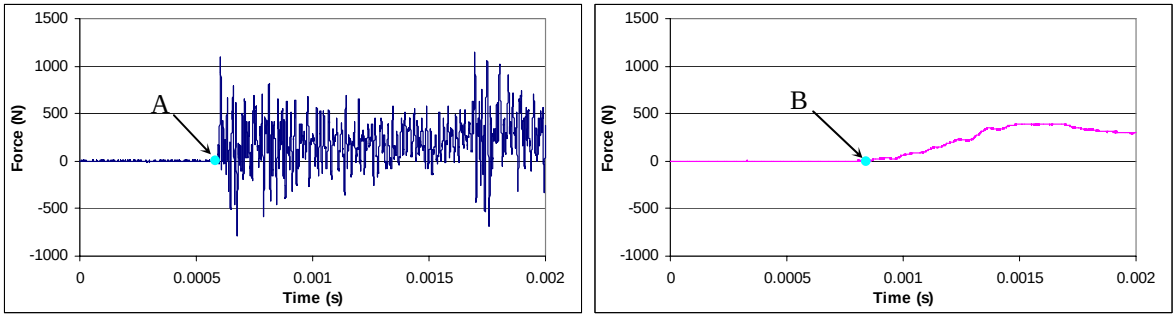


(a) input signal (b) output signal

**Fig. I- 4** Actual stress signals from impact tests on ring array

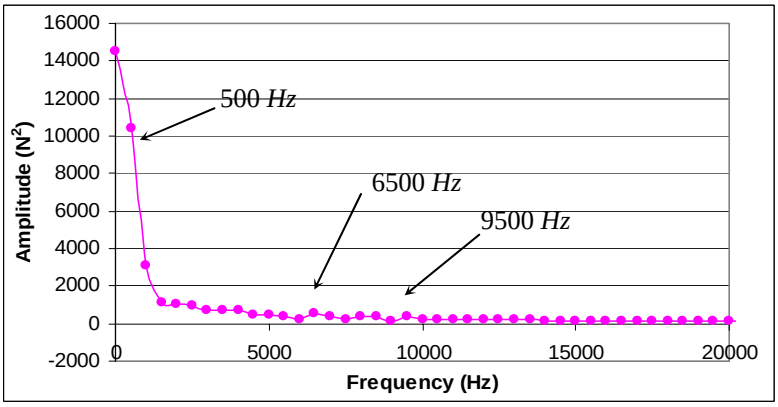


**Fig. I- 5** DFT of output signal

Setting all frequency components to zero except for these three dominant components and applying inverse DFT results in three sinusoidal waves, as shown in Figure I-6. As point B had been identified as the commencement of the output signal, all frequency components must appear after point B. Therefore, the first point on the right hand side of point B that crosses the zero level in the filtered signal is the starting point of that frequency component. Fig I-6 illustrates the process of identifying the commencements of different frequency components. Points A and B are respectively the commencements of the input and output signals. In the 500 Hz filtered signal, point C is the first point on the right hand side of B where the 500 Hz signal crosses zero and is therefore the commencement of the 500Hz component. Hence, the interval AC is the travel time for the 500 Hz frequency component. Similarly, AD and AE are identified respectively as the travel times for the 6,500Hz and 9,500 Hz frequency components.

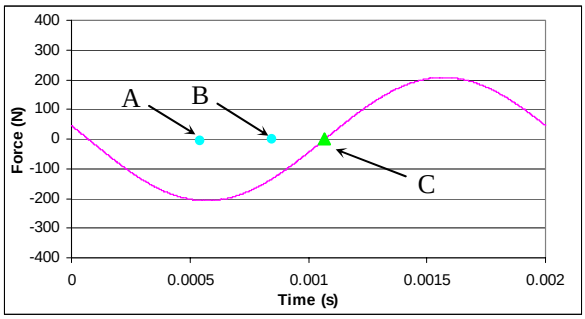


(a) 500 Hz filtered signal

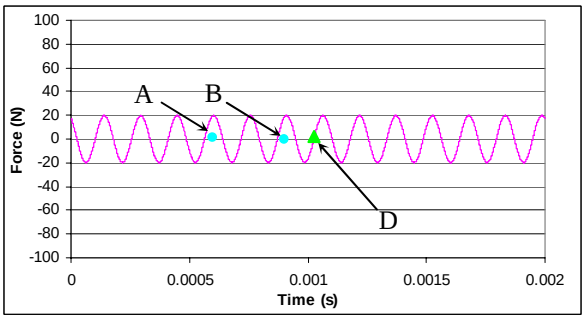


(b) 6500 Hz filtered signal

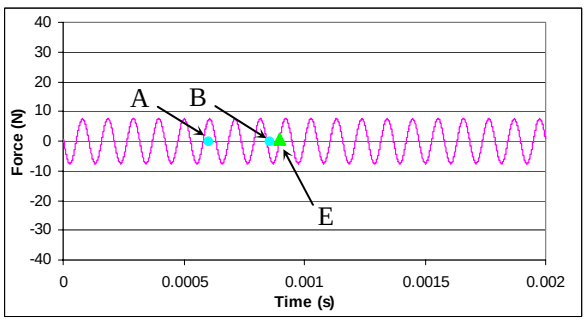


(c) 9500 Hz filtered signal

**Fig. I- 6** Determination of commencement of different frequency components

**Appendix J** DSO Signals from Impact Test on Metal Tubes

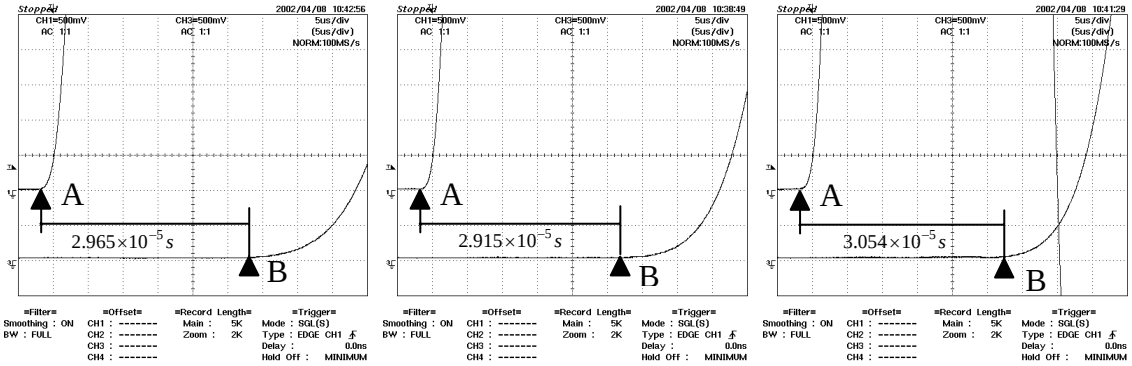


(1) (2) (3)

**A.** DSO signals for Al alloy tube with a 50.5 mm length

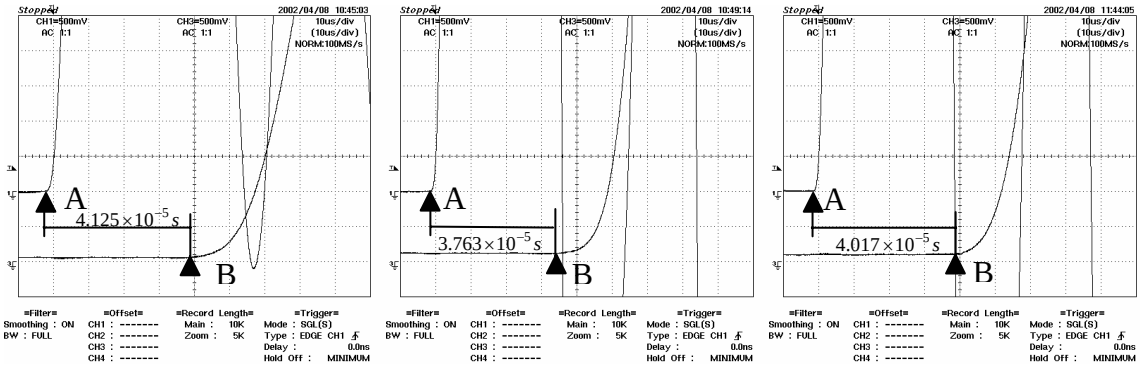


(1) (2) (3)

**B.** DSO signals for Al alloy tube with a 101.8 mm length

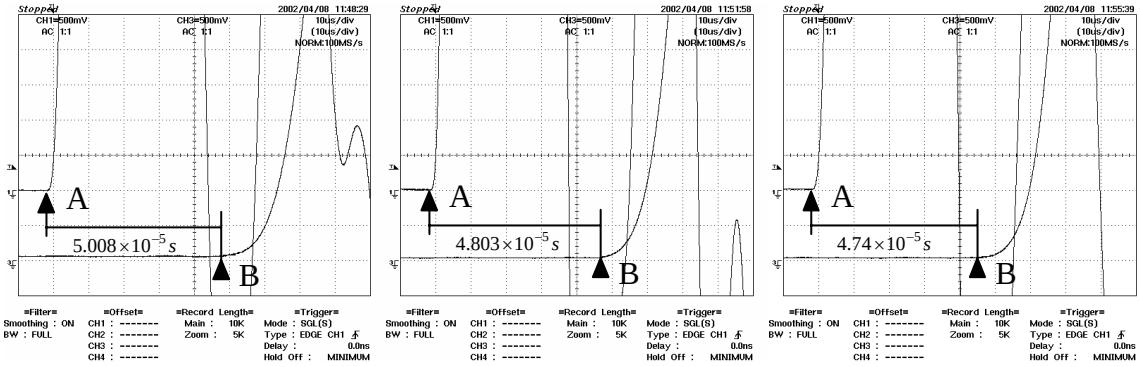


(1) (2) (3)

**C.** DSO signals for Al alloy tube with a 150.2 mm length

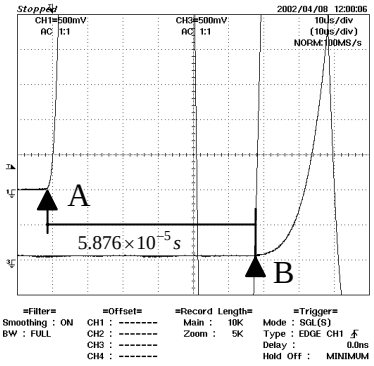


(1)

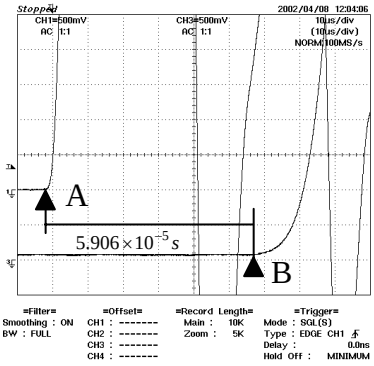


(2)

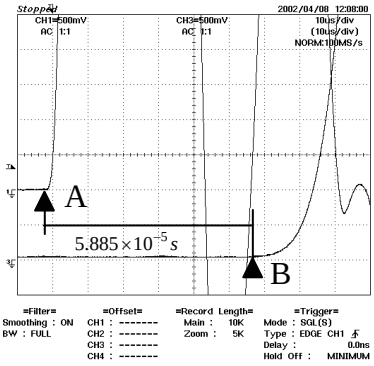


(3)

**D.** DSO signals for Al alloy tube with a 200 mm length

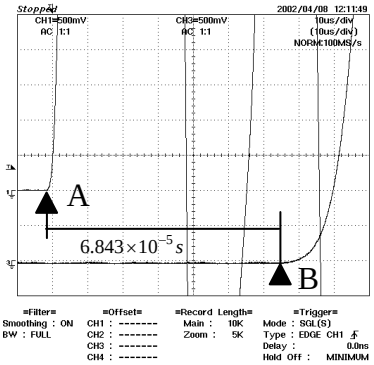


(1)

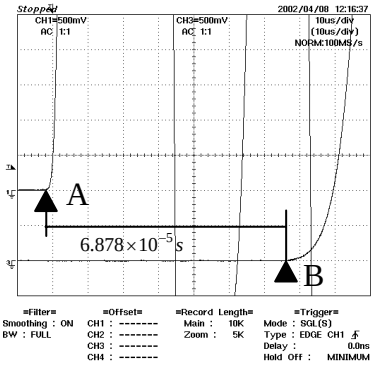


(2)

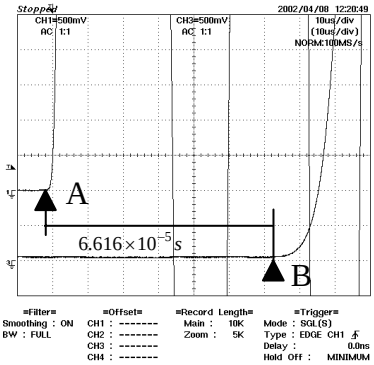


(3)

**E.** DSO signals for Al alloy tube with a 250.8 mm length

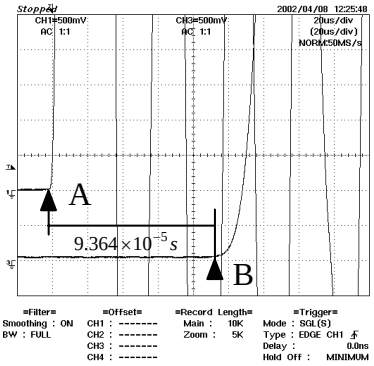


(1)

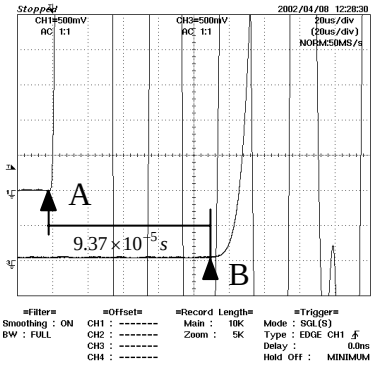


(2)

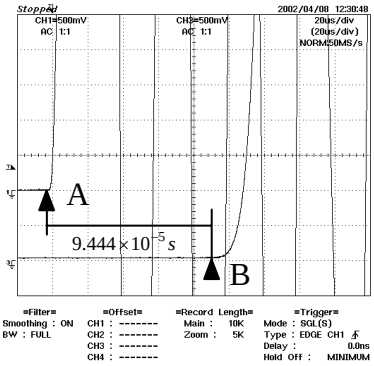


(3)

**F.** DSO signals for Al alloy tube with a 382 mm length

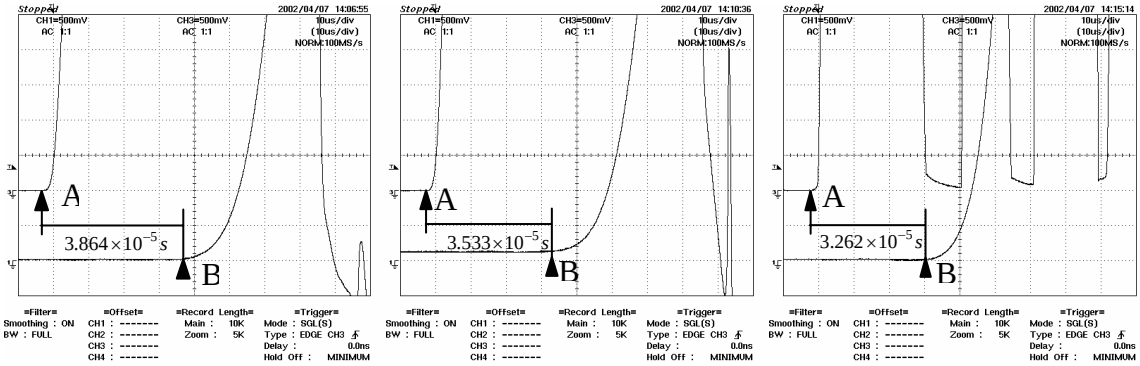


(1) (2) (3)

**G.** DSO signals for Brass tube with a 49.3 mm length

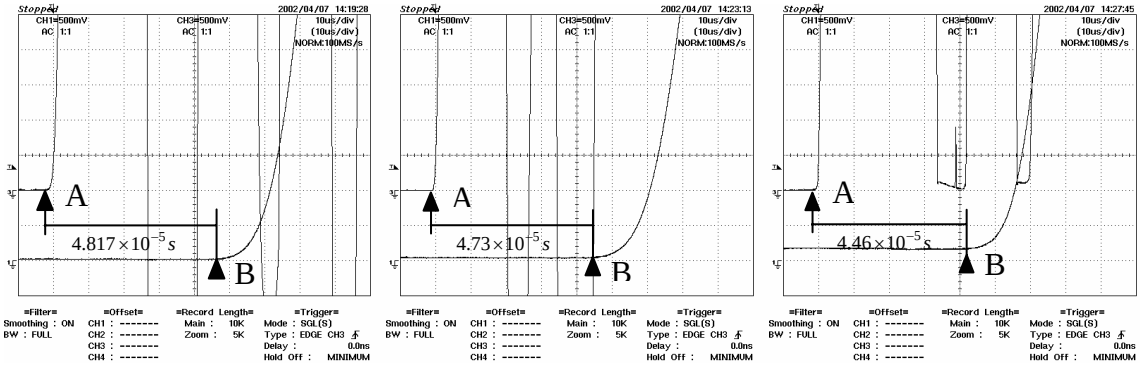


(1) (2) (3)

**H.** DSO signals for Brass tube with a 99 mm length

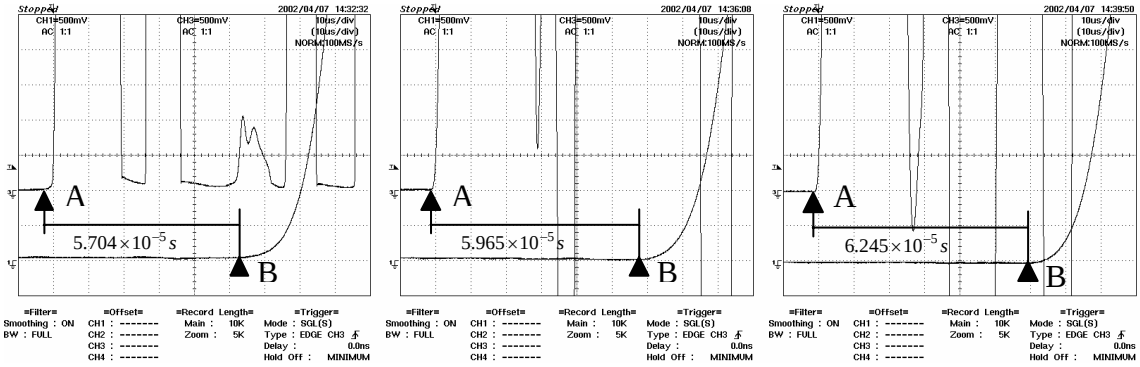


(1) (2) (3)

**I.** DSO signals for Brass tube with a 148.9 mm length

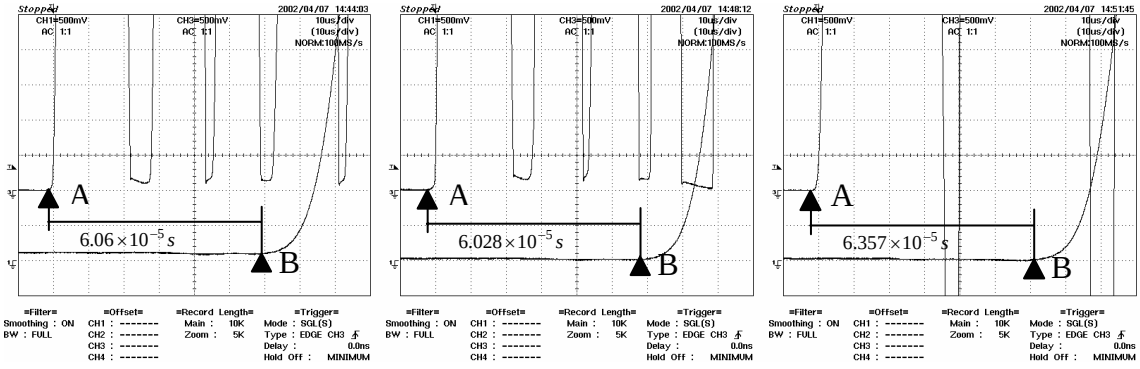


(1) (2) (3)

**J.** DSO signals for Brass tube with a 161.7 mm length

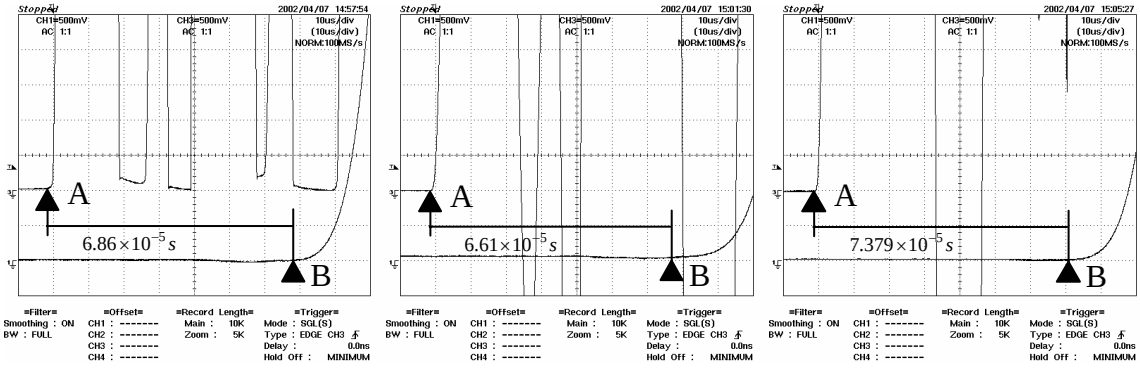


(1) (2) (3)

**K.** DSO signals for Brass tube with a 198.9 mm length

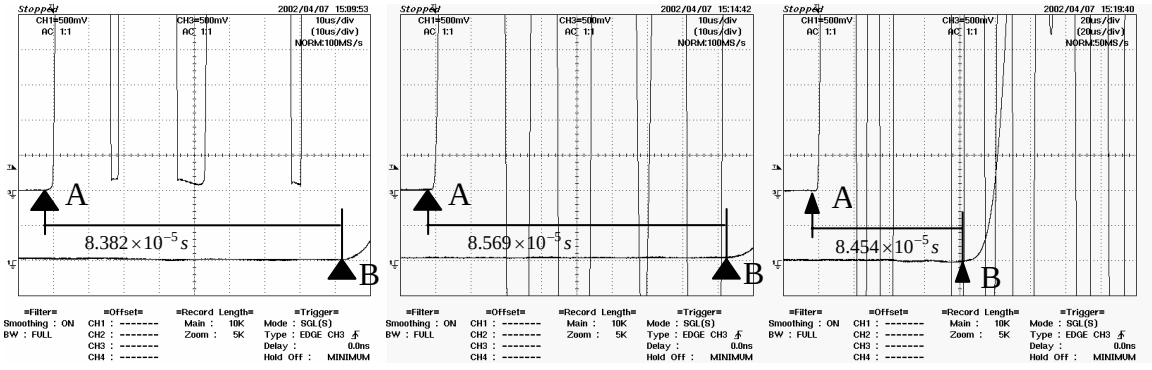


(1) (2) (3)

**L.** DSO signals for Brass tube with a 248.8 mm length

**Appendix K** DSO Signals from Impact Tests on Single Rings

(a)

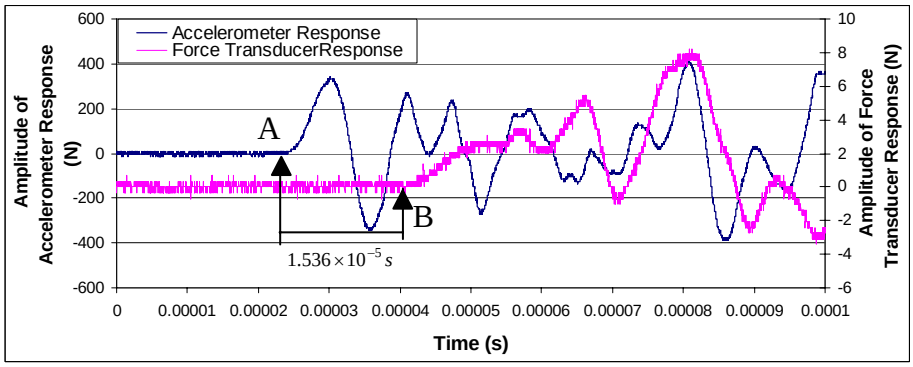


(b)

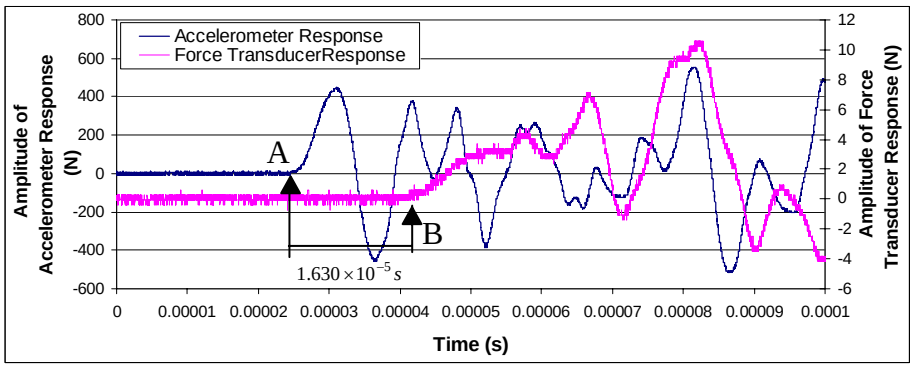


**A. 38.1x1 Brass ring** (average time interval = $1.583\times10^{-5}\,s$)

---

(a)

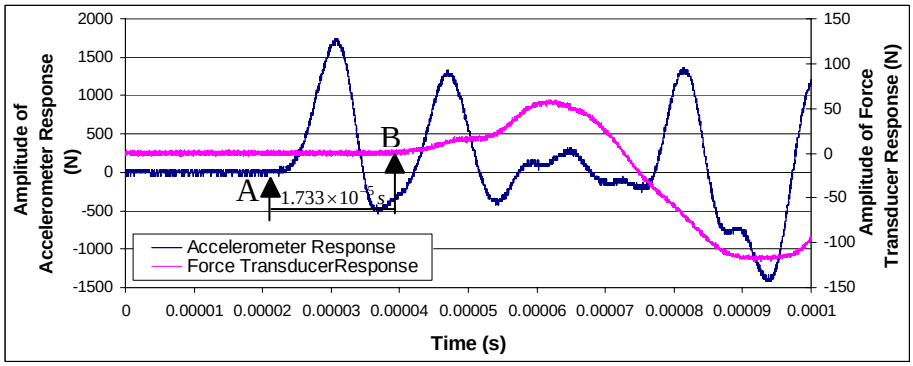


(b)

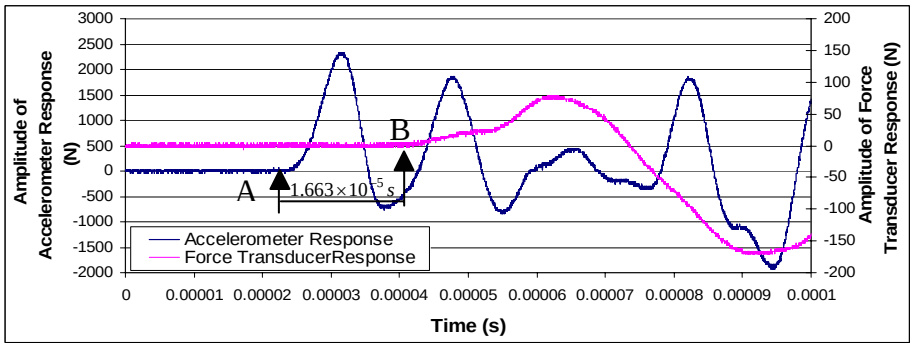


**B. 38.1x3 Brass ring** (average time interval = $1.698\times10^{-5}\,s$)

(a)

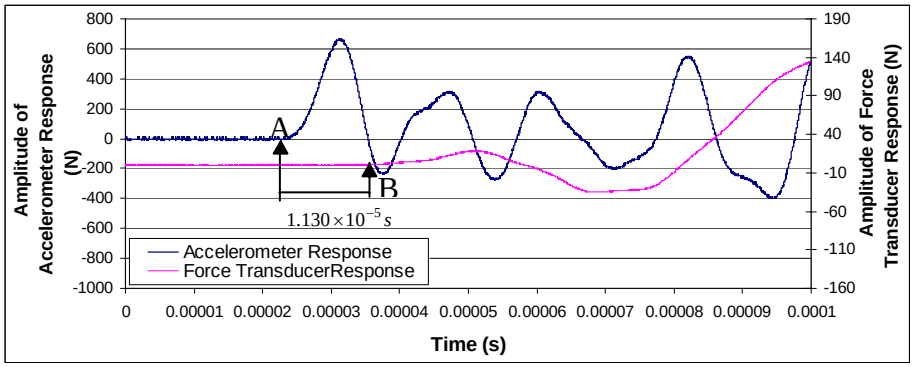


(b)

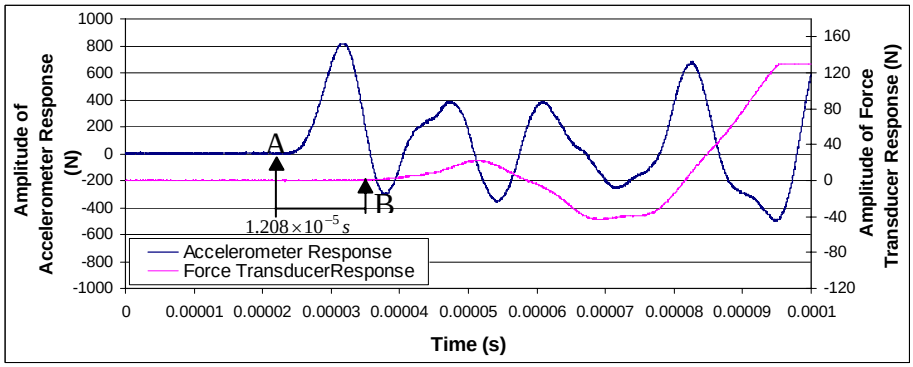


**C. 38.1x1 Al alloy ring** (average time interval = $1.169\times10^{-5}s$)

(a)

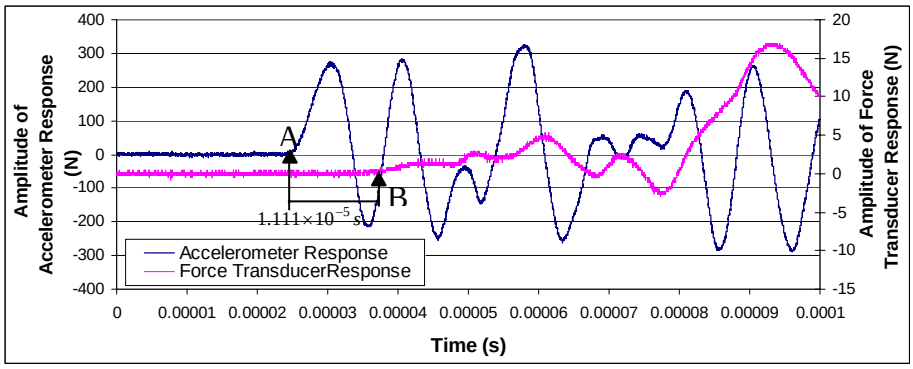


(b)

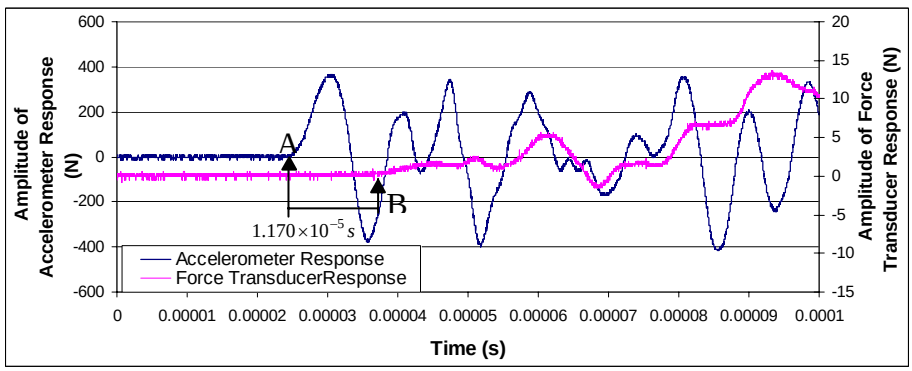


**D. 38.1x3 Al alloy ring** (average time interval = $1.141\times10^{-5}s$)

(a)

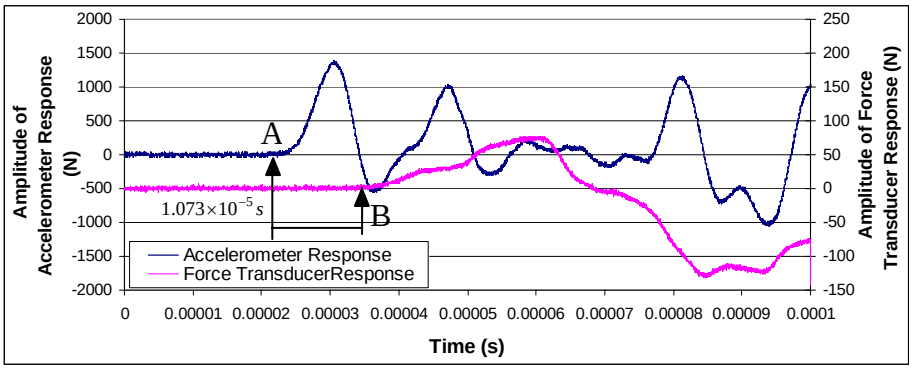


(b)

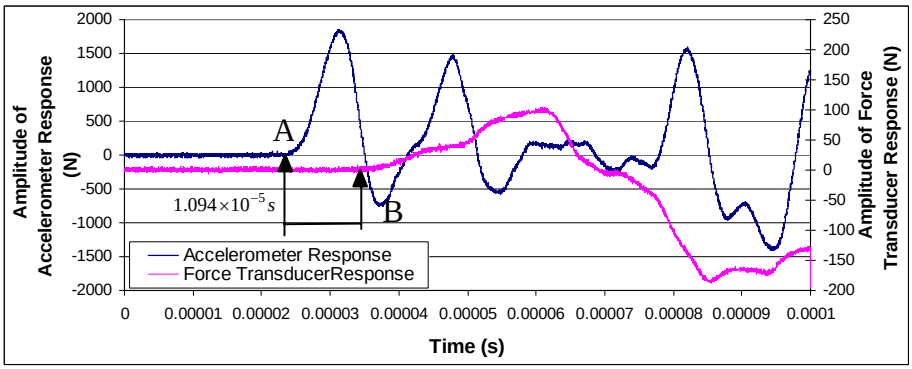


**E. 25.4x1 Brass ring** (average time interval = $1.084\times10^{-5}s$)

**Appendix L** DSO Signals from Impact Tests on Ring Arrays

38.1x1 Brass rings in square packed arrangement with unconstrained sides

Height of the array = 0.229 m

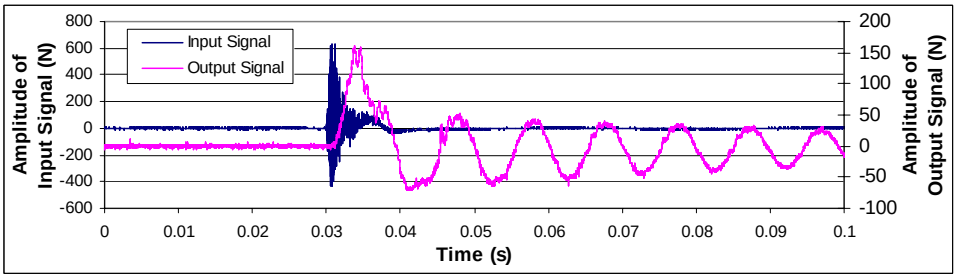


Complete view of the first impact wave

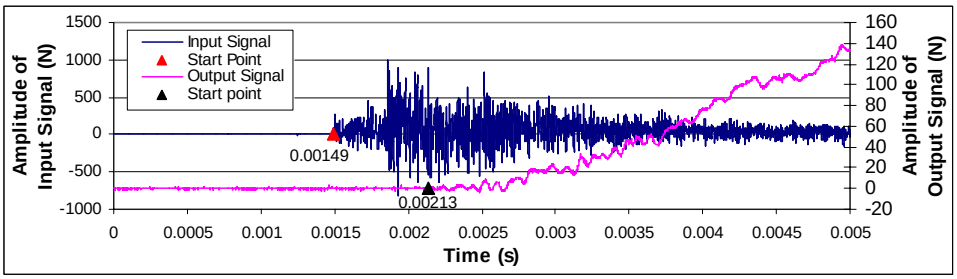


Enlarged view of the wave front

Time interval = 0.00064 s

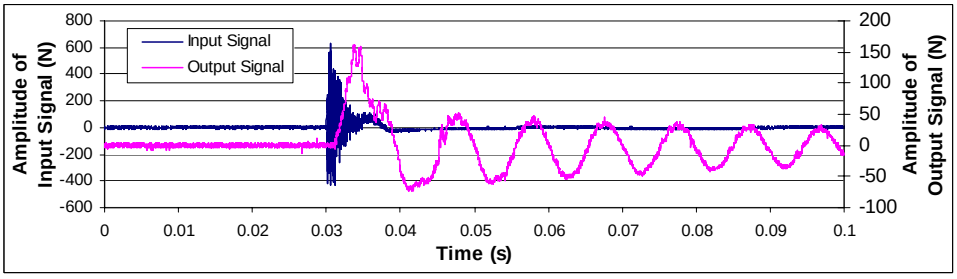


Complete view of the second impact wave

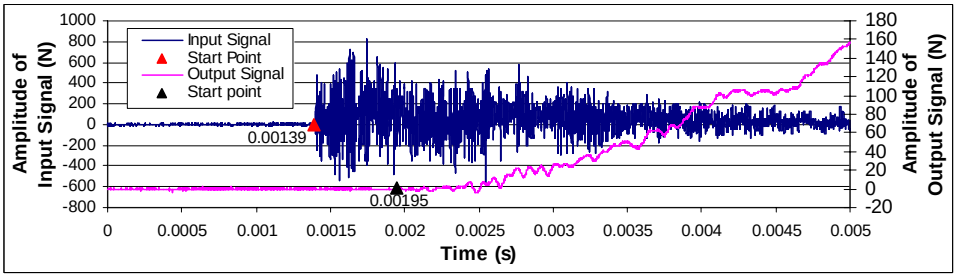


Enlarged view of the wave front

Time interval = 0.00056 s

Average time interval = 0.00060 s; Apparent wave speed = 382 m/s

38.1x1 Brass rings in transverse close packed arrangement with unconstrained sides

Height of the array = 0.236 m

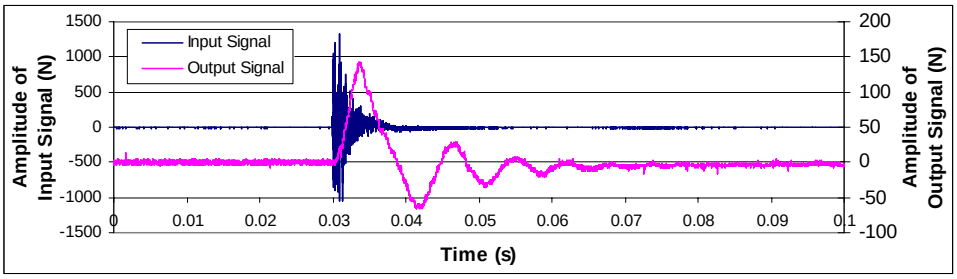


Complete view of the first impact wave

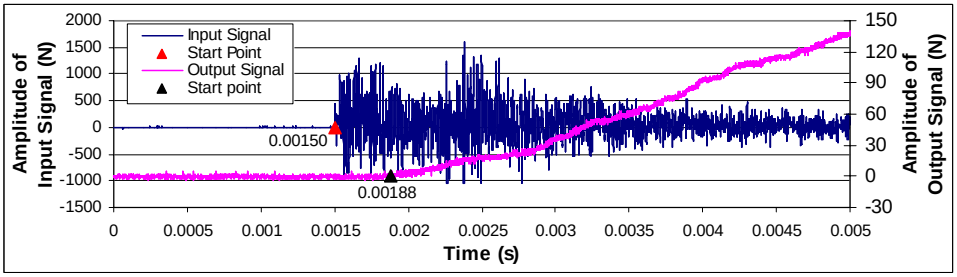


Enlarged view of the wave front

Time interval = 0.00038 s

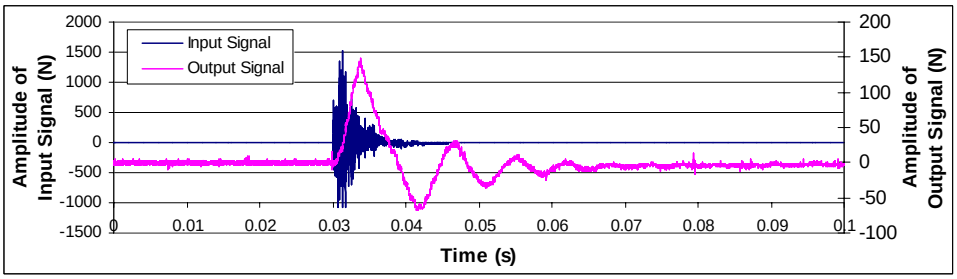


Complete view of the second impact wave

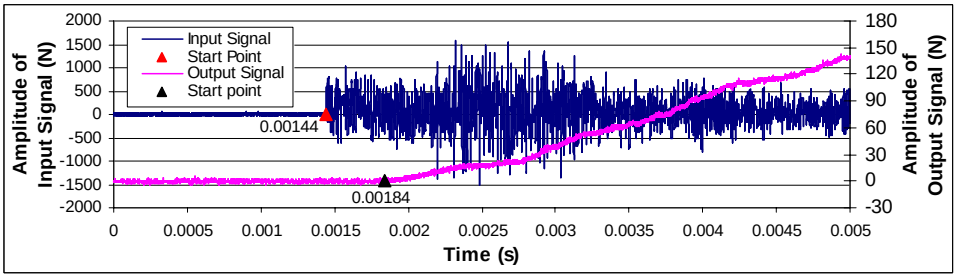


Enlarged view of the wave front

Time interval = 0.00040 s

Average time interval = 0.00039 s; Apparent wave speed = 611 m/s

38.1x1 Brass rings in vertical close packed arrangement with unconstrained sides

Height of the array = 0.210 m

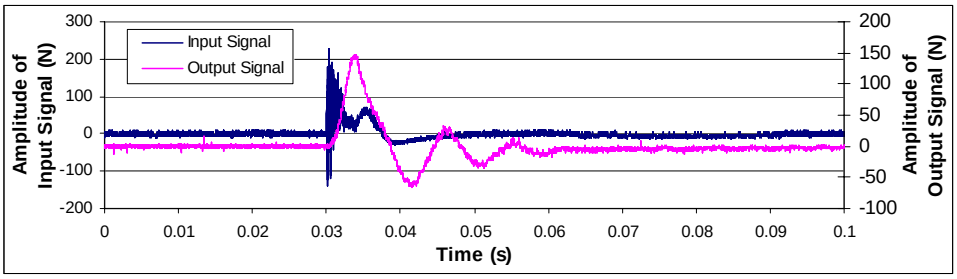


Complete view of the first impact wave

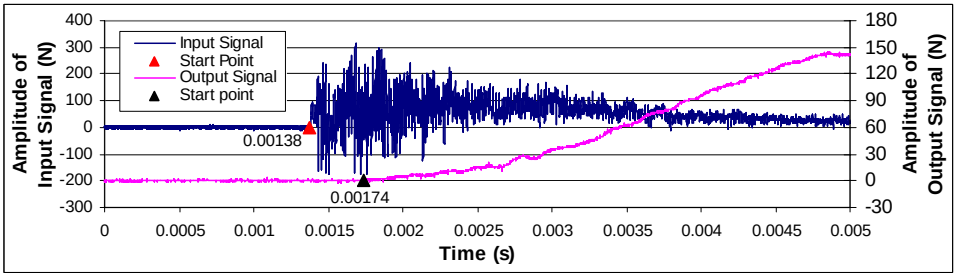


Enlarged view of the wave front

Time interval = 0.00036 s

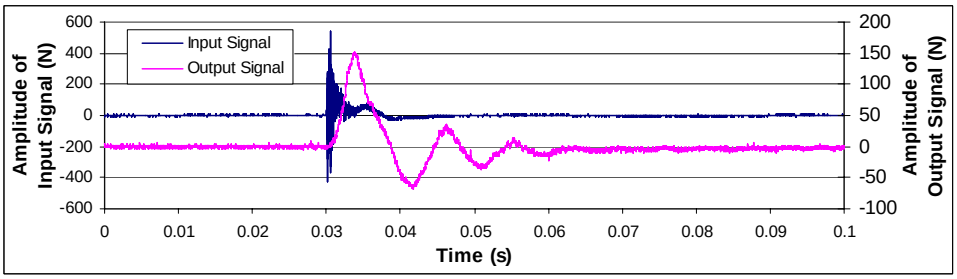


Complete view of the second impact wave

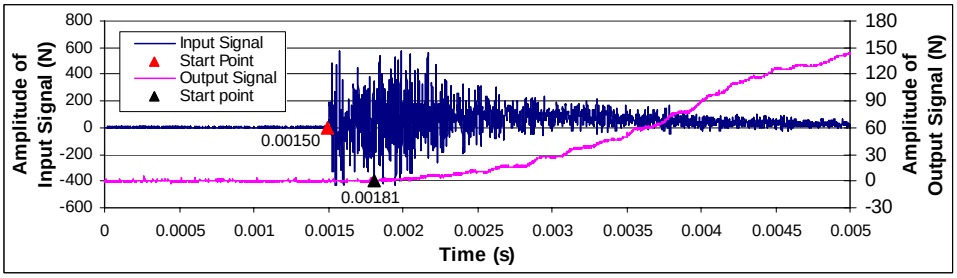


Enlarged view of the wave front

Time interval = 0.00031 s

Average time interval = 0.00034 s; Apparent wave speed = 617 m/s

38.1x3 Brass rings in square packed arrangement with unconstrained sides

Height of the array = 0.229 m

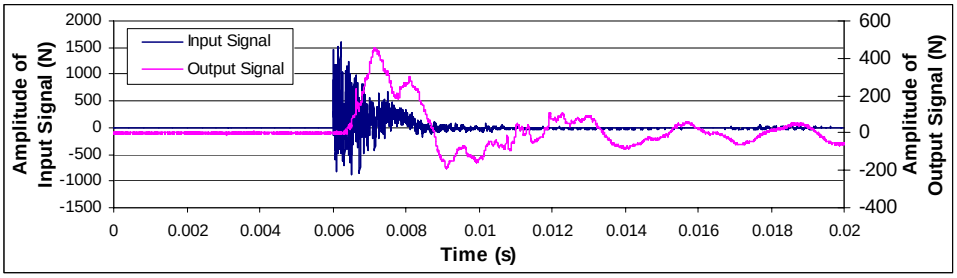


Complete view of the first impact wave

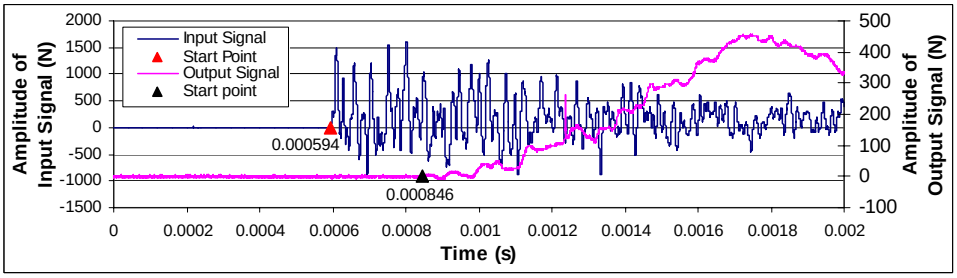


Enlarged view of the wave front

Time interval = 0.000252 s

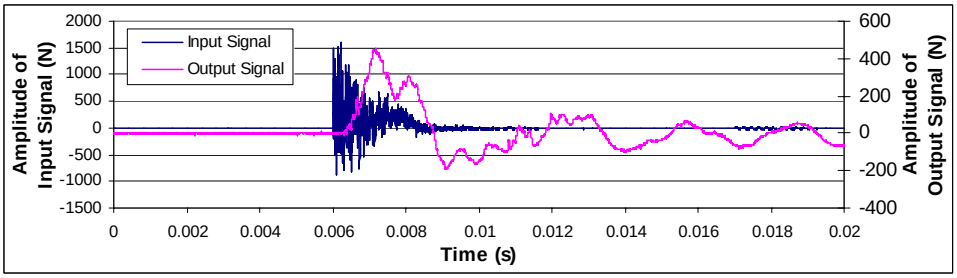


Complete view of the second impact wave

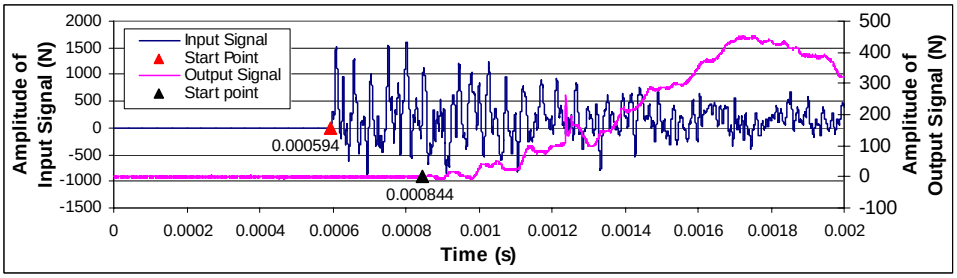


Enlarged view of the wave front

Time interval = 0.000250 s

Average time interval = 0.000251 s; Apparent wave speed = 911 m/s

38.1x3 Brass rings in transverse close packed arrangement with unconstrained sides

Height of the array = 0.236 m

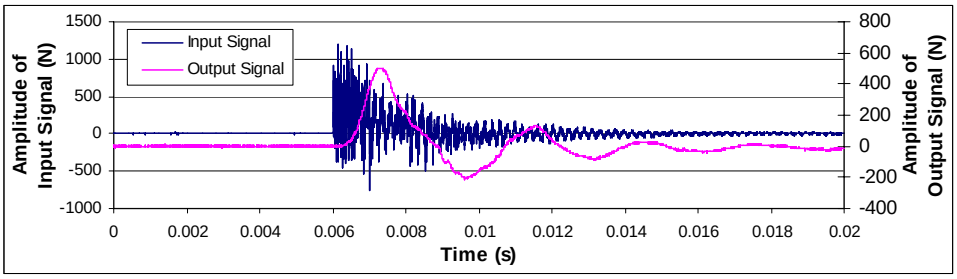


Complete view of the first impact wave

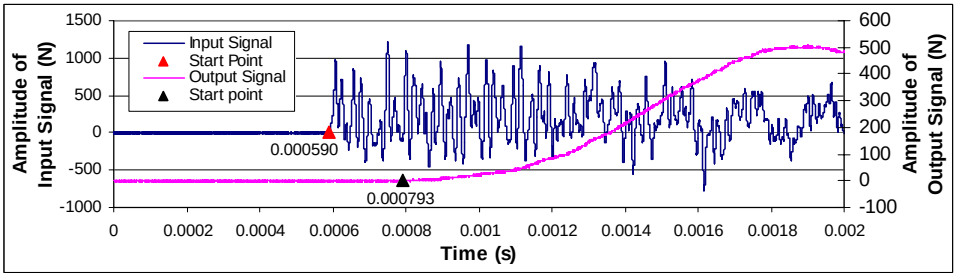


Enlarged view of the wave front

Time interval = 0.000203 s

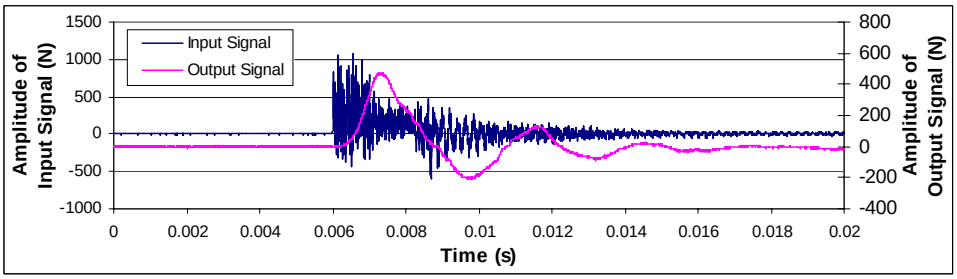


Complete view of the second impact wave

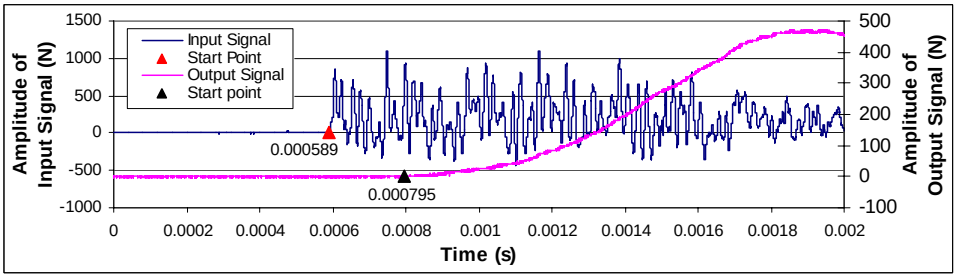


Enlarged view of the wave front

Time interval = 0.000206 s

Average time interval = 0.000204 s; Apparent wave speed = 1156 m/s

38.1x3 Brass rings in vertical close packed arrangement with unconstrained sides

Height of the array = 0.210 m

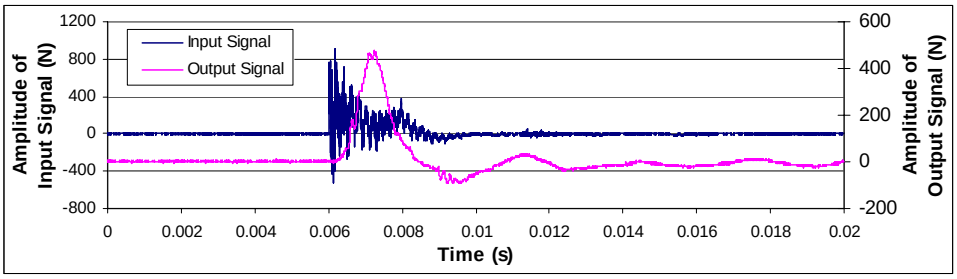


Complete view of the first impact wave

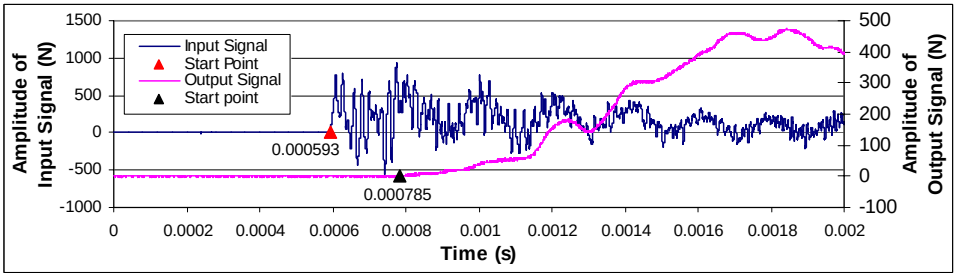


Enlarged view of the wave front

Time interval = 0.000192 s

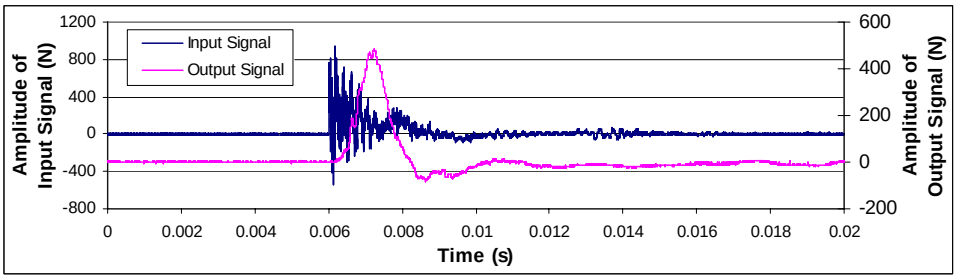


Complete view of the second impact wave

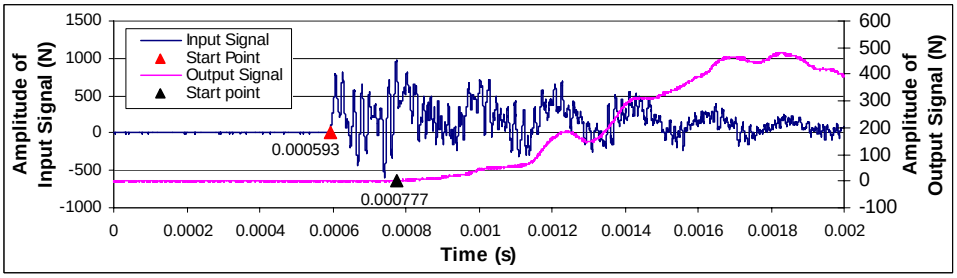


Enlarged view of the wave front

Time interval = 0.000184 s

Average time interval = 0.000188 s; Apparent wave speed = 1115 m/s

38.1x1 Al alloy rings in square packed arrangement with unconstrained sides

Height of the array = 0.229 m

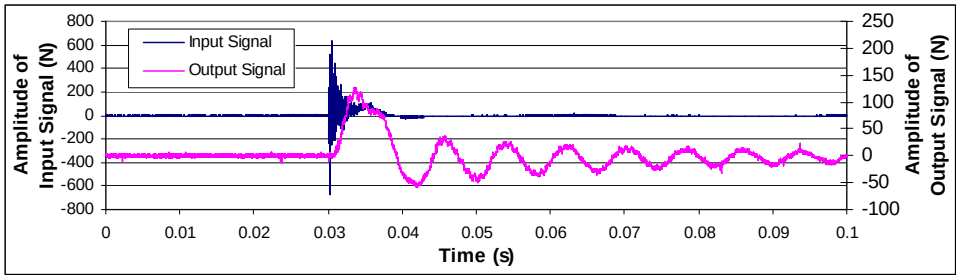


Complete view of the first impact wave

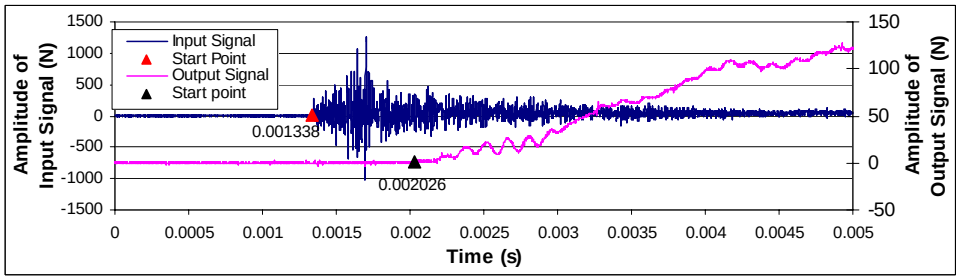


Enlarged view of the wave front

Time interval = 0.000689 s

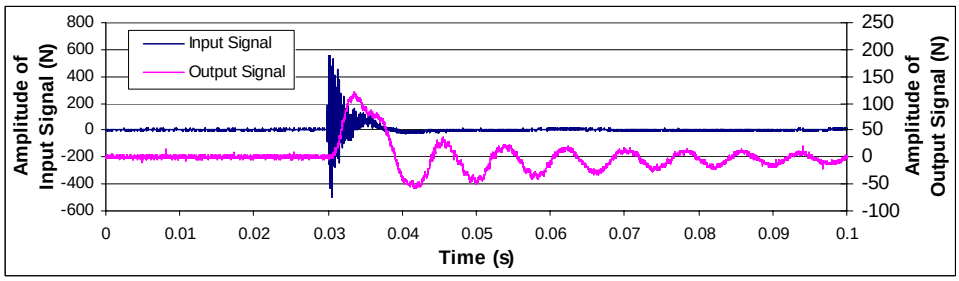


Complete view of the second impact wave

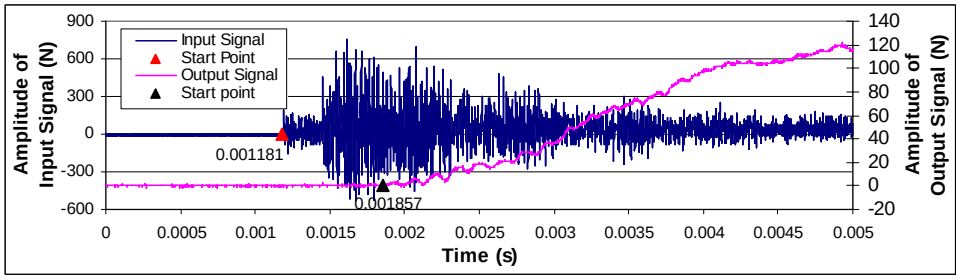


Enlarged view of the wave front

Time interval = 0.000676 s

Average time interval = 0.000682 s; Apparent wave speed = 335 m/s

38.1x1 Al alloy rings in transverse close packed arrangement with unconstrained sides

Height of the array = 0.236 m

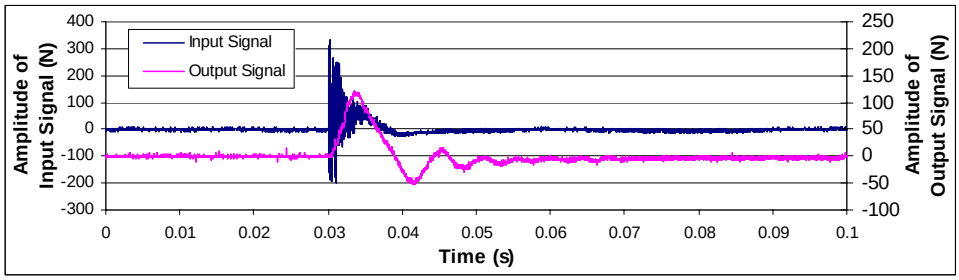


Complete view of the first impact wave

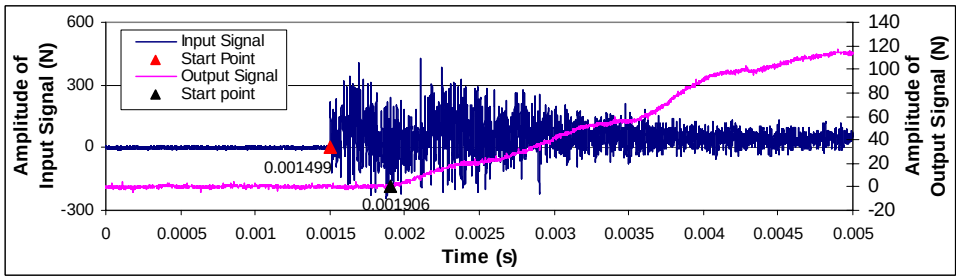


Enlarged view of the wave front

Time interval = 0.000407 s

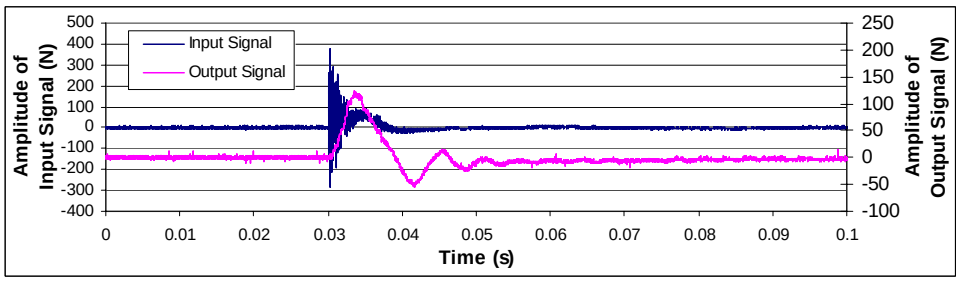


Complete view of the second impact wave

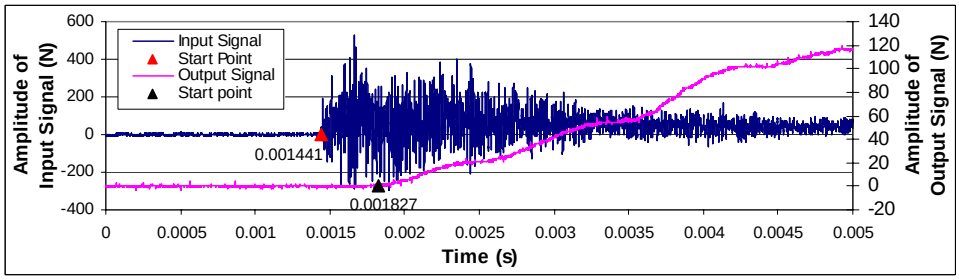


Enlarged view of the wave front

Time interval = 0.000386 s

Average time interval = 0.000396 s; Apparent wave speed = 596 m/s

38.1x1 Al alloy rings in vertical close packed arrangement with unconstrained sides

Height of the array = 0.210 m

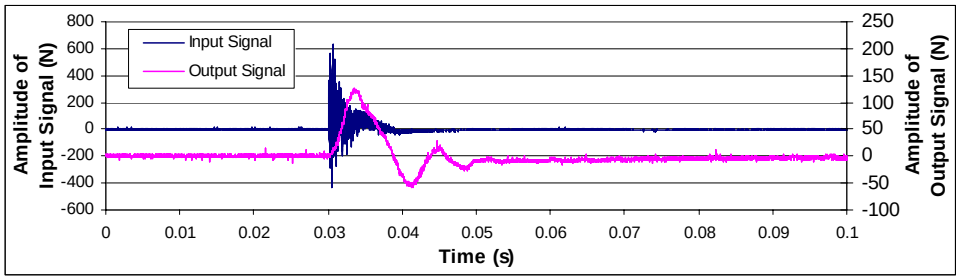


Complete view of the first impact wave

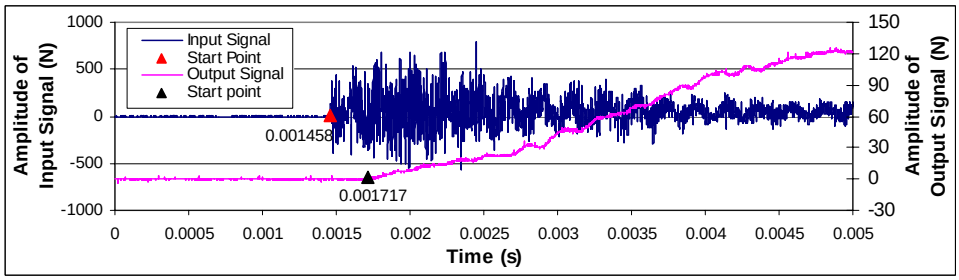


Enlarged view of the wave front

Time interval = 0.000259 s

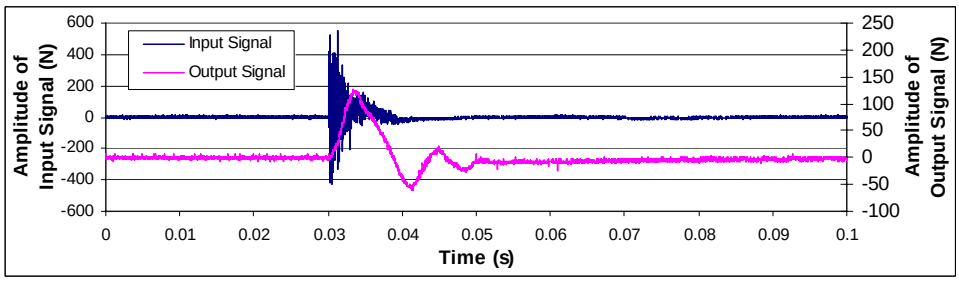


Complete view of the second impact wave

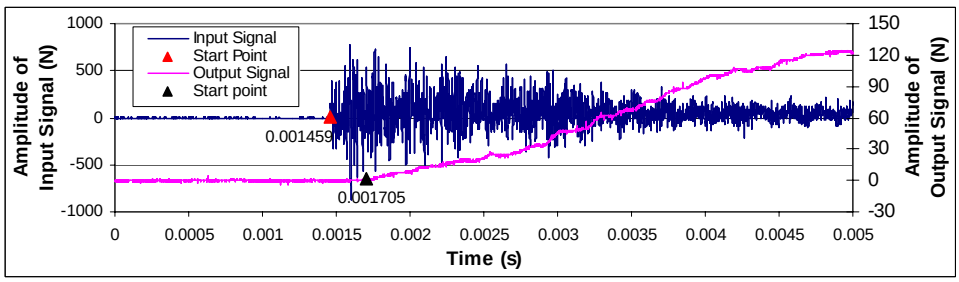


Enlarged view of the wave front

Time interval = 0.000246 s

Average time interval = 0.000253 s; Apparent wave speed = 830 m/s

38.1x3 Al alloy rings in square packed arrangement with unconstrained sides

Height of the array = 0.229 m

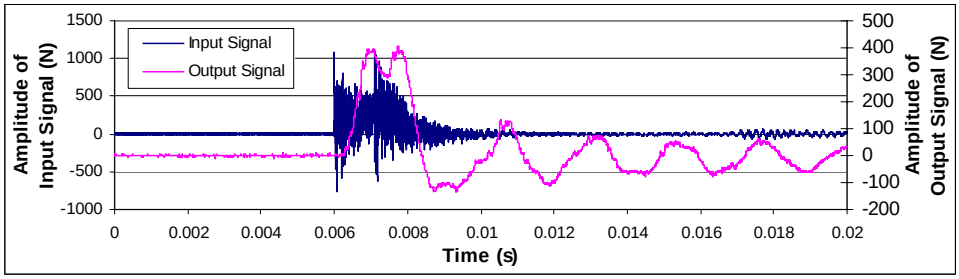


Complete view of the first impact wave

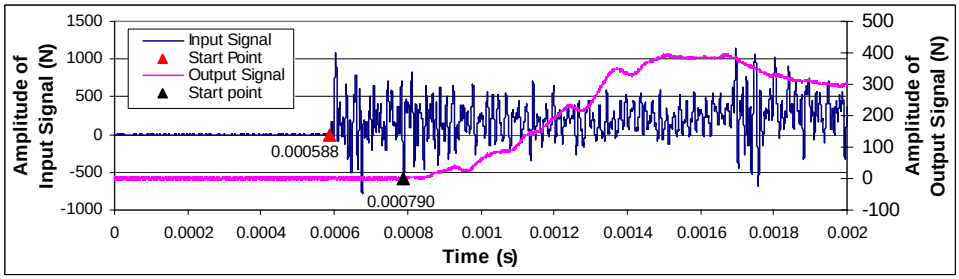


Enlarged view of the wave front

Time interval = 0.000202 s

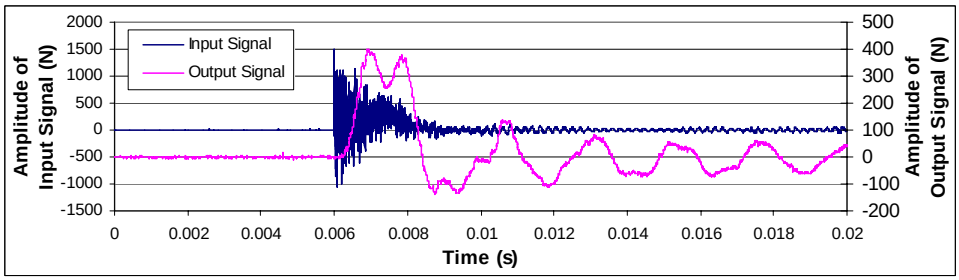


Complete view of the second impact wave

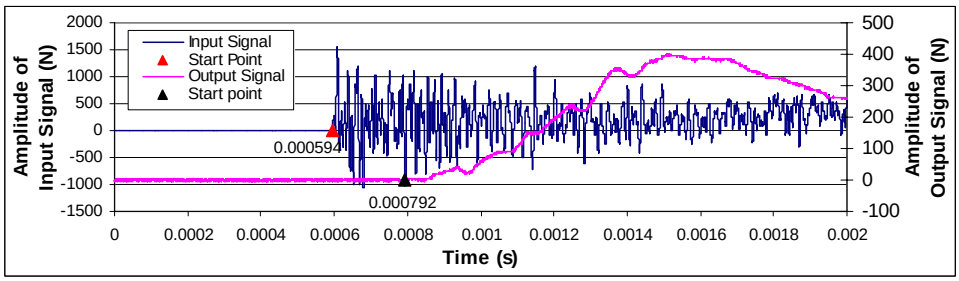


Enlarged view of the wave front

Time interval = 0.000198 s

Average time interval = 0.00020 s; Apparent wave speed = 1144 m/s

38.1x3 Al alloy rings in transverse close packed arrangement with unconstrained sides

Height of the array = 0.236 m

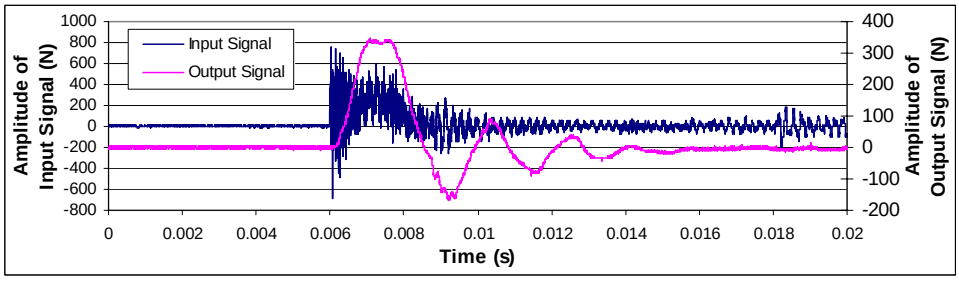


Complete view of the first impact wave

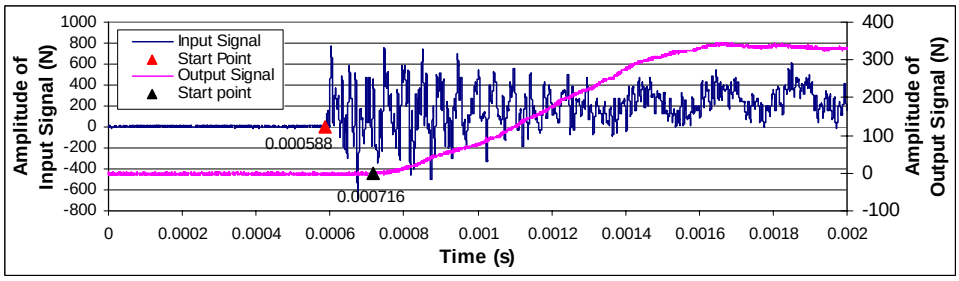


Enlarged view of the wave front

Time interval = 0.000128 s

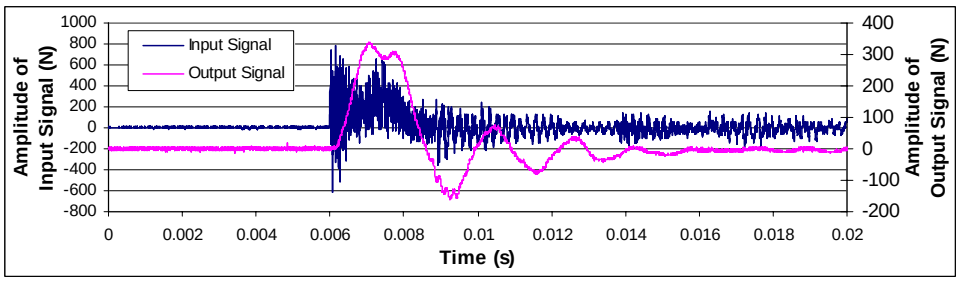


Complete view of the second impact wave

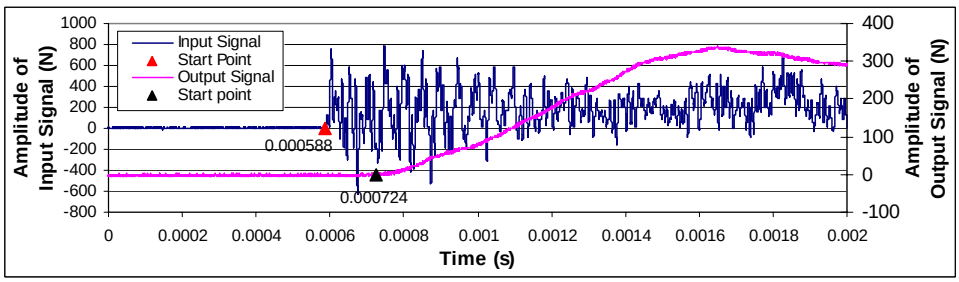


Enlarged view of the wave front

Time interval = 0.000136 s

Average time interval = 0.000132 s; Apparent wave speed = 1793 m/s

38.1x3 Al alloy rings in vertical close packed arrangement with unconstrained sides

Height of the array = 0.210 m

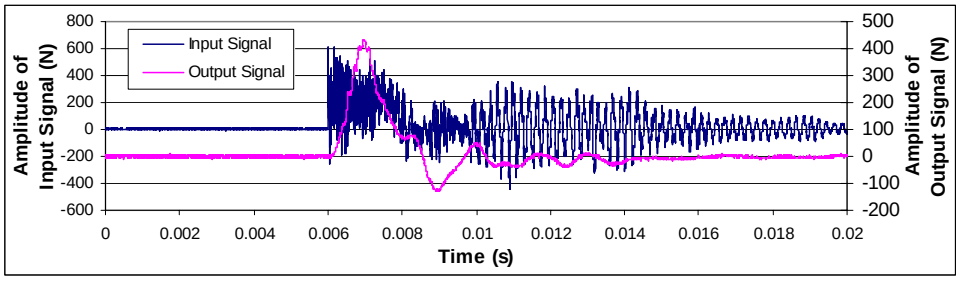


Complete view of the first impact wave

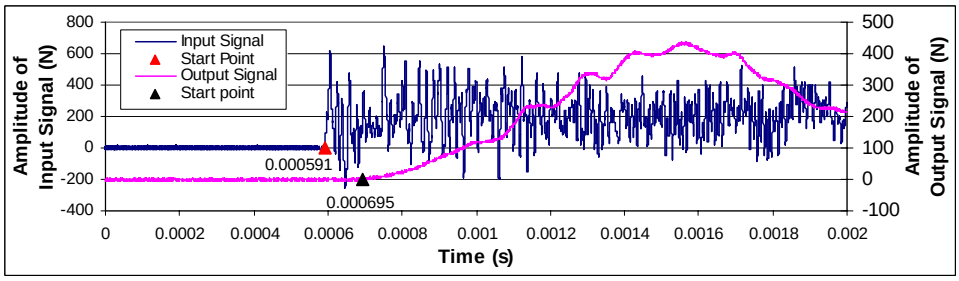


Enlarged view of the wave front

Time interval = 0.000104 s

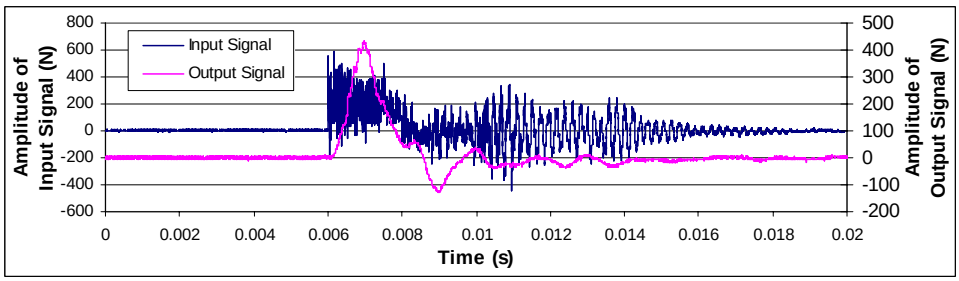


Complete view of the second impact wave

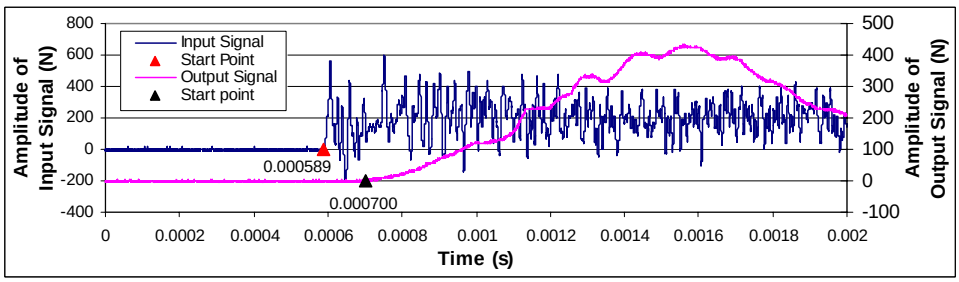


Enlarged view of the wave front

Time interval = 0.000111 s

Average time interval = 0.000108 s; Apparent wave speed = 1946 m/s

25.4x1 Brass rings in square packed arrangement with unconstrained sides

Height of the array = 0.152 m

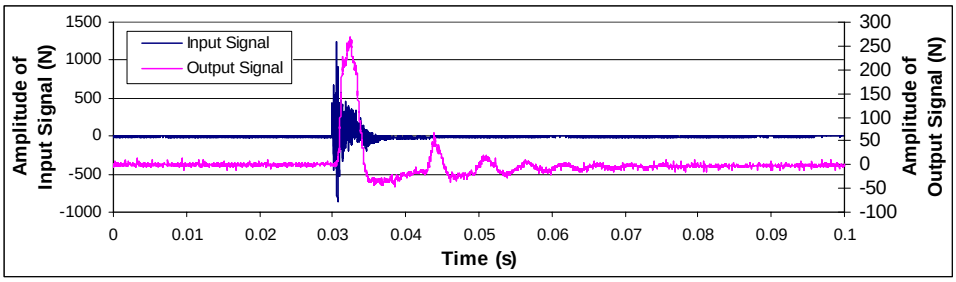


Complete view of the first impact wave

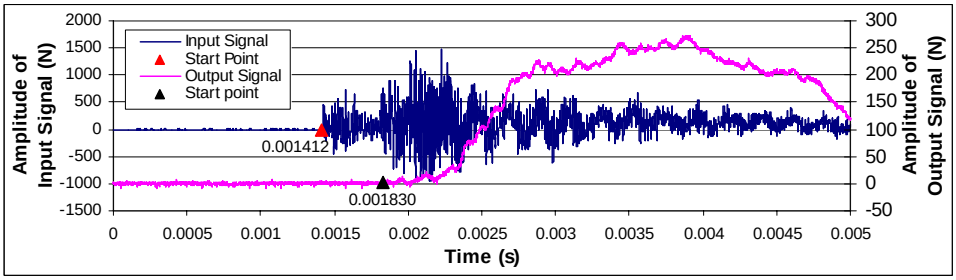


Enlarged view of the wave front

Time interval = 0.000418 s

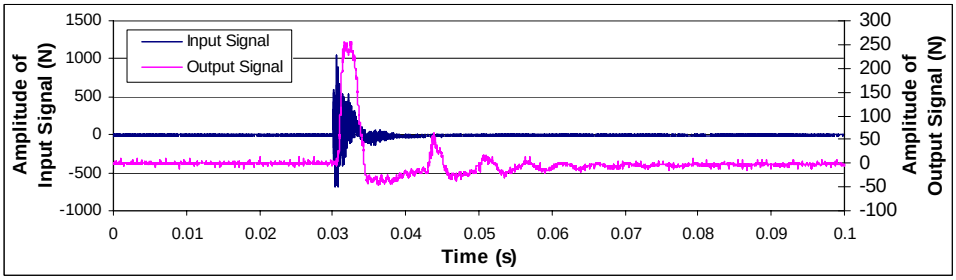


Complete view of the second impact wave

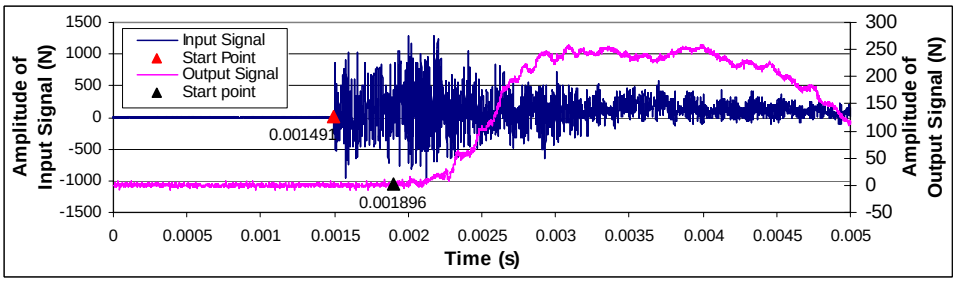


Enlarged view of the wave front

Time interval = 0.000405 s

Average time interval = 0.000411 s; Apparent wave speed = 371 m/s

25.4x1 Brass rings in transverse close packed arrangement with unconstrained sides

Height of the array = 0.157 m

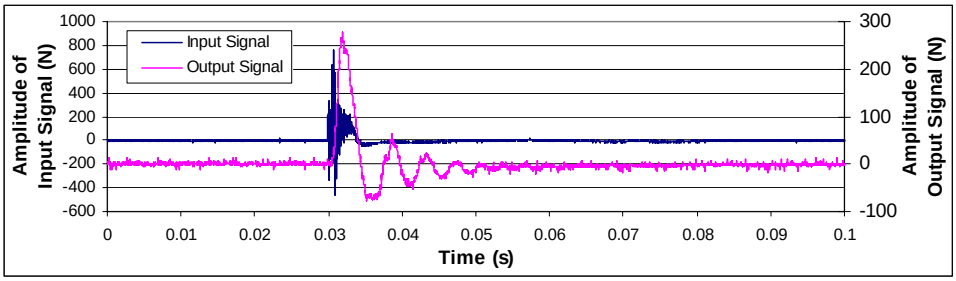


Complete view of the first impact wave

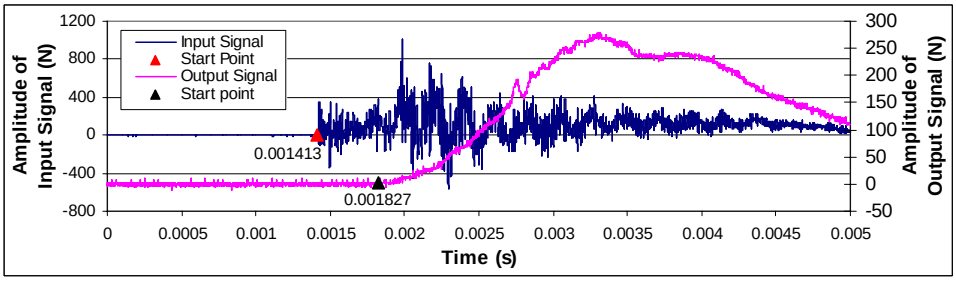


Enlarged view of the wave front

Time interval = 0.000414 s

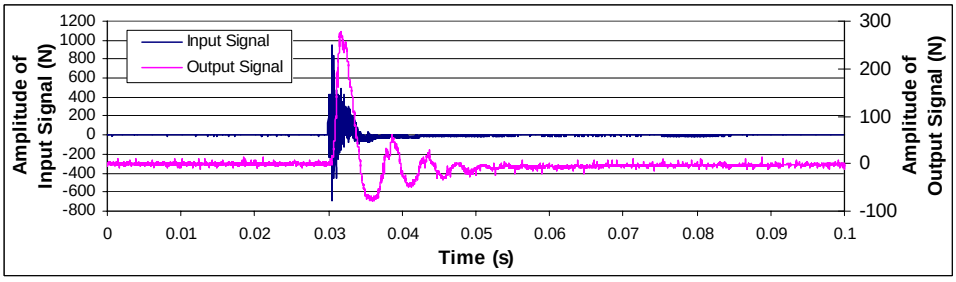


Complete view of the second impact wave

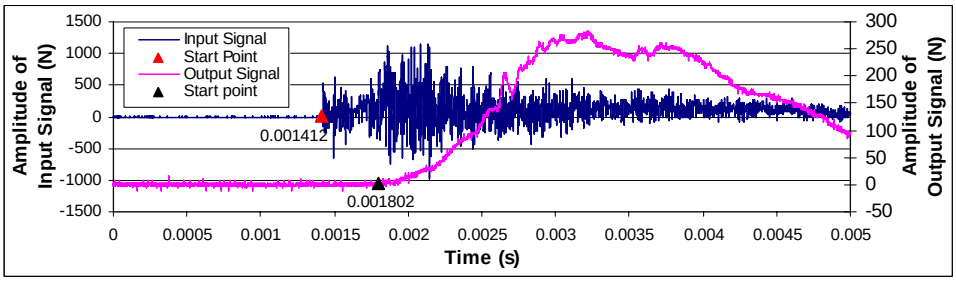


Enlarged view of the wave front

Time interval = 0.000390 s

Average time interval = 0.000402 s; Apparent wave speed = 392 m/s

25.4x1 Brass rings in vertical close packed arrangement with unconstrained sides

Height of the array = 0.152 m

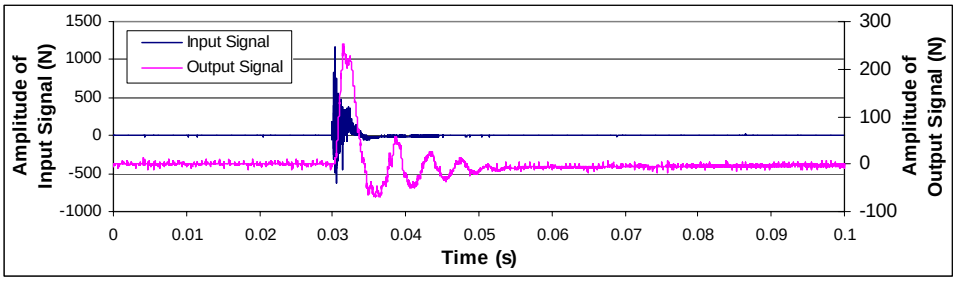


Complete view of the first impact wave

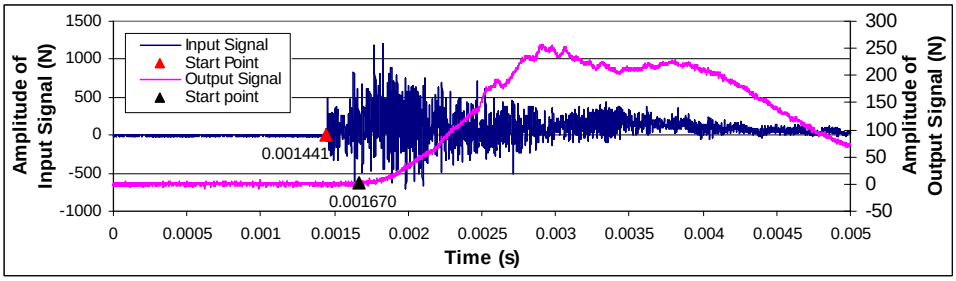


Enlarged view of the wave front

Time interval = 0.000229 s

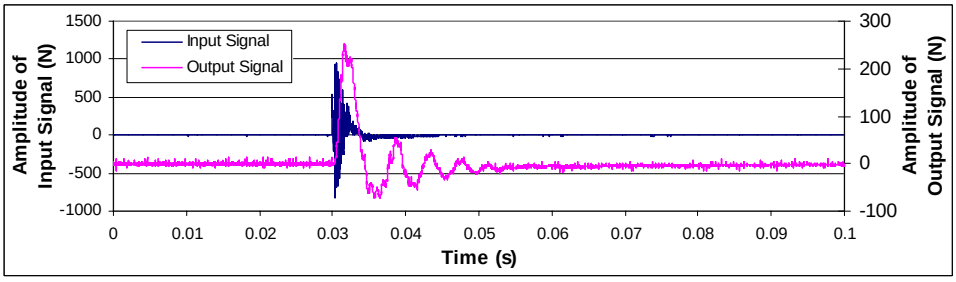


Complete view of the second impact wave

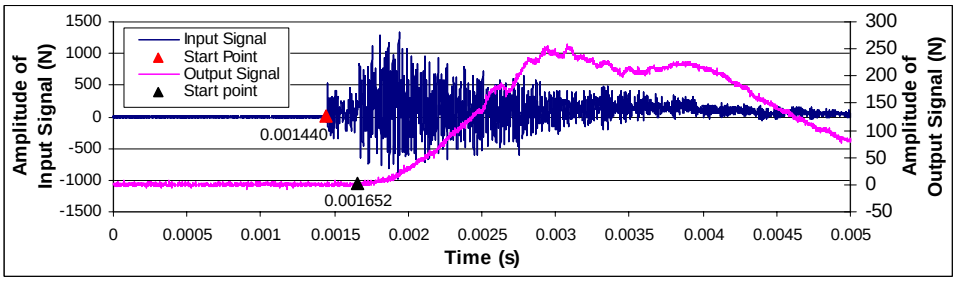


Enlarged view of the wave front

Time interval = 0.000213 s

Average time interval = 0.000221 s; Apparent wave speed = 691 m/s

38.1x1 Brass rings in square packed arrangement with constrained sides

Height of the array = 0.229 m

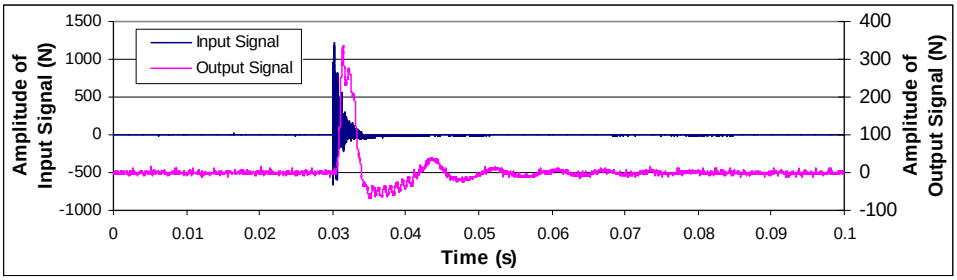


Complete view of the first impact wave

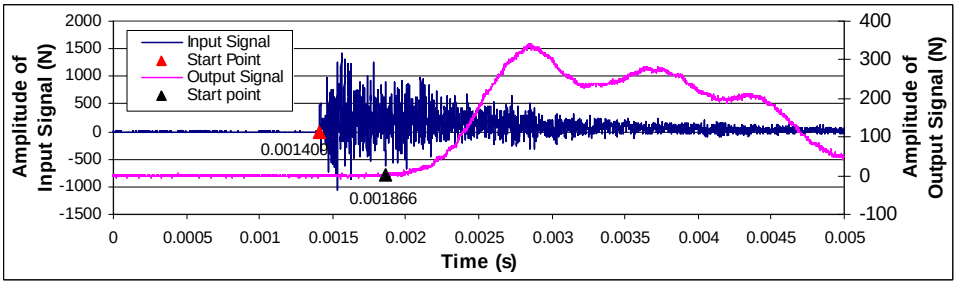


Enlarged view of the wave front

Time interval = 0.000457 s

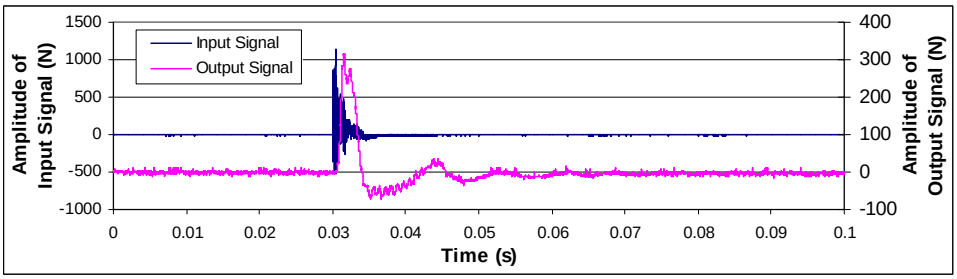


Complete view of the second impact wave

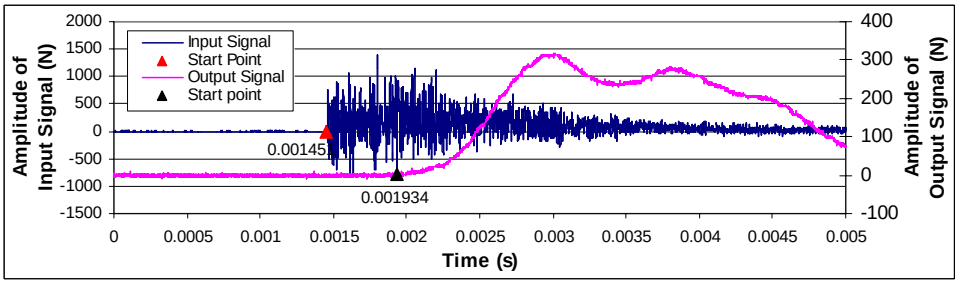


Enlarged view of the wave front

Time interval = 0.000483 s

Average time interval = 0.00047 s; Apparent wave speed = 487 m/s

38.1x1 Brass rings in transverse close packed arrangement with constrained sides

Height of the array = 0.236 m

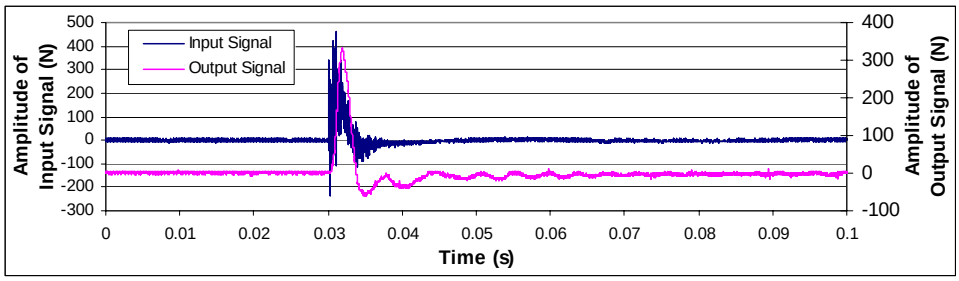


Complete view of the first impact wave

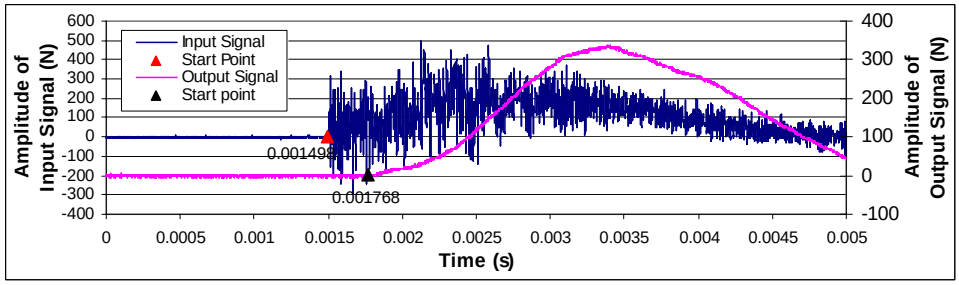


Enlarged view of the wave front

Time interval = 0.00027 s

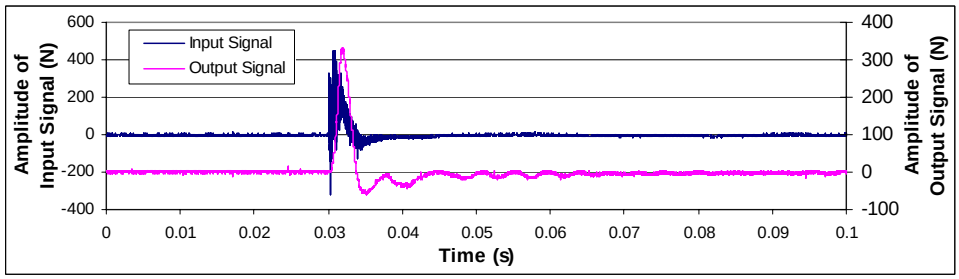


Complete view of the second impact wave

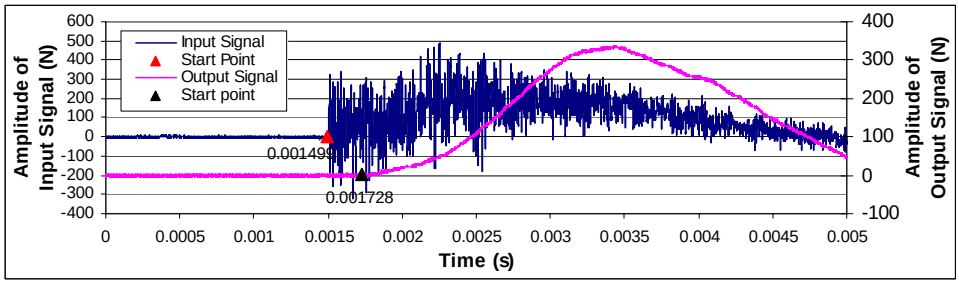


Enlarged view of the wave front

Time interval = 0.00023 s

Average time interval = 0.00025 s; Apparent wave speed = 946 m/s

38.1x1 Brass rings in vertical close packed arrangement with constrained sides

Height of the array = 0.210 m

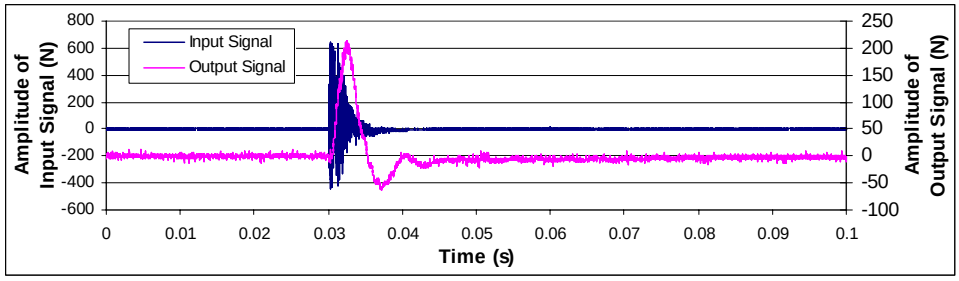


Complete view of the first impact wave

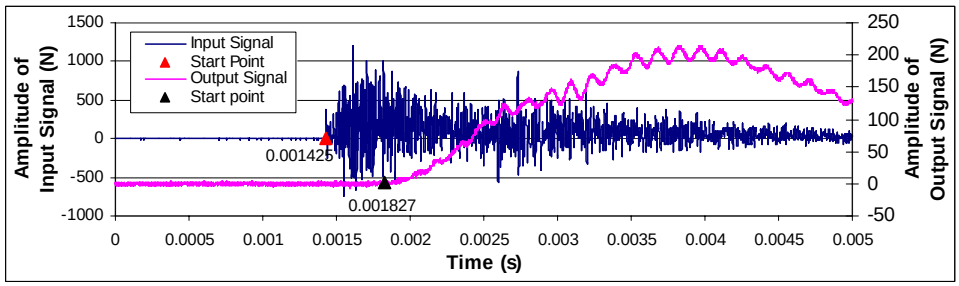


Enlarged view of the wave front

Time interval = 0.000402 s

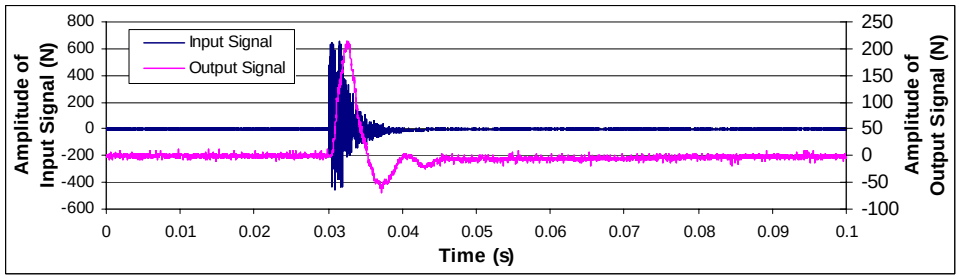


Complete view of the second impact wave

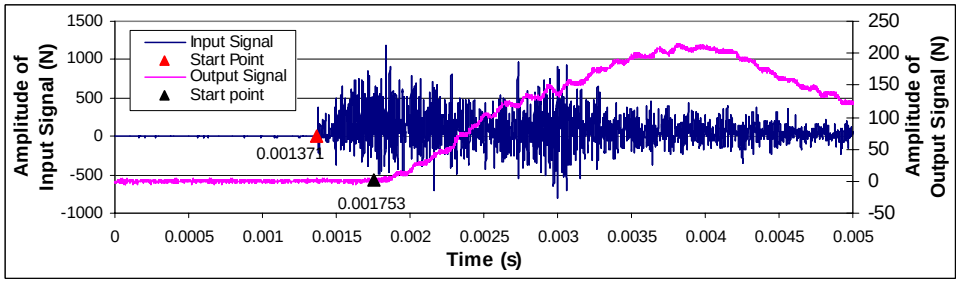


Enlarged view of the wave front

Time interval = 0.000382 s

Average time interval = 0.000392 s; Apparent wave speed = 535 m/s

38.1x1 Al alloy rings in square packed arrangement with constrained sides

Height of the array = 0.229 m

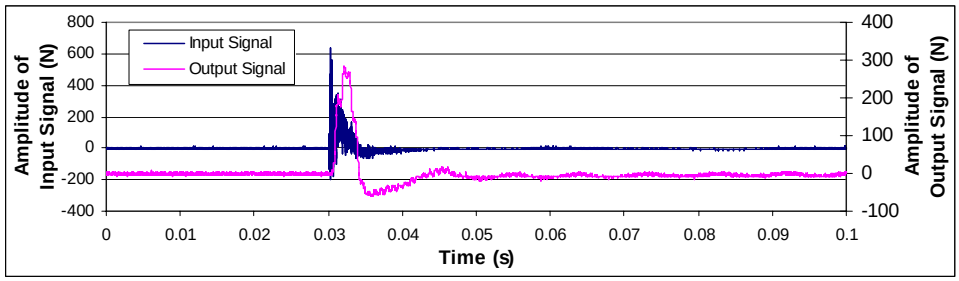


Complete view of the first impact wave

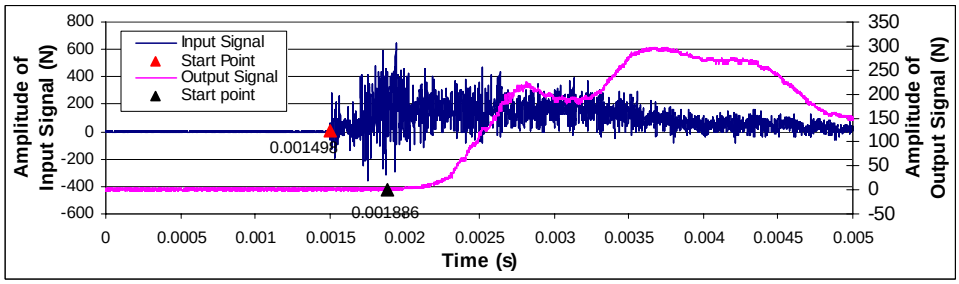


Enlarged view of the wave front

Time interval = 0.000388 s

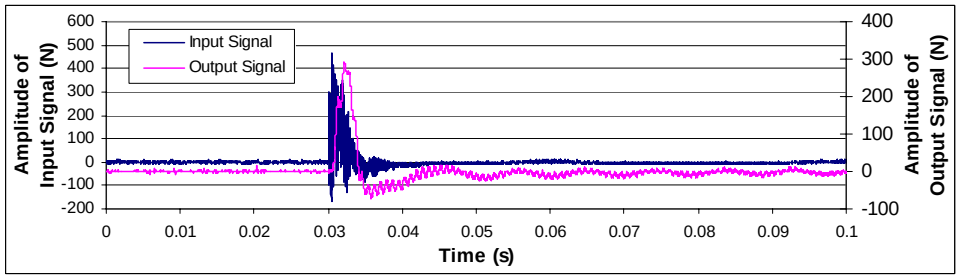


Complete view of the second impact wave

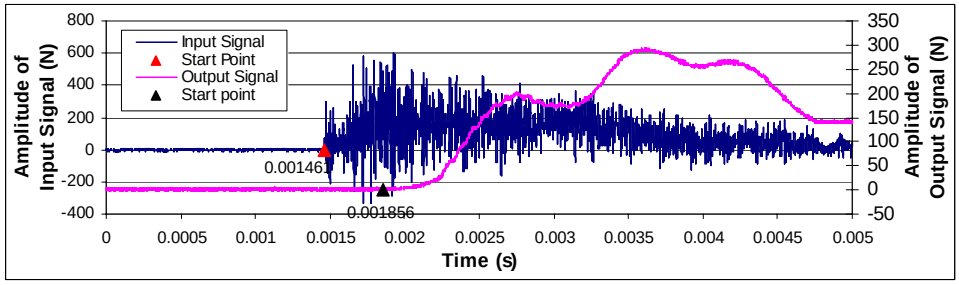


Enlarged view of the wave front

Time interval = 0.000396 s

Average time interval = 0.000392 s; Apparent wave speed = 584 m/s

38.1x1 Al alloy rings in transverse close packed arrangement with constrained sides

Height of the array = 0.236 m

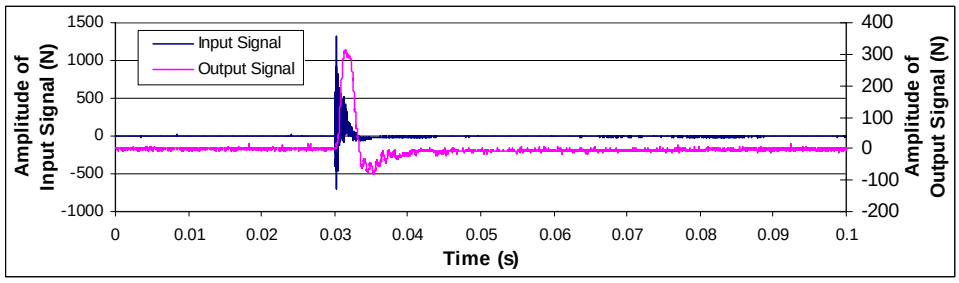


Complete view of the first impact wave

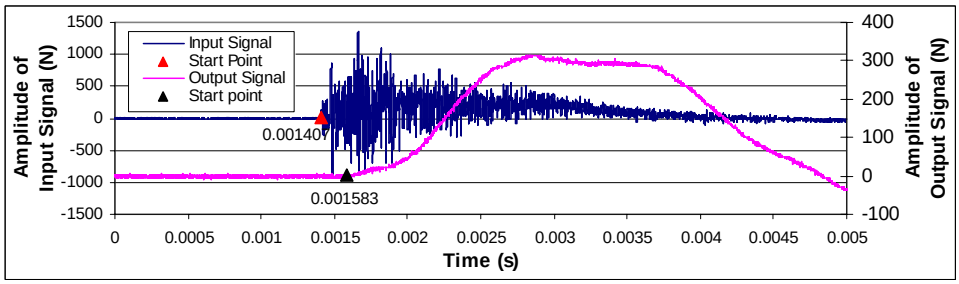


Enlarged view of the wave front

Time interval = 0.000176 s

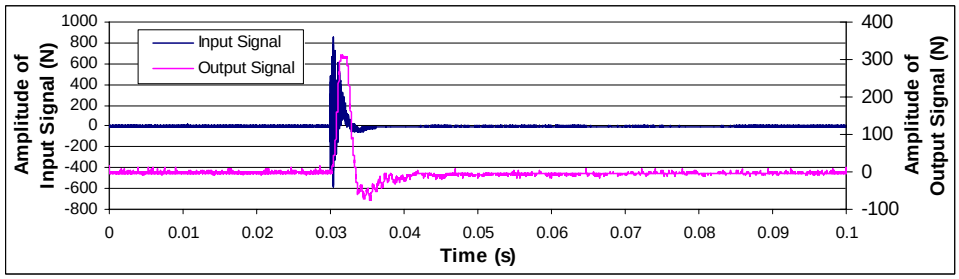


Complete view of the second impact wave

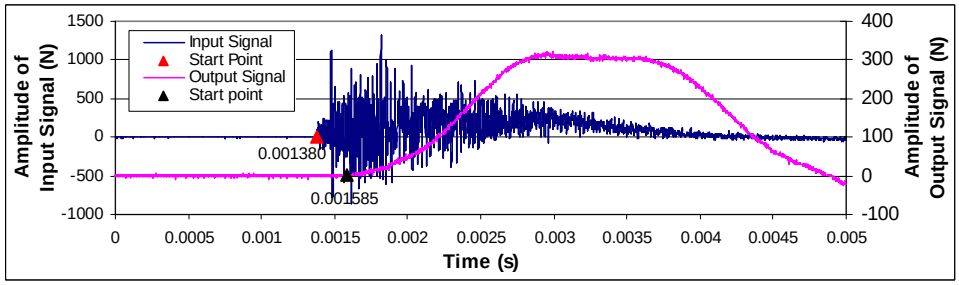


Enlarged view of the wave front

Time interval = 0.000205 s

Average time interval = 0.00019 s; Apparent wave speed = 1241 m/s

38.1x1 Al alloy rings in vertical close packed arrangement with constrained sides

Height of the array = 0.210 m

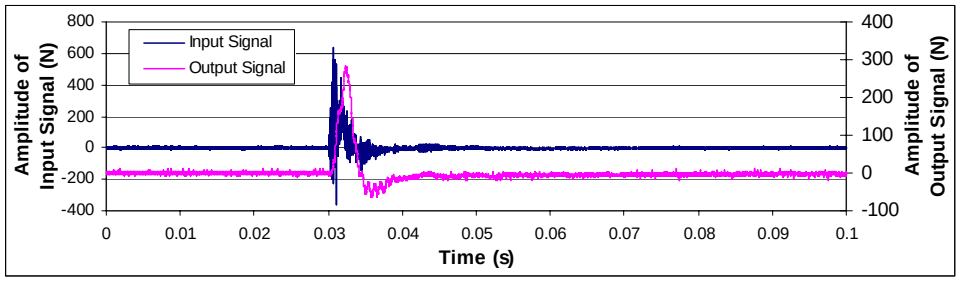


Complete view of the first impact wave

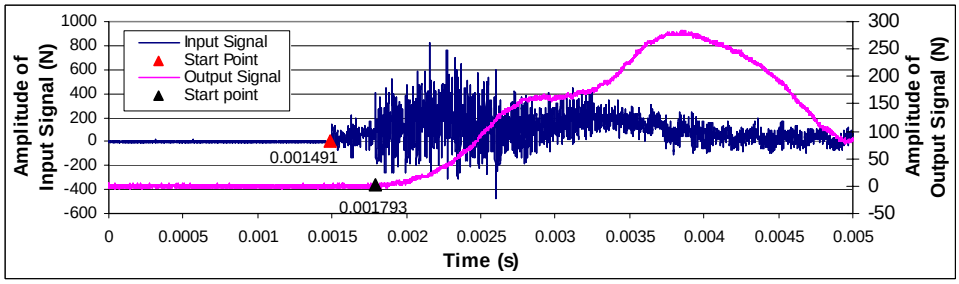


Enlarged view of the wave front

Time interval = 0.000302 s

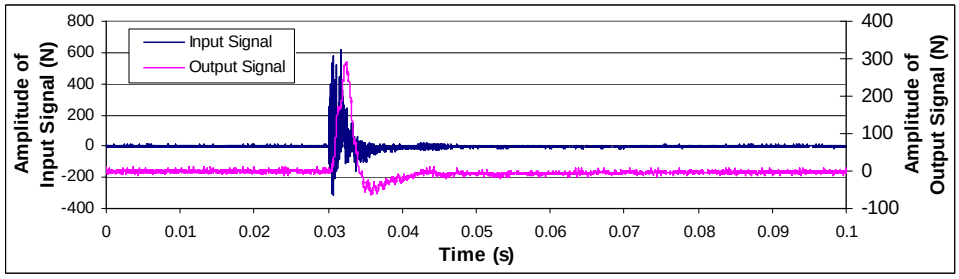


Complete view of the second impact wave

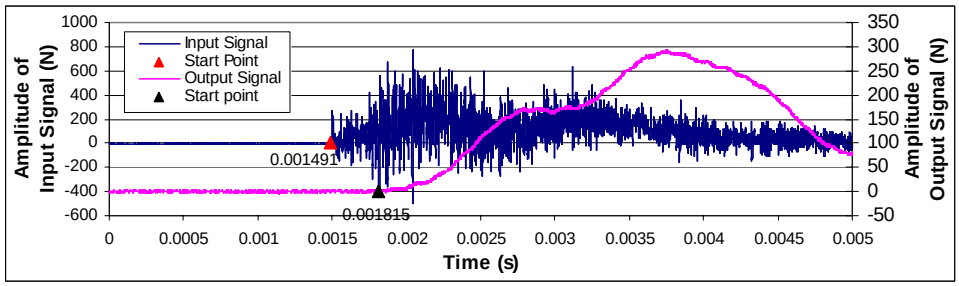


Enlarged view of the wave front

Time interval = 0.000324 s

Average time interval = 0.000313 s; Apparent wave speed = 669 m/s

**Appendix M** Stress-strain Curves from Compression Tests on Ring Arrays

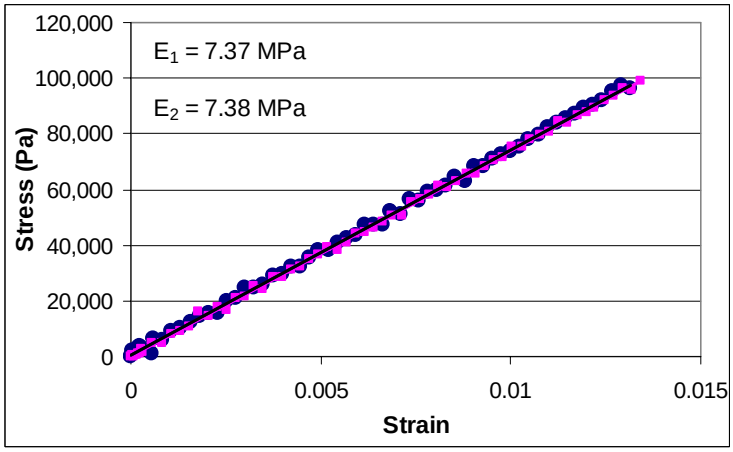


38.1x1 Al alloy rings
in square packed arrangements with unconstrained sides
[Average apparent elastic modulus *E=7.38 MPa*]

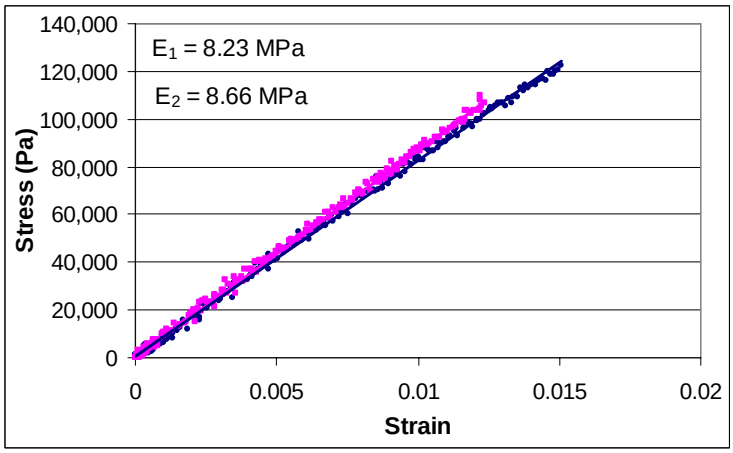


38.1x1 Al alloy rings
in transverse close packed arrangements with unconstrained sides
[Average apparent elastic modulus *E=8.46 MPa*]

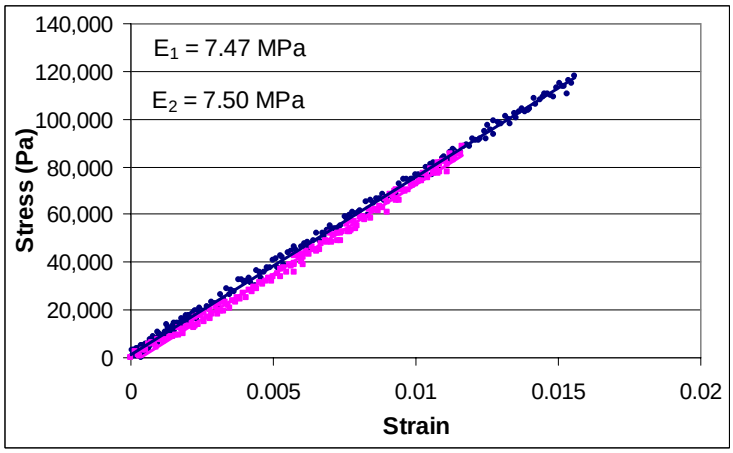


38.1x1 Al alloy rings
in vertical close packed arrangements with unconstrained sides
[Average apparent elastic modulus *E=7.48 MPa*]

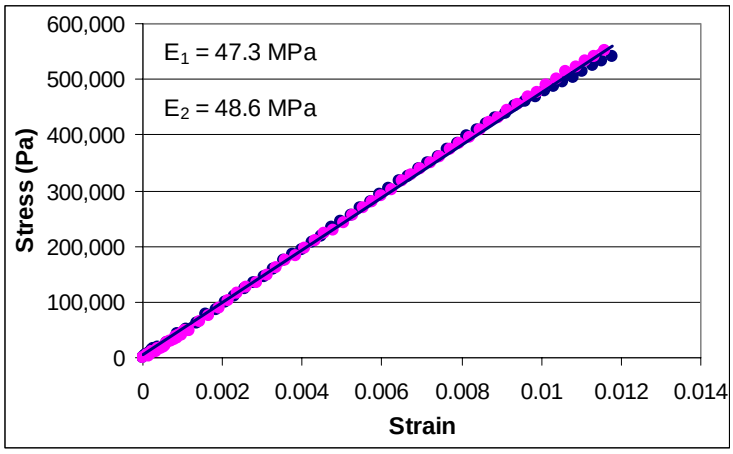


38.1x1 Al alloy rings
in square packed arrangements with constrained sides
[Average apparent elastic modulus *E=47.93 MPa*]

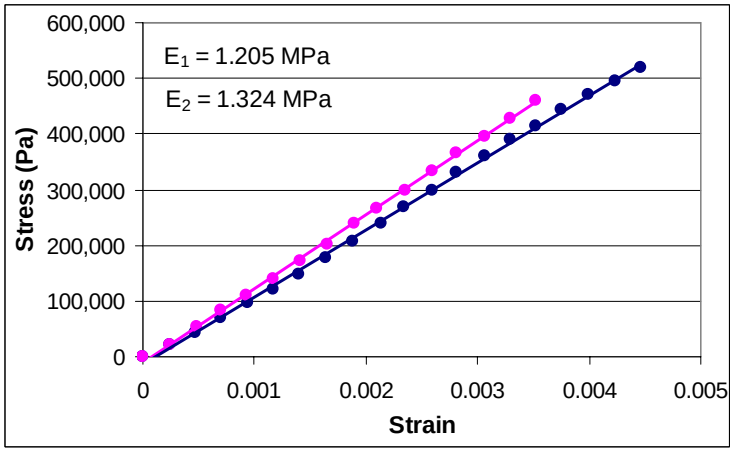


38.1x1 Al alloy rings
in transverse close packed arrangements with constrained sides
[Average apparent elastic modulus *E=126.50 MPa*]

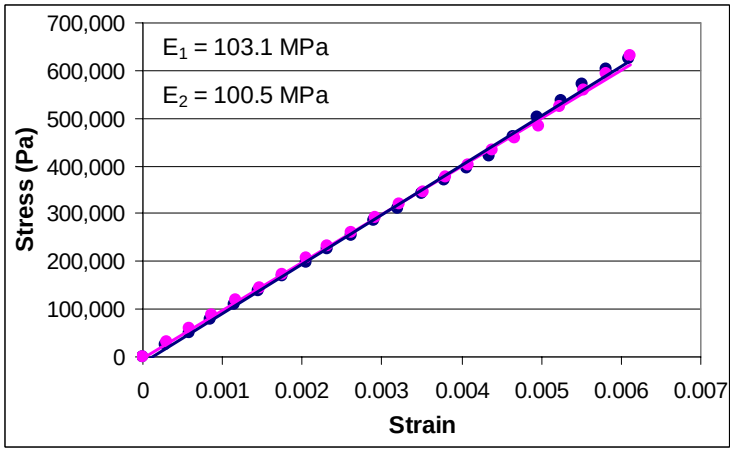


38.1x1 Al alloy rings
in vertical close packed arrangements with constrained sides
[Average apparent elastic modulus *E=101.80 MPa*]

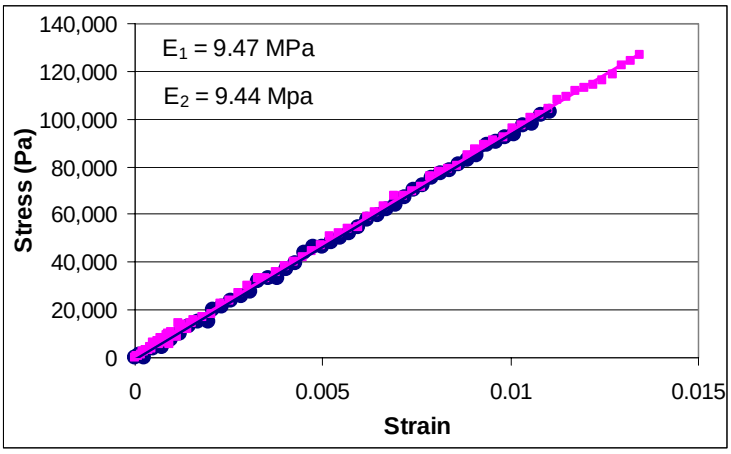


38.1x1 Brass rings
in square packed arrangements with unconstrained sides
[Average apparent elastic modulus *E=9.45 MPa*]

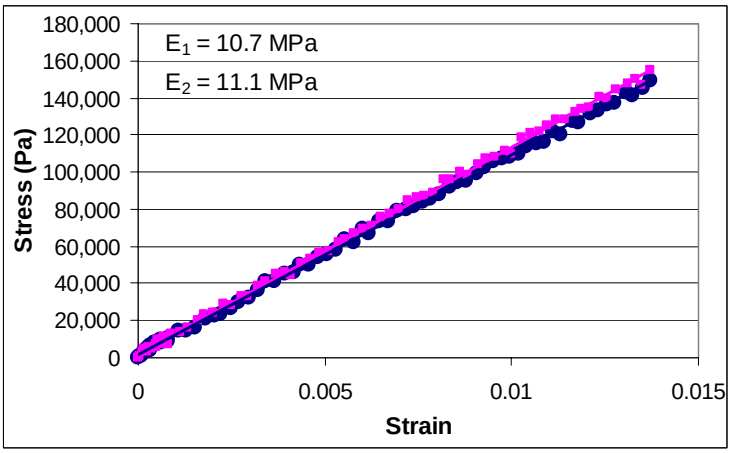


38.1x1 Brass rings
in transverse close packed arrangements with unconstrained sides
[Average apparent elastic modulus *E=10.95 MPa*]

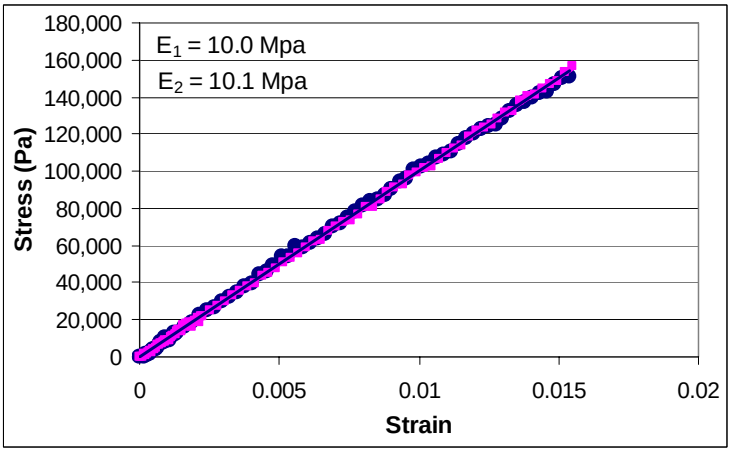


38.1x1 Brass rings
in vertical close packed arrangements with unconstrained sides
[Average apparent elastic modulus *E=10.04 MPa*]

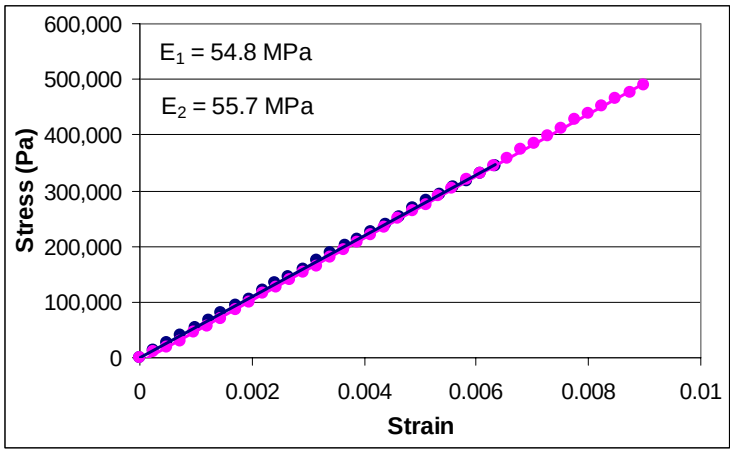


38.1x1 Brass rings
in square packed arrangements with constrained sides
[Average apparent elastic modulus *E=55.27 MPa*]

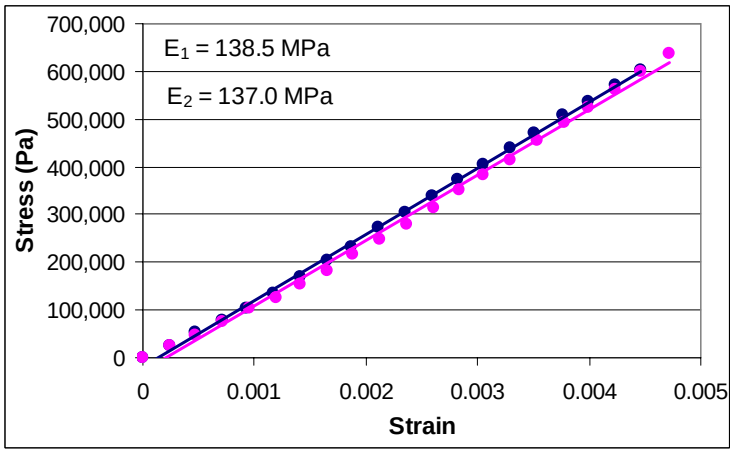


38.1x1 Brass rings
in transverse close packed arrangements with constrained sides
[Average apparent elastic modulus *E=137.75 MPa*]

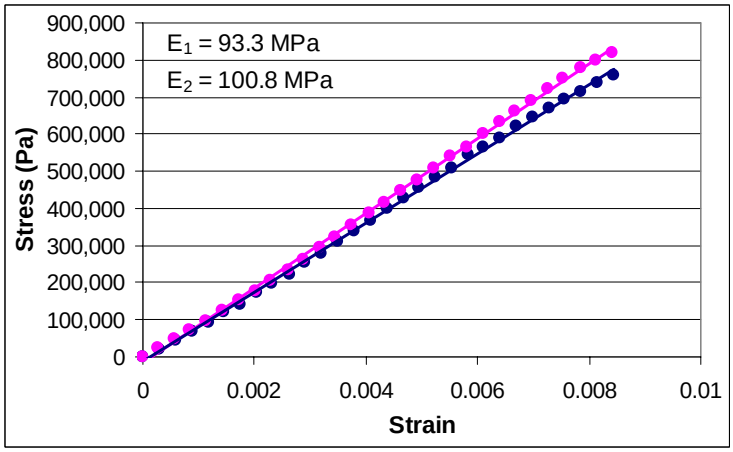


38.1x1 Brass rings
in vertical close packed arrangements with constrained sides
[Average apparent elastic modulus *E=97.03 MPa*]

**Appendix N** Results of Discrete Fourier Transformation of Impact Signals

38.1x1 Brass rings in square packed arrangement with unconstrained sides

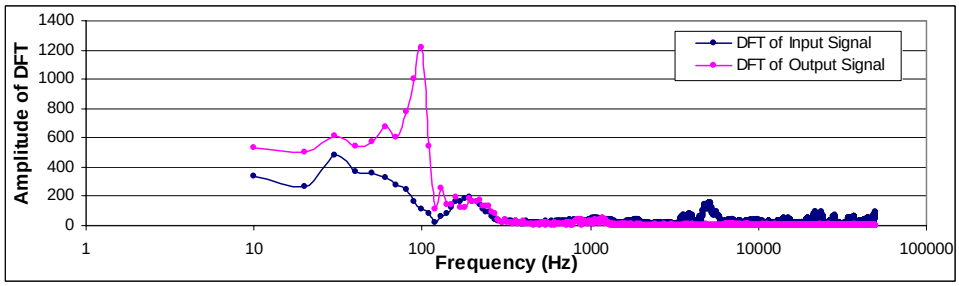


DFT of the complete wave

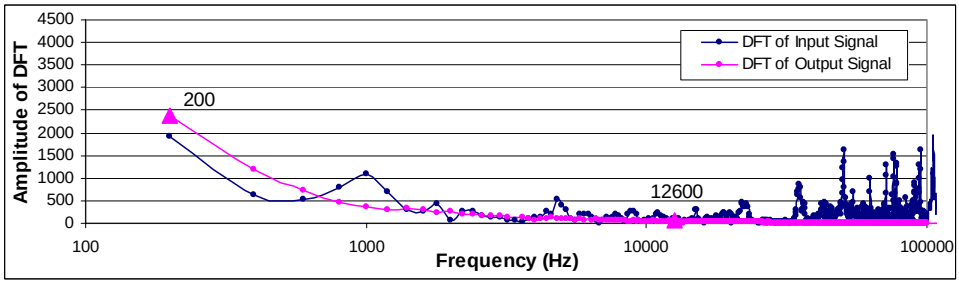


DFT of the wave front

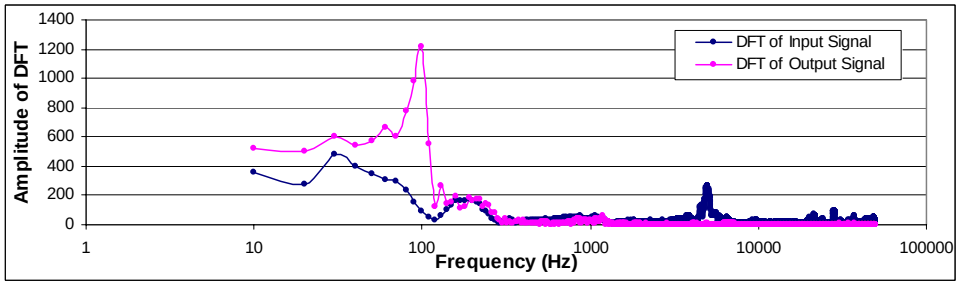


DFT of the complete wave

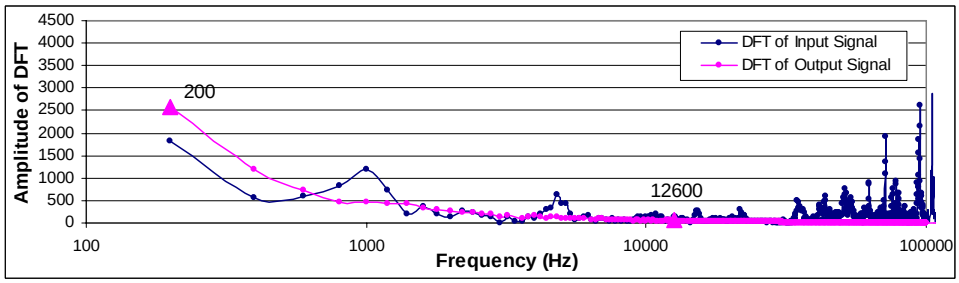


DFT of the wave front

Selected frequency components are 200 Hz and 12600 Hz

38.1x1 Brass rings in transverse close packed arrangement with unconstrained sides

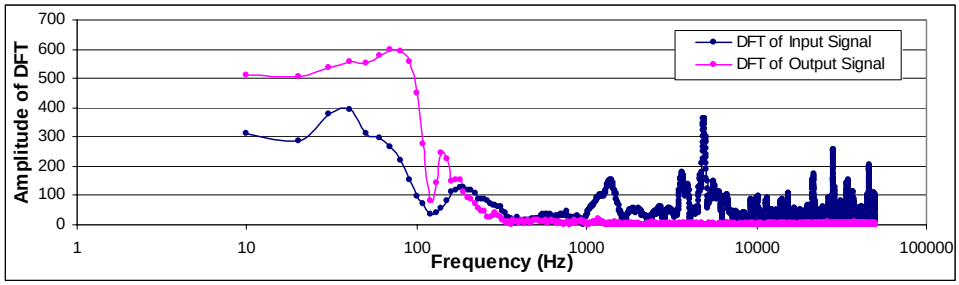


DFT of the complete wave

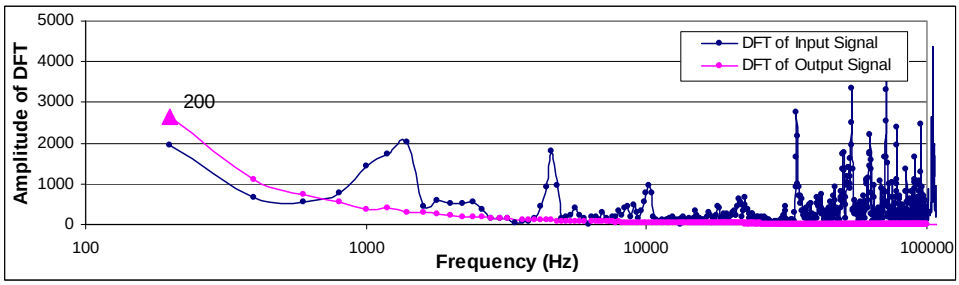


DFT of the wave front

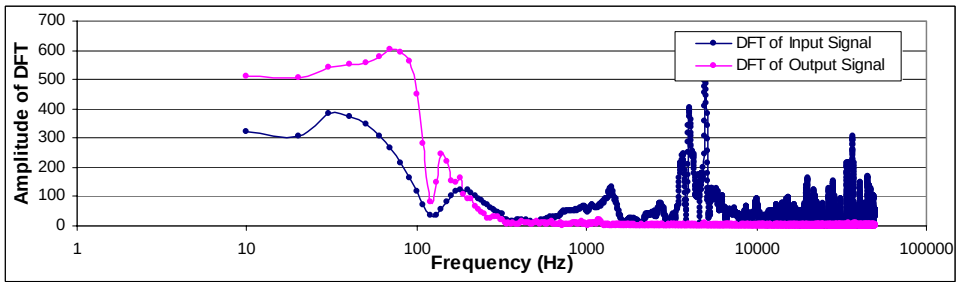


DFT of the complete wave

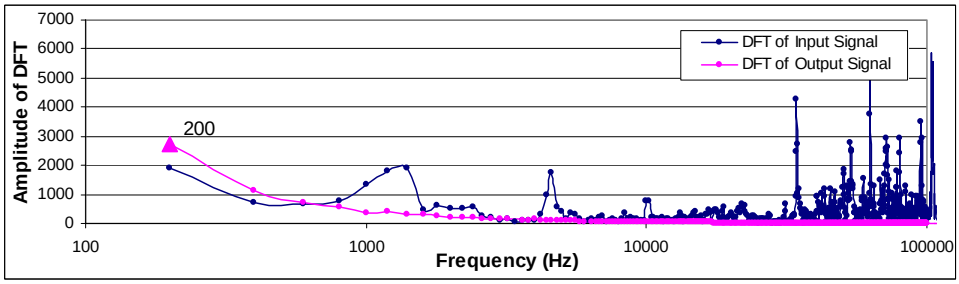


DFT of the wave front

Selected frequency component is 200 Hz

38.1x1 Brass rings in vertical close packed arrangement with unconstrained sides

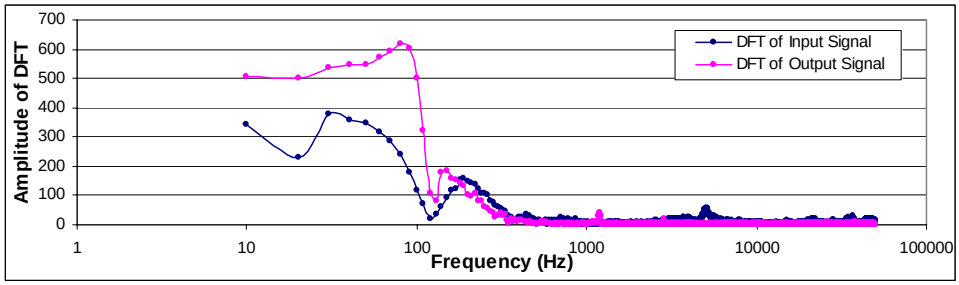


DFT of the complete wave

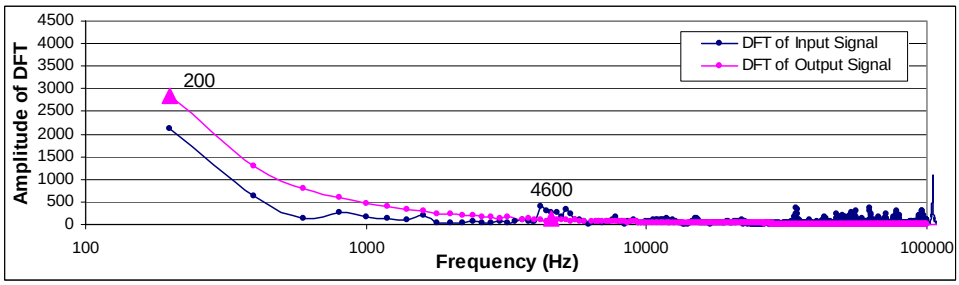


DFT of the wave front

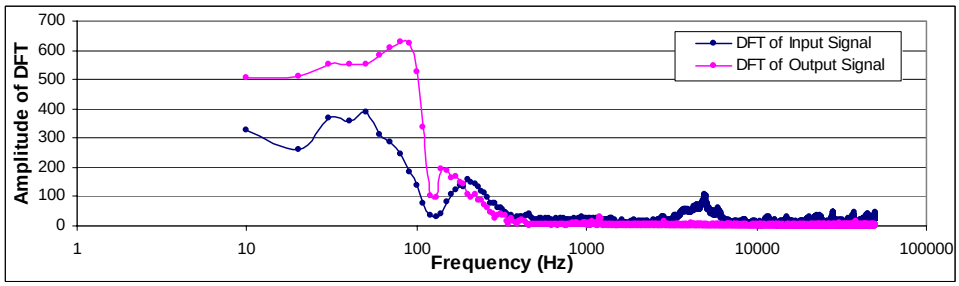


DFT of the complete wave

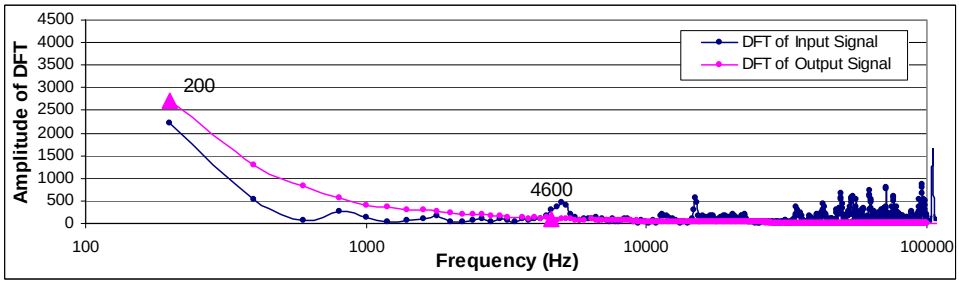


DFT of the wave front

Selected frequency components are 200 Hz and 4600 Hz

38.1x3 Brass rings in square packed arrangement with unconstrained sides

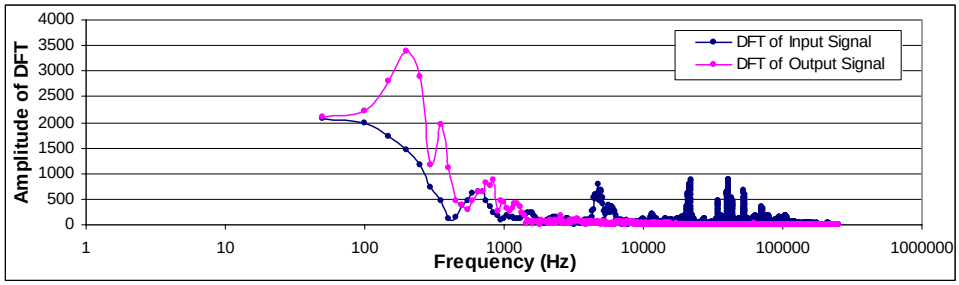


DFT of the complete wave

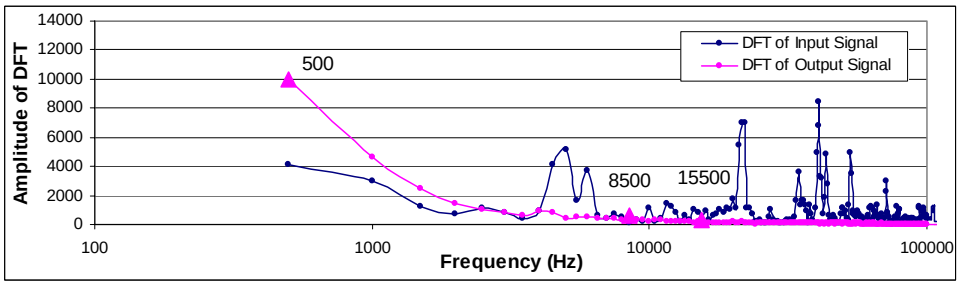


DFT of the wave front

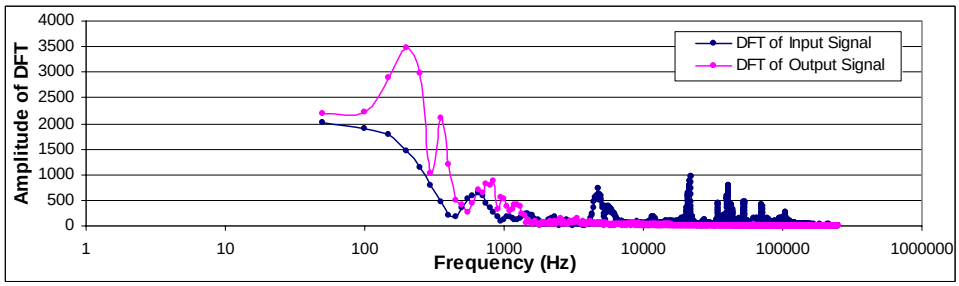


DFT of the complete wave

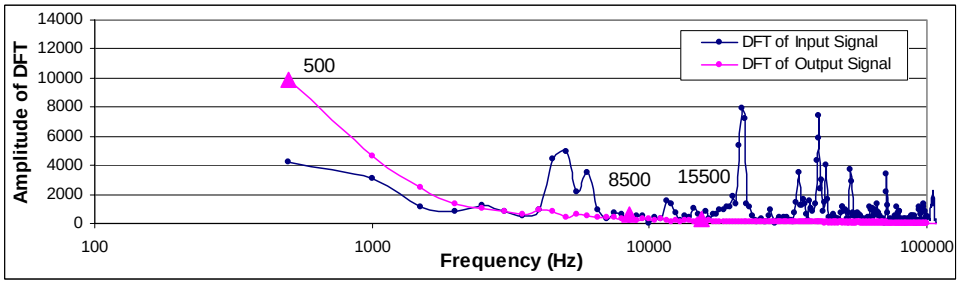


DFT of the wave front

Selected frequency components are 500 Hz, 8500 Hz and 15500 Hz.

38.1x3 Brass rings in transverse close packed arrangement with unconstrained sides

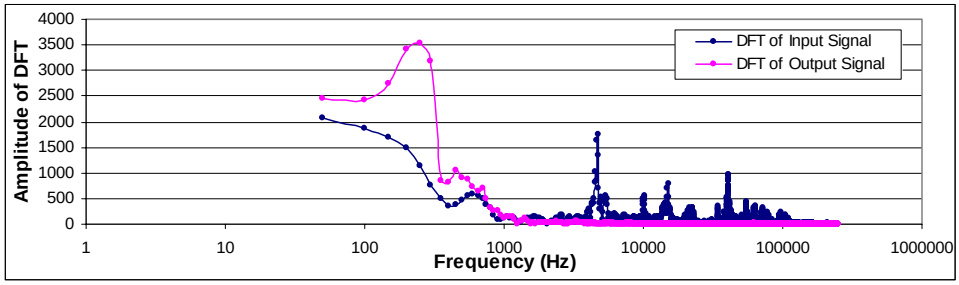


DFT of the complete wave

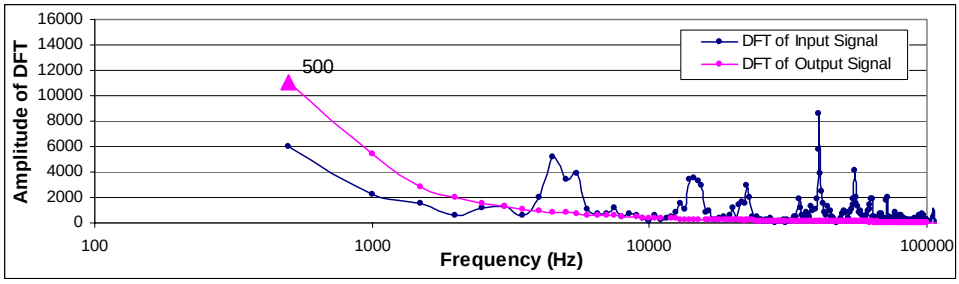


DFT of the wave front

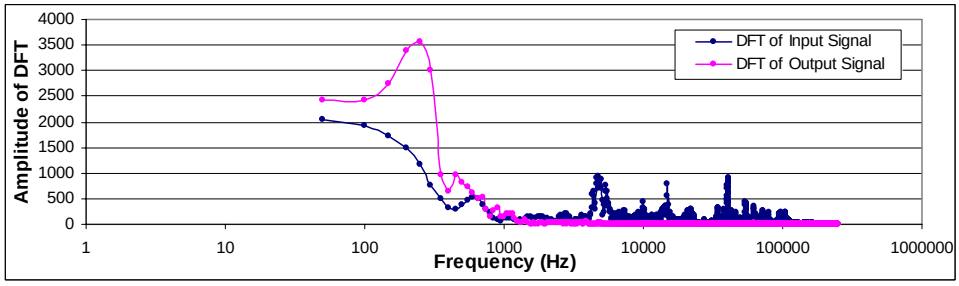


DFT of the complete wave

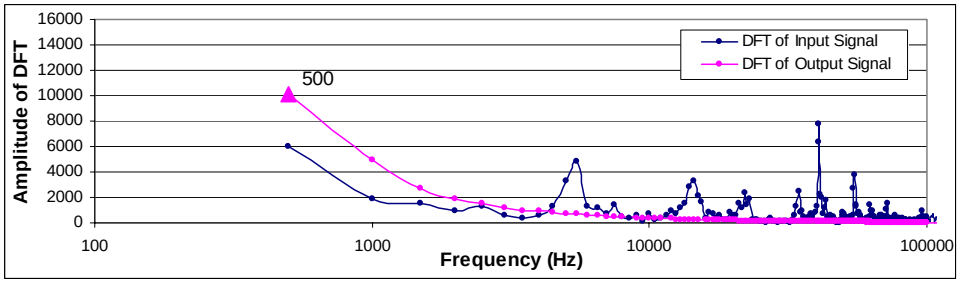


DFT of the wave front

Selected frequency component is 500 Hz.

38.1x3 Brass rings in vertical close packed arrangement with unconstrained sides

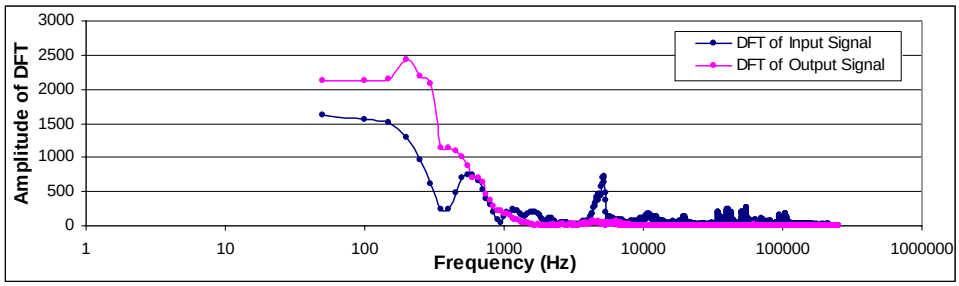


DFT of the complete wave

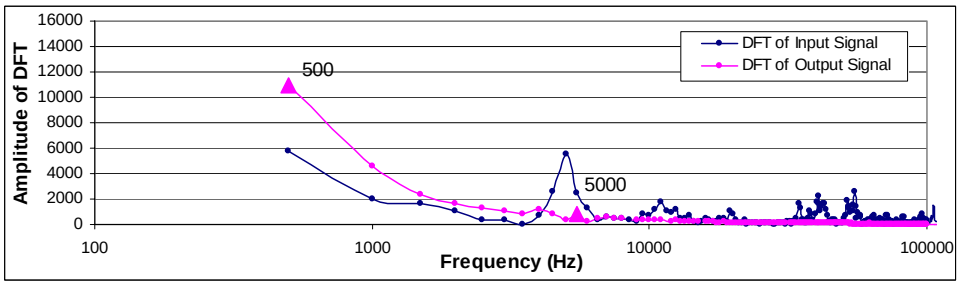


DFT of the wave front

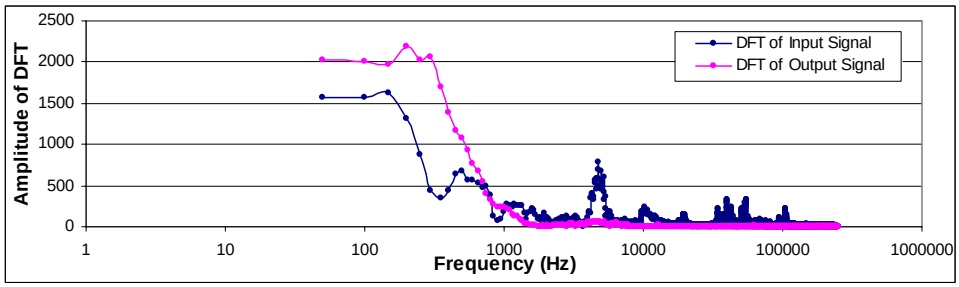


DFT of the complete wave

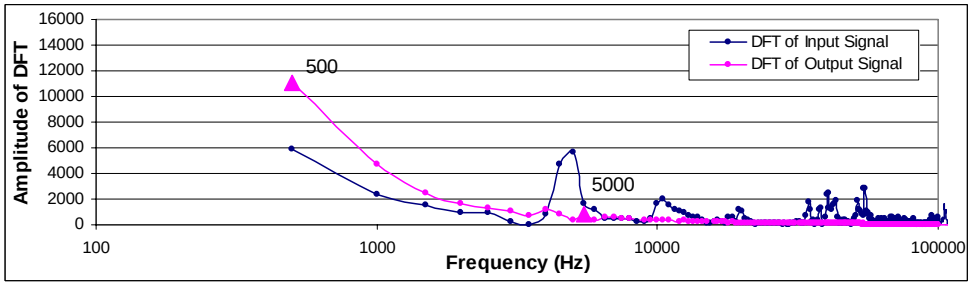


DFT of the wave front

Selected frequency components are 500 Hz and 5000 Hz

38.1x1 Al alloy rings in square packed arrangement with unconstrained sides

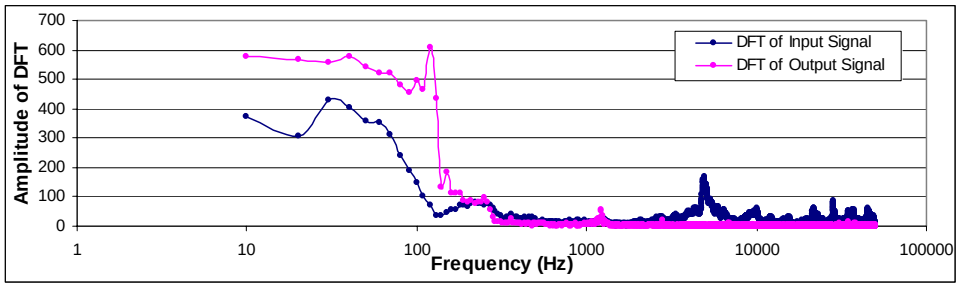


DFT of the complete wave

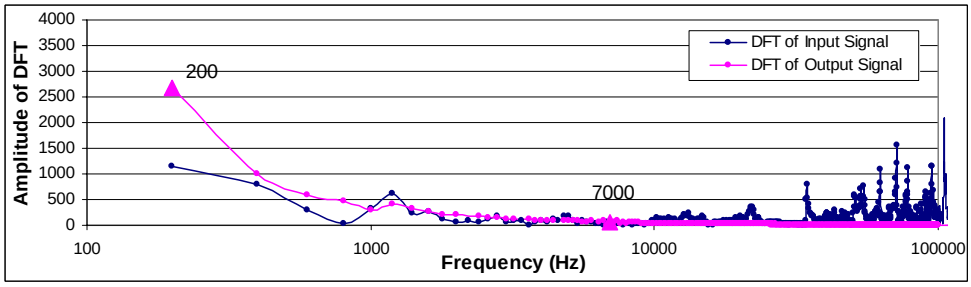


DFT of the wave front

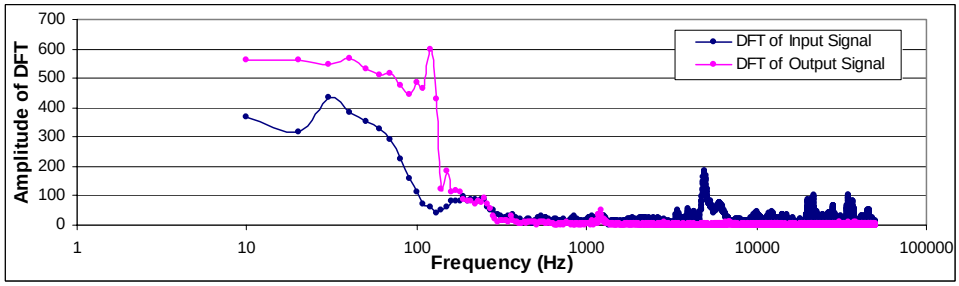


DFT of the complete wave

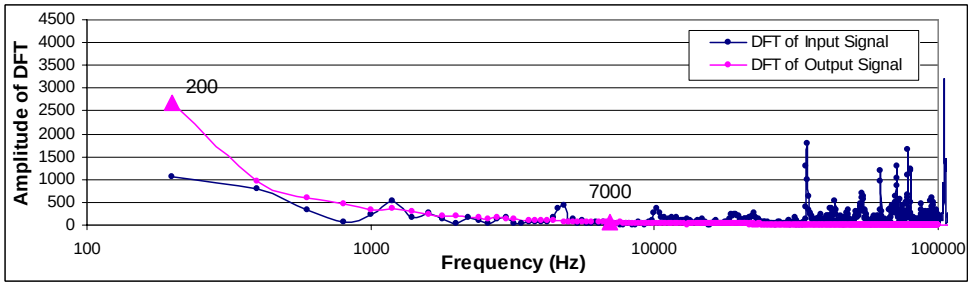


DFT of the wave front

Selected frequency components are 200 Hz and 7000 Hz

38.1x1 Al alloy rings in transverse close packed arrangement with unconstrained sides

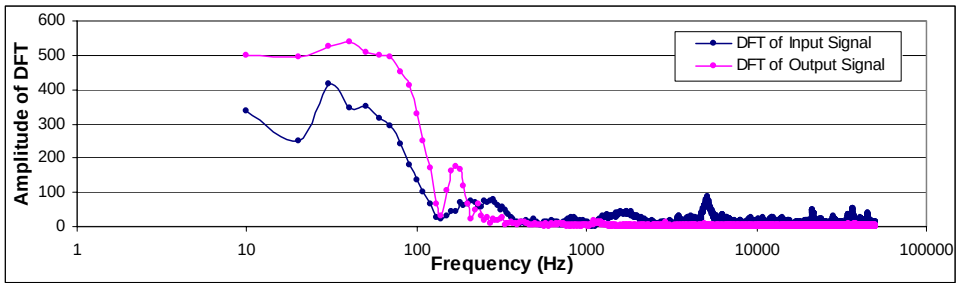


DFT of the complete wave

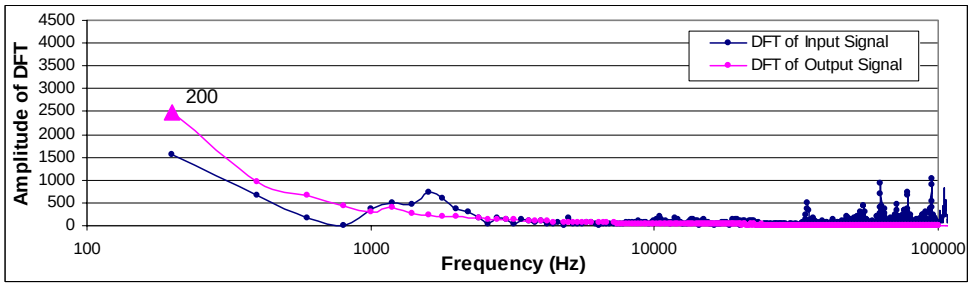


DFT of the wave front

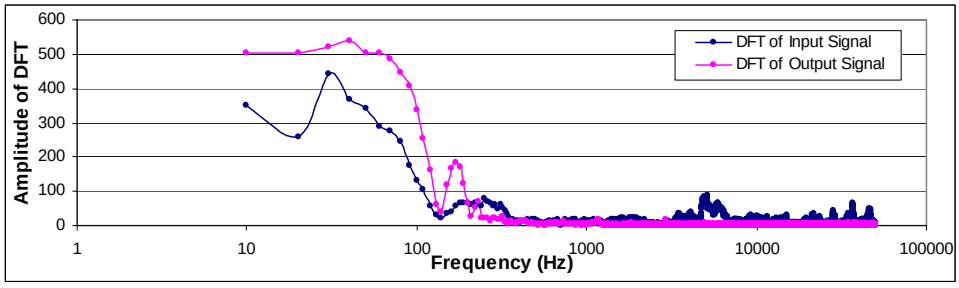


DFT of the complete wave

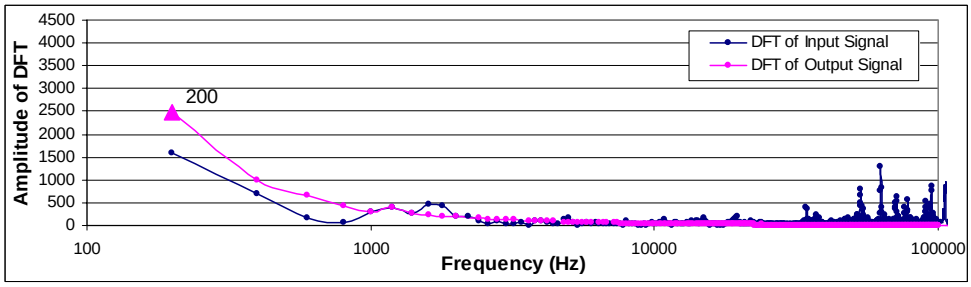


DFT of the wave front

Selected frequency component is 200 Hz.

38.1x1 Al alloy rings in vertical close packed arrangement with unconstrained sides

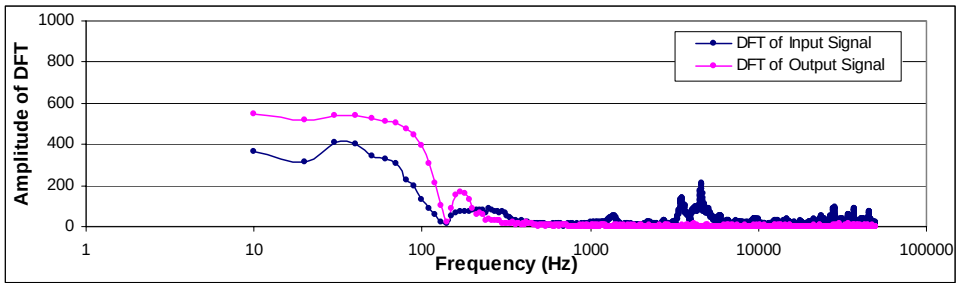


DFT of the complete wave

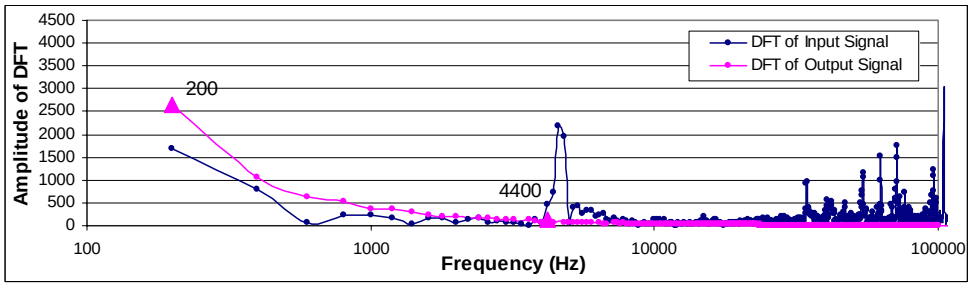


DFT of the wave front

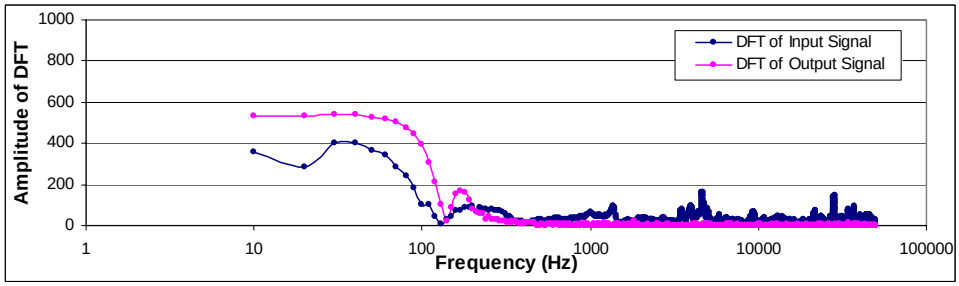


DFT of the complete wave

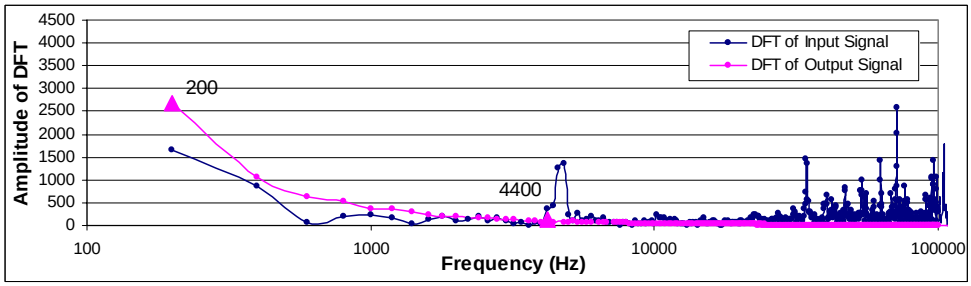


DFT of the wave front

Selected frequency components are 200 Hz and 4400 Hz.

38.1x3 Al alloy rings in square packed arrangement with unconstrained sides

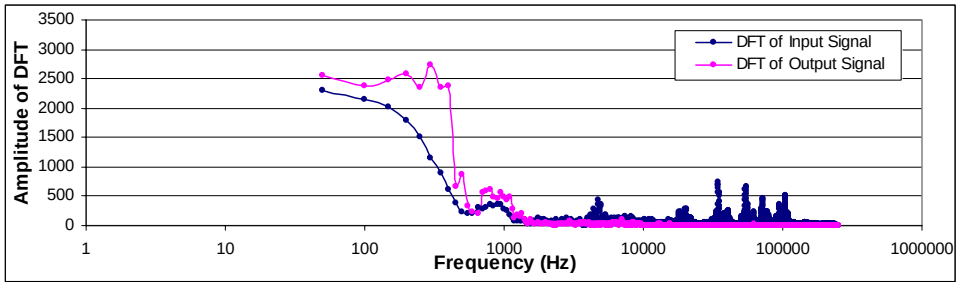


DFT of the complete wave

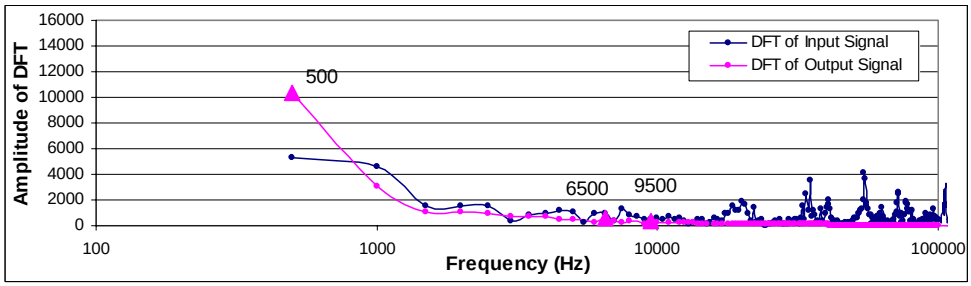


DFT of the wave front

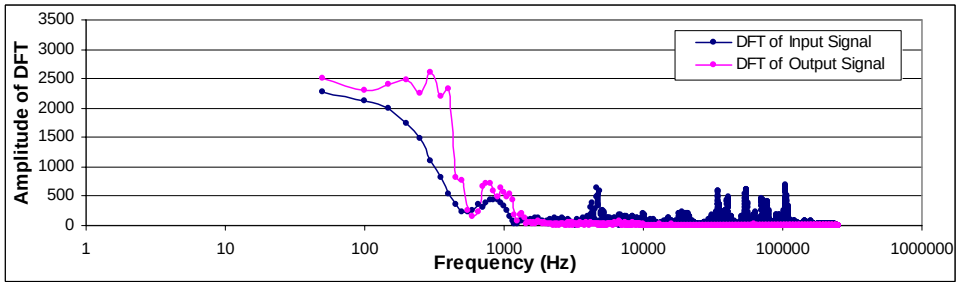


DFT of the complete wave

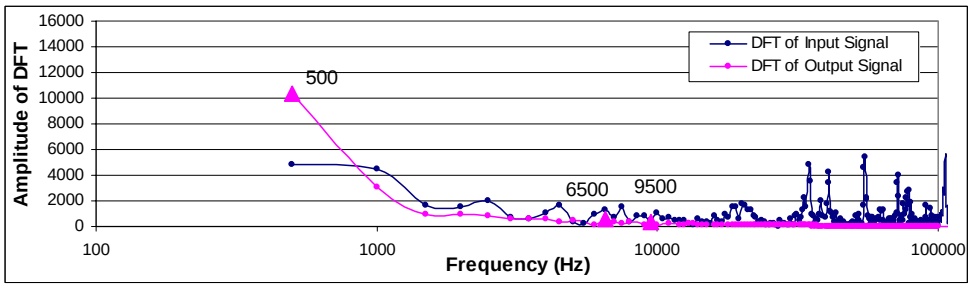


DFT of the wave front

Selected frequency components are 500 Hz, 6600 Hz and 9500 Hz.

38.1x3 Al alloy rings in transverse close packed arrangement with unconstrained sides

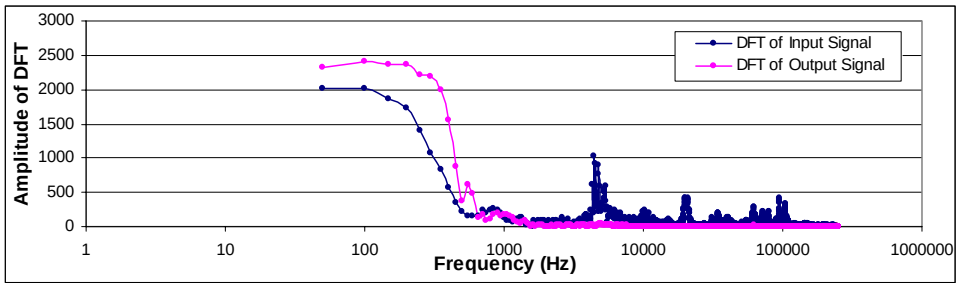


DFT of the complete wave

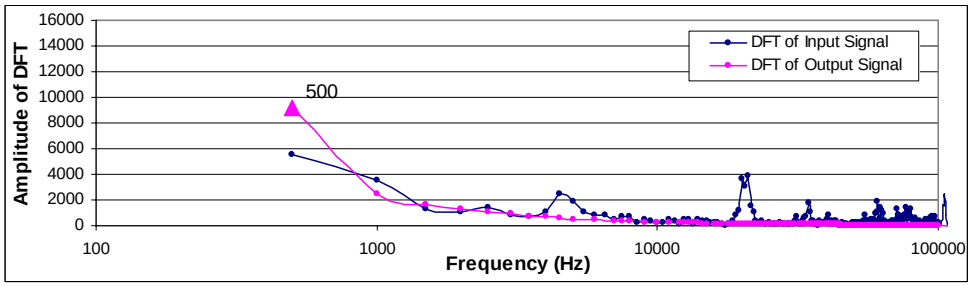


DFT of the wave front

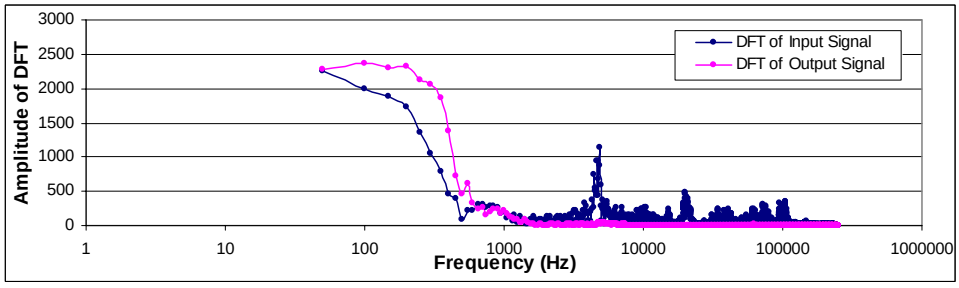


DFT of the complete wave

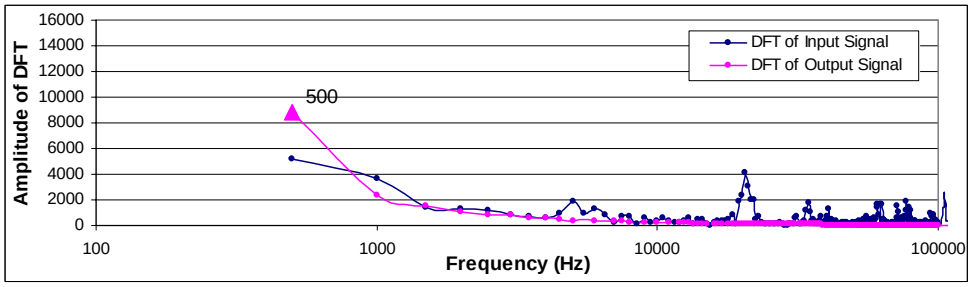


DFT of the wave front

Selected frequency component is 500 Hz.

38.1x3 Al alloy rings in vertical close packed arrangement with unconstrained sides

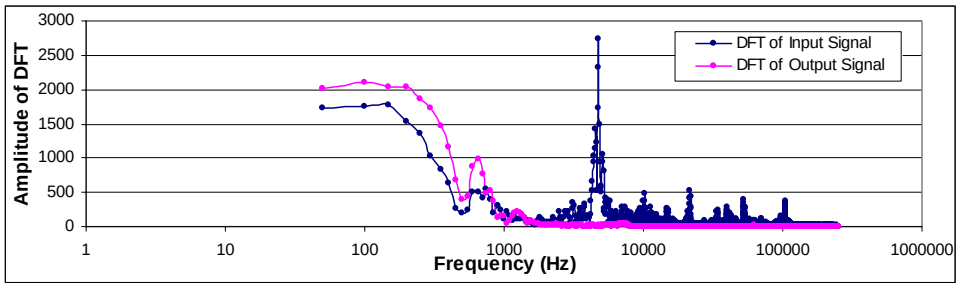


DFT of the complete wave

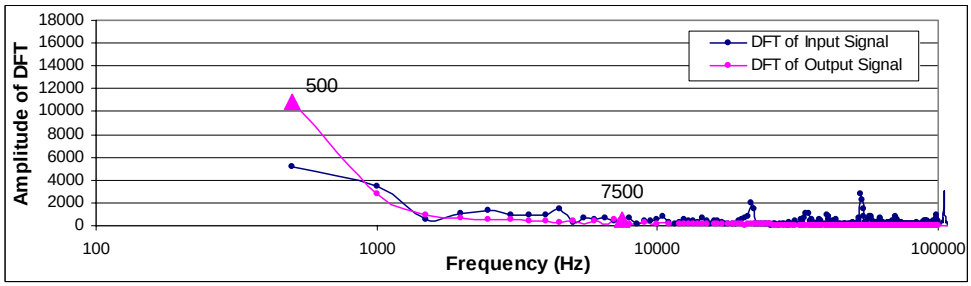


DFT of the wave front

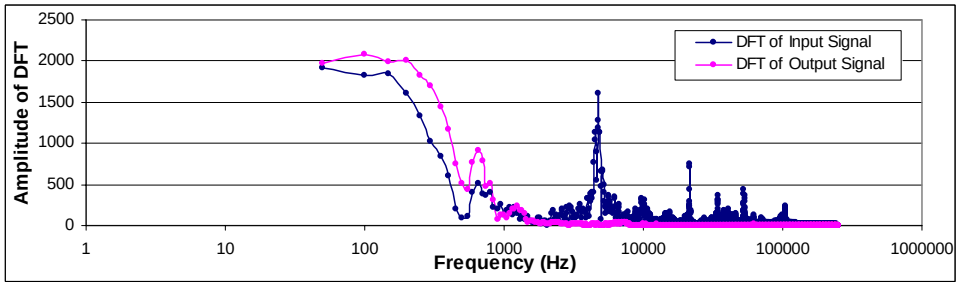


DFT of the complete wave

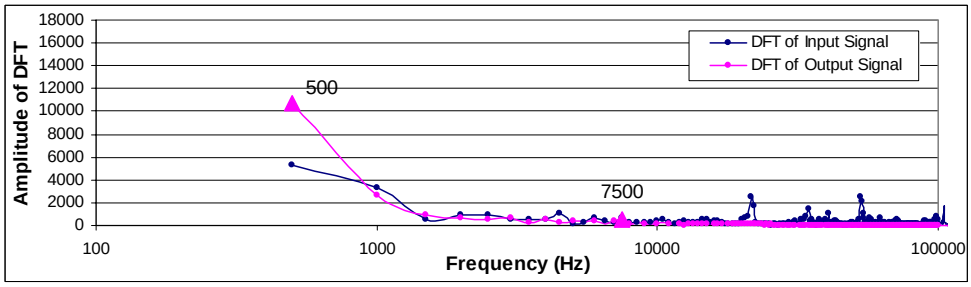


DFT of the wave front

Selected frequency components are 500 Hz and 7500 Hz

25.4x1 Brass rings in square packed arrangement with unconstrained sides

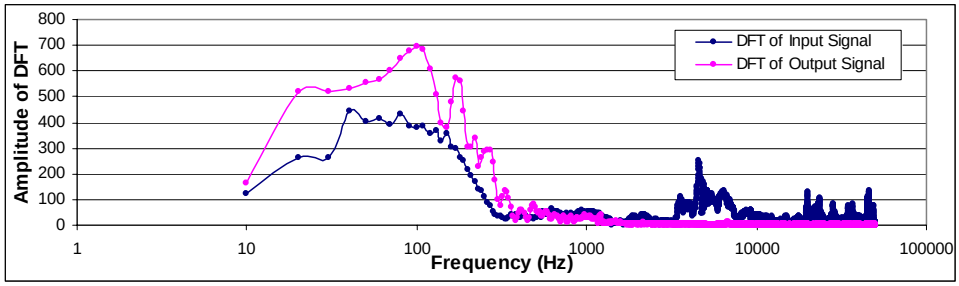


DFT of the complete wave

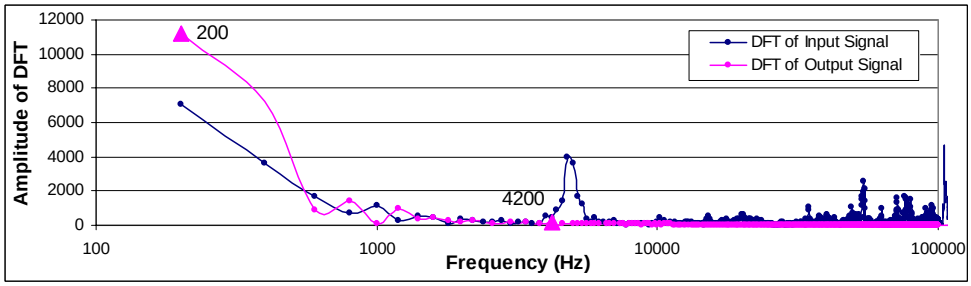


DFT of the wave front

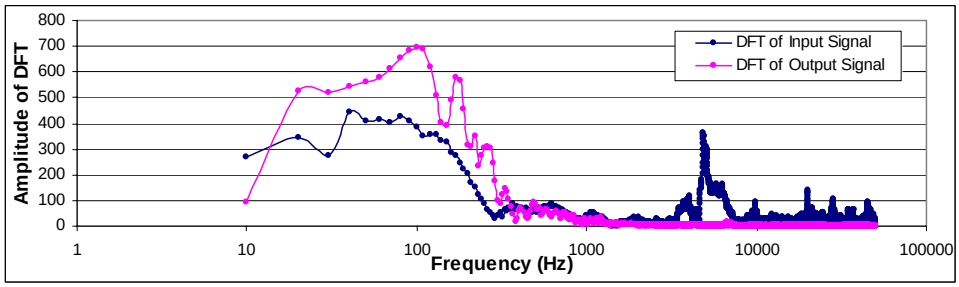


DFT of the complete wave

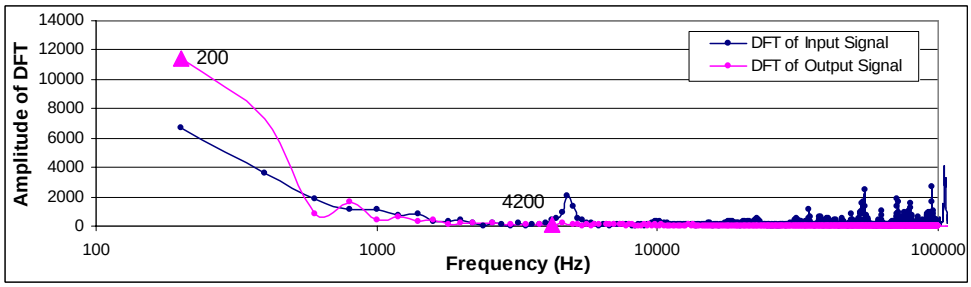


DFT of the wave front

Selected frequency components are 200 Hz and 4200 Hz.

25.4x1 Brass rings in transverse close packed arrangement with unconstrained sides

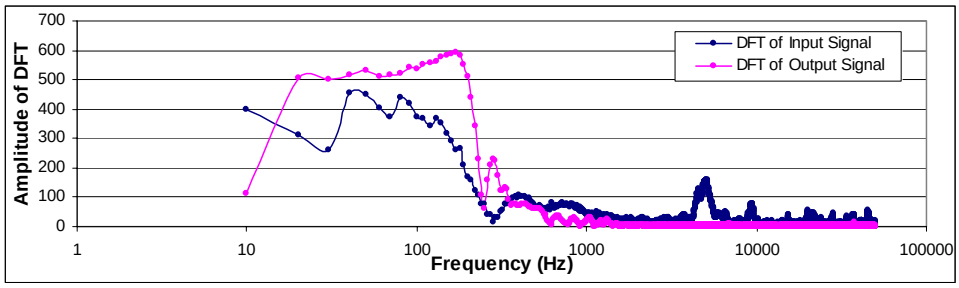


DFT of the complete wave

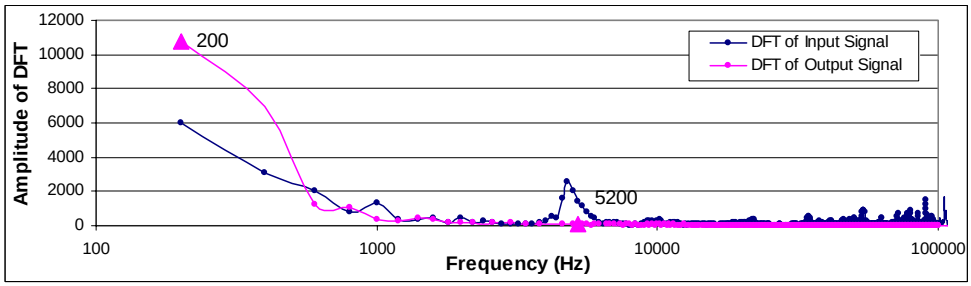


DFT of the wave front

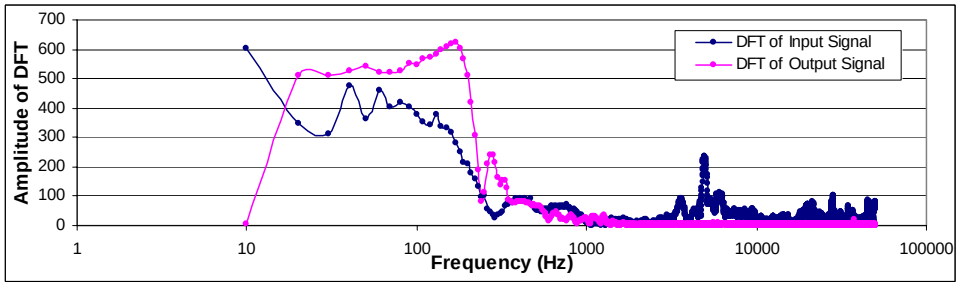


DFT of the complete wave

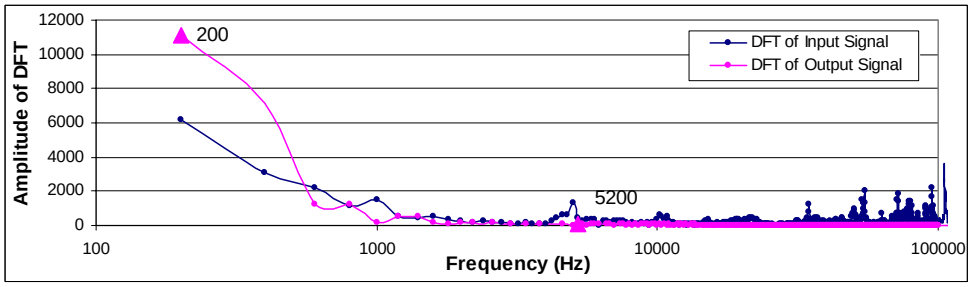


DFT of the wave front

Selected frequency components are 200 Hz and 5200 Hz.

25.4x1 Brass rings in vertical close packed arrangement with unconstrained sides

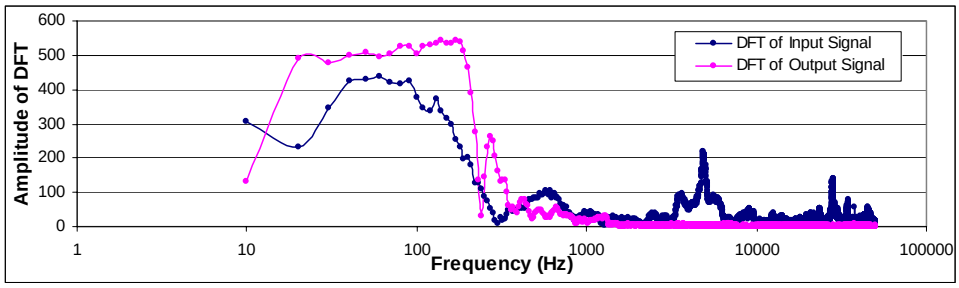


DFT of the complete wave

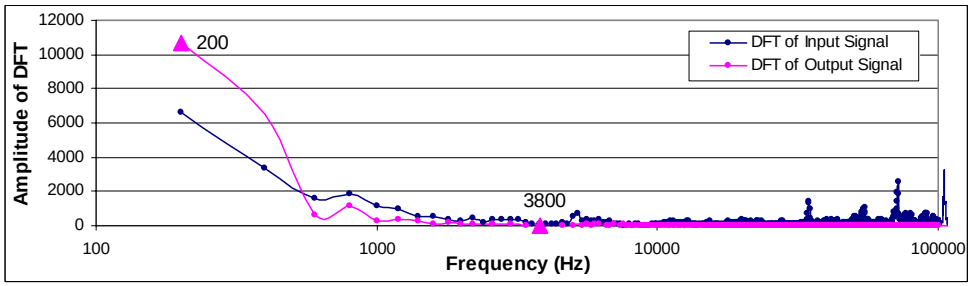


DFT of the wave front

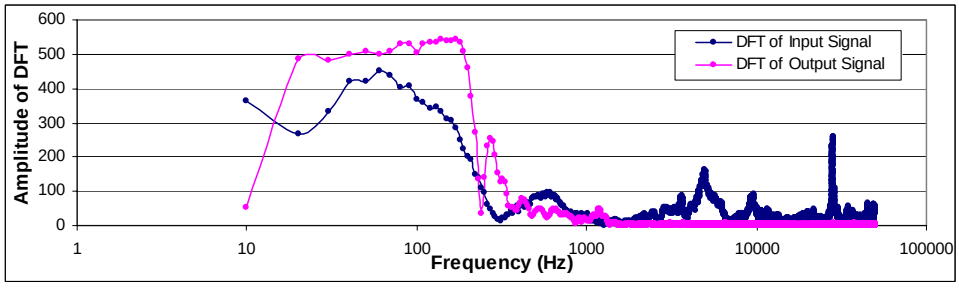


DFT of the complete wave

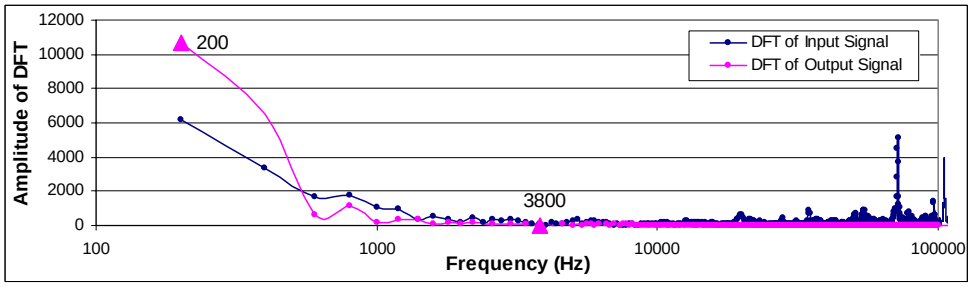


DFT of the wave front

Selected frequency components are 200 Hz and 3800 Hz.

38.1x1 Brass rings in square packed arrangement with constrained sides

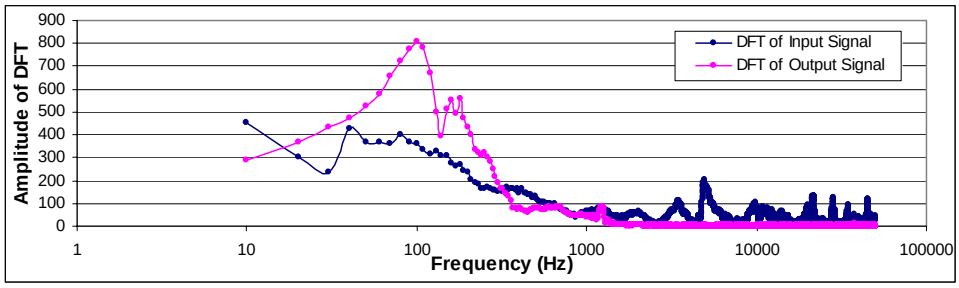


DFT of the complete wave

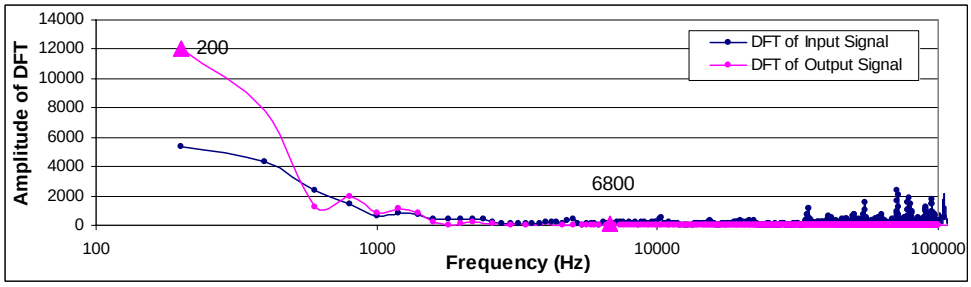


DFT of the wave front

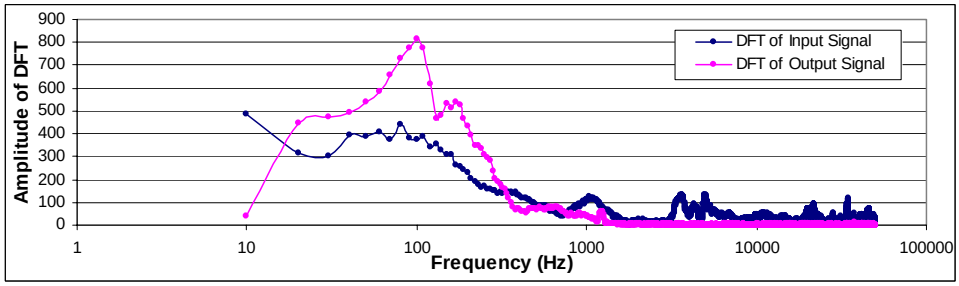


DFT of the complete wave

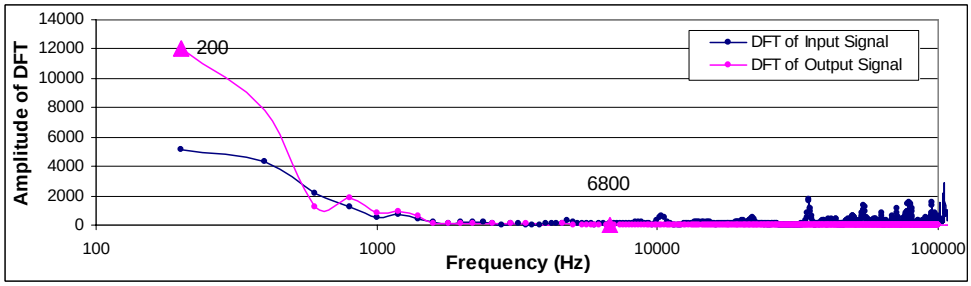


DFT of the wave front

Selected frequency components are 200 Hz and 6800 Hz

38.1x1 Brass rings in transverse close packed arrangement with constrained sides

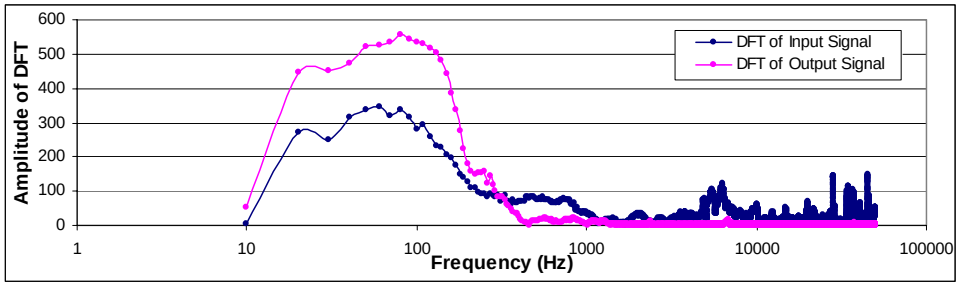


DFT of the complete wave

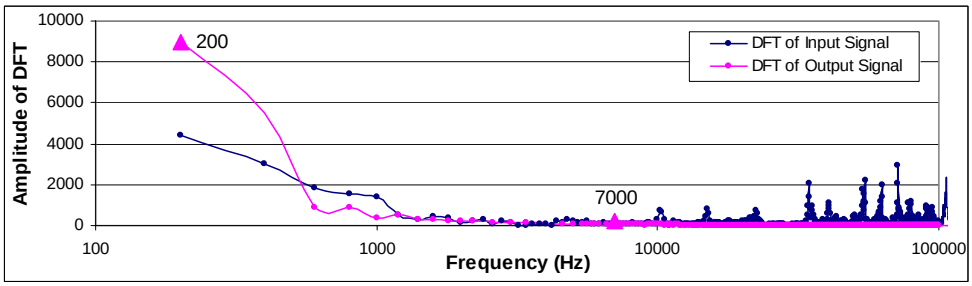


DFT of the wave front

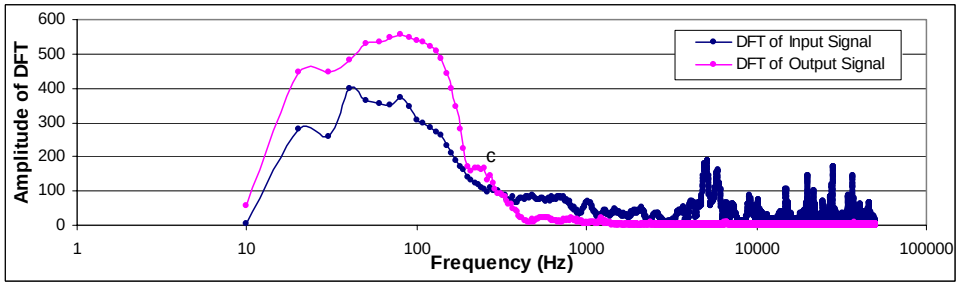


DFT of the complete wave

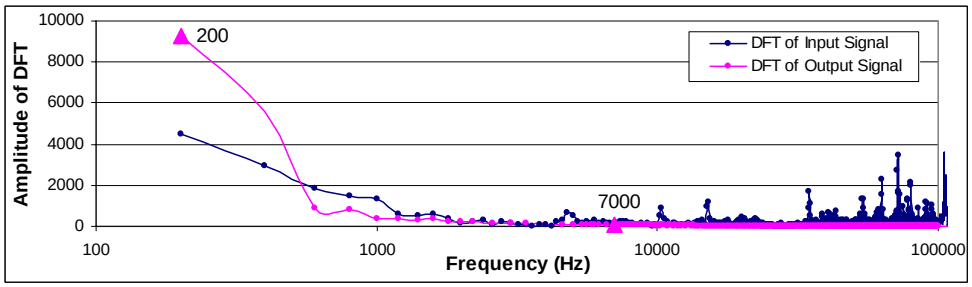


DFT of the wave front

Selected frequency components are 200 Hz and 7000 Hz.

38.1x1 Brass rings in vertical close packed arrangement with constrained sides

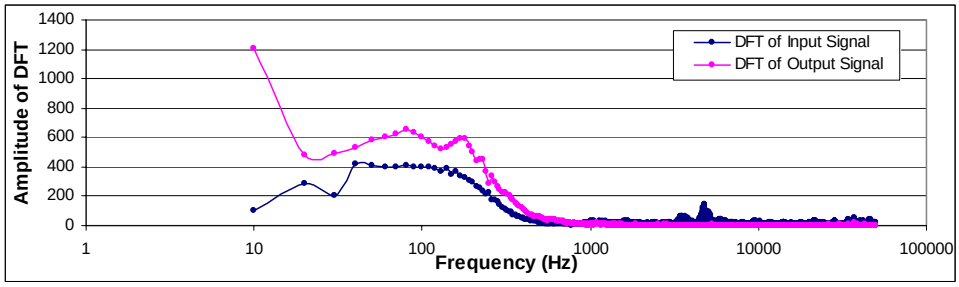


DFT of the complete wave

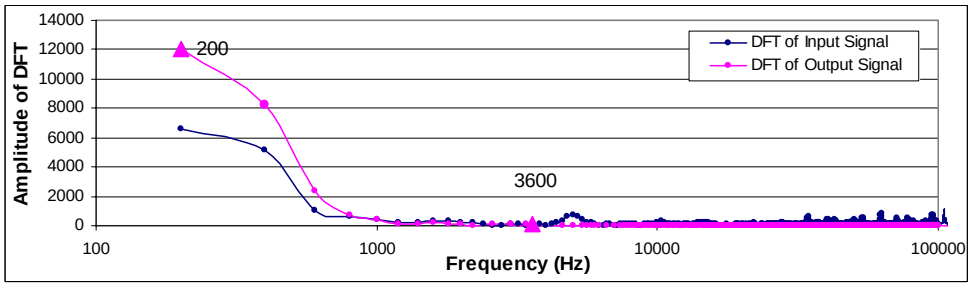


DFT of the wave front

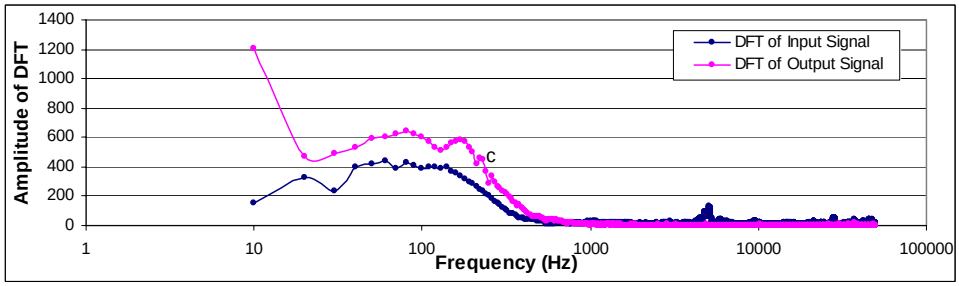


DFT of the complete wave

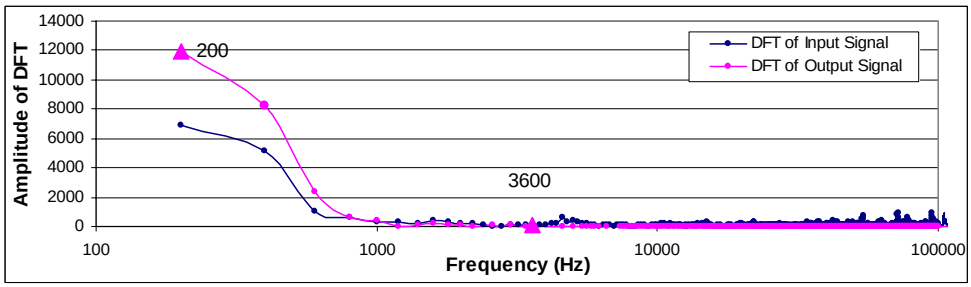


DFT of the wave front

Selected frequency components are 200 Hz and 3600 Hz

38.1x1 Al alloy rings in square packed arrangement with constrained sides

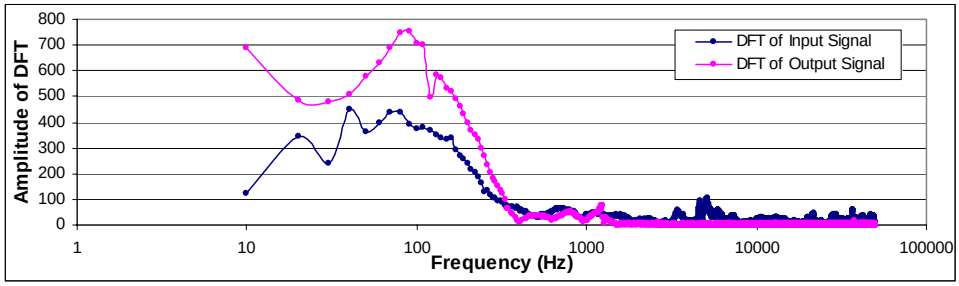


DFT of the complete wave

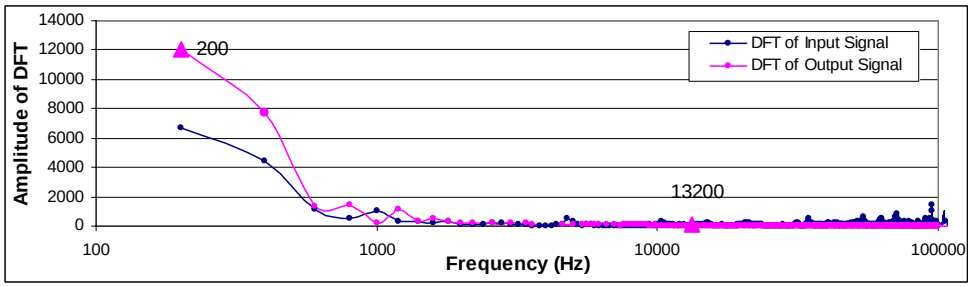


DFT of the wave front

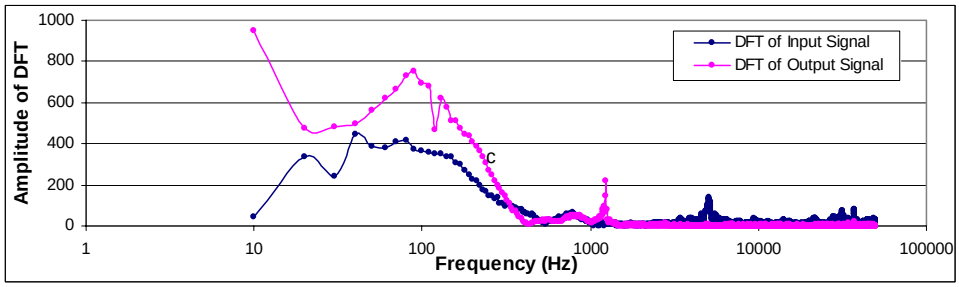


DFT of the complete wave

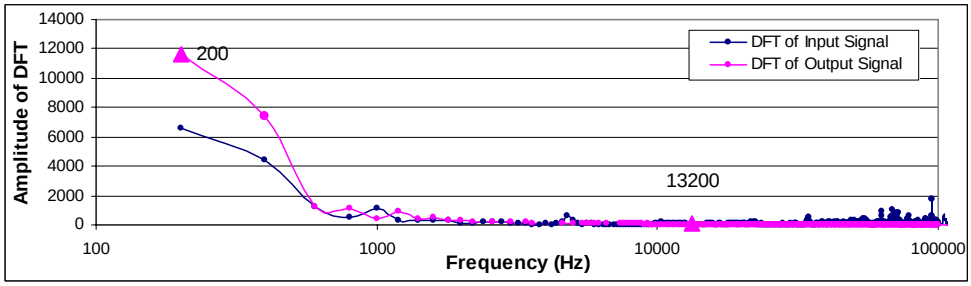


DFT of the wave front

Selected frequency components are 200 Hz and 13200 Hz.

38.1x1 Al alloy rings in transverse close packed arrangement with constrained sides

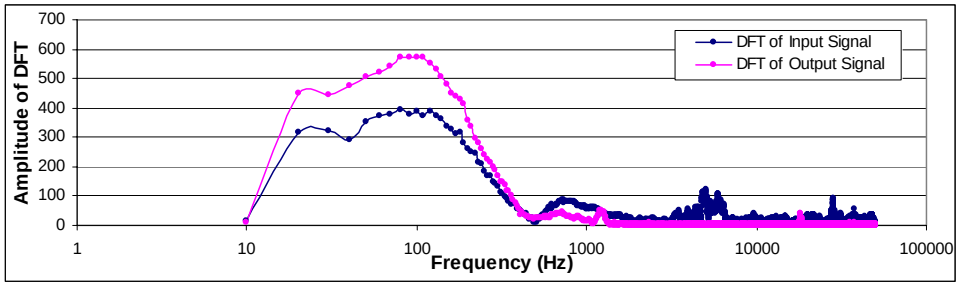


DFT of the complete wave

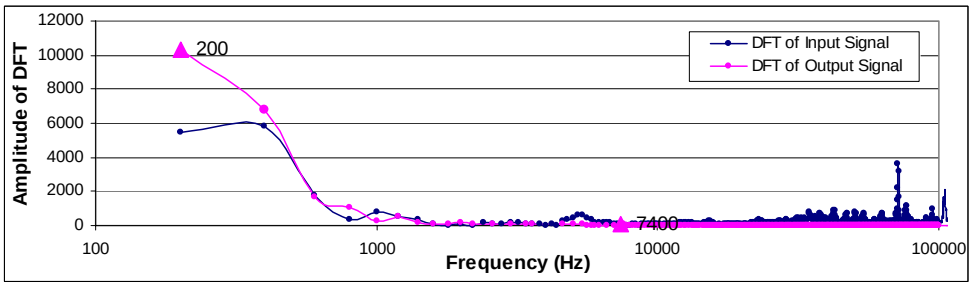


DFT of the wave front

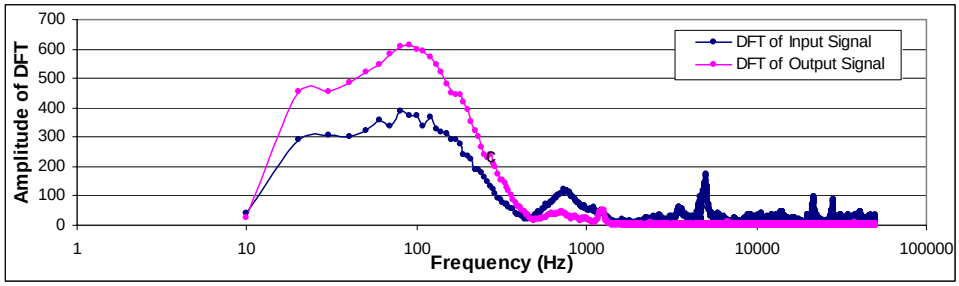


DFT of the complete wave

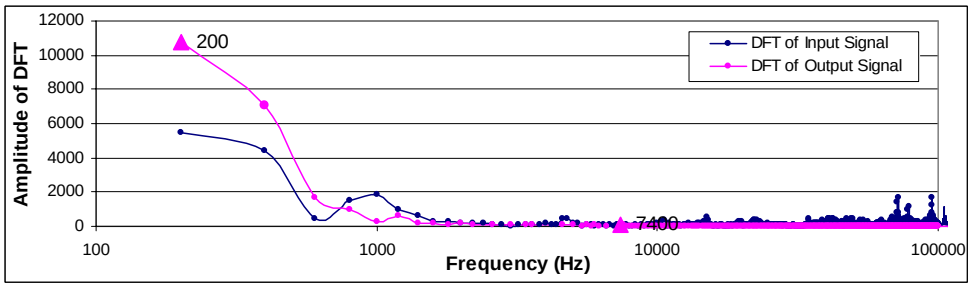


DFT of the wave front

Selected frequency components are 200 Hz and 7400 Hz

38.1x1 Al alloy rings in vertical close packed arrangement with constrained sides

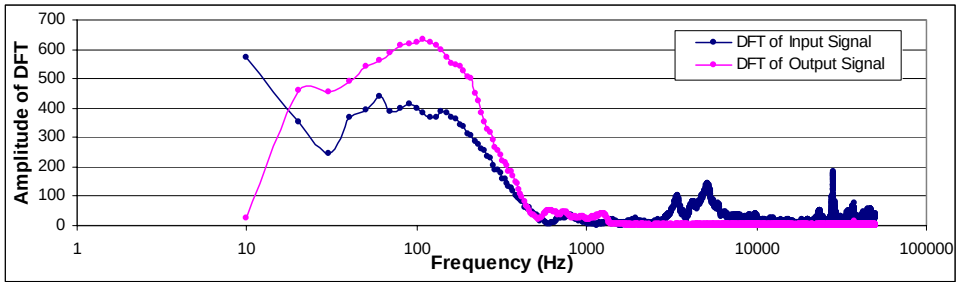


DFT of the complete wave

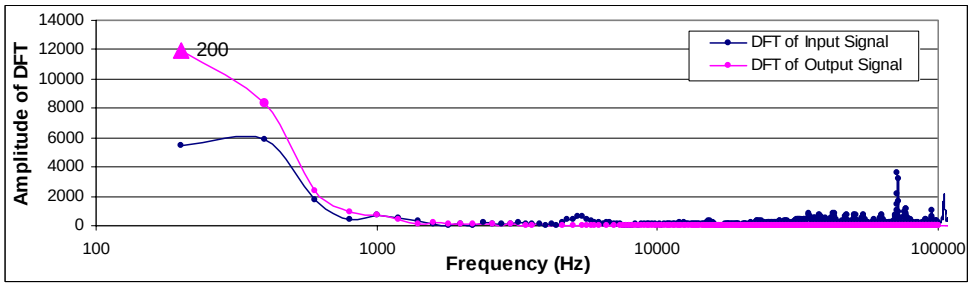


DFT of the wave front

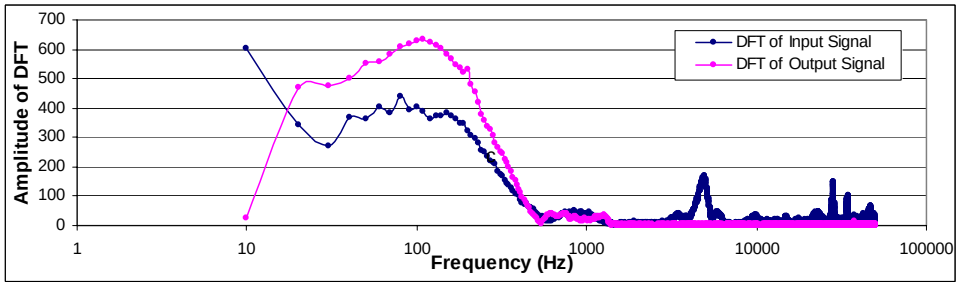


DFT of the complete wave

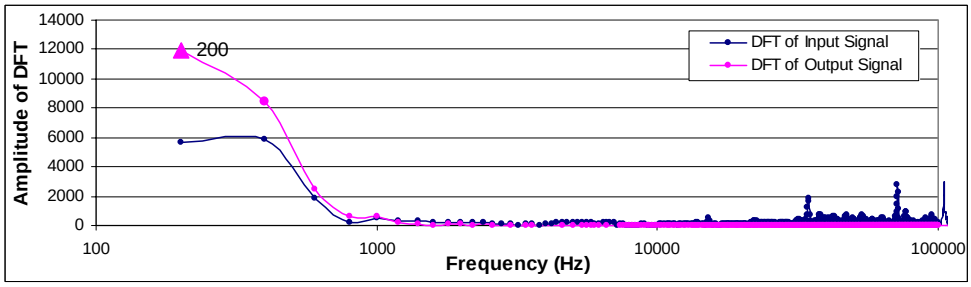


DFT of the wave front

Selected frequency component is 200 Hz.

**Appendix O** Filtered Components of Transmitted Signals and Determination of their Propagation Speeds

38.1x1 Brass rings in square packed arrangement with unconstrained sides

Shortest route along solid walls = 0.3591 m

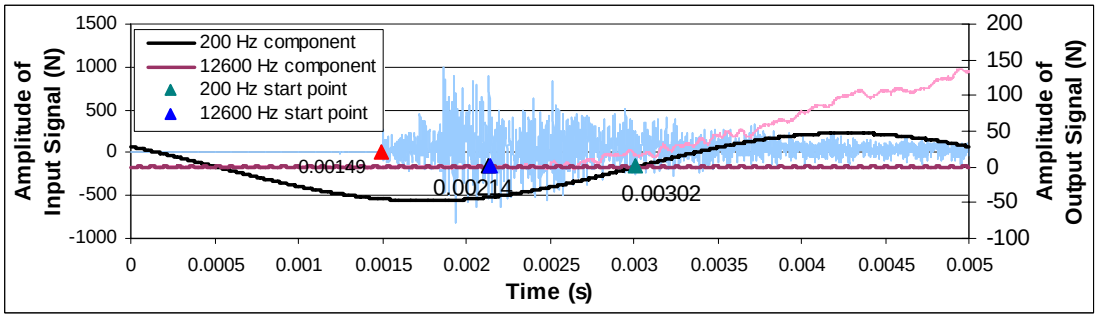


$$T\Big|_{f=200} = 0.00302 - 0.00149 = 0.00153 \text{ s}$$

$$T\Big|_{f=12800} = 0.00214 - 0.00149 = 0.00065 \text{ s}$$

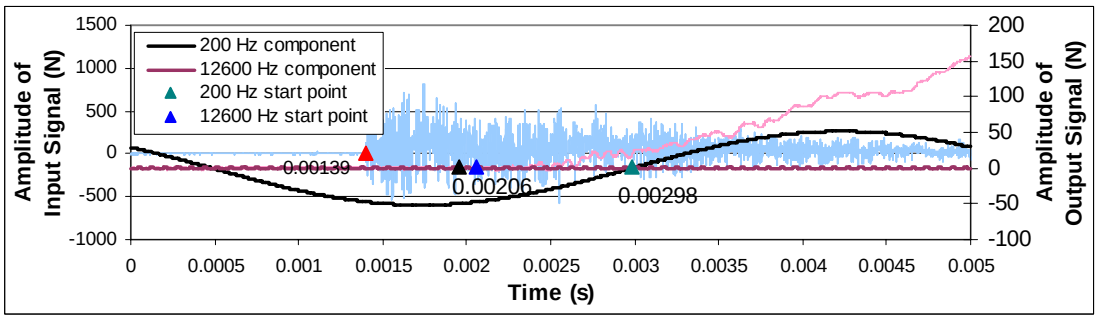


$$T\Big|_{f=200} = 0.00298 - 0.00139 = 0.00159 \text{ s}$$

$$T\Big|_{f=12800} = 0.00206 - 0.00139 = 0.00067 \text{ s}$$

Average time interval: $\overline{T}\Big|_{f=200} = 0.00156$ s $\overline{T}\Big|_{f=12800} = 0.00066$ s

Component velocity along ring walls:

$V\Big|_{f=200} = 230.7$ m/s $V\Big|_{f=12800} = 544.7$ m/s

38.1x1 Brass rings in transverse close packed arrangement with unconstrained sides

Shortest route along solid walls = 0.2992 m

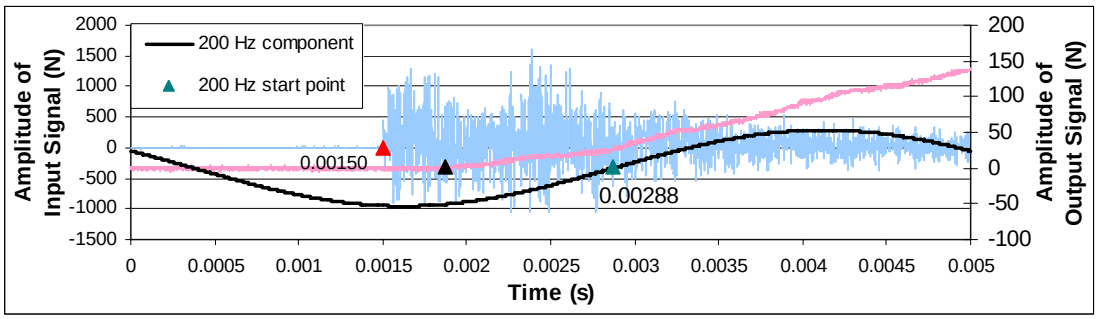


$$T\big|_{f=200} = 0.00288 - 0.00150 = 0.00138 \text{ s}$$

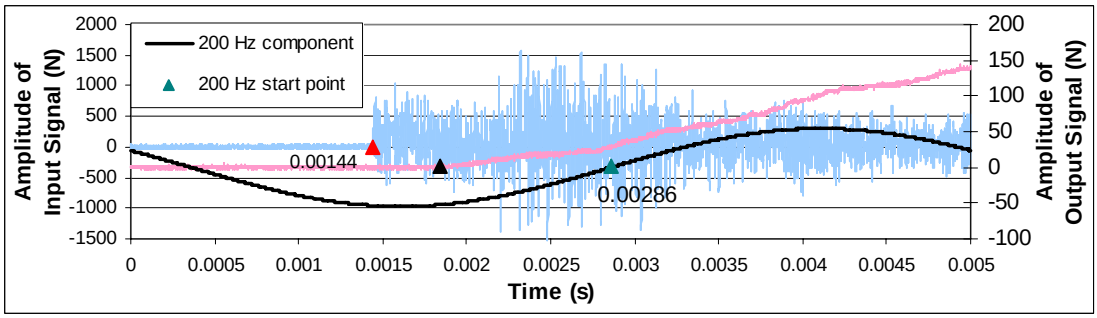


$$T\big|_{f=200} = 0.00286 - 0.00144 = 0.00142 \text{ s}$$

Average time interval: $\overline{T}\big|_{f=200} = 0.00140$ s

Component velocity along ring walls:

$$V\big|_{f=200} = 214.3 \text{ m/s}$$

38.1x1 Brass rings in vertical close packed arrangement with unconstrained sides

Shortest route along solid walls = 0.2194 m

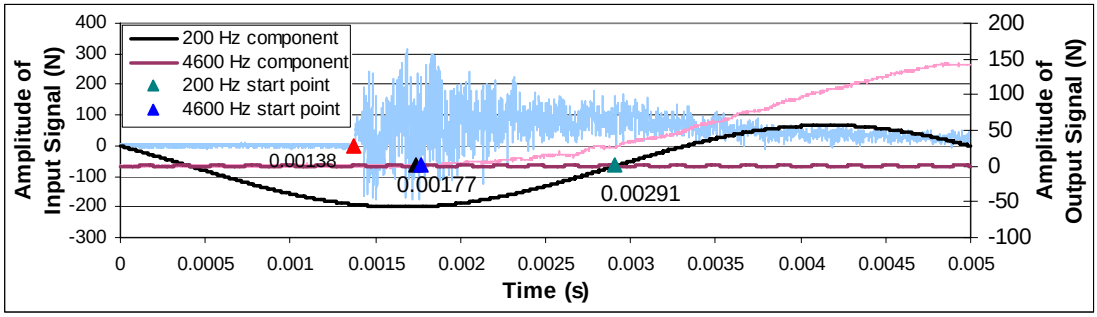


$$T\big|_{f=200} = 0.00291 - 0.00138 = 0.00153 \text{ s}$$

$$T\big|_{f=4600} = 0.00177 - 0.00138 = 0.00039 \text{ s}$$

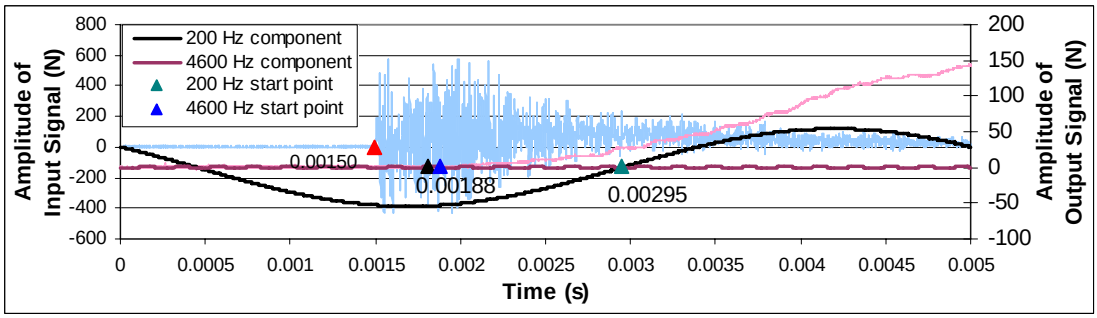


$$T\big|_{f=200} = 0.00295 - 0.00150 = 0.00145 \text{ s}$$

$$T\big|_{f=4600} = 0.00188 - 0.00150 = 0.00038 \text{ s}$$

Average time interval: $\overline{T}\big|_{f=200} = 0.00149$ s $\overline{T}\big|_{f=4600} = 0.000385$ s

Component velocity along ring walls:

$V\big|_{f=200} = 146.9$ m/s $V\big|_{f=4600} = 569.6$ m/s

38.1x3 Brass rings in square packed arrangement with unconstrained sides

Shortest route along solid walls = 0.3591 m

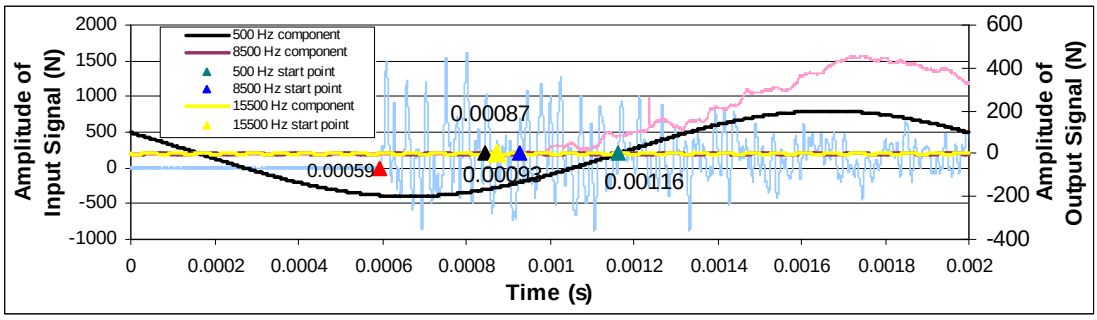


$$T\big|_{f=500} = 0.00116 - 0.00059 = 0.00057 \text{ s}$$

$$T\big|_{f=8500} = 0.00093 - 0.00059 = 0.00034 \text{ s}$$

$$T\big|_{f=15500} = 0.00087 - 0.00059 = 0.00028 \text{ s}$$

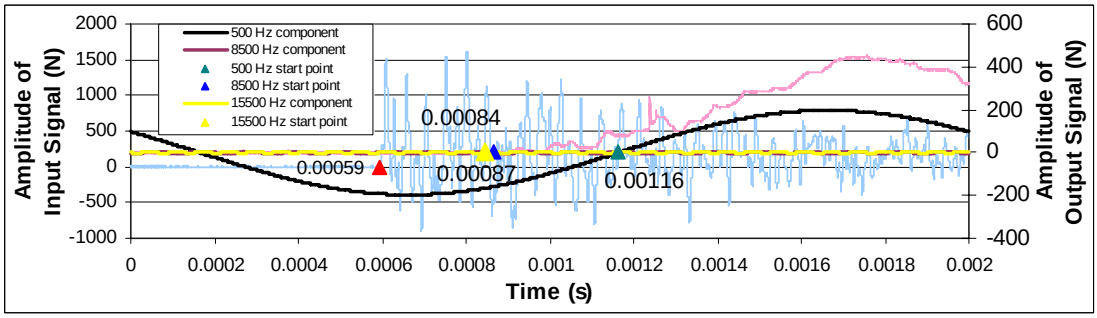


$$T\big|_{f=500} = 0.00116 - 0.00059 = 0.00057 \text{ s}$$

$$T\big|_{f=8500} = 0.00087 - 0.00059 = 0.00028 \text{ s}$$

$$T\big|_{f=15500} = 0.00084 - 0.00059 = 0.00025 \text{ s}$$

Average time interval:

$$\overline{T}\big|_{f=500} = 0.00057 \text{ s} \qquad \overline{T}\big|_{f=8500} = 0.00031 \text{ s} \qquad \overline{T}\big|_{f=15500} = 0.000265 \text{ s}$$

Component velocity along ring walls:

$$V\big|_{f=500} = 630.2 \text{ m/s} \qquad V\big|_{f=8500} = 1190.2 \text{ m/s} \qquad V\big|_{f=15500} = 1356.6 \text{ m/s}$$

38.1x3 Brass rings in transverse close packed arrangement with unconstrained sides

Shortest route along solid walls = 0.2992 m

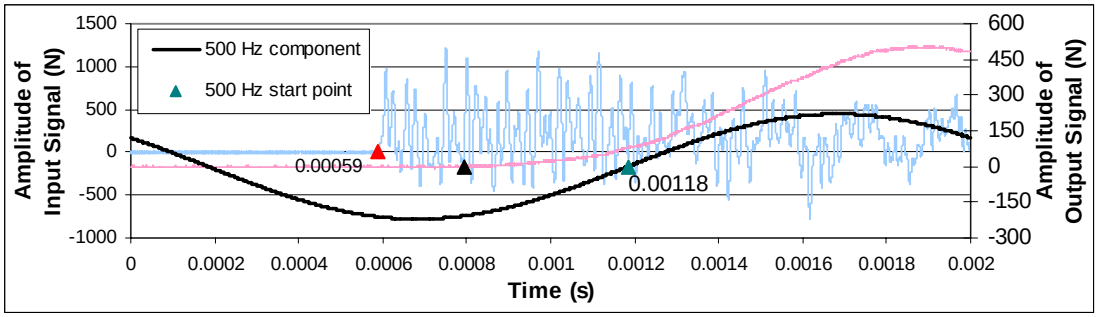


$$T\big|_{f=500} = 0.00118 - 0.00059 = 0.00059 \text{ s}$$

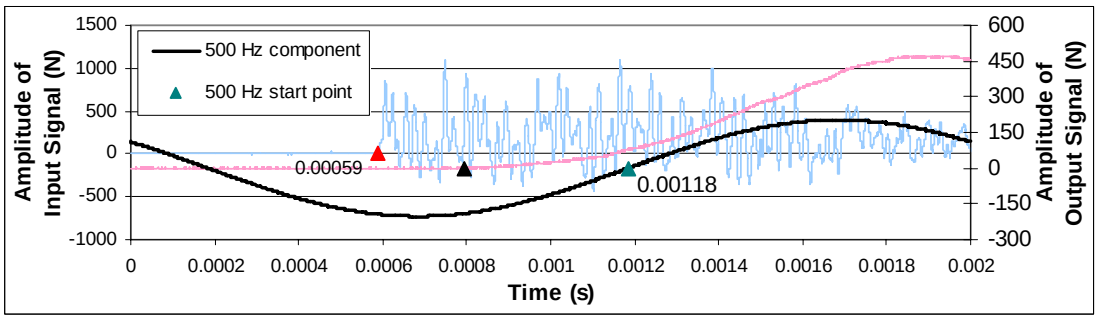


$$T\big|_{f=500} = 0.00118 - 0.00059 = 0.00059 \text{ s}$$

Average time interval: $\bar{T}\big|_{f=500} = 0.00059$ s

Component velocity along ring walls: $V\big|_{f=500} = 503.4$ m/s

38.1x3 Brass rings in vertical close packed arrangement with unconstrained sides

Shortest route along solid walls = 0.2194 m

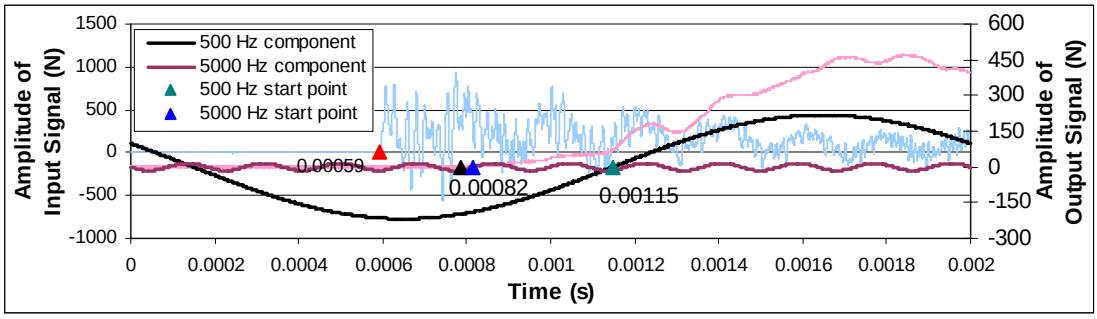


$$T\big|_{f=500} = 0.00115 - 0.00059 = 0.00056 \text{ s}$$

$$T\big|_{f=5000} = 0.00082 - 0.00059 = 0.00023 \text{ s}$$

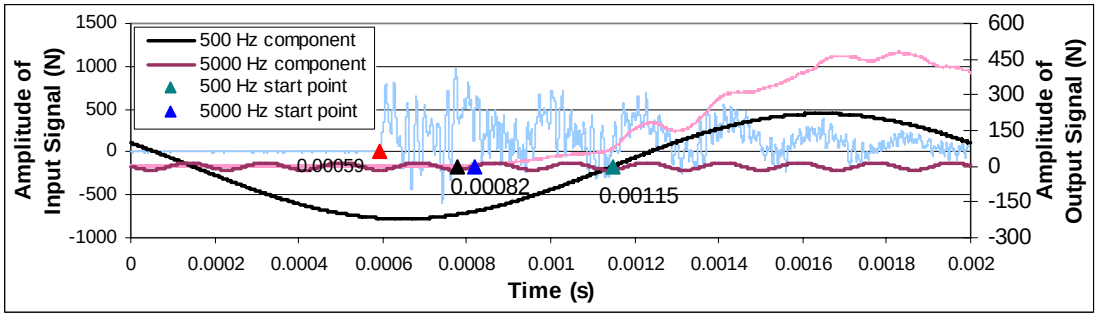


$$T\big|_{f=500} = 0.00115 - 0.00059 = 0.00056 \text{ s}$$

$$T\big|_{f=5000} = 0.00082 - 0.00059 = 0.00023 \text{ s}$$

Average time interval:

$$\bar{T}\big|_{f=500} = 0.00056 \text{ s} \qquad \bar{T}\big|_{f=5000} = 0.00023 \text{ s}$$

Component velocity along ring walls:

$$V\big|_{f=500} = 395.7 \text{ m/s} \qquad V\big|_{f=5000} = 974.0 \text{ m/s}$$

38.1x1 Al alloy rings in square packed arrangement with unconstrained sides

Shortest route along solid walls = 0.3591 m

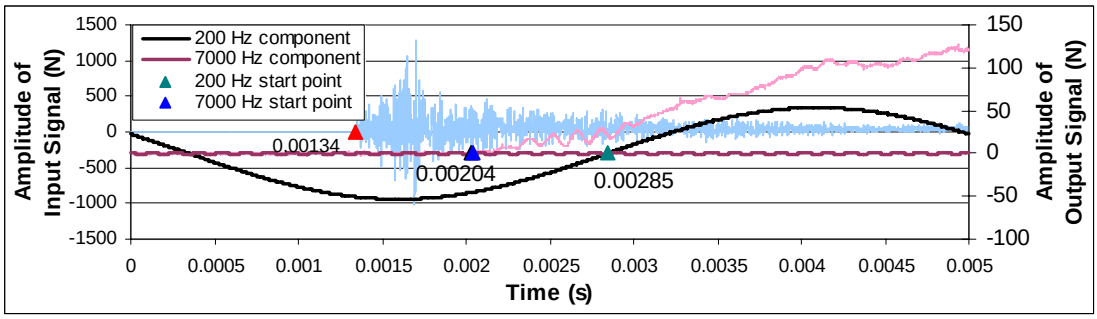


$$T\big|_{f=200} = 0.00285 - 0.00134 = 0.00151 \text{ s}$$

$$T\big|_{f=7000} = 0.00204 - 0.00134 = 0.00070 \text{ s}$$

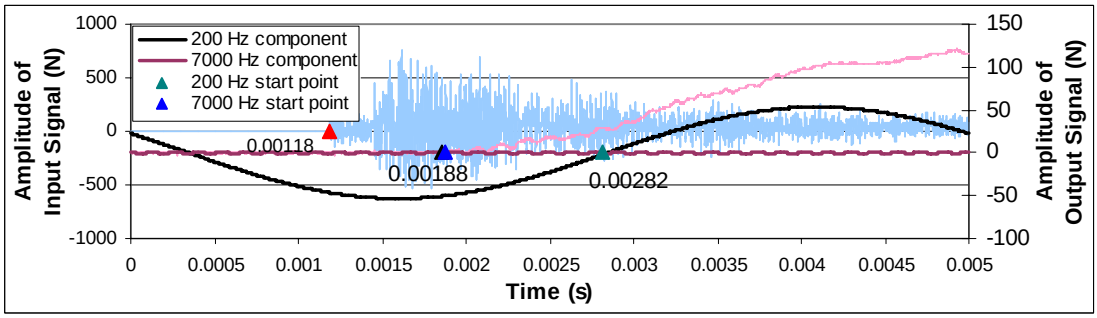


$$T\big|_{f=200} = 0.00282 - 0.00118 = 0.00164 \text{ s}$$

$$T\big|_{f=7000} = 0.00188 - 0.00118 = 0.00070 \text{ s}$$

Average time interval:

$$\overline{T}\big|_{f=200} = 0.00158 \text{ s} \qquad \overline{T}\big|_{f=7000} = 0.00070 \text{ s}$$

Component velocity along ring walls:

$$V\big|_{f=200} = 228.4 \text{ m/s} \qquad V\big|_{f=7000} = 513.2 \text{ m/s}$$

38.1x1 Al alloy rings in transverse close packed arrangement with unconstrained sides

Shortest route along solid walls = 0.2992 m

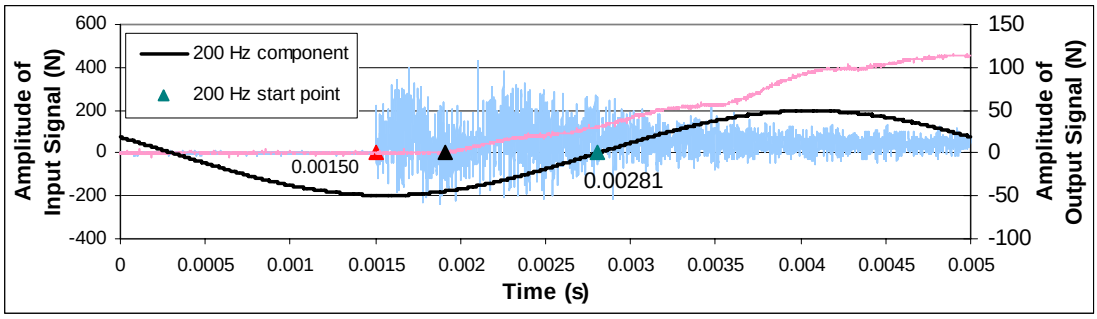


$$T\Big|_{f=200} = 0.00281 - 0.00150 = 0.00131 \text{ s}$$

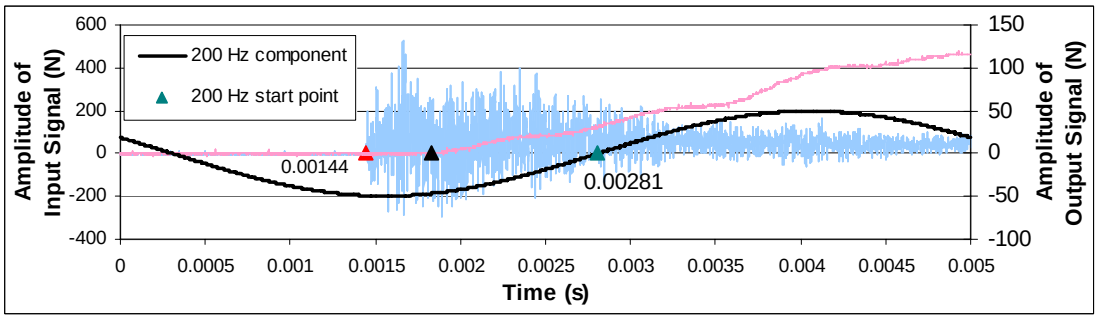


$$T\Big|_{f=200} = 0.00281 - 0.00144 = 0.00137 \text{ s}$$

Average time interval: $\overline{T}\Big|_{f=200} = 0.00134$ s

Component velocity along ring walls: $V\Big|_{f=200} = 223.8$ m/s

38.1x1 Al alloy rings in vertical close packed arrangement with unconstrained sides

Shortest route along solid walls = 0.2194 m

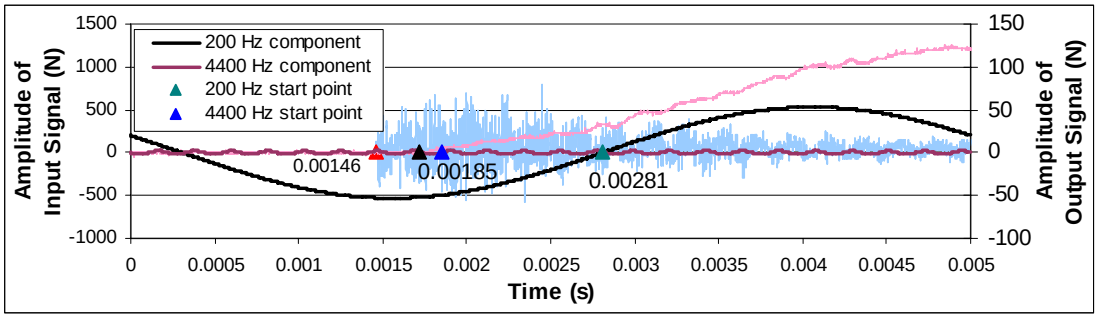


$$T\Big|_{f=200} = 0.00281 - 0.00146 = 0.00135 \text{ s}$$

$$T\Big|_{f=4400} = 0.00185 - 0.00146 = 0.00039 \text{ s}$$

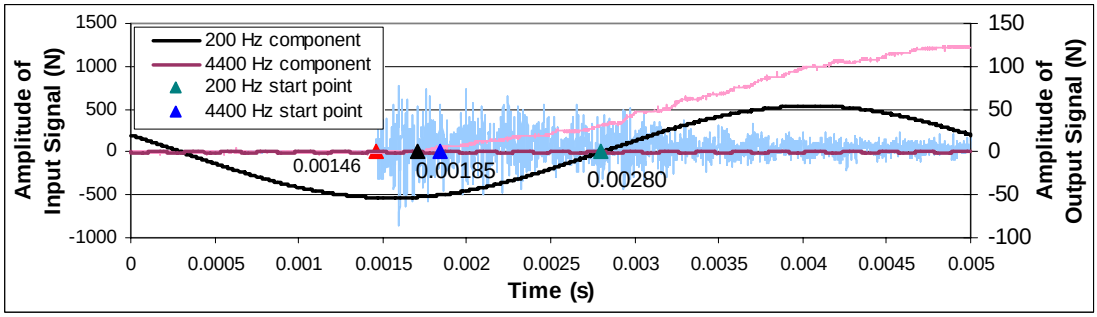


$$T\Big|_{f=200} = 0.00280 - 0.00146 = 0.00134 \text{ s}$$

$$T\Big|_{f=4400} = 0.00185 - 0.00146 = 0.00039 \text{ s}$$

Average time interval:

$$\overline{T}\Big|_{f=200} = 0.001345 \text{ s} \qquad \overline{T}\Big|_{f=4400} = 0.00039 \text{ s}$$

Component velocity along ring walls:

$$V\Big|_{f=200} = 162.9 \text{ m/s} \qquad V\Big|_{f=7000} = 563.4 \text{ m/s}$$

38.1x3 Al alloy rings in square packed arrangement with unconstrained sides

Shortest route along solid walls = 0.3591 m

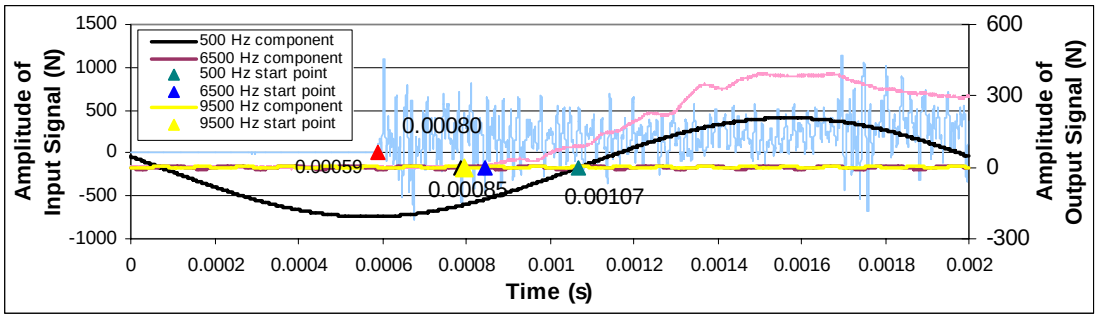


$$T\big|_{f=500} = 0.00107 - 0.00059 = 0.00048 \text{ s}$$

$$T\big|_{f=6500} = 0.00085 - 0.00059 = 0.00026 \text{ s}$$

$$T\big|_{f=9500} = 0.00080 - 0.00059 = 0.00021 \text{ s}$$

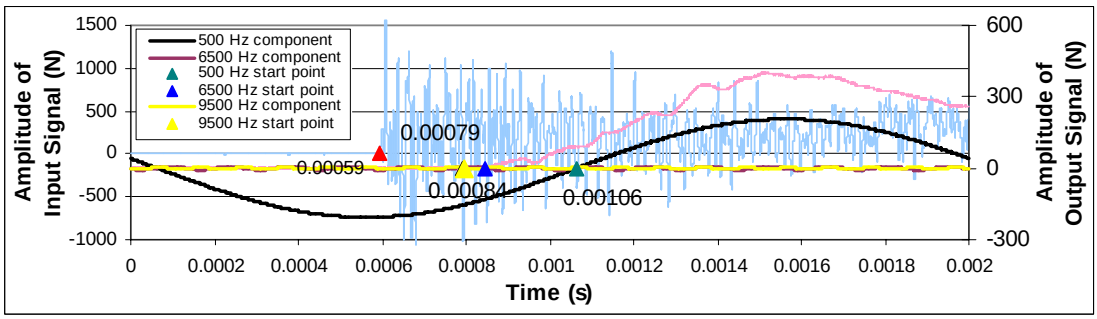


$$T\big|_{f=500} = 0.00106 - 0.00059 = 0.00047 \text{ s}$$

$$T\big|_{f=6500} = 0.00084 - 0.00059 = 0.00025 \text{ s}$$

$$T\big|_{f=9500} = 0.00079 - 0.00059 = 0.00020 \text{ s}$$

Average time interval:

$$\overline{T}\big|_{f=500} = 0.000475 \text{ s} \qquad \overline{T}\big|_{f=6500} = 0.000255 \qquad \overline{T}\big|_{f=9500} = 0.000205 \text{ s}$$

Component velocity along ring walls:

$$V\big|_{f=500} = 808.6 \text{ m/s} \qquad V\big|_{f=6500} = 1410.9 \text{ m/s} \qquad V\big|_{f=9500} = 1757.6 \text{ m/s}$$

38.1x3 Al alloy rings in transverse close packed arrangement with unconstrained sides

Shortest route along solid walls = 0.2992 m

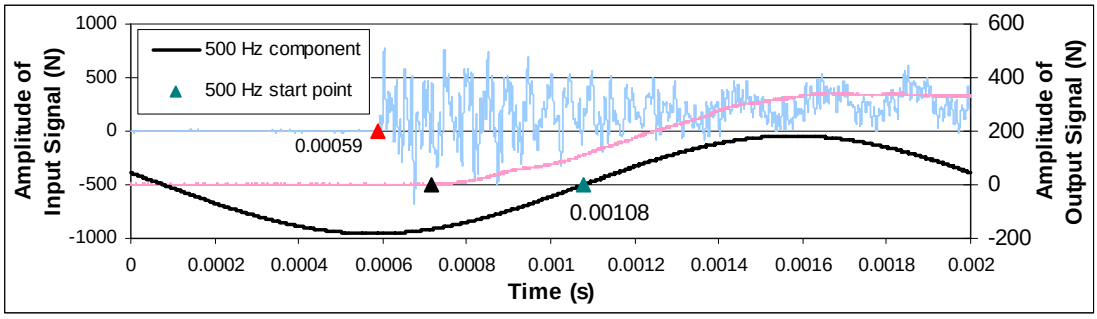


$$T\Big|_{f=500} = 0.00108 - 0.00059 = 0.00049 \text{ s}$$

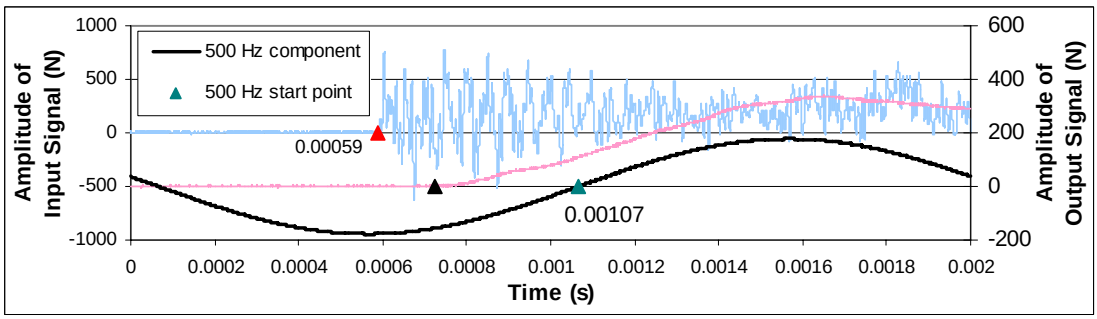


$$T\Big|_{f=500} = 0.00107 - 0.00059 = 0.00048 \text{ s}$$

Average time interval: $\bar{T}\Big|_{f=500} = 0.000485$ s

Component velocity along ring walls: $V\Big|_{f=500} = 618.1$ m/s

38.1x3 Al alloy rings in vertical close packed arrangement with unconstrained sides

Shortest route along solid walls = 0.2194 m

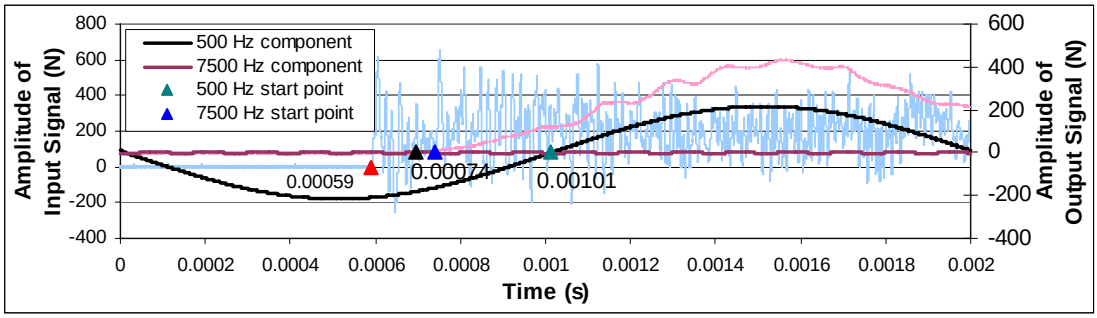


$$T\big|_{f=500} = 0.00101 - 0.00059 = 0.00042 \text{ s}$$

$$T\big|_{f=7500} = 0.00074 - 0.00059 = 0.00015 \text{ s}$$

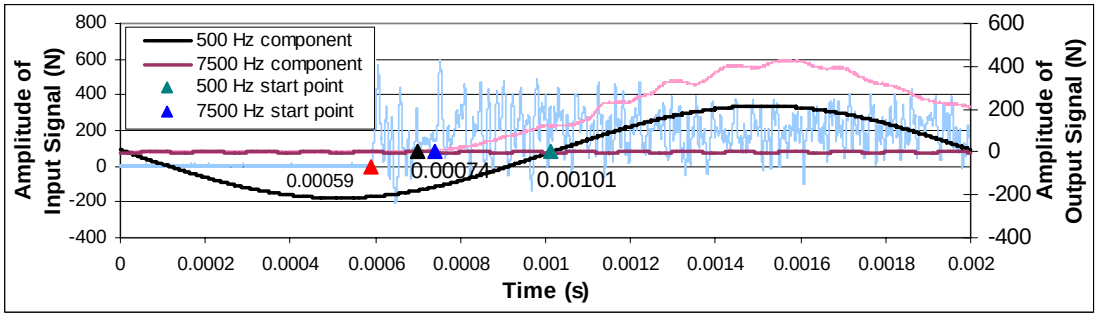


$$T\big|_{f=500} = 0.00101 - 0.00059 = 0.00042 \text{ s}$$

$$T\big|_{f=7500} = 0.00074 - 0.00059 = 0.00015 \text{ s}$$

Average time interval:

$$\bar{T}\big|_{f=500} = 0.00042 \text{ s} \qquad \bar{T}\big|_{f=7500} = 0.00015 \text{ s}$$

Component velocity along ring walls:

$$V\big|_{f=500} = 518.2 \text{ m/s} \qquad V\big|_{f=7500} = 1473.7 \text{ m/s}$$

25.4x1 Brass rings in square packed arrangement with unconstrained sides

Shortest route along solid walls = 0.2394 m

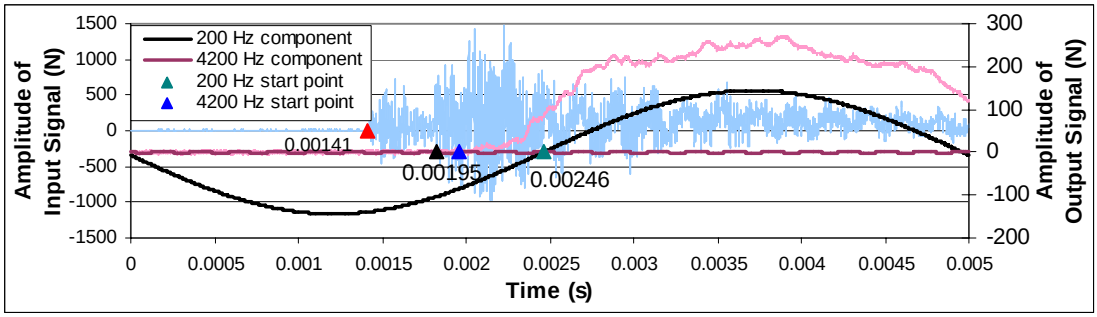


$$T\big|_{f=200} = 0.00246 - 0.00141 = 0.00105 \text{ s}$$

$$T\big|_{f=4200} = 0.00195 - 0.00141 = 0.00054 \text{ s}$$

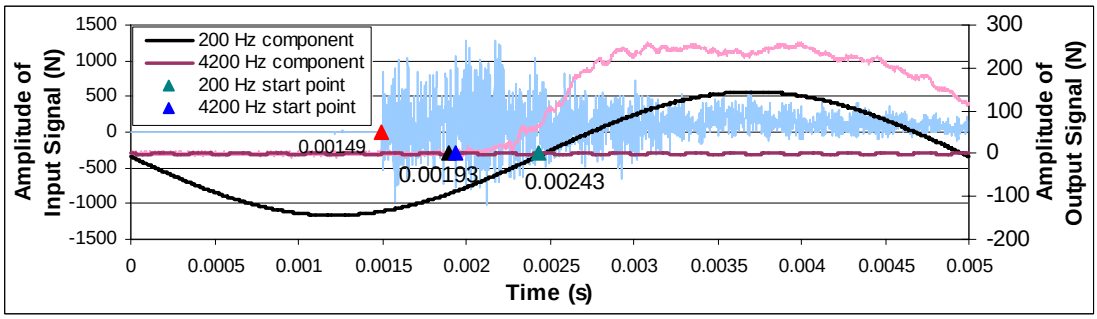


$$T\big|_{f=200} = 0.00243 - 0.00149 = 0.00094 \text{ s}$$

$$T\big|_{f=4200} = 0.00193 - 0.00149 = 0.00044 \text{ s}$$

Average time interval:

$$\overline{T}\big|_{f=200} = 0.000995 \text{ s} \qquad \overline{T}\big|_{f=4200} = 0.00049 \text{ s}$$

Component velocity along ring walls:

$$V\big|_{f=200} = 240.4 \text{ m/s} \qquad V\big|_{f=4200} = 485.6 \text{ m/s}$$

25.4x1 Brass rings in transverse close packed arrangement with unconstrained sides

Shortest route along solid walls = 0.1995 m

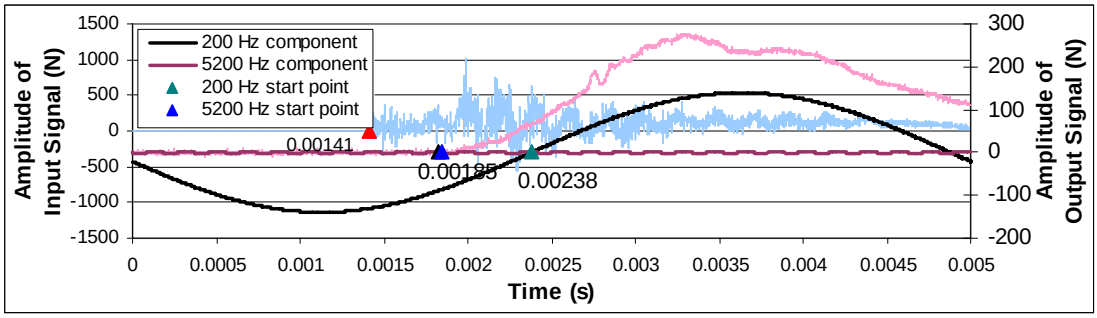


$$T\big|_{f=200} = 0.00238 - 0.00141 = 0.00097 \text{ s}$$

$$T\big|_{f=5200} = 0.00185 - 0.00141 = 0.00044 \text{ s}$$

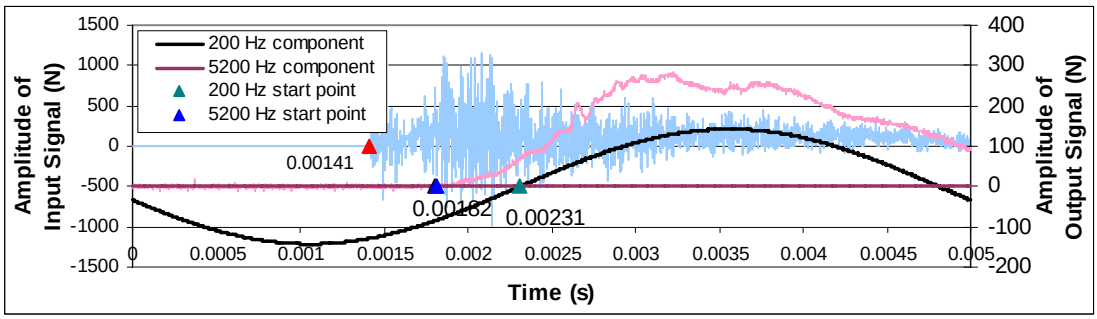


$$T\big|_{f=200} = 0.00231 - 0.00141 = 0.0009 \text{ s}$$

$$T\big|_{f=5200} = 0.00182 - 0.00141 = 0.00041 \text{ s}$$

Average time interval:

$$\bar{T}\big|_{f=200} = 0.00094 \text{ s} \qquad \bar{T}\big|_{f=5200} = 0.00043 \text{ s}$$

Component velocity along ring walls:

$$V\big|_{f=200} = 213.7 \text{ m/s} \qquad V\big|_{f=5200} = 472.7 \text{ m/s}$$

25.4x1 Brass rings in vertical close packed arrangement with unconstrained sides

Shortest route along solid walls = 0.1596 m

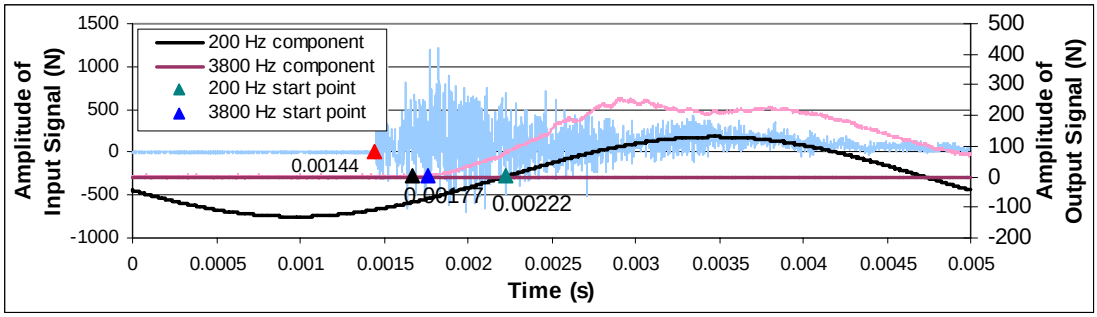


$$T\big|_{f=200} = 0.00222 - 0.00144 = 0.00078 \text{ s}$$

$$T\big|_{f=3800} = 0.00177 - 0.00144 = 0.00033 \text{ s}$$

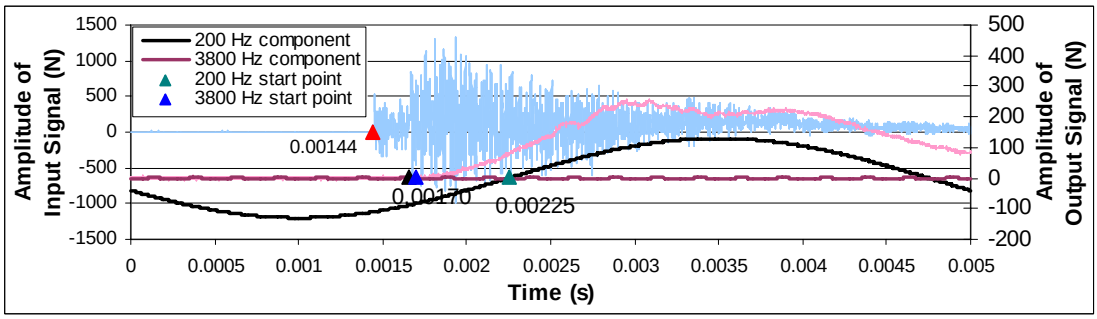


$$T\big|_{f=200} = 0.00225 - 0.00144 = 0.00081 \text{ s}$$

$$T\big|_{f=3800} = 0.00170 - 0.00144 = 0.00026 \text{ s}$$

Average time interval:

$$\overline{T}\big|_{f=200} = 0.0008 \text{ s} \qquad \overline{T}\big|_{f=3800} = 0.0003 \text{ s}$$

Component velocity along ring walls:

$$V\big|_{f=200} = 200.5 \text{ m/s} \qquad V\big|_{f=3800} = 544.2 \text{ m/s}$$